Silk Based Tissue Engineered Strategies to Repair Damaged Intervertebral Disc

A Thesis

Submitted in Partial Fulfillment of the

Requirements for the Degree of

DOCTOR OF PHILOSOPHY

by

BIBHAS KUMAR BHUNIA

Department of Biosciences and Bioengineering

Indian Institute of Technology Guwahati

Guwahati – 781039, Assam, India

July 2021

Dedicated to my

Family and Friends

INDIAN INSTITUTE OF TECHNOLOGY GUWAHATI

DEPARTMENT OF BIOSCIENCES AND BIOENGINEERING

STATEMENT

I do hereby declare that the research findings of this thesis is the result of research work carried out by me in the Department of Biosciences and Bioengineering, Indian Institute of Technology Guwahati, Guwahati, India, under the supervision of **Prof. Biman B. Mandal.**

As per the general norms of reporting research findings, due acknowledgments have been made, wherever the research findings of other researchers have been cited in this thesis.

Bibhas Kumar Bhunia

Date: 18.03.2022 **Bibhas Kumar Bhunia**

INDIAN INSTITUTE OF TECHNOLOGY GUWAHATI

DEPARTMENT OF BIOSCIENCES AND BIOENGINEERING

CERTIFICATE

It is certified that the work described in this thesis entitled "**Silk based tissue engineered strategies to repair damaged intervertebral disc**" by **Mr. Bibhas Kumar Bhunia** for the award of degree of Doctor of Philosophy is an authentic record of the results obtained from the research work carried out under my supervision in the Department of Biosciences and Bioengineering, Indian Institute of Technology Guwahati, India, and this work has not been submitted elsewhere for the award of any other degree.

Bibhas Kumar Bhunia

CERTIFIED

Bibhas Kumar Bhunia
(Candidate)
Roll No: 146106029

Biman B. Mandal, Ph.D.
(Thesis Supervisor)

ACKNOWLEDGEMENT

My heart fills with gratitude to acknowledge the people in my life for their constant support and motivation throughout without whom my Ph.D. would not have been successful.

First and foremost, I would like to express my sincere gratitude to my Ph.D. advisor **Prof. Biman B. Mandal** for his continuous support and encouragement. His guidance helped me throughout the whole duration of my research and writing of this thesis. I thank him for his valuable suggestions during lab meetings. Without his support and guidance, it would have been impossible for me to complete this thesis work.

I would also extend my gratitude to the esteemed members of my Doctoral Committee (DC), Dr. Shankar Prasad Kanaujia (DC chairperson), Dr. Senthilkumar Sivaprakasam, Dr. Rajkumar P. Thummer, and Dr. Pranjal Chandra (former DC member), Department of Biosciences and Bioengineering (BSBE), for their valuable and constructive suggestions throughout this journey.

I would like to thank the present and former Heads of the BSBE department, Prof. Latha Rangan, Prof. Kannan Pakshirajan, and Prof. V. Venkata Dasu for providing the necessary facilities including infrastructural and departmental central instruments facilities (DCIF) that helped me to pursue my research at IIT Guwahati.

I am also grateful to all faculty members and staffs of Dept. BSBE, R&D section, Student Affairs and Academic section for supporting me throughout my Ph.D. tenure. I would also like to thank all the staffs and scientific officers of central instruments facilities (CIF), IIT Guwahati for providing high-end equipment to execute my experiments.

I would like to thank the funding agencies that provided me the financial support to conduct my research. I am grateful to Department of Biotechnology (DBT), Department of Science and Technology (DST), Department of Atomic Energy (DAE), Science and Engineering Research Board (SERB), and Defence Research and Development Organization (DRDO), Government of India, for supporting the research grants. I am grateful to Ministry of Education (MoE) and IIT Guwahati for the fellowship during my Ph.D. tenure.

It is my pleasure to thank my current lab members Shreya, Yogendra, Prerak, Janani, Joseph, Ashutosh, Souradeep, Bibrita, Chitra, Dipanwita, Ananya, Sayanti, Saptarshi, Subham, Amritha, Rupam, Nakhul, Priyanka for their feedback and cooperation. I would also like to thank former lab members Dr. Manishekhar, Dr. Praveen, Dr. Dimple, Dr. Ankit, Dr. Rocktatpal, Dr. Biswajeet, Dr. Deepika, Dr. Chandramauli, Dr. Bhaskar, Dr. Aparajita, Dr. Vimal, Dr. Rajiv, Omkar, Sohenii and Salma for sharing their knowledge and stimulating discussion with me. I would also like to thank Sween, Rnajana, Surojeet, Ahana, Korah, Deepak, Mayurakkhi, Garima, Mimi, Prateek, Bharat, Washim, Kunal, Sadanand, Smriti, Anupam, Gaurang, Nikhil, Shivanshi, Tarishi, Manisha, Sanu, Rituparna, Madhurima, Princy, Shakshi, Ayushi, Triya, Soumashree, Swapnil, Priyanka (Ranta), Prerana, Vaishali, Jenny, Sangeeta, Sangetha, Neelabho, Rishabh, Namit, and Suvro for their great company during my Ph.D. journey. Thank you all for constantly providing the friendly environment in the lab.

My special thanks to Dr. I Putu Mahendra with whom I have gathered some great memories while working together as colleagues, particularly during Covid-19 pandemic situation.

I would like to extend my sincere gratitude to Dr. Uttam Manna and his research team, and Dr. Shyam Biswas and his research team, Department of Chemistry, IIT Guwahati, and Dr. Biswatrish Sarkar and his research team, BIT Mesra for the scientific collaboration.

I wish to thank my co-authors Prof. David L. Kaplan, (Tufts University, U.S.A.), Dr. Nandana Bhardwaj (IIIT Guwahati), Souradeep, Ashutosh, Yogendra, Dr. Rocktatpal, Dr. Deepika, Dr. Adil, Dr. Rana, Janani, Saket and Arpita. I would also like to thank Dr. Bruce Panilaitis, (Tufts University, U.S.A.), Shreya and Lohe for assistance during the *in vivo* testing and also, I acknowledge the support provided by National Institute of Pharmaceutical Education and Research (NIPER), Guwahati, India in animal experiments. I thank to Dr. M. Agarwala, GNRC, North Guwahati, for providing human umbilical cord samples which were used to isolate Wharton's Jelly for my thesis work. My special thanks to Joseph who always helped me in scientific experiment and improving in my writing skill in this journey. I would like to acknowledgement all the individuals who supported me throughout and contributed significantly to the outcome of this thesis work, their time and their effort is greatly appreciated.

My sincere thanks to all the news reporters who conveyed our research to the common people throughout India.

Last but not the least; I would like to thank my family for supporting me throughout this journey. Simple thanks are not enough to convey my deep respect and gratitude towards my family.

Thanks to God, The Almighty for showering his grace to complete my research work successfully.

Bibhas Kumar Bhunia

BIBHAS KUMAR BHUNIA

CONTENTS

(dWJECM) for nucleus pulposus (NP) tissue replacement therapy

ABBREVIATIONS

µL	Microliter
µm	Micrometer
3D	3-dimentional
AA	*Antheraea assamensis*
AAV	Adeno-associated virus
ADAMTSs	Disintegrins and metalloproteinases with thrombospondin motifs
ADMSCs	Adipose derived rat mesenchymal stem cells
AF	Annulus fibrosus
AM	*Antheraea mylitta*
ASCs	Adipose stromal cells
ASTM	American society for testing and materials
BDDE	1,4-butanediol di-glycidyl ether
BDNF	Brain-derived neurotrophic factor
bFGF	Basic fibroblast growth factor
BI	Biomaterial ink
BM	*Bombyx mori*
BMDCs	Bone marrow derived stem cells
BMG	Bone matrix gelatin
BMPs	Morphogenic proteins
BSA	Bovine serum albumin
CA	Carrageenan

Abbreviations

CAD	Computer aided design
CEP	Cartilaginous endplates
CMC	Carboxymethylcellulose
CS	Chondroitin sulfate
CTGF	Connective tissue growth factor
DLP	Digital light processing
DLS	Dynamic light scattering
DMEM	Dulbecco's modified eagle medium
DMMB	1,9-dimethylmethylene blue
DNA	Deoxyribonucleic acid
DOD	Droplet-on demand
DTGS	Deuterated triglycine sulfate
DWI	Diffusion weighted imaging
dWJECM	Wharton's jelly extracellular matrix
ECM	Extracellular matrix
EDC	1-ethyl-3(3-dimethyl aminopropyl) carbodiimide
EDTA	Ethylenediaminetetraacetic acid
EGF	Epidermal growth factor
ESI	Epidural steroid injection
FB	Fibroblast cell layer
FBS	Fetal bovine serum
FDA	Food and drug administration
FGF	Fibroblast growth factor
FTIR	Fourier transform infrared spectroscopy

FWHM	Full width half maxima
G′	Storage modulus
G″	Loss modulus
GAPDH	Glyceraldehyde-3-phosphate-dehydrogenase
GDF-5	Growth and differentiation factor-5
GDR	German democratic republic
GelMA	Methacrylate gelatin
GFP	Green fluorescence protein
GFs	Growth factors
GG	Gellangum
GG-MA	Gellangum methacrylate
GPa	Gigapascal
GT	Gelation time
h	hour
H&E	Hematoxylin and eosin
h/m/sMWBM	High/medium/short molecular weight *B. mori*
HA	Hyaluronic acid
hADSCs	Human adipose derived stem cells
hBMSCs	Human bone marrow derived stem cells
HCL	Hydrochloric acid
HIF-1α	Hypoxia inducible factor-1α
HRP	Horseradish peroxidase
IAF	Inner annulus fibrosus
IDD	Intervertebral disc degeneration
IDE	Investigational device exemption

IGF-1	Insulin like growth factor-1
IHME	Health Metrics and Evaluation
IL-1, -6	Interleukin-1, -6
IPN	Interpenetrating network
iPSCs	Induced pluripotent stem cells
ITS+	Insulin, transferrin, and selenious acid
IVD	Intervertebral disc
KBR	Potassium bromide
kDa	Kilo Dalton
kPa	Kilopascal
kV	Kilo volt
LBP	Low back pain
LiBr	Lithium bromide
LIFT	Laser-induced forward transfer
LMP	Laminin-mimetic peptides
LMP-1	Latent membrane protein-1
LPS	Lipopolysaccharide
LS	Lamellar scaffold
LVER	Linear viscoelastic region
M	Mole
MAPK	Mitogen activated protein kinase
mg	Milligram
mL	Milliliter
mm	Millimeter
mM	Millimole

Abbreviations

MMPs	Matrix metalloproteinases
MPa	Megapascal
MPCs	Mesenchymal precursor cells
MRI	Magnetic resonance imaging
MSCs	Mesenchymal stem cells
mTOR	Mammalian target of rapamycin
MW	Molecular weight
N	Newton
NBF	Neutral buffered saline
NCM	Notocordal cells-rich-matrix
NF-κB	Nuclear factor kappa B
ng	Nanogram
NGF	Nerve growth factor
NHS	N-hydroxysuccinimide
nM	Nanomole
nm	Nanometer
NO	Nitric oxide
NP	Nucleus pulposus
NSAIDs	Nonsteroidal anti-inflammatory drugs
OAF	Outer annulus fibrosus
OP-1	Osteogenic protein-1
p(HEMA-co-APMA)g-PAA	Polyhydroxyl-ethyl-methacrylate-co-N-(3-aminopropyl)-methacrylamide grafted with polyamidoamine
PAN	Polyacrylonitrile

PBS	Phosphate buffered solution
PCL	Poly(ε-caprolactone)
PD	Parallel direction
PDLLA	Poly(d,l-lactide)
PDMS	Polydimethylsiloxane
PDN	Prosthetic disc nucleus
PEAD	polycation poly(ethylene argininylaspartate diglyceride
PEGDA	Poly (ethylene glycol) diacrylate
PG	Proteoglycan
pg	Picogram
PGA	Polyglycolic acid (PGA)
PLGA	Poly(lactic-co-glycolic)
PLLA	Poly (L-lactic acid)
PNIPPAm	Poly(N-isopropyl acrylamide)
POM	Poly(1,8-octanediol malate)
PPCLM	Poly(polycaprolactonetriol malate)
PPCLM	Poly(polycaprolactonetriol malate
PPD	Perpendicular direction
PPS	Pentosan polysulphate
PR	*Philosamia ricini*
PRP	Platelet rich plasma
PTMC	Poly(trimethylene carbonate)
PTMC	Poly(trimethylene carbonate)
PU	Polycarbonate urethane

PVA	Polyvinyl alcohol
PVP	Poly(vinyl pyrrolidone)
RGD	Arginine-glycine-aspartic acid
RNAi	RNA interferences
ROS	Reactive oxygen species
RT	Room temperature
RT-PCR	Real time polymerase chain reaction
SD	Standard deviation
SDS	Sodium dodecyl sulfate
SEM	Scanning electron microscopy
SF	Silk fibroin
sGAGs	Sulfated glycosaminoglycans
SLRPs	Small leucine-rich proteoglycans
SNP	Single nucleotide polymorphism
STMP	Trisodium trimetaphosphate
SVF	Stromal vascular fraction
tan δ	Loss modulus/storage modulus
TCP	Tissue culture plate
TDR	Total disc replacement
TGF-β	Transforming growth factor-β
TIMPs	Tissue inhibitors of MMPs
TNF-α	Tumor necrosis factors-α
TT	Translucent time
TZ	Transition zone
UTM	Universal testing machine

v/v	Volume/volume
VDR	Vitamin D receptor
VEGFs	Vascular endothelial growth factors
VEP	Vertebral end plate
VNTR	Variable number of tandem repeats
VP	Vacuum phenomena
VT	Viscous time
w/v	Weight/volume
WAXD	Wide angle x-ray diffraction
WJ	Wharton's Jelly
YLDs	Years lived with disability
γ	Shear strain
η*	Complex viscosity
µg	Microgram
ω	Angular frequency

LIST OF TABLES

LIST OF FIGURES

CHAPTER 6

Chapter 1

Introduction and Literature Review

Introduction and Literature Review

1.1. Introduction

Low back pain (LBP) is considered as one of the most common musculoskeletal problem associated with socio-economic conditions affecting the population indiscriminately across the globe. It is the leading cause of disabilities and absenteeism from work, and the second most common reason for visit to the doctor. LBP is commonly classified into three broad categories *i.e.,* (i) acute when pain lasts for > 6 weeks, (ii) sub-acute when patients continue to experience the pain up to 3 months, and (iii) chronic if it lasts for more than 3 months[1]. In fact, LBP is considered as first appeared symptom of intervertebral disc (IVD) degeneration (IDD), which is eventually transformed into more serious pathophysiological problems like disc herniation. Approximately 80% of the global population experiences LBP at some point in their lifetime. According to the US national health interview survey, 2018, 31.6% of women and 28% of men aged ≥ 18 had experienced LBP in past three months[2]. Several factors *viz*., age, sex, poor education and low socioeconomic status, previous history of spine problems, physical factors like holding or lifting of heavy objects, habitual poor standing or sitting, prolonged static posture, types and frequency of sport activities, and psychological factors including stress, anxiety and depression have been found to be associated with the prevalence and years lived with disability (YLDs) of LBP[3]. According to the GBD (the global burden and disease, injuries and risk factor study) report, the global LBP prevalent population was approximately 577 million in 2017, wherein the prevalence was higher in females than males and increased with the age[4]. In 1990, the global YLDs of LBP were 42.5 million which was increased by 52.7% to 64.9 million in 2017. However, the prevalence of LBP in India has also reached to the alarming situation with the range from 42% to 83% of the population[5, 6]. A recent report shows that the prevalence of LBP is 42.4% per year and 22.8% per week in young Indian population age bracket between18 and 35[7]. A large variation in prevalence of LBP (as low as 6.2% to high as 92%) has been found due to the heterogeneity of lifestyle and occupational groups of Indian population. For instance, the high prevalence of LBP has been shown in case of cotton spinning workers (65.86%), dental professionals (70.23%), long distance truck drivers of mountainous terrain (73.53%), zari workers of urban slum (76.35%) and construction workers (92.54%)[3]. Moreover, the socioeconomic and

educational status also play important roles in prevalence of LBP. It is reported that the prevalence of LBP is higher (7.5%) in rural areas than the urban areas (5.5%). The population with low PCI (per capita income) and primary or middle level education are shown to be suffering from musculoskeletal problem more commonly (91.9%) than the population with higher PCI (8.1%)[8-10].

LBP imposes a serious economic burden on society and family. This is directly related to the high healthcare expenditures and indirectly by disability or loss of productivity. According to a study of Institute for Health Metrics and Evaluation (IHME), the total cost of LBP and other musculoskeletal disorders was an estimated of $ 380 billion in 2016, wherein low back and neck pain exhibited the highest expenditures ($ 134.5 billion) in U.S.A. A cohort study on nearly 2.5 million patients of LBP between 2008 and 2015 in U.S.A. showed that only 1.2% patients received surgery and the expenditure was ~ 29.3% of their total 12-month costs ($ 784 million). The remaining 98.8% patients accounted for $ 1.8 billion for receiving the care and clinical guideline for LBP[11]. In India also, the treatment cost is not so much affordable as the estimated cost ranges from $ 5,000 to $ 12,000 depending on person, surgeons, types of surgery and post treatment, hospitals and cities where the surgery is going to be performed. However, expenditures are expected to be increased in coming days.

1.1.1. Anatomy, physiology and function of intervertebral disc (IVD)

It is of foremost importance to acquire the comprehensive knowledge on anatomy, function and pathophysiology of intervertebral disc (IVD) in order to understand the proper research direction for prevention and reversal of IDD. IVD is the fibrocartilaginous cushion like organ lying between two adjacent vertebrae surrounded by muscles and ligaments. There are total 23 IVDs (8-10 mm in height and ~ 4 cm in diameter) in the human spinal column comprising ~ 25% of total column height. The size of discs varies from region to region; the dimension of lumber discs is greater as compared to cervical discs, although they possess nearly similar biochemical compositions. IVDs provide mechanical support and flexibility to the spine transmitting the loads from body weight and muscle tension during our daily activities. The estimated pressure inside a disc is shown to be ~ 0.1 MPa when lying, 0.95 MPa during jogging, and 2.3 MPa when lifting 20 kg weight[12]. IVDs actually act as ligament to hold all the vertebrae together allowing the spine to move in three planes i.e., flexion-extension, axial rotation, and lateral bending. Overall, IVD also acts as shock

absorber that prevents the vertebrae from grinding against one another[13]. IVD is composed of three main distinct components; 1) annulus fibrosus (AF), (2) nucleus pulposus (NP), and 3) vertebral end plate (VEP) (**Figure. 1.1**)[14].

1.1.1.1. Annulus fibrosus (AF)

AF is an intrinsically complex tissue that consists of 20-25 concentric rings surrounding the gelatinous NP tissue. These rings are mainly composed of collagen nano-fibers oriented at the angle varies from ± 30°-60° (from the central NP outward to the edge of the disc) against its vertebral axis, but in successive layers forming a criss-cross structure[15]. This angle-ply criss-cross structure provides the high mechanical strength to IVDs. The tensile and compressive moduli of AF tissue have been shown to be in the ranges 0.5-29 MPa and 0.5-1.5 MPa, respectively[16]. The lamellar alignment of collagen fibers in AF tissue is mainly due to the precise and identical organization of AF cell-sheets established during the early foetal developmental stage[17]. The cell surface heparan sulfate proteoglycan (syndecan-4) plays the potential role in lamellar organization of these collagen fibers interacting between actin cytoskeleton of AF cells and nascent extracellular matrix molecules[18]. In the healthy IVDs, AF is comprised of more than 2/3 collagen (50-70% per dry weight), elastin (2% per dry weight) and lesser amount of water (65-80%) and proteoglycans (PGs, 10-35% per dry weight) as compared to NP tissue[19] [20-22]. The most abundant collagen type in AF is type I, although very less amount of collagen type II and III are also present. The PGs and elastin fibers are found in the areas between lamellae[23]. The elastin fibers extend radially and orthogonally from one lamella to another acting as binder of all lamellae and allow the collagen fibers to return to their original arrangement following flexion-extension. AF layers are strongly adhered to the vertebral endplates (VEP), wherein the collagen fibers are firmly attached to the anterior and posterior longitudinal ligaments, and VEP[24]. However, this attachment is relatively weaker for posterior longitudinal ligaments as compared to anterior part. This fact can be correlated with the frequent incidence of posterior protrusions than anterior bulging[14].

The AF can be subdivided into two layers; outer (OAF) and inner AF (IAF). In OAF, the layers are highly organized and densely packed with collagen fibers, whereas IAF consists of less fibers and few orientations[20]. The biochemical and biomechanical properties remarkably alter along the radial direction. The proportion and the organization of extracellular matrix (ECM)

components vary with the spatial position in AF. For instance, concentration of type I collagen increases towards the OAF layers, whereas type II collagen increases towards center. Similarly, aggrecan content is higher in the inner layers of AF (11-20%) than the outer layers (5-8%)[25]. Such variations in ECM composition are maintained by the specific cell types that reside in that spatial region and their associated cellular activities in the corresponding zone possessing different biophysical environments. This regional distinction in cellular function and ECM composition play a vital role on biomechanics of the discs. For example, the outer layers of AF resist the tensile stresses, whereas compressive loads are compensated by IAF[26].

The AF contains nearly 9 x 10^6 cells.cm^{-3} which are arranged parallel to the collagen fibers within the concentric lamellae. The cells are fibrochondrocytic in nature as they express both types of markers; collagen type I for fibroblasts, and collagen type II and aggrecan for chondrocytes[27, 28]. The cells of IAF and toward the NP are mostly oval in shape and chondrocytic in nature, whereas the cells of OAF tend to be thin and elongated possessing the fibrochondrocytic characteristics[29]. One unique feature of IVD cells is that of thin cytoplasmic projections (> 30 mm) differentiating them from articular cartilage cells. The function of these projections is mostly unknown, but it has been hypothesized that they may have the important role in mechanical sensing[30]. In addition, small free nerve endings can also be found penetrating up to 3 mm into the OAF layers[31]. These nerves are designated as Luschka nerve or sinuvertebral nerve originated from ventral ramus and are mainly associated with discogenic pain.

1.1.1.2. Transition zone (TZ)

The zone that separates AF to NP is called transition zone (TZ). The TZ is observed to be an area of high metabolic activity and, sensitive to physical forces and also to the chemical and hormonal regulations. TZ is referred as an area of remodeling and growth plate of NP.

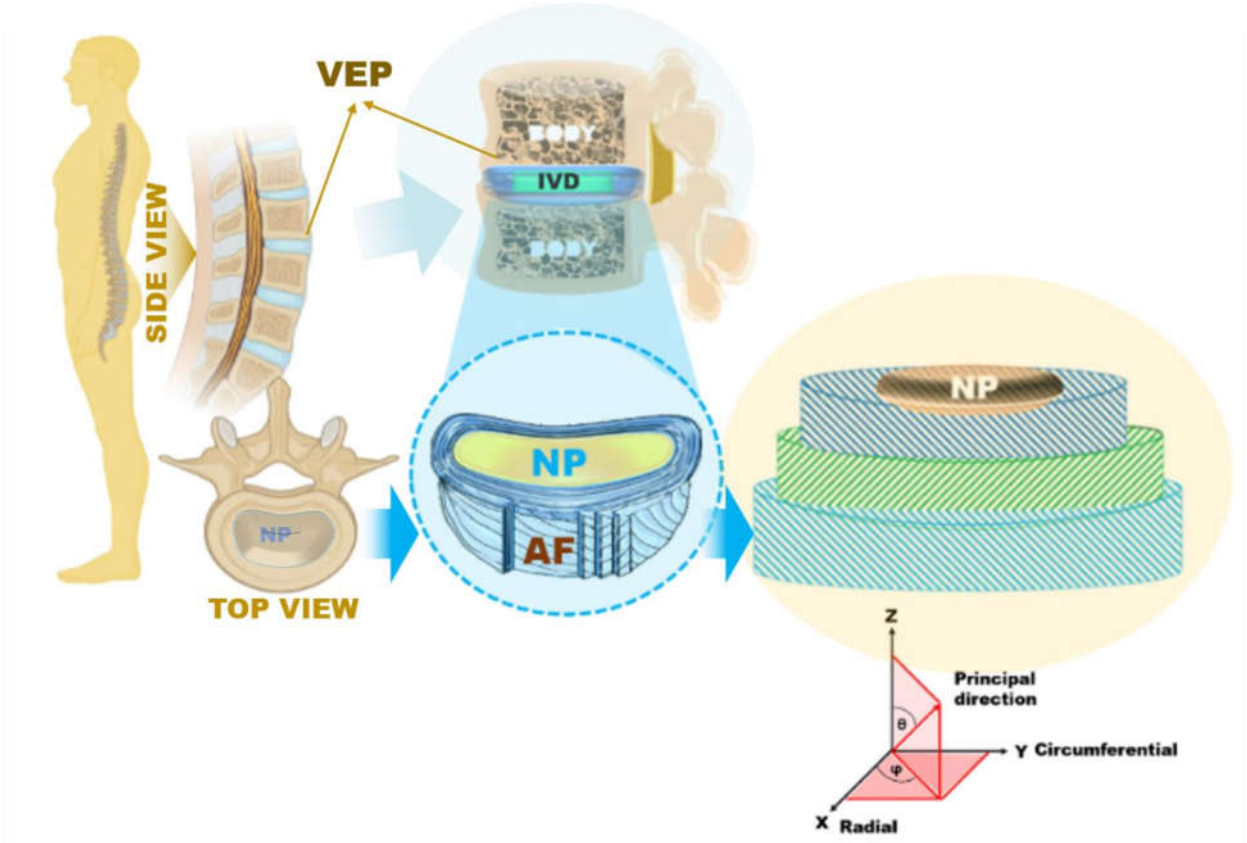

Figure 1.1. Schematic diagram illustrating anatomy of intervertebral disc.

1.1.1.3. Nucleus pulposus (NP)

The central gelatinous NP tissue is mainly composed of hydrophilic extracellular matrix including PGs (25-60% per dry weight), randomly organized collagens (10-25% per dry weight), irregularly shaped elastin fibers (less dense than AF tissue), water, and few chondrocytes[22]. It mainly consists of high amount of water (~ 90%), and the rest is a composite of proteins and polysaccharides in the ratio of 1:2[32]. The predominant type of collagen is type II and the concentration of which is gradually decreased towards the periphery. However, other collagen types including collagen III, VI and IX are also present in minor quantities. Moreover, significant amount of some non-collagenous proteins like elastin, laminin and fibronectin are also found in NP[33]. The elastin fibers in NP are oriented radially and vertically integrating into the VEP[23]. The most prevalent PG in NP tissue is aggrecan which is covalently linked to the highly sulfated glycosaminoglycans (sGAGs) like hyaluronic acid (HA), chondroitin sulfate and keratin sulfate providing negative charge to the matrix. In a healthy disc, this negatively charged composite gel

maintains the osmotic pressure by taking up high amount of water allowing it to swell and distributes the hydrostatic loads to the surrounding AF tissue[34, 35]. Apart from this major PG *i.e.,* aggrecan, minor quantities of small PGs *viz.,* versican, decorin, lumican, biglycan and fibromodulin are also found in NP gel[36]. All of these small PGs molecules are mainly involved in repairing the extracellular matrix (ECM) of NP[37].

NP tissue is not only composed of extracellular matrix (ECM) components, but also contains around 4×10^6 NP cells.cm^{-3} which is quite lower than the surrounding AF tissue (~ 9×10^6 cells.cm^{-3})[20]. These cells are round in morphology with larger cytoplasm and more complex structure compared to AF cells[38]. At least two distinct sets of cell population are found in NP. The first type is small and round in morphology similar to the chondrocytes, whereas the later type is relatively larger in size and vacuolated in appearance with prominent cellular processes and deposited intracellular glycogen particles. These later type cells are thought to be descended from notochord at the time of embryonic development and gradually disappear after birth[39, 40]. However, other reserachers suggest the integration and migration of these cells from IAF or VEP replacing the notochordal cells, gradually[41]. Though NP cells have low mitotic and regeneration capability, they can survive under certain stress conditions like low pH, hypoxia, and low glucose level. In disc degeneration, a larger portion of NP cells undergo apoptosis and senescence that finally leads to the overall loss of NP matrix followed by decrease in water content[28, 42]. NP cells express the chondrogenic markers *e.g.,* sox9, col II and aggrecan, and also possess some specific markers like CD24, CA12, HIF-1, OVOS2, PAX1, KRT19 and FOXF1[1, 38, 43, 44]. KRT19 is the specific marker expressed both in human NP and AF cells, but in latter case it is relatively less expressed providing the additional distinguishing characteristic of NP cell to AF cells[45]. NP tissue also contains some immune cells e.g., macrophages, lymphocytes and T-cells, and their number is shown to be gradually increased with age. They are actively involved in sensitization and growth of new sensory neurons[46-48].

In a healthy disc, NP gel releases pressure and water molecules to the surrounding AF tissue upon compression, and water molecules in turn get back to the NP upon decompression, driven by osmotic force. This pumping effect is very crucial to maintain the disc biomechanics (unconfined compressive modulus of 3–6 kPa)[49, 50]. However, this load transfer mechanism gets disrupted

in disc degeneration as the water content of NP gel gradually decreases resulting in declined hydrostatic pressure[51].

1.1.1.4. Vertebral end plate (VEP)

Vertebral endplates (VEP) or cartilaginous endplates (CEP) is the most cephalad and caudal region (superiorly and inferiorly) of the IVD separating AF and NP from the adjacent vertebral body. The fine collagen fibers (collagen II) of IAF and NP are deeply integrated into the VEP. It is mainly formed by a layer of hyaline cartilage and the thickness of it varies inferior to 1 mm depending on different zones. It is relatively thinner in the central portion where it interacts with NP tissue[52, 53]. However, the thickness gradually decreases with age. Though the biochemical composition of VEP is very similar to the other regions of disc, it has its own unique morphology and functions other than AF tissue and vertebral body. VEP is primarily composed of PGs reinforced by collagen fibers (predominantly type II). This collagen network is mostly accumulated at the periphery of VEP, whereas the central area consists of PGs and water[54]. This unique morphology helps in nutrient exchange through diffusion to the interior portions of the discs from the adjacent subchondral bone. In the early stages of life, VEP remains highly vascularized, but dramatically decreases within 1 year of life, and completely devoid of blood vessels by third decade[55]. It has three main functions; 1) safeguarding the vertebral body ends from stress, 2) confining the AF-NP boundaries, and 3) exchange of nutrient and waste to the disc interior.

1.1.2. Degeneration of IVD or degenerative disc disease (IDD)

Intervertebral disc degeneration (IDD) is one of the major causes of LBP and disabilities. IDD is a complex multifactorial phenomenon influenced by the natural aging process, pathological issues, altered disc nutrition and transport, and mechanical injuries. It is characterized by disc cells death, loss of extracellular matrix (ECM), and upregulation of matrix metalloproteinases (MMPs) that cause the gradual dehydration of NP gel transforming it more fibrous in nature. All these facts lead to an imbalance in intradiscal pressure resulting reduction of shock-absorbing capacity of IVDs. However, it is believed that the early stages of degeneration, in particular the degradation of aggrecan and collagen, mainly start from the NP. As degeneration progresses, the “slit-like” spaces are created in NP, which are then propagated through AF by disrupting the collagen and elastin networks. This creates the radial fissures in the multilamellar AF initiating the irreversible

degenerative cascade in IVD structure. Due to this degeneration, the ratios of different collagen types and their crosslinking appear to be altered resulting in inferior disc mechanical properties[56]. As discs lose height, they may bulge out pinching the nearby central nerve or rub together leading to LBP. Some pains are also associated with the nerve (Luschka nerve) or bony ingrowth inside the degenerated discs[57, 58]. The following are the most important causes of disc degeneration discussed below.

1.1.2.1. Imbalance in matrix turnover

The disintegration of extracellular matrix (ECM) is a hallmark characteristic of disc degeneration. Matrix or protein turnover is the normal process in healthy cells. In IDD, imbalance in matrix turnover is influenced by over expressions and activities of catabolic factors *e.g.,* matrix metalloproteinases (MMPs), Disintegrins and metalloproteinases with thrombospondin motifs (ADAMTSs), cytokines (IL-1 and -6), nitric oxide (NO) and prostaglandin E2 rather than the anabolic factors[59]. There are different types of MMPs with distinct function of each. For instance, MMP-1, 8 and 13 act on collagen, MMP-2 and 9 act as gelatinase, and MMP-3 acts as stromelysin[60]. The MMP-3 and 8 are consistently and substantially expressed in degenerated discs. This is also associated with the up-regulation of tissue inhibitors of MMPs-1 and 2 (TIMPs) which are the endogenous inhibitors regulating MMPs activities[61]. ADAMTS-4 (as aggrecanase-1) and ADAMTS-5 (as aggrecanase-2) are two major aggrecanases, which are found to be highly expressed in degenerated discs[62]. These catabolic activities of MMPs and ADAMTSs are balanced by TIMPs in IVD matrix. However, the expression and activities of these regulatory genes are modulated by several factors including aging, different kind of stresses like oxidative, mechanical and inflammatory stress, several kinds of environmental and habitual factors like smoking, physical injuries, excessive mechanical strain, and genetic predispositions.

1.1.2.2. Inflammatory pathways

The Inflammatory pathways are also closely associated with IDD. Elevated levels of various cytokines including tumor necrosis factors (TNF-α), interleukin-1 and 6 (IL-1 and IL-6) are often detected in degenerated discs[63-65]. IL-1 up-regulates the expressions of ADAMTS-4, MMP-3, and 13 as well as down-regulates the ECM-specific genes[66]. Similarly, TNF-α also influences the expressions of MMPs and few catabolic mediators *e.g.,* NO and prostaglandin E2[62]. The

degenerating discs also release brain-derived neurotrophic factor (BDNF) and nerve growth factor (NGF) that also play the vital role in activation of immune cells as well as releasing inflammatory cytokines[67]. These cytokines mainly sensitize the nerves or/and promote the neurite growth in the degenerated disc. In addition, the acidic pH of degenerated disc can also promote the production of both BDNF and NGF, thereby stimulating inflammatory pathways in back pain[68].

1.1.2.3. Oxidative stress

With the growing age, the oxidative damage also plays a key role in disc degeneration[62]. The reactive oxygen species (ROSs) are shown to be generated by disc cells in response of these cytokines. In addition, the oxidative stress in degenerating discs is also the result of neovascularization, wherein IL-1β activates the vascular endothelial growth factors (VEGFs) inducing angiogenesis when the aged discs accumulate fissures.

1.1.2.4. Altered disc nutrition and cell death

IVD is the largest avascular organ in the body, though very small blood vessels can be found penetrating 1-2 mm into the OAF layers. The disc nutrition and waste exchange mainly depend on the diffusion based mechanism through VEP. Unfortunately, this diffusion capacity is shown to be very poor even in healthy discs and reaches to the worst when discs are degenerated. In a computational study, the concentration of glucose is calculated to ~ 5 mM at the AF boundary, whereas the value is ~ 0.8 mM at the center of a healthy disc, which can be decreased to below critical concentration in degenerating discs[69]. In the aged or degenerated discs, calcium phosphate crystals are deposited (known as calcification) on the VEP surface hindering the diffusion process[70]. This increasing level of deposited calcium on VEP surface reduces the secretion of ECM components by disc cells through activation of extracellular calcium sensing receptor[71]. Moreover, the disc microenvironment is anaerobic in nature due to the low oxygen diffusion. The cells mainly perform anaerobic respiration with lactate (typical range of 2-6 mM) as a by-product creating acidic microenvironment inside the discs[72]. However, pH can be further decreased to as low as 6.1 when discs are, particularly, in stress[73]. In this low pH environment, cells stop metabolism contributing to further disc matrix distortion.

1.1.2.5. Genetic predisposition

The genetic predisposition has also been confirmed to contribute to disc degeneration. It is mainly associated with the polymorphisms or mutations in the genes (*e.g.,* collagen, MMPs, aggrecan and cytokines) involved in ECM turnover of the discs. For instance, a Sp1 polymorphism in collagen gene, particularly at the binding sites of transcription factors for *COL1A1* gene, is linked to disc degeneration[74, 75]. This polymorphism alters the ratio of *COL1A1*and *COL1A2* proteins increasing the risk of disc degeneration[76]. In addition, due to the mutations in *COL9A2* and *COL9A3* genes, the polar amino acid is replaced with the hydrophobic amino acid tryptophan disrupting the intra-chain interactions in the collagen triple helix[77]. This tryptophan in collagen chain also inhibits the lysyl oxidase involved in cross-linking among the collagen chains forming the networks, thus helping onset and progression of age-related disc degeneration. Similarly, a single nucleotide polymorphism (SNP) in *MMP-3, IL-1* and *-6* genes, variable number of tandem repeats (VNTR) polymorphism in aggrecan gene, and VDR (vitamin D receptor) gene polymorphisms (TaqI and FokI) have also been observed to be associated with the disc degeneration[78-82].

1.1.3. Current diagnostic tools

There is a need for a proper diagnosis system to manage the growing prevalence of asymptomatic IDD. Though researchers have developed several methods, magnetic resonance imaging (MRI) is thought to be the most clinically effective method to analyze the disc degeneration by measuring water content, height, tears or any irregularities in the discs[83]. MRI has several advantages over the existing methods. For instance, it is a radiation free process that allows multiplanar evaluation and precise interpenetration of the discs offering great potential for diagnosis of disc degeneration. Recently, several MRI-based imaging tools including diffusion weighted imaging (DWI), zoomed echo-planar diffusion tensor imaging, and multi-detector computed tomography scan are being used in diagnosis of IDD[84]. The DWI utilizes anisotropic diffusion data to analyze and visualize the peripheral nerve roots in the degenerated discs[85]. Similarly, the zoomed echo-planar diffusion tensor imaging tools are also applied to assess the relationship of nerve fibers with disc degeneration. On the other hand, the multi-detector computed tomography scan measures the shape and distribution of the vacuum phenomena (VP) in the intradiscal area, which is significantly

linked to the degree of disc degeneration[86]. This VP is known as gaseous radiolucent area which is generally appears at the onset and progression of disc degeneration.

1.1.4. Grading of IDD

Modic *et al.,* first radiologically characterized the changes in VEP associated with IDD[87]. The Modic classification system describes three types of changes in degenerating disc. Type I is characterized by marrow edema, while the fatty infiltration of the marrow is the hallmark of type II grade. Finally, endplate sclerosis is observed in type III grade. However, nowadays the Pfirrmann grading system is being widely used, particularly in the research purposes[88]. This gradation is mainly based on the routine MRI T2 spin-eco weighted imaging of degenerated discs. According to this classification system, disc degeneration can be graded I through V. In grade I, disc is homogeneous with bright hyperintense white signal and the disc height is shown to be normal. Grade II is characterized by inhomogeneous, but possessing the hyperintense white signal and normal disc height can be seen. In grade III, discs height is slightly decreased and the AF-NP boundary becomes unclear. In grade IV, disc becomes inhomogeneous with a hypointense dark gray signal. Moreover, the AF-NP boundary disappears and the disc height is moderately decreased. Finally, grade V is characterized by collapsed disc with hypointense black signal. Later on, however, Griffith *et al.,* introduced a modified Pfirrmann grading system wherein 8-level grading system is used to discriminate the severity of degeneration in elderly spine[89].

1.1.5. Current clinical solutions for IDD

It is very important to correlate the concordant sign with imaging which is the routine practice performed, nowadays, to diagnose IDD. If symptoms are not correlated with MRI imaging, doctors usually suggest for the conservative management *e.g.,* resting, meditation, physiotherapy and medication like oral analgesia, rather interventional treatment as it is associated with several inherent risks like infection, recurrence of pain, neural injury, and many post-surgical complications. However, patients with significant symptoms of LBP who do not get desired benefits with this conservative treatment, can consider provocative discectomy. The details of all these strategies including conservative and intervention procedures are discussed below (**Figure 1.2**).

1.1.5.1. Conservative management

1.1.5.1.1. Physical exercises

The prime goal of the conservative management is to control the symptoms and relieve pain so that patients can resume their normal daily activities. After evaluating a patient, a physiotherapist designs the personalized back exercise program that improves the flexibility of tight muscles of back, buttock and hip positions helping the patient move easier and with less pain[90]. The physiotherapy includes stretching (*e.g.,* hamstring stretches and psoas major muscle stretches), strengthening (*e.g.,* dynamic lumber stabilization exercise) and low impact aerobic exercises (*e.g.,* water exercise, cycling and walking) that recover the spinal and hip joints mobility and load bearing capacity. Majority of the patients (up to 80%) with acute LBP get benefited from this conservative strategy over the course of few weeks[91]. Similarly, yoga is also often practiced to treat LBP. Yoga can improve LBP within three to six months with low- to moderate-certainty, when compared to non-exercise groups[92]. The clinical guidelines recommended by various countries discourage the bed rest as a part of LBP treatment. However, few guidelines (*e.g.,* Austria, Germany, New Zealand and Spain) recommend bed rest for a short period of time due to intense pain, but it should not be more than 2 days[93].

1.1.5.1.2. Medications

Recommendation of medicines for LBP treatment prescribed by doctors are generally consistent as given in various guidelines[93]. In most guidelines, paracetamol or acetaminophen is recommended as a first choice because of less evidence of side effects. Nonsteroidal anti-inflammatory drugs (NSAIDs) *e.g.,* ibuprofen and naproxen are the second choice if acetaminophen/paracetamol does not work. NSAIDs and acetaminophen are the class of drugs known as antipyretics (fever reducer) and analgesics (pain reliever) that reduce the prostaglandins production responsible for inflammation, swelling and pain. However, physicians also recommend for co-medication for pain relief *e.g.,* muscle relaxant, opioids, antidepressants, and anti-convulsion medications depending on the severity of symptoms.

Epidural steroid injection (ESI) is more effective in immediate relief for pain and possibly functions, when compared to conservative treatments. In this process, the anti-inflammatory drug

is directly injected into the epidural space of the spine. However, the effect is not sustained for prolonged period of time[94].

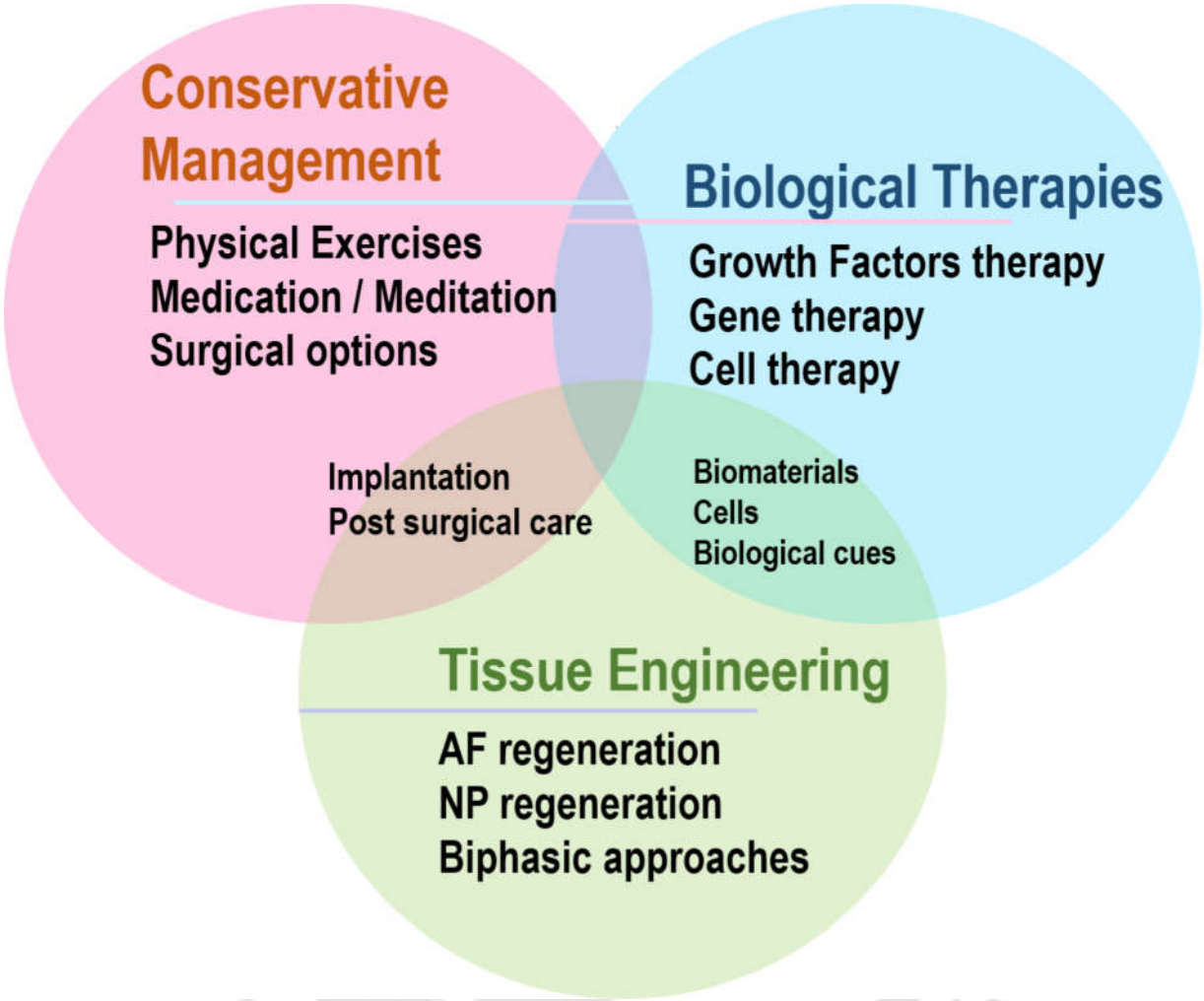

Figure 1.2. Current clinical strategies for treating disc degeneration

1.1.5.1.3. Percutaneous therapies

Patients who are diagnosed with advanced stages of disc degeneration (when disc herniates one-third or half of the canal diameter in MRI imaging) are suggested for the percutaneous therapies[95, 96]. These techniques are referred to as minimally invasive surgical procedures and are also considered as intermediate steps between conservative therapies and surgical options. It is generally prescribed for those patients who fail to recover from pain even after 4-6 weeks of conservative therapies and one course of steroid injection. Percutaneous therapies include mechanical, thermal and chemical depression, and biomaterial implantation[84]. Mechanical

decompression devices include metallic wires, spiral tips, and water/air driven suction cutting probes that remove ~ 1-3 g of tissue from the herniated portion of discs using fluoroscopic guidance, thus decompression occurs in spinal cannel[95]. Mechanical decompression is more effective technique than the conservative therapies in treating discogenic pain in terms of its efficacy and long-lasting pain relief[97]. Thermal decompression inactivates the cytokines involved in inflammation, and destroys the nociceptors in the periphery of the disc using thermal energy which is usually generated by lasers or radiofrequency probes[98]. In chemical decompression techniques, two main components *i.e.,* oxygen-ozone gas mixture and radiopaque gelified ethanol are commonly utilized to reduce the intradiscal pressure. Oxygen-ozone gas mixture is administrated into the NP space, which reacts with the glycosaminoglycans leading to the dehydration and shrinkage of the discs, thereby decompressing the nerve[99]. Similarly, injection of radiopaque gelified ethanol into the NP space also causes the dehydration and shrinkage of bulging disc, thereby releasing pressure from the OAF zone[100]. Comparatively, the usage of biomaterial based hydrogels with good biocompatibility in the management of disc pathology is relatively new and emerging technology that aims the NP tissue regeneration (*details are discussed in the section 1.1.5.2.3.2 and 1.2.1.3*).

1.1.5.2. Surgical options

Patients with severe pathology related to IDD that cannot be managed by conservative or percutaneous therapies are considered for surgical intervention. Three common surgical procedures currently used to treat the patients with severe stages of disc degeneration are (i) discectomy or disc removal, (ii) arthrodesis or spinal fusion, and (iii) arthroplasty or disc replacement.

1.1.5.2.1. Discectomy or disc removal

Discectomy is a common surgical process to remove the herniated materials of the degenerated discs that pinch the central nerve causing pain. This process typically leads to a loss in disc height and the associated biomechanics. Sometimes, discectomy is combined with laminotomy or laminectomy that removes the part or whole lamina, respectively, of the selected vertebrae. This combined process can relieve pain temporarily, but IVD tissue regeneration does not take place.

This process further accelerates disc degeneration and instability with the incidence of recurrence ranged as low as 3% to as high 36% within 6 to 24 months[101, 102].

1.1.5.2.2. Arthrodesis or spinal fusion

Due to several disadvantages of discectomy process, the clinicians turn to arthrodesis wherein two or more vertebrae adjacent to the diseased disc are fused together in a permanent way[103]. This technique restricts spine motions within the diseased section, thus decreases patient's received pain. Spinal fusion is often performed along with discectomy that removes the damaged disc. After discectomy, the free space of the disc between two vertebrae is packed with bone graft that maintains the correct disc height and induces ossification. The bone graft may be an autograft collected from patient's own pelvic bone or an allograft from bone bank. However, limited clinical success is achieved with this spinal fusion technique as it compromises with spine flexibility leading to a possible degeneration of the adjacent segments[104].

1.1.5.2.3. Arthroplasty or disc replacement

Unlike discectomy and arthrodesis, arthroplasty provides a relatively long-term solution to recurring disc degeneration. One of the major advantages of arthroplasty is the preservation of spinal movements like re-establishment of flexibility and unlimited axial rotation, thereby preventing the adjacent segments from further degeneration. Two main procedures of disc replacement are total disc replacement (TDR), and NP replacement.

1.1.5.2.3.1. Total disc replacement (TDR)

In TDR, the diseased disc is replaced with an artificial disc implant that provides biomechanics similar to the natural disc. The implantable artificial discs should be biocompatible, durable and most importantly, need the FDA (Food and Drug Administration, U.S.A.) approval. FDA looks into the Investigational Device Exemption (IDE) trials that allow the use of medical devices in human subjects. IDE permits the investigational devices for clinical research to collect safety and efficacy data prior to their market approval. The current status of commercially available different artificial disc implants is summarized in the **Table 1.1.**

Table 1.1. Summary of commercially available artificial lumber discs

Name of the deices	Type, design and composition	Year	Production company	Clearance of FDA approval	Current market status
Charité artificial disc	Type- composite. Cobalt-chrome-molybdenum alloy body with ultra-high molecular weight polyethylene sliding core with three fixation teeth (2.5 mm) both in anterior and posterior position.	SB Charité I and II were developed in 1982-84. SB Charité III in 1987	SB Charité I and Mark II were manufactured by German Democratic Republic (GDR). SB Charité III by LINK and modern design by DePuy Spine Inc, Raynham, Massachusetts[105].	October 26, 2004	Discontinued
ProDisc-L	Type- composite. Similar to Charité, but central keel with lateral spikes is placed in the middle position to secure the metal end plates into the vertebral body	It was first clinically tested in 1990 and second generation as ProDisc II was developed in 1999[106].	Centinel Spine, West Chester, Pennsylvania.	August 14, 2006	Continuing

activL	Type- composite. Similar to Charité and ProDisc-L. Endplate features three anterior horizontal spikes or central keel.	It is available since 2005 in Europe[107].	Aesculap Implant Systems, Center Valley, Pennsylvania.	June 11, 2015	Continuing
AcroFlex	Type- elastic. Two titanium end plates (ASTM F-136 grade) bound together by hexene-based polyolefin rubber core.	Acroflex disc project was developed in 1986-1999[108].	Acromed Corporation, Cleveland, Ohio.	No FDA approval	Discontinued
Maverick	Metal-on-metal design (cobalt-chromium-molybdenum alloy), preserving motion by a ball-and-socket	The first clinical application was approved in January 2002[109].	Medtronic, Dublin, Ireland.	IDE trial is completed . No FDA approval.	Outside the US
FlexiCore	Similar to Maverick	Antonio and Thomas have designed	Stryker, Allendale, NJ.	No FDA approval	Discontinued

		and evaluated the FlexiCore in 2004 [110].			
Freedom lumbar Disc	A single-piece technology wherein titanium alloy end plates bonded by elastomeric core[111].	AxioMed Freedom disc was implanted in 2010	AxioMed, Malden, MA.	USA IDE trial is completed . No FDA approval.	Continuing
M6-L	Titanium end plates with polycarbonate urethane (PCU) core. Core is again surrounded by ultra-high-molecular weight-polyethylene (UHMWPE) fibers[112].	It was first implanted in 2009.	Spinal Kinetics, Inc., Sunnyvale, CA	No USA IDE trial and No FDA approval	Outside the US

However, apart from these devices listed in Table 1.1, there are several other artificial discs for lumber implants including Welldisc-L (Eden Spine, Europe, SA), Triumph (Globus Medical, Pennsylvania, United States), Mobi-Disc (Zimmer Biomet, Warsaw, Indiana, United States),

Physio-L (NexGen Spine Inc., Whippany, New Jersey, U.S.A.), and eDisc (Theken, Ohio, U.S.A.), which are now in different phages of their clinical trials.

The limitations of disc replacement include the restriction of spinal motion (though it is advantageous over the fusion technique), lake of reproducibility, mismatched biomechanics, extrusion and chances of infection that lead to revision operation. TDR may be associated with several possible disadvantages in long term studies. For instances, the microscopic toxic metal wire debris may cause foreign body responses and the metal endplate secured in the vertebral body may dislocate out of the bone. Although there is still a room for improvement in long term durability and sustainability of arthroplasty, in this situation, it can be accepted as alternative therapy for discogenic pain management.

1.1.5.2.3.2. NP replacement

For NP replacement, the implants should be biocompatible, fatigue resistant, and tough enough to wear and resist particulate debris formation. They should also have high water absorbing capacity to fill up the disc space comfortably and promote water movement during the loading-unloading cycles mimicking the native disc like environment. The biomechanical nature in terms of rheological (visco-elastic) behavior and stiffness of NP, implants should match the native NP tissue to avoid detrimental stress shielding effects. Moreover, implants must be inserted through incision in the surrounding AF tissue using a minimally invasive approach without much damage in it, otherwise promoting inflammation that ultimately causes further disc degeneration. The current status of commercially available different NP replacements is summarized in the **Table 1.2:**

Table 1.2. Summary of commercially available NP replacements.

Name of the deices	Type, design and composition	Year	Production company	Clearance of FDA approval /CE mark	Current market status
Prosthetic disc nucleus	Type-single-device implant. Hydrogel pellet (composed of	PDN was first introduced in 1996.	Raymedica, Minneapolis, MN	No FDA approval	Outside the US

(PDN)-SOLO	polyacrylamide and polyacrylonitrile) ineased in a polyethylene jacket[113].				
HydraFlex	Similar to PDN-SOLO, but with softer core and anatomically equivalent structure.	Raymedica introduced it in 2006.	Raymedica, Minneapolis, MN	FDA approval for clinical evaluation in 2006.	Under clinical evaluation in the US
DASCOR	Type- In situ injectable gel. It consists of a 2-part curable polyurethane and an expandable polyurethane balloon.	Clinical study was conducted by Ahrens et al., in 2003[114].	Disc Dynamics, Eden Prairie, Minnesota	It has been CE marked in Europe	Company shutdown
NeuDisc	Small and coin in size. It consists of modified hydrolyzed poly-acrylonitrile polymer[115].	Data not found	Replication Medical, Cranbury, New Jersey	It was approved in the US in 2005 and also has been CE marked.	Discontinued
GelStix	Minimally invasive injectable hydrogel (hydrolysed polyacrylonitrile (HPAN))	A clinical trial was started in 2016[116].	Replication Medical, Cranbury, New Jersey	In clinical trial. No FDA approval	Outside the US

NUBAC	Type- a ball-and socket articulation. Polyether ether ketone (PEEK)–on–PEEK system with metal end plates	Clinical trial was initiated in 2009 in USA[117].	Pioneer Surgical Technology(RTI surgical), Michigan and Invibio, Green-ville, Netherlands	Received FDA approval for IDE pivotal study in 2008.	Available commercially in Europe
NuCore	Type- a synthetic recombinant protein based hydrogel. Silk fibroin and elastin based composite hydrogel	The first arm of an IDE trial was performed in 2006.	Spine Wave; Shelton, CT, USA	The second arm of an IDE trial was started in 2011 in Europe[118]. In clinical trial.	Outside the US
AxiaLIF+	Type- PNR (Percutaneous Nucleus Replacement). Titanium screw system (for anchoring the vertebrae) with curable material filled central membrane.	First clinical data was published in 2006 by Morotta *et al.,*[119].	TranS1, Wilmington, North Carolina	The AxiaLIF+ implant first received FDA 510(k) clearance in 2006[120].	Continuing
BioDisc	Type-a protein hydrogel composed of serum albumin and gluteraldehyde.	It was first successfully implanted in UK in 2005[121].	Cryolife, Kennesaw, Georgia	Under clinical evaluation	Lack of updated information

However, there are also several other devices such as DiscCell (Gentis, Wayne, Pennsylvania), Oxiplex (FzioMed, San Luis Obispo, California), Sinux (DePuy Spine, Raynham, Massachusetts), SaluDisc (SpineMedica, Marietta, US), Aquarelle Hydrogel Nucleus (Stryker Corp., Kalamazoo, Michigan) and Hydrafil (Synthes Spine), which are now in different phases of clinical investigations.

1.1.5.3. Biological therapies - the regenerative strategies for treatment of IDD

Reduced cell viability is the hallmark of degenerating discs due to cell necrosis and/or apoptosis. Cell survival is vital for synthesizing the matrix proteins that can repair and regenerate the degenerated discs. Thereby, disc cells are considered to be the key target to manipulate their functions for synthesizing the end proteins utilizing the biological therapies. The main aim of biological therapies is to improve the matrix synthesis, thus restoring the disc biomechanics. The biological therapies include molecular therapy (peptides/growth factor and gene therapy), cell therapy and tissue engineering, which can trigger disc regeneration, while lowering the discogenic pain. Although, these pro-anabolic approaches are shown to be very effective, they are still largely at different stages of their clinical trials.

1.1.5.3.1. Peptides/growth factors therapy

Growth factors (GFs) can be defined as naturally occurring biologically active diffusible signaling molecules that can bind to the specific receptors on cell surface, and thereby promoting cell proliferation and differentiation. GFs can directly be injected into the intradiscal position alone or in combination with cells, scaffolds or gene therapy to promote the anabolic pathways for extracellular matrix (ECM) secretion, while delaying the degeneration process and inhibition of inflammation. Usually, GFs attempted in augmentation of ECM secretion need the presence of viable cells to be effective. Therefore, growth factors therapies target the early-stages of disc degeneration, typically Pfirrmann grade 1 to 3, wherein cells still maintain physiology similar to the normal discs[88]. The members of bone morphogenic proteins (BMPs) and transforming growth factor-β (TGF-β) are the most known GFs that are being used in disc regeneration therapy for decades. Thompson *et al.,* first demonstrated a therapeutic approach to treat the degenerated discs by exogenous GFs in canine model[122]. In this study, they observed the significant response of TGF (transforming growth factor) and EGF (epidermal growth factor) in NP, rather AF and TZ

when compared to the response of FGF (fibroblast growth factor) and IGF-1 (insulin like growth factor-1). **Table 1.3** summarizes the significant findings of various GFs when exposure to disc cells.

Table 1.3. Growth factors therapy approach for disc degeneration.

Growth factors	Approach/Experimental design	Model system	Significant findings	References
Bone morphogenic proteins (BMPs); recombinant BMP-2 (rhBMP-2) and rhBMP-12	Disc cells (both AF and NP) were incubated with rhBMPs for 6 days.	*In vitro* mono layer cell culture system	rhBMPs enhanced the synthesis of collagen, non-collagen and proteoglycans in NP cells while having negligible effects on AF cells.	Gilbertson *et al.,*[123]
	Disc cells were cultured in alginate beads for 6 days.	*In vitro* three-dimensional culture system	rhBMP-2 up-regulated chondrogenic genes expression, but not the osteogenic genes.	Kim *et al.*[124]
Transforming growth factor-β 1 (TGF- β1) and rhBMP-2	Bone marrow derived stem cells (BMDCs) were exposed to TGF- β1 and rhBMP-2 synergistically or alone	*In vitro* mono layer cell culture system	There were synergistic effects on chondrogenic gene expression except for collagen type I.	Kuh *et al.,*[125]
TGF-β3, BMP-4, and Tissue	Chitosan hydrogels containing GFs and		The combination of chitosan and GFs	Gandhi *et al.,*[126]

inhibitors of metalloproteinases (TIMP-2)	TIMP-2 were injected into intradiscal position in rabbit model. T2 MRI mapping was performed after 6 weeks of injury and intervention.	*In vivo* rabbit disc model system	promoted significant regeneration in acutely injured discs.	
TGF-β1 and Insulin like growth factor-1 (IGF-1)	High density micromass culture system was exposed to GFs for 5 days.	*In vitro* micromass culture system	GFs pushed the foetal AF cells towards fibrocartilaginous phenotype	Hayes and Ralphs[127]
IGF-1 and BMP-2	GFs were loaded in a polyvinyl alcohol (PVA)-based scaffold to evaluate the effect of the sustained release on AF/NP cells proliferation and metabolism.	*In vitro* 3D cell culture system	Sustained release of GFs enhanced cell proliferation and ECM secretion, but no expression of COL2A1 was observed.	Akyuva *et al.,*[128]
BMP-7	NP cells were cultured in the hydrogel system containing BMP-7 and BMP-2 for 14 days. Hydrogels were also injected into an *ex-vivo* whole organ system.	*In vitro* three-dimensional culture system; *Ex-vivo* whole organ system	Hydrogel system up-regulated the collagen type II and proteoglycan genes expression, but no osteogenic and fibroblastic effects were observed.	Li *et al.,*[129]

BMP-13	BMP-13 was directly injected into the intradiscal position in an annular stab injury model.	*In vivo* ovine model	A single injection improved disc health with enhanced ECM production, thus preventing disc from narrowing.	Wei *et al.,*[130]
Osteogenic protein-1 (OP-1)	OP-1 in combination with chondroitinase ABC was injected into the intradiscal position in rabbit model.	*In vivo* disc degeneration model	OP-1 reversed the effect of chondroitinase ABC that decreased disc height.	Imai *et al.,*[131]
	OP-1 was directly injected into intradiscal position from where NP tissue was aspirated out.	*In vivo* disc degeneration model	OP-1 delayed the disc degeneration.	Liu *et al.,*[132]
Growth and differentiation factor-5 (GDF-5)	Disc cells were isolated from GDF-5 (-/-) mice and treated with GDF-5.	*In vitro* monolayer cell culture system	Dose dependent upregulation of aggrecan and collagen type II genes expression were noticed.	Li *et al.,*[133]
	Rabbit IVD received a single injection of GDF-5	*In vivo* rabbit annular puncture model	A single dose improved disc height and histological grading score.	Chujo *et al.,*[134]

	post 4 weeks of annular puncture.			
	Poly(lactic-co-glycolic acid) (PLGA) microspheres loaded with GDF-5 were injected into rat tail degenerated discs.	*In vivo* rat annular puncture model	The sustained release of GDF-5 restored dis height and improved proteoglycan and collagen type II synthesis.	Yan *et al.,*[135]
	GDF-5 was incorporated into a delivery system composed of heparin and the synthetic polycation poly(ethylene argininylaspartate diglyceride) (PEAD) for sustain release. The polymer-GDF-5-hADSC (adipose derived stem cells) composite was administrated into the degenerated disc.	*In vivo* rat annular puncture model	The polymer-GDF-5-hADSCs composite delayed the degeneration process.	Zhu *et al.,*[136]
Platelet rich plasma (PRP)	Disc cells were treated with PRP in bead culture system.	*In vitro* bead culture system	PRP stimulated proteoglycan and collagen synthesis, but had mild proliferation effect.	Akeda *et al.,*[137]

Autologous PRP was injected into the degenerated discs after 4 weeks of annular puncture.	*In vivo* rabbit annular puncture model	PRP injected discs showed restorative sign.	Obata *et al.,*[138]
Stromal vascular fraction (SVF) suspended in PRP was injected into the NP of degenerated disc.	12 months of Human clinical trial	No incidence of severe adverse effect (SAE)	Comella *et al.,*[139]

Although GFs play a significant role in regenerative pathways, but they do have several limitations including short half-life and undesired side effects. The regenerative efficacy of GF depends on dosage of it as well as the stage (acute to chronic) of degeneration. One of the key limitations of GFs therapy is the short biological half-life limiting to hours or a day, therefore multiple injections may be required in order to achieve the long-term biological effect. In addition, the overdoses, direct injection or leakages of liquid GFs in adjacent tissue may lead to several unpredictable side effects[140]. For instance, blood vessel cells of IVD possess the receptors for IGF and TGF. Therefore, injection of these GFs give rise to angiogenesis and consequently nerve ingrowth. Moreover, an immediate structural change and restoration of biomechanics of the degenerated discs cannot be achieved only by GFs therapies. To overcome these issues, GFs can be delivered with some sustained delivery systems like gene therapy, hydrogel or scaffolds systems that again provide the additional structural advantages.

GFs have the anabolic effects promoting ECM synthesis, while there are few anti-catabolic factors involved in delaying the degeneration cascades, which are also being explored in treatment of discogenic pain. For instance, Link-N, a small naturally occurring peptide containing 16 amino acids, can enhance the expression of *SOX9*, and synthesis of proteoglycan, collagen type II, BMP-4 and -7, while down-regulates the expression of MMP-3, -13, and ADAMTS-4 and -5 in a dose dependent manner[141-143]. In addition, it also acts as an anti-inflammatory mediator when

applied in degenerating discs[144]. In a recent study, Mwale *et al.,* showed the regenerative properties of the first 1-8 residues of Link-N peptide when injected into the degenerated discs in a rabbit annular puncture model[145]. All these biochemical changes are thought to be due to the interaction of Link-N peptide with BMP-II receptors activating the intracellular *Smad1/5* signaling pathway[146]. One of the major advantages associated with the Link-N peptide therapy is that it does not induce the bone formation in the degenerated disc.

Recently, researchers have shown the beneficial effects of small leucine-rich proteoglycans (SLRPs) that delay or reverse the degeneration cascades[147]. SLRPs (*e.g.,* biglycan, decorin, chondroitin sulphate and luminal) have been shown to play the important role in ECM integrity and functions, hence maintain the disc health. Therefore, these molecules can be used as therapeutic agents targeting disc degeneration in near future.

The antagonists for proinflammatory cytokines (*e.g.,* IL-1 and TNF-α) which are involved in triggering the catabolic cascades as well as blocking the anabolic pathways directly or indirectly, can be used as an alternative and effective strategy for therapy in disc degeneration. These pro-inflammatory cytokines up-regulate the expression of nerve growth factors (NGF) inducing nerve ingrowth into the degenerated discs, and also increase the level of MMP-1, -3 and -9 resulting disc matrix disaggregation[47, 66, 148]. Therefore, a direct injection of antagonists into the degenerated disc may inhibit or reverse the degeneration process. For instance, Maitre *et al.,* demonstrated the direct delivery of IL-1 receptor antagonist (IL-1Ra) that inhibited the degradation of ECM of the intact human disc in an *in situ* model[149]. Similarly, etanercept, a TNF-α antagonist, provided relief of discogenic pain when it was injected directly into the degenerated discs[150]. However, due to short half-life, one may need repeated injections or gene therapy approach to achieve the desired clinical outcomes.

1.1.5.3.2. Gene therapy

To overcome the limitations related to the direct delivery of GFs into the degenerated discs, gene therapy has been introduced as an alternative approach that ensures the prolonged anabolic effects once the genes of interest are transfected into the target cells. The engineered cells continue to produce ECM components that help discs recovering from the damages. There are two main methods of gene therapy that can be followed: (i) *in vivo* gene therapy wherein vectors containing

candidate genes are directly injected into the body, and (ii) *ex vivo* gene therapy that involves the transfection of genes to target cells *in vitro* (called genetically modified cells) and re-implanting them back to the target organs[151]. The *ex-vivo* technique is more suitable than the *in vivo* method as very less number of healthy cells are populated in the degenerated discs. In gene therapy, genes are delivered through vectors that can be viral or non-viral. The viral vectors are often used as they offer the highest efficiency to transfect the target cells. Two most common viral vectors for disc regeneration therapy are adenovirus and adeno-associated virus (AAV). They are used because of their high efficiency to infect even the non-dividing cells like IVD cells[152]. However, there are few reports on use of retrovirus, lentivirus and baculovirus as vectors for gene therapy of IVD[153]. In contrast, there are limited reports on non-viral gene therapy approaches for IVD cells. The non-viral gene therapy uses microbubbles, lipid-based reagents, cationic polymeric system (polyplexes micelle), RNA interferences (RNAi) and CRISPR-Cas9 technology[154]. **Table 1.4** summarizes target genes and the approaches followed for gene therapy of IVD.

Table 1.4. Gene therapy approaches (viral and non-viral) to restore degenerated discs.

Target genes	Approaches	Model systems	Outcomes	References
Virus mediated gene therapy approaches				
TGF-β1	Recombinant Adenovirus (Ad/CMV-hTGF- β1) was directly injected into the intradiscal position.	*In vivo* rabbit model	The NP tissue showed 30-fold increase in TGF-β1 production and 100% increase in proteoglycan synthesis.	Nishida *et al.,*[155]
TGF-β1, IGF-1 and *BMP-2*	Recombinant adenovirus constructs containing Ad/hTGF- β1, Ad/IGF-1 and Ad/BMP-2 were transfected into NP and	*In vitro* "cocktail" therapeutic gene transfer	Triple gene combination increased 4.7-fold of the proteoglycan synthesis.	Moon *et al.,*[156]

	inner AF cells isolated from human lumber discs.			
(Latent membrane protein-1) *LMP-1*	AF cells were transduced with Ad/LMP-1	*In vitro* monolayer culture system	Elevated mRNA expression for aggrecan, collagen type -I and –II, BMP-2 and -7, and LMP-1 was found.	Kuh *et al.*,[157]
SOX9	Ad/SOX9 was directly injected into degenerated IVD in a rabbit model.	*In vivo* rabbit model	The sustained expression of SOX9 preserved NP cells phenotype and histological appearance.	Paul *et al.,*[158]
IL-1Ra	Disc cells were transduced with Ad/IL-1Ra and injected into degenerated discs.	*Ex vivo* gene transfer to human degenerated discs	The transfected cells produced high level of IL-1Ra showing resistance to IL-1 for prolonged period of time.	Maitre *et al.,*[159]
	IL-1Ra was inserted into the chondrocytic end plate cells by retrovirus mediated gene transfer.	*In vitro* monolayer culture system	The transduced cells produced 24 $ng.ml^{-1}$ per 10^6 cells in 48 h.	Wehling *et al.,*[160]
TIMP-1	Disc cells were isolated from human degenerated discs and cells were	*In vitro* 3D pellet culture system	Gene delivery of TIMP-1 increased the proteoglycan synthesis.	Wallach *et al.,*[161]

	transduced with Ad/TIMP-1			
OP-1	The adeno-associated virus (AAV) mediated OP-1 and SOX9 double gene co-transfection was performed and mixed solution was directly injected into the degenerated rabbit IVD.	*In vivo* rabbit model	Double-gene transfection system improved the disc height of degenerated disc and increased the proteoglycan and collagen type II synthesis.	Ren *et al.,*[162]
Green fluorescence protein (*GFP*)	Rabbit disc cells were transduced with vectors containing GFP (*Autographa californica* nucleopolyhedrovirus/GFP). The transduced cells were injected into rabbit IVD.	*In vivo* rabbit model	GFP expression was observed without inducing any symptoms.	Liu *et al.,*[163]
TGF-β1, connective tissue growth factor (*CTGF*) and *TIMP-1*	The recombinant leniviral plasmid (lenti-TGFβ3-P2A-CTGF-T2A-TIMP1) was directly injected into needle punctured IVD in a rabbit model.	*In vivo* rabbit model	The co-transduction method ameliorated the disc condition when compared to control and promoted proteoglycan and collagen type-II synthesis.	Liu *et al.,*[164]
Non-virus mediated gene therapy approaches				
GFP and firefly luciferase	Plasmid DNA containing target genes was mixed with microbubbles and intradiscally injected in a	*In vivo* rat model	GFP and luciferase transfected cells	Nishida *et al.,*[165]

	rat model followed by irradiation with ultrasound.		were observed after seven days.	
MicroRNA-29a (*MiR-29a*)	A MMP responsive two-stage delivery system was designed to deliver MiR-29a into NP cells.	*In vivo* rat model	The delivered (*MiR-29a* silenced the MMP-2 expression inhibiting the fibrosis process.	Feng *et al.,*[166]
Luciferase	NP cells isolated from both rat and scoliosis patients were co-transfected with SiRNA targeting the luciferase gene.	*In vitro* monolayer cell culture system	This process drastically inhibited the luciferase expression in both rat and human NP cells.	Kakutani *et al.,*[167]
ADAMTS-5	Rabbit discs were exposed to ADAMTS5 siRNA oligonucleotide post one week of puncture.	*In vivo* rabbit annular puncture model	The injection improved the MRI and histologic grade score.	Seki *et al.,*[168]
Caspage-3	Caspage-3 siRNA was injected with siRNA-Invivofectamine Reagent into the center of L4/5.	*In vivo* rabbit external compression model	The local injection of Caspage-3 siRNA inhibited NP cell apoptosis suppressing the degenerative changes.	Yamada *et al.,*[169]
TNF receptor 1 (*TNFR1*) and IL-1 receptor 1 (*IL1R1*)	Human NP cells isolated from patients were successfully tested for lentivirus CRISPR epigenome editing system	*In vitro* monolayer cell culture system	CRISPR epigenome editing systems significantly downregulated TNFR1, but not IL1R1signaling.	Farhang *et al.,*[170]

to regulate the TNFR1/IL1R1 signaling.

Although gene therapy is a promising technique showing desired clinical outcomes, the major concerns include safety, efficiency, and the duration of gene expression. There are always risks of virus related complications *e.g.,* viral infection, mutations, and immunoresponse. The adenovirus are widely accepted vector for gene therapy, but they are associated with severe immune response. In contrast, although non-viral approaches have lower possibility of viral infection, the transfection efficiency of these systems has not yet reached the satisfactory level. Several investigators are involved in developing some advanced techniques to overcome the limitations of non-viral mediated gene therapy. So far, the gene therapy for IVD degeneration is limited to *in vitro* laboratory settings and *in vivo* animal studies rather than human clinical trials due to safety concerns.

1.1.5.3.3. Cell therapy

Number of viable cells and their metabolic activities are shown to gradually decrease in degenerating discs. In advanced stages of disc degeneration, the decreased efficiency of gene and/or growth factors therapies is noticed as very less number of healthy cells remain within the disc to respond to these signals. To maintain disc homeostasis, it needs an adequate amount of healthy cells. Therefore, in the later stages of degeneration, cell based therapy is considered as an alternative and effective approach that repopulates the disc by replacing the necrotic or apoptotic cells. Cells from both autologous and allogeneic sources are used in cell therapy for disc regeneration. Commonly used cells are (i) notochordal cells that are mainly isolated from embryonic NP tissue, (ii) chondrocytes-like cells or NP cells, which can be autologous or allogeneic, (iii) mesenchymal stem cells (MSCs), which can be obtained from autologous bone marrow, adipose tissue or allogeneic umbilical cord tissue, and (iv) induced pluripotent stem cells (iPSCs). Notocordal cells play key role in regulation of inflammation and vascularization during disc development, but the rapid decrease of their population after birth is thought to be one of the reasons for onset of disc degeneration[171]. In addition, notocordal cells are shown to be more metabolically active producing higher amount of PGs than NP cells[172]. Therefore, scientists

have found more interest in differentiating the stem cells (iPSCs or MSCs) into notocordal cells than NP cells in treatment of degenerated discs with stem cell based therapy[173, 174]. Recently, Vries *et al.,* investigated the regeneration capacity and anti-inflammatory properties of notocordal cells-rich-matrix (NCM) when tested on bovine NP cells cultured in alginate beads for 4 weeks[175].

Autologous disc cells are also being used for the treatment of disc degeneration in various models. In this case, cells are generally harvested from the herniated discs, expanded *in vitro* and implanted back into the degenerated disc[176]. However, use of autologous cells leads to the donor cite morbidity, thus xenogeneic cells can be considered as an alternative source. The amount of cells isolated from a single disc may not be enough to reconstruct the degenerated disc, thereby necessitating the *in vitro* expansion[177]. However, cellular phenotype and anabolic activity are prone to alter when autologous or xenogeneic cells are cultured to expand *in v*itro for many passages[178]. For this reason, MSCs can be a promising candidate for use in cell-based therapy as they have several advantages *e.g.,* they have the potential to differentiate into chondrogenic lineage and can expand *in vitro* for several passages without altering the phenotype[179, 180]. Moreover, MSCs can easily be isolated avoiding the donor site morbidity. Implantation of MSCs in degenerated disc is generally considered as safe, but there is a chance of osteophyte formation due to cell leakage during the injection process[181]. To overcome this issue, it is recommended to deliver cells with the scaffolding materials including hyaluronan, fibrin or atelocollagen that prevent MSCs from ectopic osteoblast differentiation.

Survival of the implanted cells and upholding their regenerating potency in the harsh conditions of acidic, hypoxic, and osmotic environment in the degenerated disc are the biggest challenges. Despite these challenges, advantages are that cells can be injected into the central NP area through the AF tissue that restricts the cell migration and it is an immune-privileged milieu.

1.1.5.3.4. Other targets

Despite these above-mentioned strategies, there are few small molecules (MW < 900 Dalton) that are also being used targeting various pathways involved in disc degeneration. The commonly used small molecules are naringin, estradiol, icariin, cannabidiol, resveratrol, celecoxib, tofacitinib, berberine, SM04690, INK-128, and MK-2206 and so on[182]. Being small in size, these molecules

can easily be absorbed in the digestive system and also rapidly be diffused through cell membrane stimulating the anabolic processes or suppressing the catabolic signals[183]. For instance, icariin, resveratrol and berberine can exclusively inhibit the NF-κB (nuclear factor kappa B) and *p38/MAPK* (mitogen activated protein kinase) signaling pathways involved in inflammatory response, thus preventing degenerative cascade[184-186]. INK-128 and MK-2206 can increase the survival rate of disc cells by modulating the *mTOR* (mammalian target of rapamycin) signaling that acts as a negative regulator of autophagy[187]. Similarly, SM04690 not only reduces the inflammation and apoptosis, but also inhibits fibrosis of AF by suppressing *Wnt* signaling, thereby enhancing NP cell proliferation, and ECM secretion in the degenerated disc[188].

1.2. Review of literature

1.2.1. Tissue engineering approaches for IVD regeneration

Unlike the conservative methods that simply manage the pain, the tissue engineering approaches are aimed to regenerate the damaged discs. The ultimate goal of IVD tissue engineering is the restoration of biomechanical stability in the short term and regeneration of disc tissue in the long term utilizing a suitable scaffolding system in combination with cells, signaling factors or both. Tissue engineering is the multidisciplinary field of combining knowledge and technologies of the areas of biology, medicine, chemistry, physics, and material sciences to develop tissue analog or engineered tissues for repair or replacement of diseased tissues or organs[189]. To develop the engineered tissues, two main approaches are generally followed; (i) designing of scaffolds recapitulating the structure and functions of the native tissues, and (ii) modifying the scaffold systems with biological cues like growth factors. In the early stages, scaffolds provide mechanical support to the damaged tissues and thereafter act as template to guide the cells to ensure the remodeling through biological processes.

1.2.1.1. Biomaterials for tissue engineering

A variety of biomaterials (both natural and synthetic) have been investigated for IVD tissue engineering. The choice of biomaterials to be used as scaffolds depends upon the physical and mechanical properties of IVD, which calls for the use of a highly strong and durable material. The synthetic biomaterials commonly investigated in fabricating the AF anatomical constructs include polyglycolic acid (PGA), poly(lactic-co-glycolic acid) (PLGA) and poly(ε-caprolactone) (PCL), poly(polycaprolactonetriol malate) (PPCLM), poly (L-lactic acid) (PLLA), poly(1,8-octanediol malate) (POM), poly(trimethylene carbonate) (PTMC), poly(ester-urethane) (PU), polyacrylonitrile (PAN), and poly(N-isopropyl acrylamide) (PNIPPAm)[190]. Similarly, natural polymers such as collagen, elastin, chitosan, hyaluronan, fibrin, alginate and silk fibroin have also been investigated for tissue engineering of IVD including the AF and NP tissue[190]. Constructs (scaffolds or hydrogels) made from these polymers supported cells adhesion, proliferation, and tissue maturation secreting the disc specific ECM proteins. However, as the current work focuses on silk based IVD tissue engineering, in this chapter, a special emphasis has given on silk fibroin as biomaterial.

1.2.1.1.1. Silk protein as biomaterial

Silk is being used as biomaterial in tissue engineering for decades due to its widespread versatility *e.g.,* biocompatibility, least immunogenicity, tunable biodegradability and mechanical properties[191]. Silk fibroin (SF) from *Bombyx mori* Linnaeus, 1758 (BM SF) was approved by US Food and Drug Administration (FDA) in 1993 as a biomaterial and it is being used in various tissue engineering applications for years[192-194]. Similarly, non-mulberry SF from *Antheraea mylitta* Drury, 1773 (AM SF) has also been extensively studied[195]. Recently, few reports suggest the potential use of non-mulberry SF from *Antheraea assamensis* Helfer, 1837 (AA SF) and *Philosamia ricini* Donovan, 1798 (PR SF) in various fields of tissue engineering including cornea, skin, cartilage, bone, blood vessel and heart[196-202].

Silk worm protein can be extracted from either cocoons or silk glands. Silk protein exists as a highly concentrated solution with α-helix and random coil conformation in glands. During biospinning, a highly specialized process, silkworms extrude protein through a spinneret with rapid elongation flow that converts the random coils to β-sheets. This process (dictated by microfluidics principle) is associated with various factors like exposure to air, shear stress and K^+ ions concentration[203]. Silk protein mainly consists of two proteins; fibroin (~ 75%) and sericin (~ 25%). Sericin is a glue-like amorphous protein that acts as an adhesive binder of fibrous fibroin chains which is semi-crystalline in nature providing stiffness and strength. The water soluble sericin can be removed by thermochemical process known as degumming.

1.2.1.1.1.1. *B. mori* silk fibroin (BM SF)

BM SF consists of a heavy (H, 391 kDa) and a light (L, 25 kDa) polypeptide chain, linked by a disulfide bond between the Cys-c20 (20^{th} residue from the COO- terminus) of the H-chain and Cys-172 of L-chain[204]. A glycoprotein, P25 (25 kDa) is attached non-covalently to both the chains. The primary structure BM SF consists of multiple repeats of AGSGAG which make up 55% of the total fibroin, conferring crystallinity to the structure. More specifically, H-chain consists of twelve domains, each domain comprising of hexapeptide sub-domains including GAGAGY, GAGAGS, GAGYGA or GAGAGA[205]. L-chain contains relatively high amount of leucine, isoleucine, valine and acidic amino acids. The structural changes from Silk I (prior to

crystallization) to Silk II (crystallized) occurs exclusively in crystalline region post spinning or alcohol treatment that induce β-sheets between the repeating units.

1.2.1.1.1.2. *P. ricini* silk fibroin (PR SF)

PR SF consists of 97 kDa (with compositional abundance of glutamic acid) and 45 kDa polypeptides chains connected through a disulfide bond. The basic repeating unit of PR SF is $(alanine)_{12-13}$ which is similar to spider (major ampullate) silk that possesses $(alanine)_{5-6}$ as repeating unit[206].

1.2.1.1.1.3. *A. assamensis* silk fibroin (AA SF)

Two fractions of 220 kDa and 20 kDa have been reported for AA SF[195]. The primary structure of AA SF comprises of 42.5% alanine, 28.9% glycine, 10.2% serine and 5.5% tyrosine. The alanine content in AA SF is greater than the BM SF that contains 30% alanine. Comparatively, BM SF contains higher amount of glycine (46%) than AA SF[207]. The secondary structure of the AA SF possesses three main motifs: A-motif, consisting of alanine residues; G-motif, primarily composed of glycine residues; and R-motif that contains arginine residues. The A-motif contains poly-alanine stretches of $(alanine)_{5-15}$ which is responsible for the crystallinity of the protein. One of the unique features of poly-alanine stretches of AA SF is the absence of any interspersing amino acid unlike their counterparts with 3-4% serine residues in other members of the saturniid family[207].

The presence of intrinsic cell binding RGD (arg-gly-asp) sequences within non-mulberry SF confers special niche to the resilient, biocompatible and biodegradable biomaterials based on the latter in the domain of tissue engineering. Furthermore, mechanical robustness of the non-mulberry SF reported in terms of its higher tensile strength than mulberry SF has been bracketed together with the lesser heterogeneity and orderly arrangement of non-polyalanine repeats in higher number, tighter poly-alanine β-crystals that are devoid of non-alanine residues and lesser amount of polar residues in the protein main chain[208].

1.2.1.2. Tissue engineering approaches for annulus fibrosus (AF) regeneration

1.2.1.2.1. Electrospun mats

Electrospinning is a robust and versatile technique for the electrostatic formation of micro-/nanofibers from both natural and synthetic polymeric solutions utilizing electrical forces[209].

The process allows the formation of micro-/nanofibers with tunable porosity, higher surface to volume ratio, flexibility to be produced in various shapes and sizes and the advantage of controlling the composition of the nanofibers according to their properties and function[209, 210]. Due to its several advantages, electrospinning has been widely used in various fields like tissue engineering, electronics, nanocatalysis and pharmaceutics[211]. A typical electrospinning system consists of a high voltage power source, a grounded collector (metal plate or rotating mandrel), a syringe consisting of polymeric solution and a spinneret. Electrospinning is an electrohydrodynamic process which electrifies a liquid droplet to produce a jet, followed by elongation and stretching to form polymeric fibers[212]. During the process, the polymeric solution is ejected from the spinneret to generate a pendant droplet due to surface tension. Upon application of electric current, the droplet is deformed into a Taylor cone and a charged jet is produced. Finally, the jet undergoes vigorous whipping motion and is stretched into thinner diameters which are then deposited as solid fibers on to the grounded collector[209, 210]. The diameter of the electrospun fibers are governed by several factors such as polymer properties (polymer, molecular weight, concentration), environmental factors (humidity, temperature) and instrument settings (distance between needle and collector, voltage, flow rate) [213]. The orientation of the fibers can be governed through the architecture or rotation of the collector[214, 215].

Electrospinning has been widely used in tissue engineering for the preparation of nanofibrous scaffolds. The diameter of the electrospun fibers are similar to the fibrils of the extracellular matrix (ECM) and have been demonstrated as a substrate to positively promote cell-cell and cell-matrix interactions [216]. Several natural and synthetic polymers have been used for the preparation of nanofibrous scaffolds such as silk fibroin, hyaluronic acid, collagen, alginate, fibrinogen, chitosan, polycaprolactone (PCL), polylactic acid (PLLA), polyurethane (PU) and combinations of these polymer. Electrospinning has been extensively used for the fabrication of highly aligned nanofibrous scaffolds for recapitulating the extracellular matrix architecture of the AF[190, 217, 218]. Nerurkar *et al.,* developed anisotropic nanofibrous laminates for recapitulating the structural hierarchy of the annulus fibrosus. The developed nanofibrous scaffolds seeded with MSCs allowed the deposition of ordered collagen extracellular matrix mimicking the angle-ply, multilamellar architecture of native AF[217]. The same research group further developed a disc like angle ply structure mimicking the architecture of the IVD. The long-term *in vitro* evaluation demonstrated functional development of the constructs [219]. Further they evaluated the acellular engineered

disc in a rat tail model. The engineered disc permitted tissue formation in the AF region and mechanical properties were found to be similar to the native disc[220]. Alternatively, the same group matured a cell seeded disc-like angle ply structure in an *in vitro* condition and further evaluated it in a rat model. In long-term *in vitro* culture, the matured constructs demonstrated the compositions and functions similar to the native disc. Additionally, the matured constructs also maintained its structure and portrayed the mechanical properties similar to the native disc in an *in vivo* rat model[221]. Similarly, Vadala *et. al.,* assessed the effectiveness of transforming growth factor (TGF)-β1 releasing PLLA scaffolds for the regeneration of AF. The developed scaffolds supported the growth of bovine AF cells and showed significant deposition of sGAG and total collagen in comparison to control[222].

Bao *et al.,* fabricated a berberine loaded PCL microfibrous scaffold to recapitulate the ECM architecture of the native AF tissue. These scaffolds exhibited antimicrobial activities and also had good biocompatibility with AF cells[223]. Tsai *et al.,* developed a co-cultured human IVD cells and human mesenchymal stem cells (hMSCs) laden scaffold as a biological substitute to replace the degenerated IVD[224]. The aligned PLLA and PCL based nanofibrous scaffolds were used to recapitulate the AF region, while PuraMatrix gel to recapitulate the NP region, and circular nonwoven nanofibrous mats seeded with hMSC-derived osteoblasts were used to recapitulate the osseous end plate. This biomimetic stem cell seeded IVD scaffolds supported cell-cell, cell matrix and mechanobiological interaction to enhance the disc matrix regeneration. Liu *et al.,* developed a PU based aligned fibrous scaffolds to engineer a functional AF replacement[225]. The aligned scaffolds seeded with AF derived stem cells showed a better cell alignment, enhanced gene expression and matrix production in comparison to the control random fibrous scaffolds. Gluais *et al.,* fabricated a cell free aligned electrospun PCL scaffold for repair and regeneration of damaged AF[226]. The *in vitro* evaluation of this developed scaffolds demonstrated cell colonization, alignment, and deposition of AF-like extracellular matrix. The scaffolds also permitted defect closure and neo-tissue formation, and integration with the surrounding tissue in an AF impaired ovine model. Most recently, Shamsah *et al.,* developed the electrospun fiber scaffolds by blending PCL and PLLA that mimicked the architecture and biomechanics of native AF tissue[227]. The arrangement of nanofibers in the developed bilayer scaffolds mimicked the $\pm 30^{o}$ angle of collagen fibers as shown in the native AF lamellar layers and supported the growth and alignment of the bovine AF cells.

1.2.1.2.2. Hydrogels

Hydrogels have been widely used for IVD tissue engineering due to its advantageous features like biocompatibility, tunable mechanical and degradation properties, adjustable gelation properties and exceptional water retention properties[228]. Hydrogels can be developed from both natural or synthetic polymers incorporating cells or biochemical factors with tailored biomechanical properties for the repair of AF tissue[229, 230]. Grunert *et al.,* developed a high density collagen gel cross-linked with riboflavin for the repair of AF tissue in rat tail model[231]. This cross-linked collagen gel suppressed disc degeneration over 18 weeks, preserved the physiological disc hydration, and maintained the hydraulic permeability in comparison to the untreated control discs. Similarly, Günay *et al.,* developed a hyaluronan-based hydrogel cross-linked with 4-arm polyethylene glycol (PEG) for AF repair [229]. The fabricated hydrogels maintained the native like morphology and metabolic activities of the encapsulated hAF cells for up to 7 days. Liu *et al.,* developed a hybrid decellularized AF matrix and chitosan based hydrogel loaded with basic fibroblast growth factor (bFGF) as a biological substitute for the AF[232]. The bFGF loaded hydrogels exhibited enhanced proliferation, up-regulated AF specific gene expression and ECM synthesis by the seeded AF derived stem cells in comparison to the pristine hybrid hydrogels.

Scheibler *et al.,* compared a potential preclinical genipin cross-linked fibrin hydrogel with clinically available adhesive comprising of glutaraldehyde and albumin as AF defect sealants in an cruciate AF injury model[233]. Similarly, the functionalized biomaterials such as silk amalgamated with genipin-enhanced fibrin hydrogel has also been used as a potential approach for disc repair. The combination of the two biomaterials repaired an injury in the bovine whole organ IVD culture[234]. Most recently, Doench *et al.,* fabricated a cellulose nanofiber encapsulated chitosan hydrogel for the regeneration of AF tissue[235]. In a spine pig model, the developed hydrogel system restored the disc biomechanics and also served as contention patches against nucleus protrusion.

1.2.1.2.3. Scaffolds

The fabrication of tissue engineered scaffolds for AF have been challenging due to its complex architecture. But, several biomaterial scaffolds mimicking the structure and compositional properties of the native AF, and supporting the physiological loading have been developed for AF

tissue engineering. Specially, the structural mimicry of the AF region is important to provide directional cues for cell alignment and matrix deposition[22, 236]. Wilda *et al.,* investigated the efficacy of poly(d,l-lactide) (PDLLA)/bioglass composite foams to repair AF tissue of degenerated IVD[237]. The scaffolds supported the proliferation and deposition of ECM by hAF cells. Cabraja *et al.,* developed a PGA and hyaluronan (HA) based resorbable scaffold for regeneration and repair of AF tissue[238]. The fabricated scaffolds in the presence of human serum showed the formation of AF-like matrix and promoted AF cell redifferentiation. Notably, Park *et al.,* developed the silk fibroin based lamellar scaffolds for AF tissue restoration[239]. The lamellar scaffolds showed an enhanced proliferation and ECM secretion by the seeded porcine AF cells in comparison to the control porous silk scaffold. Further the lamellar scaffolds also allowed the formation of AF-like tissue in an *in vitro* condition. Likewise, Bhattacharjee *et al.,* developed a silk based scaffold with aligned silk fibers for reconstructing the native architecture of the AF tissue[240]. In these scaffolds, the silk fibers were cross-linked with chondroitin sulfate that supported the cellular alignment and deposition of ECM by the human chondrocytes.

Guillaume *et al.,* fabricated a shape memory alginate-collagen based composite scaffold for filling AF defects in degenerated IVD[241]. The scaffolds supported the proliferation of and ECM deposition by both the AF cells and MSCs. Additionally, the scaffolds also maintained the viability of MSCs in an *ex vivo* organ defect model up to 5 weeks. McGuire *et al.,* developed a multi-laminate angle-ply patches from decellularized porcine pericardium tissue[242]. The patches supported the proliferation of AF cells and portrayed tensile strength similar to the native human AF tissue. Decellularized bovine IVD has also been used for fabricating the complete IVD scaffold. The adopted decellularization process preserved the sGAG content, maintained the architecture of the collagen fibrils and mechanical properties of the discs, and removed up to 70% of the endogenous cells[243]. Pirvu *et al.,* investigated the potential of a poly(trimethylene carbonate) (PTMC) based scaffold seeded with human bone marrow derived mesenchymal stromal cells for AF rupture repair in a bovine organ culture annulotomy model under 14 days of dynamic loading[244]. The scaffold in combination with a sutured PU membrane restored the height of the annulotomized discs and prohibited the herniation of NP. Moreover, mesenchymal stromal cells incorporated in the PTMC scaffolds positively modulated the phenotype of the adjacent native disc tissue. Frost *et al.,* developed a PU scaffold reinforced with cellulose nanocrystals for AF tissue repair and replacement[245]. The fabricated scaffolds closely mimicked the mechanical properties

of the native IVD tissue. Du *et al.,* evaluated the efficacy of a PU scaffold incorporated with TGF-*β*1-supplemented collagen type I hydrogel and human AF cells for AF tissue regeneration and rupture repair[246]. The polyurethane scaffolds promoted the functional cell phenotype of the human AF cells *in vitro* and *in situ* also.

1.2.1.2.4. Biphasic constructs

Tissue engineering of the biphasic structure of IVD involves the combination of cells and biomaterials to reproduce the structure and functions of both NP and AF regions, simultaneously. In this strategy, the AF region has mainly been reconstructed using biomaterials such as PGA, gelatin, silk fibroin, collagen, and demineralized bone matrix gelatin, while the NP region has been reconstructed with hydrogels of gelatin, alginate, agarose, and hyaluronic acid [247]. Bowles *et al.,* developed a collagen and alginate based biphasic IVD construct based on the MRI and microcomputed tomography imaging techniques of a rat spine[248]. The developed scaffolds precisely mimicked the dimensions of the native disc and showed good integration with the vertebral bodies upon *in viv*o implantation in athymic rats. Park *et al.,* developed a biphasic scaffold to mimic the whole IVD, wherein the lamellar silk scaffolds were treated as AF equivalent, and the fibrin/HA composite gels were used as NP substitute[249]. Porcine AF cells seeded lamellar scaffolds allowed the formation of AF-like tissue, while the composite hydrogel system maintained the NP phenotype of the seeded chondrocytes over 4 weeks of *in vitro* culture. Similarly, Du *et al.,* constructed a silk-fibroin based biphasic scaffold as an integrated tissue engineered IVD structure[250]. The AF region was constructed using a paraffin sphere-leaching method, while the NP region was fabricated using phase separation method. Both the regions were perfectly integrated and allowed the proliferation and migration of rabbit AF and NP cells. The pig bone matrix gelatin and acellular cartilage ECM have also been used to fabricate the AF and NP regions, respectively, using freeze drying and crosslinking technique. The composite scaffolds supported the growth of AF and NP cells *in vitro* and formed IVD-like tissue on subcutaneous implantation in nude mice[251]. Hudson *et al.,* developed a tissue engineered whole IVD using type I collagen to reconstruct the AF region and alginate gel to reconstruct the NP region[252]. The ovine IVD cells seeded tissue engineered discs showed an enhanced biochemical and mechanical properties when exposed to the dynamic unconfined compression. Similarly, Choy *et al.,* fabricated a biphasic scaffolds, wherein the AF region was reconstructed using multiple

lamellae of collagen membranes, while the NP region consisted of collagen-GAG co-precipitate[253]. Overall, the dynamic mechanical performance of the biphasic scaffolds was similar to the native disc. Moriguchi *et al.,* investigated the efficacy of collagen and alginate based tissue engineered whole IVD constructs in canine cervical spine model[254]. The collagen-based AF region and alginate-based NP region was incorporated with adult canine AF and NP cells, respectively. The developed IVD scaffolds successfully preserved their position, structure, hydration and disc height in the *in vivo* condition for over 16 weeks. Du *et al.,* fabricated a biomimetic IVD composite construct with PCL microfibers recapitulating the AF region and alginate hydrogels recapitulating the NP region[255]. The PCL micro fibers and the alginate hydrogel supported the seeded AF and NP cells, respectively. Moreover, the IVD implants exhibited improved mechanical properties, and adequate deposition and organization of ECM components when implanted subcutaneously in nude mice.

1.2.1.2.5. 3-dimentional (3D) printing

3D printing is driving the major innovations in the field of tissue engineering and regenerative medicine. Recent advances in 3D printing technologies have facilitated the fabrication of complex 3D functional tissues that closely mimics the native human tissues. Moreover, the advent of 3D bioprinting has enabled tissue engineers to address the need of transplantable tissues and organs and *in vitro* tissue models[256, 257]. 3D bioprinting has been defined as a group of additive manufacturing techniques that assembles biological materials, biomolecules, living cells or combinations thereof, in a precisely controlled manner to fabricate clinically viable 3D tissues and organs that mimic the structural and functional integrity of the native tissues and organs[257, 258]. Advancement in high-resolution 3D bioprinters, numerically guided programming languages such as G-codes and computer-aided design (CAD) software have enabled the development of complex macro- and microscopic structures. One of the paramount factors for the success of 3D printing/bioprinting in the field of tissue engineering and regenerative medicine is the development of suitable biomaterial inks/bioinks. Aqueous formulation of biopolymers or hydrogel consisting of biologically active factors is termed as biomaterial ink, while cells encapsulated into such formulation is termed as bioink[259]. Several natural and synthetic biomaterials have been chosen for the formulation of biomaterial- or bioinks. The biomaterials used for bioprinting are mainly classified into hydrogels, photo cross-linkable resins, thermoplastic polymers, and

composites[260]. To exactly mimic the complex architecture of the native tissues, 3D bioprinting technology requires a 3D computer aided design (CAD) model, which is acquired from either computed tomography (CT) or magnetic resonance imaging (MRI). The obtained CAD models are further processed into G-code files and fed to the 3D printer. The 3D printer then fabricates the 3D constructs based on the G-code provided[256]. In recent years, 3D printing technology has progressed immensely, giving rise to several modes of creating 3D objects.

The various 3D printing technologies include pressure-assisted, thermal assisted, piezo-assisted, magnetic assisted, light-assisted, and microfluidics based printing. The most commonly used 3D printing techniques include pressure-assisted and light-assisted printing. Pressure assisted 3D printing utilizes one or more cartridges for dispensing biomaterial inks or bioinks through a nozzle on application of gaseous pressure. In this type of 3D printing the resolution is mainly dependent on the type of biomaterial ink, the deposition speed, the nozzle diameter and even the gas pressure[260]. Inkjet and micro-extrusion based 3D printing are mainly categorized under pressure assisted printing [257]. Thermal-assisted 3D printing utilizes the droplet-on demand (DOD) technology for bioprinting of cells and biomaterials. It consists of an electrical component which vaporizes the biomaterial to form a droplet followed by its ejection through a narrow capillary channel. This technique of 3D printing is less popular in tissue engineering as the applied heat reduces cell viability during and post bioprinting. Other drawbacks include nozzle clogging and sedimentation when printed along with cells[261]. Similarly, piezo-assisted 3D printing technique employs piezoelectric materials for ejections of biomaterial ink in the form of droplets. This mode of printing accurately allows dispensing of picolitre to nanolitre droplets. This type of printing uses a mechanical element for droplet formation and is mainly used for the development of microarrays and similar tissue models[262]. Acoustic 3D printing applies acoustic waves for the generation of printing droplets. It has the capability of organizing cells precisely in specific orientations with an accuracy of forming picolitre cell droplets[263]. Recently, acoustophoretic 3D bioprinting has been used to fabricate cell-laden 3D structures[264].

Mainly, two types of light assisted 3D printing techniques (initially termed as stereolithography; SLA) are used in fabricating the tissue engineered constructs; (i) laser- or light-based, and (ii) digital light processing (DLP) based printing[265, 266]. In both cases, photosensitive biomaterial ink is used in printing of constructs. In laser-based systems photosensitive material is cross-linked

in a point by point based manner, while DLP-based systems cross-link all points simultaneously in each layer of the sliced 3D model. There are few other laser-based 3D printing systems, also known as laser-induced forward transfer (LIFT), that rely on DOD technology. In LIFT method, a fast-pulse laser beam induces the formation of bioink droplet from a donor cell laden hydrogel coated glass slide towards a hydrogel coated collection glass slide. The 3D constructs are formed by the deposition of the droplets in a layer-by layer pattern based on the sliced 3D model[267]. Two-photon polymerization is a type of light-based 3D printing technique that creates 3D structures by accurately cross-linking voxels of interest [268]. Volumetric SLA is another light assisted system that is capable of cross-linking a volume of photosensitive bioink/biomaterial ink by accurately projecting light in a coordinated way[269, 270]. Recently this technique has been developed and used to bioprint the complex 3D constructs by exposing light for less than 1 min[270]. Additionally, Microfluidics based 3D printing has been adapted recently by incorporating microfluidic chips on dispensing heads of 3D printers. These printers have gained the popularity as it is a well-established technology allowing precise printing of low viscous bioinks, and has the provision for easily developing customizable print heads[271-274].

Current advances in 3D printing techniques have brought exponential developments in the field of tissue engineering. Novel biomaterial inks and 3D printing techniques have made it possible to fabricate complex heterogeneous structures of native tissues and organs. 3D printing technology has been utilized for the fabrication of various tissues like skin, liver, heart, bone, blood vessels, and IVD as well[260, 275]. The main challenge in 3D printing of IVD is to develop a suitable biomaterial ink that is mechanically robust, biocompatible, non-immunogenic, biodegradable, and most importantly it should possess the appropriate rheological properties for printing the complex architecture of the IVD. Several biocompatible thermoplastic polymers *e.g.,* polycaprolactone (PCL) [276-278], polylactic acid (PLA) [279], and polyurethane (PU) [280] are being used in 3D printing of IVD constructs. Oner *et al.,* developed a PCL based patient specific IVD model with different internal architecture using the patient's magnetic resonance imaging (MRI) information[276]. Similarly, Uden *et al.,* utilized the reverse engineering and rapid prototyping to fabricate AF scaffolds [277]. In this study, the reverse engineered IVD architecture was designed to mimic the original rabbit IVD using polycaprolactone (PCL) as biomaterial ink. Christiani *et al.,* fabricated a PCL based multi-layer angle-ply constructs exhibiting the mechanical properties similar to the native AF tissue[278]. The developed scaffolds supported the viability and

proliferation of bovine AF cells, as well as the enhanced expression AF specific genes by the cells. Likewise, Whatley *et al.,* fabricated polyurethane (PU) based biomimetic elastic vertebral disc using a custom-designed computer aided 3D manufacturing device[280]. The developed PU scaffolds exhibited mechanical properties similar to the native disc. Similarly, Hu *et al.,* developed the 3D bioprinted scaffolds using poly(lactic acid) (PLA) along with gellangum, and poly(ethylene glycol) diacrylate (PEGDA) to demonstrate IVD regeneration[279]. The developed hybrid constructs possessed tunable mechanical and degradation properties, and also supported the proliferation of bone marrow stromal cells.

Despite the thermoplastic polymers, several naturally derived biomaterials *e.g.,* silk fibroin, gelatin, elastin, hyaluronic acid, and sodium alginate have also been used for 3D printing of IVD [256] [275, 281]. For instance, Costa *et al.,* bioprinted a patient specific IVD scaffold using silk fibroin and elastin based bioink[275]. The developed scaffolds showed the structural and mechanical properties similar to the native disc, and also supported the growth and proliferation of Human adipose-derived stem cells (hADSCs). Most recently, Sun *et al.,* also developed an 3D bioprinted IVD scaffold using gelatin, hyaluronic acid, sodium alginate, and glycerol based bioink incorporated with bone marrow mesenchymal stem cells (BMSCs)[281]. The developed bioink was also loaded with connective tissue growth factor (CTGF) and transforming growth factor-β3 (TGF-β3) to induce differentiation of BMSCs to NP and AF like cells. Altogether, the bio-printed constructs were reported to demonstrate good biomechanical function.

1.2.1.3. Tissue engineering approaches for nucleus pulposus (NP) regeneration

In healthy disc, the gelatinous NP tissue maintains the hydrostatic pressure and distributes the load to the surrounding AF tissue during our daily activities. It is believed that early stages of disc degeneration start from NP, hence most studies are currently focused on NP regeneration. For regeneration purpose, three important components *i.e.,* cells, signaling factors and injectable scaffolds or hydrogels are implanted independently or in combination with each other. A successful NP tissue analog should possess the biomechanical and functional properties similar to the native NP tissue. To date, many natural biomaterials such as hyaluronan (HA), chitosan, gellangum, alginate, collagen, fibrin and silk fibroin, and synthetic biomaterials *e.g.,* PVA (Poly-vinyl alcohol), PVP, PLA, PLGA, PEG and PNIPAm have been widely used for making hydrogels as NP substitute.

Hydrogels have been found to be effective and promising for disc regeneration strategies. Hydrogels are mainly applied for NP regeneration in disc degeneration therapy. While choosing the suitable biomaterials, there are several parameters that need special attention while preparing hydrogels *viz.,* injectability, *in situ* polymerization in response to physiological conditions, mechanical properties similar to the native NP, high water uptake capacity and controlled degradation rate matching to the *neo*-tissue regeneration rate that have to be considered[282]. Moreover, the implanted materials should degrade, ideally, at the same rate as the new ECM secreted by the healthy NP cells. A wide range of natural polymers are being utilized for decades while fabricating hydrogels for IVD regeneration because of their biocompatibility, biodegradability, bioactivity and similarity to the natural ECM[228]. The popular natural biomaterials used in NP regeneration are discussed in the following sections.

1.2.1.3.1. Hydrogels of natural biomaterials

1.2.1.3.1.1. Hyaluronan (HA)

HA in IVD tissue engineering has been explored extensively in various studies till date. Isa *et al.,* observed the inhibitory effect of HA hydrogel on hyperinnervation in discogenic pain in a rat model via regulation of glycosylation[283]. In an *in vitro* study, Yang *et al.,* developed a gelatin/chondroitin-6-sulfate/hyaluronan tri-copolymer that supported cell growth and proliferation as well as ECM production[284]. Revell *et al.,* showed that the commercially available HA derivatives (HYAFF® 120 and HYADD® 3), when implanted in a pig model, displayed no sign of necrosis or inflammation and maintained the height similar to the normal discs[285]. In a rabbit microdisectomy model, Abbushi *et al.,* showed the regeneration capacity of resorbable cell-free PGA-HA hydrogel after 6 months of implantation and validated their observations in larger animal models as well[286]. A biphasic construct made of PLLA-nanofibers mimicking AF and HA hydrogel was found to support growth and differentiation of MSCs to chondrogenic lineage in presence of TGF-β[287]. Kim *et al.,* first time investigated the effect of photo cross-linked methacrylated HA hydrogel encapsulated NP cell density on final outcome of tissue functions for a prolonged culture of 8 weeks wherein they concluded that tissue function was independent of initial cell seeding[288]. In some cases, HA or HA-derivatives are also blended with other polymers to enhance the biological functionalities. For instance, a composite hydrogel of collagen type-II-HA cross-linked by 1-ethyl-3(3-dimethyl aminopropyl) carbodiimide (EDC)

and N-hydroxysuccinimide (NHS) was investigated with rat MSCs for NP regeneration[289]. A similar, but tri-composite semi-interpenetrating injectable hydrogel system of collagen, HA and gelatin microsphere loaded with TGF-β3 showed no sign of inflammation or cytotoxicity and supported the growth and chondrogenic differentiation of MSCs indicating a good candidate for disc regeneration[290]. Moss *et al.,* developed a composite hydrogel of thiol-modified HA and elastin-like polypeptide wherein, the elastin component provided desirable biomechanics for NP replacement therapy, and HA component supported cell viability and maintained cell phenotype[291]. Another tri-composite hydrogel made of silk fibroin, fibrin and HA was developed by Park *et al.,* wherein silk provided stronger mechanical support to the hydrogel compared to only fibrin-HA hydrogel system[43]. In a recent study, Chung *et al.,* developed an hybrid hydrogel system wherein HA was cross-linked with silk fibroin by horseradish peroxidase (HRP)/H_2O_2 and 1,4-Butanediol di-glycidyl ether (BDDE). The developed hydrogel showed the viscoelastic modulus similar to the native human NP tissue that induced human bone marrow derived stem cells (hBMSCs) differentiation towards NP phenotype[4]. Chen *et al.,* introduced oxidized high molecular weight HA-adipic acid dihydrazide hydrogel that showed good biocompatibility and supported sufficient ECM secretion, but fell short of satisfactory mechanical properties. Later on, they incorporated gelatin to make tri-composite hydrogel that reflected complex shear modulus (11-14 kPa) similar to that of native NP tissues[292]. A new generation injectable PEG-HA-based hydrogel system covalently linked to pentosan polysulphate (PPS) showed good viability of mesenchymal precursor cells (MPCs), retention of round morphology and enhanced secretion of ECM components after 21 days of culture[293]. Peroglio *et al.,* developed a thermo-reversible HA-PNIPAm hydrogel as injectable NP cells carrier system that promoted ECM secretion with time[294]. Gansau *et al.,* reported that the incorporation of HA and collagen in fibrin based hydrogel promoted GAGs accumulation while fibrin helped in cell proliferation[295]. Chen *et al.,* developed a photo-cross-linked gelatin-HA methacrylate hydrogel that provided potential advantages for adipose stromal cells (ASCs) differentiation towards NP cell[296]. In a recent study, Zhang *et al.,* showed that hypoxic condition could enhance the ECM production by NP cells in presence of HA, which correlated the up-regulation of CD44 expression upon activation of HIF-1α (hypoxia inducible factor)[297]. Though, HA in different forms or in combination with other biomaterials is being used in IVD regeneration, it is cytotoxic particularly

at high concentration or exhibits osteogenic potential that sometimes raise question on its applicability in NP tissue engineering[282].

1.2.1.3.1.2. Chitosan

Chitosan as an injectable hydrogel has drawn much attention for cartilage regeneration and thereby treating IDD due to its structural similarity to GAG[298]. Mwale *et al.,* first showed that injectable chitosan hydrogel system, cross linked with genipin supported 95% viability of encapsulated disc cells and no inflammatory reaction was noticed after 4 month of subcutaneous injection intoC57BL/6 mice[299]. Thermoresponsive hydrogels fabricated via conjugation of hydroxyl-butyl group to chitosan showed potential in cell carrier (for both MSCs and disc cells) in disc degeneration therapy. Studies have investigated the use of chitosan/glycerophosphate thermosensitive hydrogels for encapsulation of NP cells and/or differentiation of MSCs into identical NP cells and the results obtained were promising in the clinical translation for disc degeneration therapy[300]. A novel triple-interpenetrating-network injectable hydrogel made of dextran, chitosan and teleostean displayed significant potential in supporting viability of NP cells and differentiation of MSCs along a chondrogenic lineage[301]. Further, this hydrogel system in combination with MSCs exhibited the significant improvement in disc height index when injected into the degenerated disc in a clinically relevant goat model[302]. Nair et al. demonstrated great potential of a composite hydrogel system of chitosan-poly(hydroxybutyrate-co-valerate) incorporated with chondroitin sulfate (CS) nanoparticle in enhancing the viability and differentiation of adipose derived rat mesenchymal stem cells (ADMSCs) along the NP lineage[303]. Zhu *et al.,* developed a composite hydrogel of chitosan and HA cross-linked with glycerol phosphate that was employed as delivery system for kartogenin promoting ADSCs differentiation towards NP cells[304]. In a recent study, decellularized NP matrix was blended with chitosan and TGF-β3 to fabricate a hydrogel that supported NP cells proliferation, maintained NP cell morphology and up-regulated NP-related gene expression[305]. Although use of chitosan has some benefits e.g., its biocompatibility, cell adherent properties or non-immunogenicity, it is associated with some disadvantages *viz,* presence of impurities, use of certain cytotoxic cross-linker or poor mechanical performance[282].

1.2.1.3.1.3. Alginate

Alginate is being used for decades in different forms viz., hydrogel, capsules, beads, foam or microspheres prepared alone or blended with other biopolymers for different biological assessments with disc cells[306, 307]. Mizuno *et al.,* fabricated a composite construct, wherein NP cells encapsulated alginate hydrogel were injected into the center of AF cells seeded polyglycolic acid/polylactic acid construct that was implanted into the subcutaneous space of the athymic mice. After 12 weeks of retrieval, the injected alginate hydrogel supported sufficient col II deposition similar to the native NP tissue[308]. In an advanced study, Bowles *et al.,* designed the collagen (AF)/alginate (NP) tissue engineered total disc to transplant into the native disc space[248]. Similarly, Moriguchi *et al.,* developed tissue engineered total disc of collagen (AF)/alginate (NP) which when implanted in canine spine, integrated into the host tissue, retained the disc height and other biochemical properties post 16 weeks of implantation[254]. In another study, tissue engineered collagen (AF)/alginate (NP) total disc enhanced the functionality of the total disc in a dose-dependent manner[252]. Yang *et al.,* developed a tissue engineered total IVD construct of alginate (NP)/ (PCL)/ (PLGA)/Col type I (PPC) (AF), which showed the excellent structural and functional maintenance upon implantation into rat caudal spine[309]. In a different study, alginate gel was used to encapsulate the disc cells to understand the effect of oxygen level on ECM secretion wherein it demonstrated that low oxygen level did not impair the disc metabolism rather had beneficial effects[310]. Similarly, McCanless *et al.,* utilized an alginate-bead culture model to evaluate the effect of bone morphogenetic protein-2 and synthetic peptide B2A on MSCs proliferation, differentiation and ECM synthesis[311]. Abbott *et al.,* used alginate hydrogel system while demonstrating the response of human NP cells (isolated from different graded degenerated disc) to different pro-anabolic stimulants. They inferred that the moderately degenerated NP cells showed greater responses to anabolic stimulants than the severely degenerated varieties[312]. One different aspect of the alginate hydrogel was to evaluate the evolutionary importance of notochordal and NP cells co-existing in IVD. It was reported that the ideal ratio between these two types of cells was ~ 50:50 for the maintenance of ECM secretion[313]. Although alginate is widely used in IVD tissue engineering, it hardly matches the mechanical properties of the native NP. To address this issue, Johannes *et al.,* studied with a series of alginate concentrations (1-6%) and demonstrated that the stiffness of 2% alginate hydrogel closely mimicked native NP and the biosynthetic phenotype of encapsulated NP cells were

maintained up to 4 weeks[314]. *Kalaf et al.,* introduced a slow and tailored gelling method using 1:2 ratio of $CaCO_3$ and glucono-δ-lactone (GDL) with 10% $CaCl_2$ for IVD tissue engineering application[315, 316]. Though the ion induced cross-linked alginate hydrogel is most commonly used, its structural integrity fails over time. To overcome this issue, Chou and Nicoll first time demonstrated the use of photo cross-linked methacrylate alginate to encapsulate NP cells[317]. Guillaume *et al.,* investigated one innovative approach to fill the defect in disc (particularly in AF portion) by delivering covalently cross-linked alginate scaffolds exhibiting shape-memory effect in minimally invasive manner. The mechanical properties of these kind of alginate hydrogel scaffolds can be modulated by cross-linkers concentration[318]. Despite photo cross-linker, Foss *et al.,* incorporated chondroprotective agents like glucosamine and chondroitin sulfate in a dose dependent manner that promoted mechanical properties of alginate hydrogel for NP tissue engineering[319]. Moreover, alginate can be amalgamated with other polymers thereby imparting beneficial properties suitable for tissue engineering applications. For instance, PCL electrospun fibers were infiltrated with alginate hydrogel to impart the mechanical robustness that mimicked the natural disc[320]. Zeng *et al.,* introduced the poly (ethylene glycol) diacrylate (PEGDA) microcryogels reinforced alginate, a non-thermo-responsive injectable hydrogel as a leak-proof delivery system. This hydrogel system gained superior mechanical properties, improved cell retention and survival capacity, and showed alleviated degeneration in canine IDD model post 6 months of implantation[321]. A preclinical study was conducted with ultra-purified alginate gel which was implanted into IVD after discectomy in sheep model showing suitable biomechanical properties without gel protrusion[322]. However, even though alginate as a biomaterial in NP tissue engineering has some advantageous properties like easy polymerization, in situ injectability, cytocompatibility and similar mechanical properties, it is associated with some limitations like long term stability or difficulty to sterilize[282].

1.2.1.3.1.4. Gellangum

Gellangum (GG) is a water soluble, linear anionic hetero-polysaccharide that has the broad applications in food and cosmetic industries as a gelling agent or stabilizer. Nowadays, GG is being used as a biomaterial for tissue engineering and regenerative medicine as it has some suitable properties like rapid and tunable gelling, mechanical properties, swellability, degradation rate and the potential to decorate with functional molecules, which can be matched as per requirement of

specific tissue application. Silva-Correia *et al*., reported that photo cross-linked GG-MA (methacrylate) exhibited improved mechanical properties, less swelling ability and non-toxicity towards NP cells. Moreover, GG based hydrogels showed non-angiogenic features which is truly beneficial for the vascular NP cells as vascularization enhances disc degeneration [323]. Different combinations of GG and its derivatives (methacrylate and high-acyl GG) were evidenced to support the growth and viability of rabbit NP cells upon seeding onto the surface of hydrogels with tunable mechanical properties, swelling capacity and degradability[324]. Similarly, Tsaryk *et al.,* demonstrated that GG-MA synthesized either by ions or photo cross-linkers showed no toxicity to chondrocytes and MSCs, and no inflammatory response to endothelial cells[325]. In a recent study, Raheem et al., investigated a biocompatible novel hydrogel-foam composite system (low-acyl GG/ agarose/ Sugi® cellulose sponge material as foam) that exhibited viscoelastic properties similar to the native NP tissue[326]. Therefore, the tunability in physicochemical including mechanical and rheological properties, and biological properties of GG based hydrogel makes them a prospective NP substitute.

1.2.1.3.1.5. Collagen

Collagen is a highly versatile biomaterial and it is being used in both biomedical and research applications because of its biocompatibility, biodegradability, low immunogenicity and good permeability. Gruber et al., investigated a comparative study with variety of biomaterials including collagen (sponge and gel), agarose, alginate and fibrin as cell carrier where they showed maximum potential of collagen in disc cells proliferation and ECM secretions[327]. Lee *et al.,* investigated the effect of TGF-β1 and BMP-2 on rabbit NP cells encapsulated in atelocollagen type II (extracted from animal dermal tissue) hydrogel, wherein enhanced cell proliferation and up-regulation anabolic genes expression were observed[328]. Yuan *et al.,* demonstrated the advantages of 3D collagen microspheres culture system over the traditional monolayer culture system as it preserved NP cells phenotype as well as helped in remodeling of template collagen matrix by depositing new ECM components including collagen type II and GAGs[329]. The stability of collagen scaffold or hydrogel system can be increased by genipin, a natural cross-linker for protein. Zhou *et al.,* optimized the genipin concentration to 0.1% that improved the bio-stability of collagen scaffolds, thereby it promoted ADSCs proliferation and differentiation towards NP phenotype[330]. However, collagen have also been investigated when blended with other polymers for NP tissue

engineering. For instance, Huang *et al.,* investigated the bioactivity of collagen II (C II) / hyaluronan (HA) / chondroitin-6-sulfate tri-copolymer, wherein chondroitin-6-sulfate was covalently cross-linked with C II-HA scaffold by EDC-NHS. The tri-copolymer scaffold system supported rabbit NP cells viability, proliferation and up-regulated col II and aggrecan gene expression, while down-regulated Col I gene expression[331]. A stabilized form of collagen type-II hydrogel enriched with HA showed nontoxicity to ADSCs (adipose derived stem cells) and NP cells, and maintained type-I collagen mRNA expression indicating an injectable reservoir for cell delivery in NP replacement therapy[332].

In terms of chemistry, gelatin is denatured collagen and it transforms into gel from the molten solution when temperature is reduced. Gelatin has also been used in various fields of biomedical and regenerative medicine including disc regeneration therapy. Strange and Oyen investigated the time dependent mechanical properties of a composite hydrogel made of gelatin and agarose using viscoelastic and poroelastic frameworks targeting the design of NP equivalent hydrogel[333]. Charron developed the gel system consisting of gelatin, polyvinyl alcohol (PVA) and PEG (polyethylene glycol) in order to achieve mechanical properties similar to the native NP tissue[334]. However, the interpenetrating network (IPN) provides a better strength and toughness to the hydrogel system. Gan *et al.,* synthesized a hydrogel system with IPN using gelatin, dextran and PEG that exhibited high toughness in the optimal formulation. In an *in vivo* study, this hydrogel not only showed the increasing cell proliferation, but also facilitated regeneration of damaged NP in a porcine model[335]. Modification in gelatin like methacrylation provides several advantages including fast gelling within few minutes or even few seconds, thereby minimizing the cytotoxicity, tunable mechanical, degradation, and biological properties depending on the ratio of methacrylamide and photoinitiator, as well as the photopolymerization time[336-338]. In a very recent study, Xu *et al.,* synthesized gelatin methacrylate based (GelMA) photosensitive hydrogel system with tunable physical and biological properties to meet the requirement of NP tissue engineering[339].

1.2.1.3.1.6. Fibrin

Fibrin is utilized as an excellent scaffolding material in different fields of tissue engineering and IVD is not an exception. Buser *et al.,* experimented with an intradiscal injection of BIOSTAT BIOLOGX fibrin sealant (FS) for disc healing purpose in pig model[340]. FS showed promising

results maintaining the structural, compositional and mechanical characteristics of FS treated discs after 12 weeks of implantation. FS was also shown to be very effective as a delivery vehicle of novel bi-laminar cell pellets (where MSCs spheres were surrounded by NP cells layers) into denucleated discs[341]. Fibrin conjugated with HA provided a stable gel system that could be treated as injectable material in nucleotomised disc model[342]. In a recent study, fibrin-HA hydrogel was used to deliver FGF-18 for NP regeneration showing positive modulatory effects when tested on human degenerated NP cells[343].

1.2.1.3.1.7. Silk fibroin

Despite SF scaffolds (lamellar or porous) being extensively used to fabricate AF constructs, silk based hydrogels are mainly recommended for NP replacement. Porous silk scaffolds prepared by paraffin-sphere-leaching process exhibited appropriate microstructure and mechanical properties that supported rabbit NP cell adhesion, proliferation and infiltration, offering a potential candidate as NP substitute[344]. It is often blended with other polymers (natural or synthetic) that forms a new class of biomaterials to achieve suitable properties according to the need (However, few of them have already discussed in previous sections). Hu *et al.,* prepared an injectable in-situ hydrogel of SF-polyurethane (PU) that exhibited appropriate physical-mechanical properties to support the vertebral disc in an *ex vivo* model. The liquid or semi-solid liquid form of this composite hydrogel could easily be delivered into the central NP portion through a small incision[345]. Neo *et al.,* developed a cryogen wherein silk fibroin was blended with PVA that offered a good physical-mechanical properties, thereby improving NP cell-hosting abilities[346]. Murab *et al.,* developed glucosamine loaded injectable silk-in silk integrated hydrogel system where glucosamine, upon release, supported ADSCs growth, maturation and differentiation and also provided sufficient mechanical support in an *ex vivo* disc degeneration model[347]. One remarkable study of NP repair was the clinical trial of NuCorer® (Spine Wave Inc., Shelton, CT, U.S.A.), a recombinant protein co-polymer of silk and elastin[348]. This nontoxic, biocompatible injectable hydrogel closely mimicked the protein and water content, pH and complex modulus to the native NP tissue. This is the first biomaterial which is clinically translated in the human patients for NP repair. A 2-year follow-up pilot study of this hydrogel showed significant improvement of back pain maintaining the disc height with no sign of herniation[349].

1.2.1.3.1.8. Platelet rich plasma (PRP)

Like other naturally derived biomaterials, platelet rich plasma (PRP) based hydrogel has also currently being used in various clinical complications including wound healing, osteoarthritis and tendinopathies[350, 351]. It is advantageous over others as it is autologous in origin and contains numerous autologous growth factors like TGF-β1, PDGF and IGF that improve cells proliferation[352]. Zhang *et al.,* developed an autologous PRP based injectable hydrogel with smooth surface and good elasticity that helped in differentiation of ADSCs towards NP cells, when cultured *in vitro*[353].

1.2.1.3.1.9. Peptides

Recent advances in NP tissue engineering based strategies employ the use of engineered peptide-functionalized hydrogel systems as emerging promising alternative for disc degeneration therapy. For instance, Tao *et al.,* synthesized two self-assembling peptides (PKP and RKP) upon linking of a short functional motif of BMP7 to RADA16-I or mixing of RKP to RADA16-I that showed biocompatibility and bioactivities to NP cells isolated from degenerated IVD[354]. In a recent work, Ligorio *et al.,* developed an injectable hybrid hydrogel consisting of graphene oxide and a self-assembling peptide FEFKFEFK (F: phenylalanine; K: lysine; E: glutamic acid) for delivering TGF-β3 to direct NP cell fate and function[355]. Similarly, Barcellona *et al.,* developed an engineered-peptide hydrogel system consisting of PEG, which was functionalized with syndecan and integrin binding laminin-mimetic peptides (LMP) modulating human NP cell phenotype through mechano-biological effects[356].

1.2.1.3.1.10. Cellulose

Likewise, nanofibrillated cellulose based composite hydrogel system was investigated for NP replacement therapy as it mimicked the mechanical and swelling behavior of native NP tissue, which could help in restoration of disc height[357, 358]. Gupta *et al.,* demonstrated that a photo cross-linked carboxymethylcellulose (CMC) hydrogel supplemented with TGF-β3 could be the potential candidate for NP tissue engineering. This biocompatible, cost effective cellulose derivative not only supported the viability of NP cells, but also promoted the differentiation of hMSCs towards NP phenotype when encapsulated into it[359]. In an advanced study, Varma *et al.,* developed an *in situ* gelling CMC hydrogel using a redox initiation system (the process is

known as radical polymerization) that induced covalent bonds among the chains. This hydrogel supported MSCs viability along with deposition of NP specific ECM components, and also maintained the mechanical and swelling behavior similar to the native NP tissue over 35 days of culture in chondrogenic media[360].

1.2.1.3.2. Hydrogels of synthetic biomaterials

While hydrogels from natural polymers provide a wide range of biological advantages, in alternate a desirable, predictable and reproducible physicochemical properties can be obtained from the synthetic polymers. Both Poly(vinyl alcohol) (PVA) and Poly(vinyl pyrrolidone) (PVP) are well explored synthetic polymers that have been used in various tissue engineering including NP tissue replacement therapy[34]. A PVP-PVA based injectable hydrogel developed by Leone *et al.,* showed the viscoelastic behavior similar to the healthy NP tissue when mixed them at 1:1 ratio and chemically cross-linked by trisodium trimetaphosphate (STMP)[361]. However, PVA could also be blended with other natural polymers like xanthan gum to fabricate a composite hydrogel system exhibiting the mechanical behavior, which made it a suitable candidate as NP substitute[362]. Liang *et al.,* developed the nanostructured 3D PLGA (poly lactic-co-glycolic acid) microsphere in which dexamethasone and bFGF loaded heparin/poly(L-lysine) nanoparticles were incorporated to function as NP tissue substitute. These engineered microspheres supported the growth and differentiation of RMSCs (rat mesenchymal stem cell) to NP cells, and also exhibited reduced immune response showing the potential for NP tissue engineering[363]. Christiani *et al.,* developed a hydrogel system, wherein PNIPAAm (a thermosensitive synthetic polymer) was covalently conjugated with chondroitin sulfate (CS) to make it enzymatically biodegradable, non-immunogenic and biologically more functional. Further, addition of alginate particles to this PNIPAAm-CS hydrogel enhanced adhesive tensile strength (important to minimize the risk of dislocation) and swelling capacity (treat as space-filling gel) which are the two critical aspects that need special attention during implantation[364, 365]. Vernengo *et al.,* investigated an *in situ* forming of PNIPAAm-PEG gel for NP replacement[366]. Later on, they incorporated poly(ethylene imine) (PEI) that provided the bio-adhesiveness properties to this PNIPAAm-PEG gel system reducing the risk of implant dislocation[367]. In a study, Malonzo *et al.,* encapsulated hMSCs in PNIPAAm gel and injected into papain induced degenerated bovine caudal discs, wherein the hydrogel system helped in significant up-regulation of NP specific ECM genes by the

encapsulated MSCs in disc cavity[368]. Varma *et al.,* demonstrated another type of thermoresponsive dual polymeric network hydrogel made of methacrylated carboxymethylcellulose (MA-CMC) and methylcellulose (MC) that restored the IVD height and biomechanical functions when implanted into nucleotomised discs indicating its strong potential in NP replacement therapy[369]. In a recent study, Mckee *et al.,* developed the acrylate and thiol functionalized PEG hydrogel that promoted hMSCs differentiation towards NP cells both *in vitro* and in *ex vivo* disc degeneration model[370]. However, several photo-curable synthetic biomaterials have also been used in repair and regeneration of NP tissue. For instance, Kumar *et al.,* demonstrated the potential use of a photo-curable, biodegradable hydrogel consisted of polyhydroxyl-ethyl-methacrylate-co-N-(3-aminopropyl)-methacrylamide grafted with polyamidoamine (p(HEMA-co-APMA)g-PAA) that promoted the differentiation of hMSCs towards NP-like cells under the hypoxic condition[371]. Overall, all these studies demonstrate the potential of cells (both autologous and MSCs) for NP regeneration using combined strategies of cell therapy and various biomaterials.

MOTIVATION AND OBJECTIVE OF THE PRESENT INVESTIGATION

MOTIVATION AND OBJECTIVES OF THE PRESENT INVESTIGATION

Low back pain (LBP) is an important clinical, socio-economic and public health burden affecting the population indiscriminately across the globe. Intervertebral disc degeneration (IDD) is the major cause of LBP, and it affects the intervertebral discs (IVD), a soft fibrocartilaginous tissue holding the vertebrae together. IDD is characterized by disc cell death, loss of extracellular matrix (ECM), and up-regulation of matrix metalloproteinases (MMPs) that cause the gradual dehydration of NP, leading to an imbalance in intradiscal pressure and reduction of shock-absorbing capacity of IVD. The radial tears or cracks occur in the multilamellar AF tissue initiating the irreversible degenerative cascade of IVD structure. The conventional therapies are only effective in symptomatic relief of pain without restoring the biomechanical function of native discs and are also associated with high expenditure of the treatment. The emergence of tissue engineering technology provides a promising alternative strategy for the treatment of IDD by replacing with tissue engineered disc that may resemble to native IVD structure and functions. The origin of the present research work and motivating factors are as follows:

1. Tissue engineers are trying to develop the biomimetic constructs with the combinations of various biomaterials and engineered aided design for structural recapitulation of IVD, in particular, the AF anatomy. The researchers have shown great interest to replicate the anatomic forms of AF with suitable biomaterials. Although, few studies have focused on recapitulation of structural features of AF, yet challenges remain for their clinical implementation because of their tremendous complexity at the cellular, biochemical, microstructural, and biomechanical levels.
2. Directional freezing is based on a simple thermodynamic principle where the velocity and morphology of the ice-front propagation is controlled through the sample in a unique direction. Moreover, use of aqueous based polymeric system (where water is the main sol fraction), avoid the introduction of any toxic products into the scaffolds. In the present study, we implemented this technique to prepare lamellar scaffolds with multi-lamellar angle-ply constructs to mimic native disc morphology.
3. Silk fibroin (SF) is a naturally derived protein polymer that is being used as a biomaterial in various biomedical applications due to its easy processability, biocompatibility,

hemocompatibility, tunable biodegradability and mechanical properties, and minimal immunogenicity. Due to easy processability and flexibility, SF can be used in the fabrication of various formats like films, scaffolds, nano-fibrous mats, hydrogels, and micro to nano-particles. SF can be isolated from both mulberry (i.e., *Bombyx mori,* BM SF) and non-mulberry (*e.g., Antheraea assamensis,* AA SF and *Philosamia ricini,* PR SF) sources.

4. Some silk varieties, *e.g.,* non-mulberry silk fibroin possesses inherent RGD-motif (arginine-glycine-aspartic acid, an integrin binding receptor) facilitating enhanced cell attachment and proliferation. Moreover, the unique molecular architecture (uninterrupted poly-alanine stretches) of AA SF or PR SF provides tunable mechanical properties. To mimic the gradual transition of mechanical gradient from inner to outer region of native AF tissue, SF proteins from these two sources can be blended that may provide differential mechanical and cell binding properties.
5. Currently, 3D printing technology is becoming popular in different tissue engineering including bone, cartilage, skin, liver, heart, and blood vessel, as well as in IVD using various biomaterials. 3D printing technology can be utilized to recapitulate the complex tissue architecture with the highest accuracy and precision in a high throughput manner. Though manual fabrication strategies have achieved the structural and functional similarities to the native IVD, precise replication and high throughput reproducibility is essential for fabricating a customized IVD construct.
6. Aqueous solutions of SF undergo self-assembly giving rise to the formation of β-sheets which results in hydrogel formation. Silk hydrogel can be fabricated following several methods that include use of chemicals or applying physical stimulus. However, silk hydrogel can also be fabricated when SFs from two different sources *i.e.,* mulberry and non-mulberry are mixed together. The protein chains in aqueous SF solution self-assembled and transformed into gel (due to alteration of the hydrophobic-hydrophilic microenvironment) in absence of any cross-linker or given external stimulus. The hydropathicity of these two types of SFs is different due to their amino acid composition, sequence and arrangement. This self-gelling property can be a potential platform for NP regeneration therapy via *in situ* gelation.

7. The north-eastern area of India is rich in these non-mulberry silk varieties, and their application is not highly explored in the biomedical field. Hence investigating biomedical applications of these silk proteins has opened up a large window for research in exploring new properties and potential of the same in tissue engineering and regenerative medicine.
8. Wharton's Jelly (WJ) is a mucosal connective tissue surrounding the umbilical cord vessels and is wrapped with an amniotic epithelium layer. The WJ matrix is rich in collagen, elastin, hyaluronan (HA), and sulfated glycosaminoglycan (sGAG). WJ matrix can provide several characteristic features in a scaffolding material used for different tissue engineering applications. In general, the 3D microenvironment of jelly potentially provides all the suitable conditions for cell proliferation and differentiation. Utilizing all these properties of WJ, a composite hydrogel with silk proteins can be designed, thereby delivering as minimally invasive injectable hydrogel for NP tissue replacement.

In light of the enormous scope of exploring silk biomaterial and its attributes for IVD tissue engineering, we would like to fabricate the AF anatomical equivalent utilizing the manual strategy and automated 3D printing technique, as well as development of minimally invasive bioactive injectable hydrogel as NP substitute. We analyzed our various hypothetical approaches through the pursuit of the following objectives.

Objectives

1. Fabrication and characterization of silk-based multilayered angle-ply construct for damaged annulus fibrosus (AF) tissue replacement.
2. Fabrication and characterization of a seamless full thickness disc-like angle-ply construct with tailored mechanical properties modulating extracellular matrix secretion by annulus (AF) fibrosus cells.
3. Design and fabrication of 3D-printed biomimetic construct to recapitulate form and function of intervertebral disc (IVD).
4. Development of an *in situ* formulation of silk hydrogel for nucleus pulposus (NP) tissue engineering.
5. Development of a minimally invasive injectable bioactive silk-hydrogel functionalized with human decellularized Wharton's jelly extracellular matrix (dWJECM) for nucleus pulposus (NP) tissue replacement therapy.

Chapter 2

Fabrication and Characterization of Silk Based Multilayered Angle-ply Construct for Damaged Annulus Fibrosus (AF) Tissue Replacement

This chapter describes the fabrication of silk-based multilayered disc-like angle-ply constructs, recapitulating the "form and function" of native annulus fibrosus (AF) tissue of intervertebral disc (IVD). Fabrication of AF anatomical constructs adopting directional freezing technique, validation and verification of structural, mechanical and biological attributes are illustrated in details.

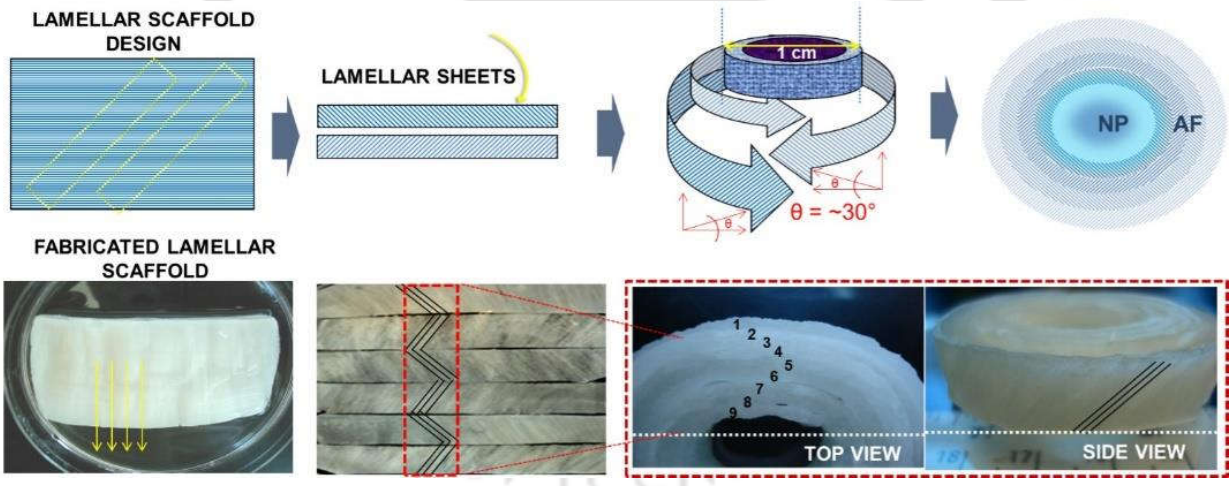

The work embodied in this chapter in published in a peer-reviewed journal as follows:

Bhunia BK, Kaplan DL, Mandal, BB. Silk-based multilayered angle-ply annulus fibrosus construct to recapitulate form and function of the intervertebral disc. **Proceedings of the National Academy of Sciences of the United States of America**. 2018;115(3):477-82.

ABSTRACT

Recapitulation of the form and function of complex tissue organization using appropriate biomaterials impacts success in tissue engineering endeavors. The annulus fibrosus (AF) represents a complex, multi-lamellar, hierarchical structure consisting of collagen, proteoglycans and elastic fibers. To mimic the intricacy of AF anatomy, a silk protein-based multilayered, disc-like angle-ply construct was fabricated, consisting of concentric layers of lamellar sheets. Scanning electron microscopy and fluorescence image analysis revealed cross-aligned and lamellar characteristics of the construct, mimicking the native hierarchical architecture of the AF. Induction of secondary structure in the silk constructs was confirmed by infrared spectroscopy and X-ray diffraction. The constructs showed a compressive modulus of 499.18 ± 86.45 kPa. Constructs seeded with porcine AF cells and human mesenchymal stem cells (hMSCs) showed ~ 2.2-fold and ~ 1.7-fold increases in proliferation on day 14, respectively, compared to initial seeding. Biochemical analysis, histology and immunohistochemistry results showed the deposition of AF-specific extracellular matrix (sulfated glycosaminoglycan and collagen type I) indicating a favorable environment for both cell types, which was further validated by the expression of AF tissue-specific genes. The constructs seeded with porcine AF cells showed ~ 11-, ~ 5.1- and ~ 6.7-fold increases in col *Iα* 1, sox 9 and aggrecan genes, respectively. The differentiation of hMSCs to AF-like tissue was evident from the enhanced expression of the AF specific genes. Overall, the constructs supported cell proliferation, differentiation and ECM deposition resulting in AF-like tissue features based on ECM deposition and morphology, indicating potential for future studies related to IVD replacement therapy

2.1. Introduction

Intervertebral disc degeneration (IDD) is the major cause of lower back pain and limited mobility, contributing significantly to healthcare expenditures[372]. IDD is characterized by progressive damage to the annulus fibrosus (AF) region which confines the gelatinous nucleus pulposus (NP). This damage to AF is associated with mechanical stress, loss of function, biological remodeling and dehydration of inner NP extracellular matrix. Current therapeutic treatments for IDD include conservative methods, such as medication and physical therapy, or surgical intervention including spinal fusion and total disc arthroplasty (TDA). However, these surgical procedures are only effective in symptomatic pain relief without restoring the biomechanical functions of the IVD, which may lead to disintegration of adjacent segments. Furthermore, these surgical procedures are case dependent and cannot be applied to all patients[372]. In this context, tissue engineering technology provides a promising alternative strategy for the treatment of IDD through implantation of *in vitro* engineered tissue discs mimicking native structure and functions.

Tissue engineers continue to develop biomimetic tissue constructs with combinations of various biomaterials and engineered designs to recapitulate AF structure and function essential for regeneration[49]. The replication of the anatomic forms of AF using different biomaterials has included both natural and synthetic polymers, however, few studies have focused on recapitulation of structural features of the tissue. Most importantly, the introduction of lamellar scaffolds in AF tissue engineering may be critical for the field due to the direct relationship between the hierarchical features and mechanical functions of the tissue[239]. One study involved the fabrication of an alginate/chitosan scaffolds to form a lamellar AF structure that supported canine AF cell growth and function[373]. Biphasic scaffolds, such as demineralized bone matrix gelatin (BMG) poly(polycaprolactonetriol malate) (PPCLM) supported the regeneration of AF tissue, structurally and mechanically close enough to native rabbit AF[374]. Similarly, silk-based lamellar constructs have also been fabricated for AF tissue engineering. A biphasic construct consisting of silk fibroin-based porous lamellar structures for AF, in combination with fibrin/hyaluronic acid gels for the NP region were reported[249]. An advanced strategy wherein silk fiber-based multi-lamellar constructs were prepared in which silk fibers or chondroitin sulfate modified silk fibers were wound to form a hierarchical and lamellar structure resembling native AF tissue[240, 375, 376]. However, the degradation rate of natural silk fibers was very slow as a constraint in the study,

limiting replacement by *neo*-tissue[377]. In silk based tissue engineering, silk fibers are often regenerated and then processed into different formats *viz.,* scaffolds, films, mats or hydrogels, prior to use as implants. Consequently, the biodegradation of these regenerated silk fibroin (SF) products is faster than the native silk fibers, both *in vitro* and *in vivo*[378]. Another approach to address the complex hierarchical design of AF is electrospinning, which has been previously introduced to engineer various aligned tissues[379]. In this technique, the fabricated constructs exhibit highly aligned arrays of polymeric nanofibers that mimic the natural organization of different fiber-reinforced soft tissues including the AF[217]. Multi-scale, biologic constructs using electrospun mats of PCL (Polycaprolactone) that were hierarchically and anatomically relevant to the native AF were reported[217]. However, electrospun scaffolds often face a number of limitations including low porosity that restrict uniform cell infiltration, and a discrepancy of mechanical properties compared to native AF.

The multi-scale, hierarchical, collagen fiber-reinforced composite structure of the AF is responsible for shock-absorption and flexibility of the spinal column. The AF consists of 15–25 concentric layers; each layer is strengthened by collagen nanofibers which are aligned at ~ 30° angle with respect to the diagonal plane of the spine axis, but in alternate directions in each successive layer[49]. This type of organization creates an angle-ply structure which is critical for proper biochemical and biomechanical functioning of the AF. Understanding of such intricate organization is key towards recent efforts to simulate anatomical features for a physiologically functional engineered disc.

In the present study, silk fibroin (SF) was used for the fabrication of lamellar 3D scaffolds. To mimic the complex organization of AF anatomy, silk based disc-like angle-ply constructs that consisted of concentric layers of lamellar sheets were prepared. The lamellar alignment represented the alternate direction of lamellae in successive layers of native AF, making an angle-ply structure. A directional freezing technique was adopted to prepare the lamellar scaffolds as described previously[380]. Mechanical properties, the impact of fiber alignment on cell proliferation, extracellular matrix secretion (sulfated glycosaminoglycan; sGAG and collagen content analysis) and specific gene expression (through real time polymerase chain reaction; RT-PCR) of AF cells and human mesenchymal stem cells (hMSCs) seeded on these scaffolds was addressed in the study.

2.2. Materials and methods

2.2.1. Isolation of silk fibroin protein

Aqueous solution of silk fibroin (SF) was derived from *Bombyx mori* silk cocoons according to the procedure previously described[381]. In brief, *B. mo*ri cocoons were collected from local sericulture farms of Assam, India. They were then cut into small pieces and boiled in aqueous solution of 0.02 M Na_2CO_3 (Sigma, U.S.A.) for 15 min to remove the glue like sericin from outer layers followed by washing thoroughly in deionized water. The extracted silk fibers were then left overnight at room temperature for drying. The sericin-free silk fibers were dissolved in 9.3 M LiBr (Sigma, U.S.A.) solution and kept it at 60 °C for 4 h. This process was followed by dialysis against deionized water using 12 kDa molecular-weight cut-off cellulose dialysis membranes (Sigma, U.S.A.) with frequent changes of water in regular time interval for 2 days. The final concentration of SF solution was 9-12% (w/v), determined gravimetrically by weighing the remaining solid after drying.

2.2.2. Preparation of biological lamellar replicates

The lamellar scaffolds were prepared using the protocol described in a previous work (**Figure A2.1**)[380]. Briefly, polydimethylsiloxane (PDMS) molds consisted of two chambers separated by a copper metal plate (**Figure A2.1 A**). The PDMS acted as the thermal insulator and facilitated relatively facile processing of the silk into various shapes, as well as easy removal of the prepared scaffolds. To prepare lamellar scaffolds, 5% (w/v) SF solution was poured into either chamber of predesigned PDMS mold and the opposite chamber of the mold was filled with liquid N_2. The metal plate was directly cooled by liquid N_2 and led to directional freezing of the SF solution. The liquid N_2 was repeatedly replenished until the whole protein solution had crystallized (**Figure A2.1 B**). The frozen SF block was transferred into a lyophilization chamber for freeze drying. The dried lamellar scaffold was then treated in 70% (v/v) ethanol to induce β-sheet in SF. The thin skin from both top and bottom side were removed by a surgical blade to open up the lamellar pores. The prepared lamellar scaffolds were then stored at 4 °C in ethanol for future use.

2.2.3. Scanning electron microscopy (SEM)

The cross-sections of lamellar scaffolds with or without cells were examined by SEM (Zeiss Ultra 55, Carl Zeiss AG, Germany) at an operating voltage of 10 kV. To prepare fractured sections,

lamellar scaffolds were dipped into liquid nitrogen followed by excision with a razor blade. The sections were sputter coated by Pt/Pd. Inter lamellar distance, lamellar channel length and the pore size of longitudinal cross sections were determined by measuring ~ 25 randomly selected pores with ImageJ 1.4 (Wayne Rasband) software.

2.2.4. Wide angle x-ray diffraction (WAXD)

The X-ray diffractogram of the alcohol treated and non-treated lamellar SF scaffolds were collected with a Bruker D2 Phaser diffractometer (U.S.A.). Ni filtered Cu Kα was the X-ray source to investigate changes in crystallinity. The diffraction range (2θ) was set between 10°-70° with a scan speed of 0.5° min^{-1}.

2.2.5. Fourier transform infrared spectroscopy (FTIR)

To confirm the secondary structure of alcohol treated lamellar SF scaffolds, FTIR analysis was carried out using an infrared spectrophotometer (Nicolet iS 10, Thermo Scientific, USA). The spectrometer was equipped with a thermo-electrically (TE)-cooled deuterated triglycine sulfate (DTGS) detector with KBr (potassium bromide) window. The spectra were measured in the range of 4000–400 cm^{-1} with a resolution of 4 cm^{-1} and 32 scans.

2.2.6. Mechanical properties

The mechanical testing of hydrated constructs was determined on an Instron 3366 (Norwood, MA, U.S.A.) equipped with a 100 N load cell. To perform the compressive strength, three sets of samples were prepared: set I was comprised of only lamellar rings (~ 4 cm in diameter x ~ 1 cm in thickness), set II was comprised of only the agarose gel in lieu of the NP gel (~ 1 cm diameter x ~ 1 cm in thickness) and set III represented the whole construct consisting of lamellar rings centering the agarose gel. The set IV was the native porcine AF used as control. All sets of constructs were hydrated at least 30 min in 0.1 M PBS at 37 °C before testing. Mechanical tests were performed with a conventional open-sided (non-confined) configuration and were accomplished using a displacement control mode at a rate of 1 $mm.min^{-1}$. After the compression tests, the compressive stress and strain curves were plotted based on the measured cross-sectional area and sample height (nominal 1 cm, measured automatically at 0.01 N tare loads), respectively. The compressive modulus was calculated based on a linear regression fitting of a small strain

section that preceded an identifiable plateau region in all tests. A total of 3 samples (n = 3) per group was analyzed.

2.2.7. Biological assessments

2.2.7.1. Isolation and culture of porcine annulus fibrosus (AF) cells and bone marrow derived human mesenchymal stem cells (hMSCs)

AF cells were isolated from porcine intervertebral discs (IVD) following previously described protocols[239]. Briefly, the lumber portion of spine of a new born porcine (14-21 days old) was collected from local abattoir within 1h post processing. Discs were procured from the lumber portion after discarding the muscles and tendons associated with the tissue. The whole procedure was conducted under sterile conditions. The AF tissues from 2-3 IVDs were finely minced followed by brief rinsing in 70% (v/v) ethanol and washing thoroughly with sterile phosphate buffered saline (PBS, pH 7.4). The chopped AF tissues were then digested in 0.2% (w/v) protease (Sigma, U.S.A.) for 1 h at 37 °C followed by overnight digestion in 0.03% (w/v) collagenase (Sigma, U.S.A.) prepared in Dulbecco's Modified Eagle Medium: Nutrient Mixture F-12 (DMEM/F12) supplemented with 10% (v/v) fetal bovine serum (FBS) and 1% (w/v) antibiotic-antimycotic (Gibco, Life Technologies, U.S.A.). The digested specimen was then centrifuged at 235 g for 5 min to collect the cell suspension.

Human MSCs were isolated from bone marrow using our previously described protocol[382]. In brief, hMSCs (Lonza Inc., Walkersville, MD, U.S.A.) were diluted in PBS (pH 7.4) followed by density gradient centrifugation (poly-sucrose gradient; 1.077 $g.cm^{-3}$, Histopaque, Sigma, U.S.A.). Thereafter, the cell pellet was resuspended in α-Minimum Essential Medium (α-MEM; Gibco, Life Technologies, U.S.A.) supplemented with 10% (v/v) FBS, 100 $U.mL^{-1}$ penicillinG and 100 $mg.mL^{-1}$ streptomycin. The cell number and viability were assessed by trypan blue exclusion. Porcine AF cells and hMSC pellets were resuspended and plated at a density of 2 x 10^5 cells cm^{-2} and placed at 37 °C in an incubator (5% CO_2 and 85% humidity). The culture medium (DMEM/F12) supplemented with 10% (v/v) FBS, 50 µg mL^{-1} ascorbic acid, 100 $U.mL^{-1}$ penicillin G and 100 $mg.mL^{-1}$ streptomycin was changed every 2nd day and cells were passaged to P3 and stored at -196 °C for future use.

2.2.7.2. Cell seeding and maintenance within constructs

To prepare *in vitro* AF-like tissue constructs, the porcine AF cells and hMSCs were seeded separately within the fabricated construct using static cell seeding procedures. These constructs were then left undisturbed for 3-4 h to facilitate the adherence of the seeded cells within the lamellar constructs. After 4 days, cell seeded scaffolds were transferred to chondrogenic medium supplemented with transforming growth factor- β 1 (TGF-β1; 10 ng.mL^{-1}), insulin (6.25 µg.mL^{-1}), transferrin (6.25 µg.mL^{-1}), ascorbic acid (50 mg.mL^{-1}), selenious acid (6.25 mg.mL^{-1}), proline (40 mg.mL^{-1}), dexamethasone (100 nM), bovine serum albumin (BSA; 1.25 mg.mL^{-1}), and sodium pyruvate (100 mg.mL^{-1}). All of these components were purchased from Sigma-Aldrich, U.S.A. The cell seeded constructs continued for 14 days in aforementioned chondrogenic medium conditions and the medium was changed every two days up to 14 days.

2.2.7.3. Imaging of cellular alignment in lamellar constructs

Cell viability and alignment of seeded porcine AF cells and hMSCs in lamellar scaffolds were screened using live/dead assay (Invitrogen, Life Technologies, U.S.A.). Following the manufacture's protocol, scaffolds were seeded with primary porcine AF cells and hMSCs separately at 0.5 x 10^6 cells per scaffold (scaffold dimensions; 6 x 2 mm) and maintained for two weeks with periodic media changes. Seeded scaffolds were then stained with live/dead assay. The solution is a mixture of three components: 2 mM ethidium homodimer-1, phosphate buffered saline (PBS) and 4 mM calcein AM. Calcein AM become fluorescent when taken up by the viable cells. The dead cells become red because of the absence of an intact cell membrane. The ethidium homodimer-1 easily passes through the damaged membrane and binds the DNA[383].

To visualize nuclei, cell seeded scaffolds were fixed in 10% (v/v) neutral buffered saline (NBF) for 30 min. Samples were then washed with PBS (pH 7.4) and preincubated with 1% (w/v) bovine serum albumin (BSA) (Sigma, U.S.A.) for 30 min followed by washing and permeabilization in 0.1% (v/v) Triton X-100 (Sigma, U.S.A.) for 5 min. After thoroughly washing with PBS, the constructs were incubated with Hoechst 33342 (Invitrogen, Life Technologies, U.S.A.) for 30 min in the dark. Images were captured using a confocal laser scanning microscope (Leica SP2 inverted microscope) equipped with argon (488 nm) and HeNe (534 nm) lasers.

2.2.7.4. Cell proliferation

Cell proliferation was monitored by total DNA content per scaffold at 1, 7 and 14 days. Equal numbers of porcine AF cells and hMSCs (0.5 x 10^6 cells per scaffold, 6 x 2 mm) were seeded within the preconditioned scaffolds (in DMEM/F12 supplemented with 10% (v/v) FBS for 24 h). The cell seeded scaffolds were then incubated at 37 °C with 5% CO_2. The medium was changed every two days. For DNA estimation, individual scaffolds of the same dry weight (n = 3) with and without cells (as control) were digested in papain digestion cocktail (125 $mg.mL^{-1}$ papain, 5 mM L-cysteine, 100 mM Na_2HPO_4, and 5 mM EDTA, pH 6.2) at 60 °C for 16 h. PicoGreen DNA assay was used to measure the total DNA content per the manufacturer's protocol (Invitrogen, Life Technologies. U.S.A.). In brief, after centrifugation of papain-digested samples, 25 µL aliquot of supernatant from each sample was added into a 96-well plate followed by addition of 75 µL of 1x Tris-EDTA (TE) buffer and 100 µL of Quant-iTPicoGreen reagent (1:200 dilutions). The lambda phage DNA in concentrations of 0, 2.5, 5, and 10 $\mu g.mL^{-1}$ were used to generate a standard curve. The data were measured using a fluorimeter (Tecan Infinite 200 PRO series) with an excitation and emission wavelength of 480 and 528 nm, respectively.

2.2.7.5. Histology of the cell seeded constructs

The lamellar scaffolds seeded with primary porcine AF cells and hMSCs were washed in PBS followed by fixation in 10% (v/v) NBF (neutral buffered formalin) for 24 h before histological analysis. Samples were dehydrated through a series of graded ethanols (50-100% v/v), embedded in paraffin, and sectioned at ~ 5 µm thickness. For histological evaluation, sections were deparaffinized, rehydrated and stained with hematoxylin and eosin (H&E). Alcian blue staining was performed to evaluate sGAG deposition in the constructs. For this purpose, sections were stained with 1% (w/v) alcian blue (Sigma, U.S.A.) in 1N HCl (hydrochloric acid) (pH 2.5) for 40 min. Similarly, representative histological sections were immunostained for porcine collagen type I. For this experiment, sections were deparaffinized, hydrated, and permeabilized followed by incubation with 1% bovine serum albumin (BSA) at 37 °C for 30 min. The sections were then treated with primary antibody for 2 h. After that the sections were washed and incubated with universal secondary antibodies (Vectastain ABC kit, CA, U.S.A.) followed by development of brown color with diaminobenzidine (DAB) treatment (Vector Laboratories, CA, U.S.A.).

2.2.7.6. Biochemical assay for secreted extracellular matrix (total collagen and sulfated glycosaminoglycan; sGAG)

Total sGAG was estimated using 1,9-dimethylmethylene blue (DMMB)[384]. For this experiment, individual scaffolds (n = 3) with and without cells (as control) were digested with papain digestion cocktail as described above and the DMMB reagent was mixed with individual sample aliquots (1, 7 and 14 days) and absorbance measured at 525 nm. To estimate sGAG secreted into the medium, the spent medium was collected from individual sets of experiments and stored at -20 °C until further sGAG quantification. Total sGAG content from individual constructs was quantified by extrapolation of a standard curve plotted using shark chondroitin sulfate (Sigma, U.S.A).

For total collagen, the lamellar constructs with (n = 3) and without cells (as control) were digested in pepsin cocktail (1mg.mL^{-1} pepsin, pH 3.0) at 4 °C for 48 h. The total collagen content was measured using a previous protocol[385]. In brief, after centrifugation of pepsin digested samples, aliquots were added in 96-well plates and dried at 37 °C for 24 h followed by reaction with Direct red (Sigma, U.S.A.) dye solution for 1 h with mild shaking. The dye solution (pH 3.5) was prepared by dissolving Direct red in picric acid–saturated solution (1.3% w/v; Sigma) to reach a final concentration of 1 mg.mL^{-1}. The dried samples were washed 4-5 times with 0.01 N HCL (hydrochloric acid) followed by resolving dye–sample complex using 0.1N NaOH and absorbance at 550 nm. Total collagen content from individual constructs was extrapolated from a standard curve generated using bovine collagen (Sigma, U.S.A.). To avoid disparities from scaffold sizes, GAG and collagen content were normalized against total scaffold weight. As the control, the same experiments were performed with native porcine AF tissue.

2.2.7.7. Real time PCR analysis

Total RNA from individual cell seeded lamellar constructs was extracted using TRIzol (Sigma. U.S.A.) RNeasy mini-spin columns (Qiagen, U.S.A.) following manufacturer's protocol. In brief, individual cell seeded scaffolds were chopped in the presence of TRI reagent and centrifuged at 12,000 rpm for 10 min, maintaining 4 °C. The supernatant was mixed with 200 µL of chloroform and left for 10 min followed by centrifugation at 12,000 rpm in 4 °C for 15 min. The upper aqueous layer was carefully transferred to the RNeasy mini-spin column. Repeated washing of RNA was carried out as mentioned in the manufacturer's instruction. Nanodrop (Eppendorf, Germany) was used to quantify the RNA and thereafter, high-capacity cDNA reverse transcription kit (Applied

Biosystems, Invitrogen, U.S.A.) was applied to prepare cDNA. SYBR Green dye (Invitrogen, U.S.A.) was used to perform real time PCR for ECM specific genes (col *Ia* 1, sox9 and aggrecan) expressed in both porcine AF cells and hMSCs. The total procedure was conducted according to the manufacturer's protocol in a PCR thermal cycler (Stratagene, CA, U.S.A.). The set conditions were 2 min at 50 °C and 10 min at 95 °C as holding stage, then 40 cycles at 95 °C for 15 s and 60 °C for 45 s for the cycling stage. Data analysis was performed using Mx3500 software (Stratagene, CA, U.S.A.) where fluorescence intensity was normalized with an internal reference dye and baseline correction. Differences in gene expression were evaluated through comparative Ct method ($2^{-\Delta\Delta Ct}$) and normalized to the expression of an endogenous housekeeping gene glyceraldehyde-3-phosphate-dehydrogenase (GAPDH). Primer sequences for porcine and human GAPDH, Col *Iα* 1, sox9 and aggrecan genes are summarized in **Table 2.1.** Probes were purchased from Assay on Demand (Applied Biosystem).

Table 2.1 Sequence of primers for real time PCR analysis

Gene		Sequence	NCBI Accession no.
GAPDH	Human	F 5′-GACCTGACCTGCCGTCTA-3′ R 5′-GTTGCTGTAGCCAAATTCGTT-3′	NM_001289746.1
	Porcine	F 5′-TCGGAGTGAACGGATTTGG-3′ R 5′-CCAGAGTTAAAAGCAGCCCT-3′	NM_001206359.1
col *Iα*1	Human	F 5′-TGACGAGACCAAGAACTGCC-3′ R 5′-GCACCATCATTTCCACGAGC-3′	NM_000088.3
	Porcine	F 5′-AGAAGAAGACATCCCACCAGTCA-3′ R 5′-AGATCACGTCATCGCACAACA-3′	XM_013981006.1
sox9	Human	F 5′-AGGAAGTCGGTGAAGAACGG-3′ R 5′-AAGTCGATAGGGGGCTGTCT-3′	NM_000346.3
	Porcine	F 5′-TTCCGCGACGTGGACAT-3′ R 5′-GGCGGCAGGTACTGGTCAAACTC-3′	NM_213843.1

aggrecan	Human	F 5′-CCACCACCTACAAACGCAGA-3′ R 5′-GATTTGGAGGGGTGAGTGGG-3′	NM_013227.3
	Porcine	F 5′-CCCAACCAGCCTGACAACTT-3′ R 5′-CCTTCTCGTGCCAGATCATCA-3′	NM_001164652.1

2.2.8. *In vivo* response to lamellar constructs

Eight male balb/c mice (Charles River breeding labs) of 5-7 weeks weighing 30-35 g were used to evaluate the *in vivo* responses to lamellar constructs. Two mice were housed per cage in an environmentally controlled room (22 ± 2 °C, 55 ± 5% humidity) under 12 h light/dark cycles. Food and water were supplied with time. All the experiments were conducted in accordance with the animal ethical guidelines approved by the Tufts University Institutional Animal Care and Use Committee.

The mice were grouped in two time points; 1 and 4 weeks and were anesthetized using an oxygen/isofluorane gas mixture. Each mouse received an implant of a lamellar scaffold in the subcutaneous pocket. Before implantation, the lamellar scaffolds were sterilized by autoclaving and incubated in sterile PBS. The subcutaneous pocket was created by a longitudinal incision of ~ 1 cm in the dorsum of the animals. The sterile lamellar construct was then positioned within the pocket followed by suturing the wound. All experiments were performed using sterile instruments and aseptic techniques. Mice were observed for any signs of infection by monitoring activity level, food intake and healing process. No death was recorded during the experiment. To investigate inflammatory responses, the lamellar constructs including the surrounding tissue area was retrieved after 1 and 4 weeks of post transplantation. The samples were then fixed in formalin and paraffinized followed by sectioning for hematoxylin and eosin (H&E, Sigma-Aldrich, U.S.A.) staining.

For immunofluorescence, the processed sections were blocked with 1% (w/v) bovine serum albumin (BSA, Sigma, U.S.A.) for 30 min at room temperature (RT, 25 °C) followed by incubation with primary antibody against CD 68 (diluted 1:200, Abcam, U.K.) for 1 h at RT. After carefully washing in PBS, the sections were incubated with fluorescein isothiocyanate-tagged secondary

anti-mouse antibody (diluted 1:200, Sigma, U.S.A.) for 1 h at RT. The experiment was performed in dark to prevent photobleaching. The images were captured using fluorescence microscope (EVOS FLc, life technologies, U.S.A.).

2.2.9. Statistical analysis

All quantitative experiments were performed at least in triplicate, and results were expressed as mean ± standard deviation for n = 3 unless specified. Statistical analysis of data was performed by one-way analysis of variance (ANOVA). Differences between groups of $*p \leq 0.05$ are considered statistically significant and $**p \leq 0.01$ as highly significant.

2.3. Results

2.3.1. Scaffold features

To replicate the gross anatomic form of the IVD, a two-step approach was adapted; first the fabrication of lamellar scaffolds and then the preparation of a disc-like angle-ply construct with the lamellar sheets. Lamellar scaffolds were fabricated by unidirectional freezing of 5% (w/v) aqueous SF solution (**Figure A2.1 B**). In our previous study, we reported the detailed procedures for the preparation of lamellar scaffolds and their use in cellular response studies with chondrocytes and bone-marrow-derived hMSCs[380]. In the present study, we implemented that strategy to prepare disc-like angle-ply constructs. To mimic the multi-lamellar hierarchy of AF anatomy, the pre-designed SF sheets with the lamellar alignment with an angle of ~ 30° to its vertical axis, were wrapped concentrically around a mold of ~ 1 cm in diameter, but in opposing directions (+ 30° and -30°) of successive layers to form an angle-ply arrangement of the lamellae (**Figure 2.1, A-B**). The cross aligned structure was confirmed by scanning electron microscopy (SEM) and histological sectioning of the construct (**Figure 2.1C, II-III**).

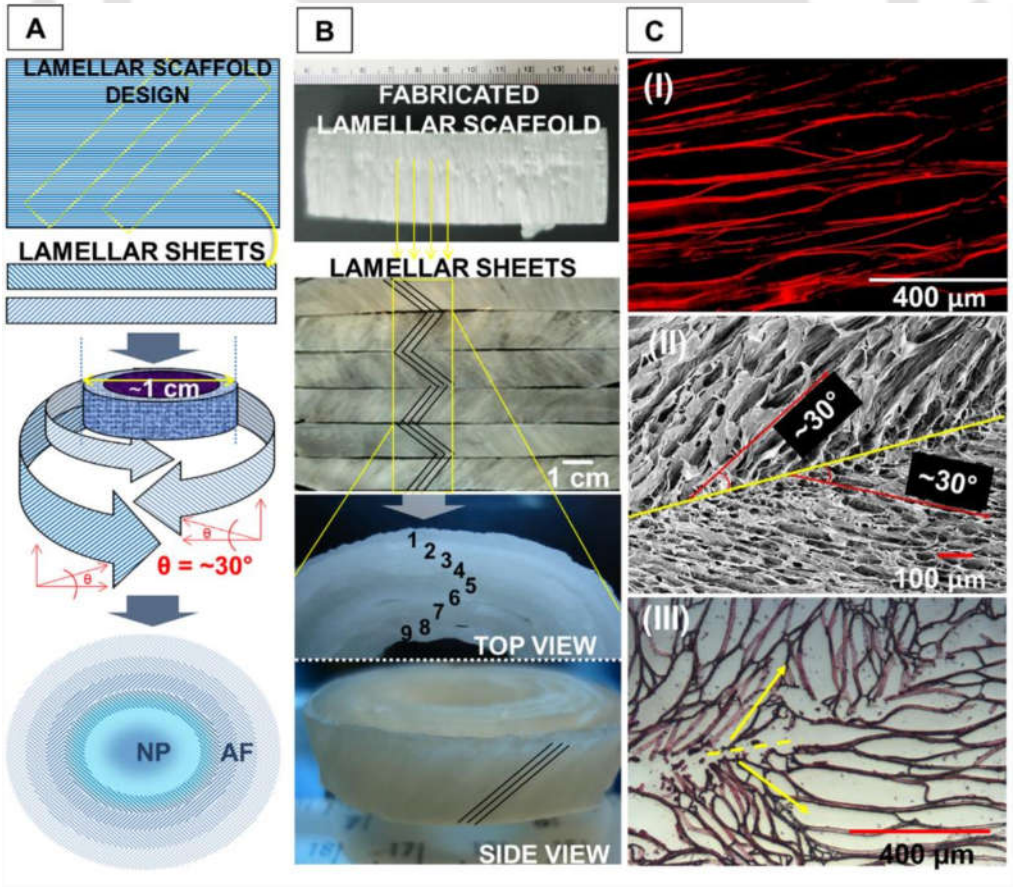

Figure 2.1. *Designing of scaffold; (A) Schematic representation of multilayered disc-like angle-ply construct preparation, (B) Images showing step-wise fabrication of the disc, and (C) Images showing basic features of lamellar construct: (I) fluorescent image of lamellar alignment, (II and III) images show the cross aligned pattern reveled by SEM and histological section, respectively.*

With the help of SEM and fluorescence image analysis, the distance between two adjacent lamellae (*i.e.,* inter-lamellar distance) and the lamellar channel length were determined and found in the range of 62 to116 µm and 167 to 393 µm, respectively (**Figure 2.1C, I and Figure 2.2A**). The transverse section of scaffolds showed the circular opening of lamellar channels having pore sizes ranging from 44 to78 µm (**Figure 2.2A**). Cell seeded scaffolds showed lamellar alignment of cells inside the lamellar pores (**Figure 2.2B**). The degree of crystallinity and secondary structure (*i.e.,* β-sheet) of the lamellar constructs were confirmed by wide angle X-ray diffraction (WAXD) and fourier-transform infrared spectroscopy (FTIR) analysis. In WAXD analysis, two X-ray diffraction peaks were observed at $2\theta = 21°$ (major peak) and 24° (minor peak) with a shoulder peak at 41° (**Figure 2.2C**), confirming the crystalline state of the protein in the scaffolding. FTIR data showed the β- sheet conformational transitions of silk with the signature peaks at 1641, 1519 and 1231 cm^{-1} for amide I, II, III respectively (**Figure 2.2D**).

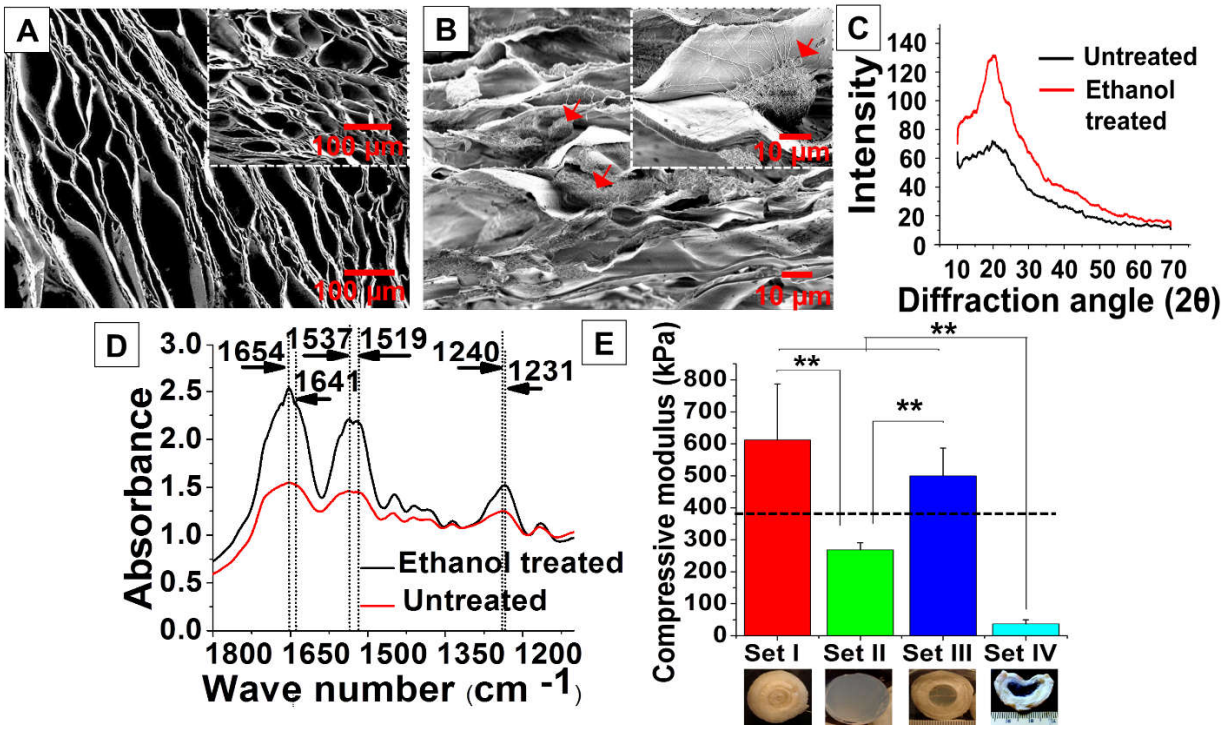

Figure 2.2. *Physical characterizations of lamellar construct; (A) SEM images showing the lamellar alignment of pores and its cross sections with circular pores (inset), (B) the cells seeded scaffolds where cells are aligned in a lamellar way (red arrows) and its magnified image (inset), (C and D) WAXD and FTIR analysis of the construct, respectively, and (E) Mechanical properties of fabricated disc; three different sets of acellular constructs were investigated for the compressive modulus study. Set IV was the porcine native AF. The dashed line indicates native human AF benchmark[386]. Data represents mean ± SD (n = 3), where **p≤0.01 and ***p≤0.001. Scale bar = 100 μm for (A) and 10 μm for (B).*

2.3.2. Mechanical properties of constructs

Assessment of mechanical properties is a critical aspect for load bearing tissue engineered constructs. For the compressive study, three sets of acellular constructs and one set of native tissue were considered; set I consisted of only multilayered angle-ply AF construct, set II was 2% (w/v) agarose gel as the replica of NP gel, set III was the combination of both as a prototype of whole IVD and set IV was native porcine AF tissue (**Figure 2.2E**). The maximum compressive modulus (612.14 ± 175.48 kPa) was measured for set I - a compact multilayered angle-ply AF construct devoid of NP zone in middle, while set III representing the whole IVD showed the value of 499.18 ± 86.45 kPa. The compressive modulus (268.52 ± 21.6 kPa) was significantly less for 2% (w/v) agarose ($p \leq 0.01$), a replica of NP region, compared to others. The least compressive modulus (37.45 ± 12.79 kPa) was calculated for native porcine AF. The value was in line of previous report[387]. All tests were performed under hydrated conditions (in PBS, pH 7.4 and 37 °C) to mimic the physiological microenvironment.

2.3.3. Cell survival, proliferation and alignment study

Cytocompatibility and cellular viability are vital for tissue engineering applications. Isolated porcine primary AF cells and hMSCs were cultured within the lamellar constructs for *in vitro* assessments of cellular viability, proliferation and arrangement. Both types of cell-seeded lamellar constructs were maintained in culture medium for 2 weeks. Based on florescence image analysis, the attachment and alignment of cells within lamellar scaffolds were studied. Cell viability was evaluated by live/dead assay kit (**Figure 2.3B, I-III)** and the cellular arrangement was studied by Hoechst 33342 staining for nuclei (**Figure 2.3B, II-IV**). Cells were evenly distributed, confluent

and aligned in a lamellar morphology for both cases (porcine AF cells and hMSCs) after 2 weeks of culture.

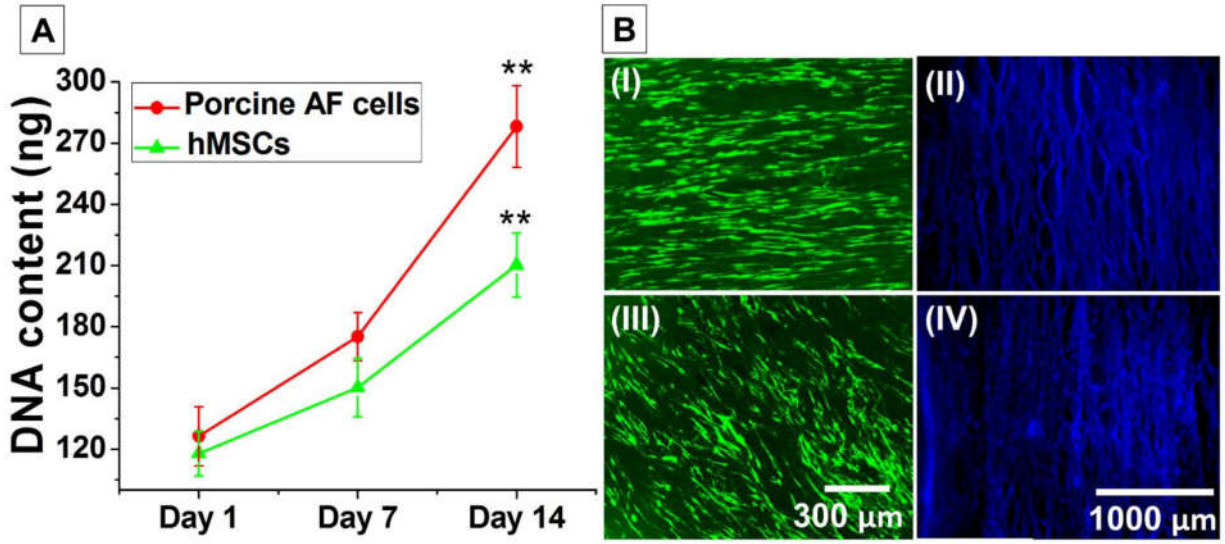

Figure 2.3. *Biological assessment; (A) Cell proliferation (porcine AF cells and hMSCs) within lamellar construct over two weeks, (B) confocal imaging of cells: (I and II) represent live cell staining (using calcein AM, green color) and nucleus staining (using Hoechst 33342, contrast blue dots) for porcine AF cells, and (III and IV) showing the same for hMSCs. Data represent mean ± SD (n = 3), where **p≤0.01.*

For cell proliferation, total DNA content was evaluated on days 1, 7 and 14 (**Figure 2.3A**). Equal number of both cells (porcine AF cells and hMSCs) were seeded to the separate lamellar constructs and continued for 14 days. On the basis of Pico-green DNA assay, an increased proliferation rate was observed for porcine AF cells compared to hMSCs at each time point. Porcine AF cells proliferated with the increase of ~ 1.4- and ~ 2.2-fold at days 7 and 14, respectively compared to initial cell number at day 1 ($p \leq 0.01$). Similarly, ~ 1.26- and ~ 1.7-fold increases in cell proliferation at days 7 and 14, respectively, were observed for the hMSCs ($p \leq 0.01$). The maximum DNA content for porcine AF cells reached 282.35 ± 14.68 ng compared to hMSCs (211.54 ± 13.55 ng) at day 14.

2.3.4. Histology and immunohistochemistry analysis

From histology and immunohistochemistry analysis, the cellular distribution and extracellular matrix (ECM) deposition within the tissue engineered constructs was assessed. For histological

analysis, cell seeded lamellar constructs were sectioned and stained with Hematoxylin and eosin (H&E). The results showed that cells (in both cases; porcine AF cells and differentiated hMSCs) were homogeneously distributed throughout the constructs and arranged in a lamellar fashion, attaching to the lamellar walls after 2 weeks of culture (**Figure 2.4, A and D**).

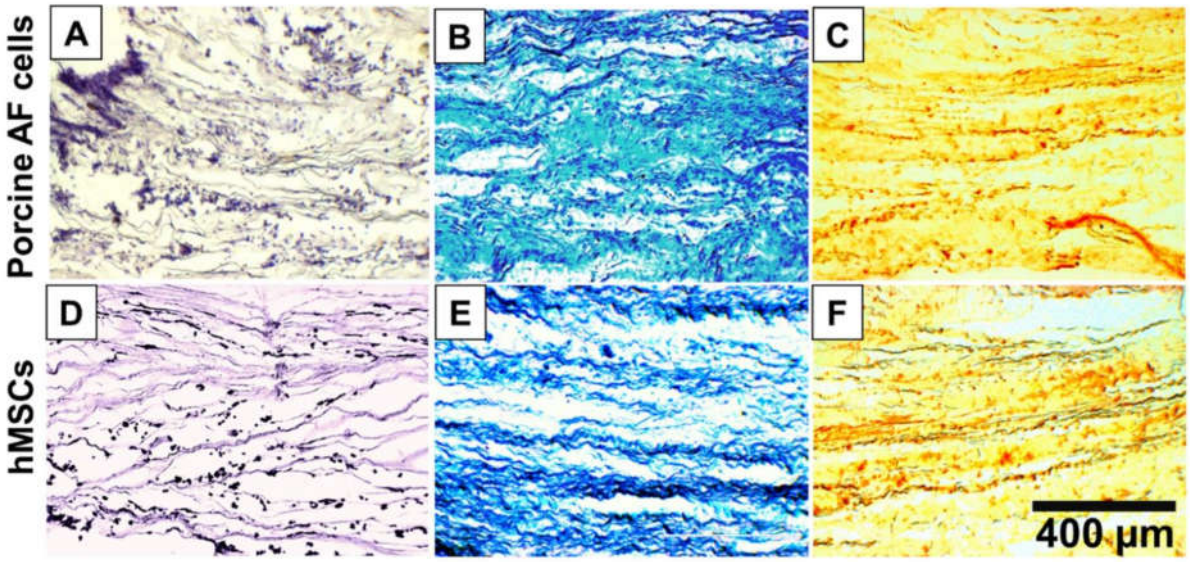

Figure 2.4. *Histology and immunohistochemistry of lamellar constructs over two weeks of culture in chondrogenic medium; (A-C) images represent porcine AF cells-seeded constructs and (D-F) images represent hMSCs seeded constructs. (A) and (D) for H&E staining showing cellular distribution within the lamellar constructs, (B) and (E) showing alcian blue staining for sGAG deposition and, (C) and (F) showing immunostaining of deposited collagen I.*

For the identification of AF specific ECM deposition, alcian blue staining (for sulfated glycosaminoglycans, sGAG) and immunohistochemistry (for type I collagen) were performed. Alcian blue staining revealed even deposition of sGAG within the entire lamellar constructs for both cases, but with more intense blue color for porcine AF cell-seeded constructs (**Figure 2.4, B and E**). Similarly, from immunohistochemistry, type I collagen was secreted abundantly by both cells *i.e.,* porcine AF cells and differentiated hMSCs, after 2 weeks of culture in chondrogenic medium (**Figure 2.4, C and F**).

2.3.5. Quantitative analysis of ECM deposition

Alcian blue staining for sGAG and immunohistochemistry for type I collagen was further supported by the quantitative biochemical analysis suggesting ECM secretion by both porcine AF cells and differentiated hMSCs in chondrogenic medium. Both collagen and sGAG deposition increased with the time for both cell types, but higher values were obtained for the porcine AF cells.

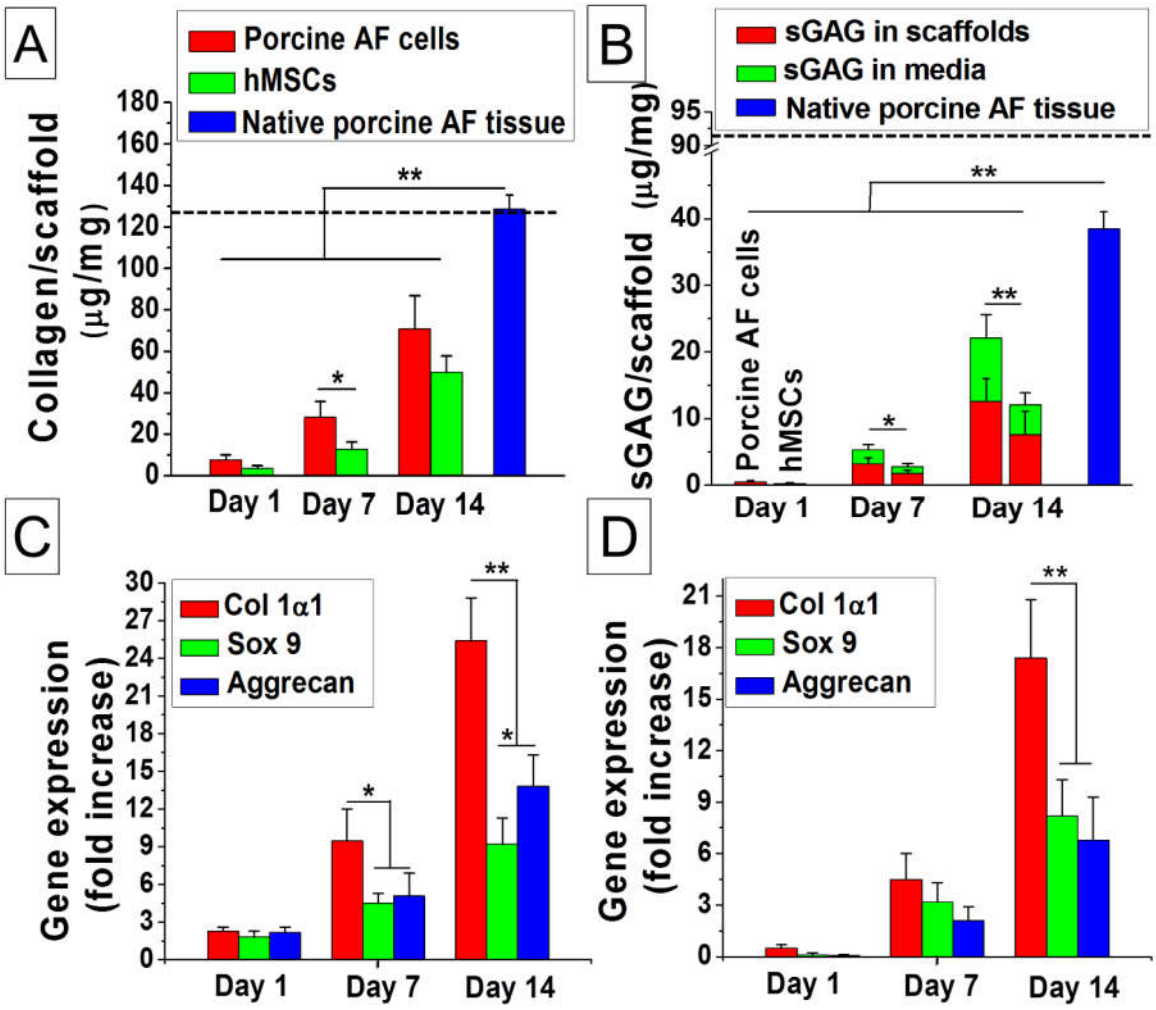

Figure 2.5. *Biochemical analysis of cell seeded lamellar constructs; (A) collagen content analysis and (B) sGAG deposition within lamellar scaffolds. The dashed line indicates native human AF benchmark[388]. Gene expression study for (C) AF cells and (D) hMSCs in a time points of day 1, 7, and, 14 cultured in chondrogenic media. Data represents mean ± SD (n = 3), where *p≤0.05 and **p≤0.01*

For type I collagen from porcine AF cells, the values increased to ~ 3.6-fold and ~ 9.8-fold at days 7 and 14, respectively, when compared to the initial seeding ($p \leq 0.01$). Similarly, for differentiated hMSCs, ~ 3.4- and ~ 13.4-fold increase in collagen secretion was monitored at days 7 and 14, respectively, compared to day 1 ($p \leq 0.01$). The amount of total collagen content per unit scaffold mass was higher in case of porcine AF compared to the differentiated hMSCs at each time frame (days 3, 7 and 14). The maximum collagen content per mg of scaffold for porcine AF cells was 70.88 ± 15.96 µg (~ 54% of native porcine AF tissue) at day 14, whereas for differentiated hMSCs, the value reached 49.9± 7.8 µg (**Figure 2.5A**). Similarly, sGAG (scaffold and media) content for porcine AF cells showed higher valued than hMSCs at each time point (day 3, 7 and 14). For porcine AF cells, the value increased to ~ 10.2 and ~ 44.1-fold at days 7 and 14, respectively, compared to day 1 ($p \leq 0.01$). In the case of differentiated hMSCs, a similar value was obtained (~ 10-fold for day 7 and ~ 44.8-fold for day 14). But when compared to the total amount of sGAG content per unit mass of scaffolds, the value (12.1 ± 5.3 µg) was much lower than that of porcine AF cells (22.08 ± 7.02 µg, ~ 55% of native porcine AF tissue) (**Figure 2.5B**).

2.3.6. Real time PCR analysis

In further support of qualitative (histology and immunohistochemistry) and quantitative (biochemical analysis) assessments, transcript levels of AF-related marker genes (col *Iα* 1, aggrecan and sox9) were assessed by real time PCR. For porcine AF cells, the mRNA expression level of the three genes increased with the time (days 7 and 14), and the maximum expression was observed for col *Iα* 1 when maintained in chondrogenic medium (**Figure 2.5C**). The expression level of col *Iα* 1 increased ~ 4.3- and ~ 11-fold at days 7 and 14, respectively, when compared to day 1 ($p \leq 0.01$). Relatively lower levels of expression were observed for both sox9 and aggrecan genes. The level of expression for both sox9 and aggrecan genes increased ~ 5.1- and ~ 6.7-fold, respectively, at day 14 compared to day 1.

The hMSCs showed increased levels of AF tissue-specific genes expression (col *Iα* 1, sox9, aggrecan) with time (**Figure 2.5D**). Similar to the porcine AF cells, maximum expression was observed for col *Iα* 1 in differentiated hMSCs at any time point taken. It was observed that col *Iα* 1 gene was expressed with an increase of ~ 9- and ~ 34.8-fold at days 7 and 14, respectively, when compared to day 1 ($p \leq 0.01$).

2.3.7. *In vivo* assessments

In vivo implantation of the tissue engineered constructs helps to evaluate the biomaterial integration and immune responses. To understand the immune response, the lamellar constructs were implanted subcutaneously in mice and retrieved at weeks 1 and 4, followed by H&E and immunofluorescence staining for macrophages **(Figure 2.6**).

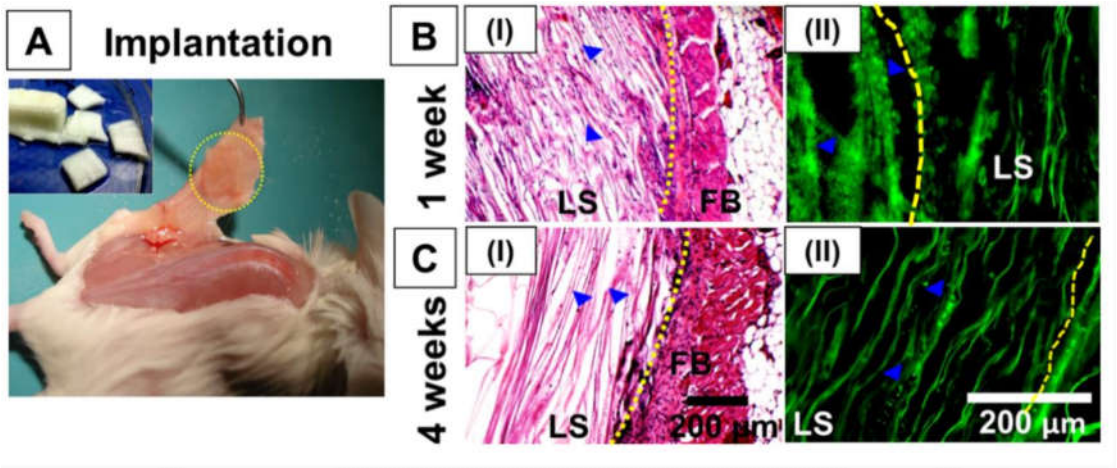

Figure 2.6. *In vivo assessment of lamellar constructs; (A) Retrieval of lamellar construct from subcutaneous pocket of mice after 4 weeks of implantation. H&E staining of implants after 1 week (B I) and 4 weeks (C I). Immunofluorescence of CD68 for macrophages infiltration in the implanted scaffolds after 1 week (B II) and 4 weeks (C II). LS = Lamellar scaffold, FB = Fibroblast cells layers, yellow dot line represents scaffold-tissue interface. Filled blue triangle used to show the macrophages (green dots) infiltration inside implants.*

After one week, the retrieved constructs showed immune cells (mainly macrophages, confirmed by immunofluorescence for CD68) surrounding the constructs **(Figure 2.6B, II)**. Few macrophages infiltrated the scaffolds. Aggregation of macrophages followed by fibroblast layers was also observed surrounding the implanted scaffolds and no sign of tissue necrosis was found. Following 4 weeks, the retrieved scaffolds showed negligible infiltration of immune cells inside the implanted scaffolds (**Figure 2.6C, II**). Scaffold-native tissue integration was also clearly visualized, while there was, negligible degradation of the lamellar constructs was observed over the 4 weeks.

2.4. Discussion

Repairing fibrocartilaginous tissues like AF of IVDs is a challenging task. The intricacy arises due to the avascular nature, low cellularity that limits regeneration, and the hierarchical structural organization of the tissue that dictates its biomechanical properties. To address such challenges, a cross aligned scaffold construct that mimics the native tissue architecture and mechanical properties was developed. In our previous study, we assessed the influence of silk-based lamellar scaffolds prepared using directional freezing in adipogenic and chondrogenic differentiation of hMSCs[380]. Directional freezing is based on a simple thermodynamic principle where the velocity and morphology of the ice-front propagation is controlled through the sample in a unique direction. Moreover, use of aqueous based polymeric system (where water is the main sol fraction), avoid the introduction of any toxic products into the scaffolds. In the present study, we implemented this technique to prepare lamellar scaffolds with multi-lamellar angle-ply constructs to mimic native disc morphology. The process was conducted in two steps: first, the preparation of lamellar scaffolds followed by excising rectangular sheets possessing ~ 30° angle of lamellar directions to the vertical axis, and second, encircling them in alternate directions so that the assembled structure had a disc like angle-ply construct (**Figure 2.1, A-B**). To prepare lamellar scaffolds, a polydimethylsiloxane (PDMS) mold was used, consisting of two hollow chambers divided by a copper metal plate. PDMS, a transparent silicon polymer offers good thermal and chemical stability, electrical resistivity, as well as mechanical flexibility, but also has poor thermal conductivity (0.15 W m^{-1} k^{-1})[389]. In contrast, the copper plate used as the divider has high thermal conductivity (401 Wm^{-1} k^{-1}). The ratio of thermal conductivity of these two components is 2673.3, thus directional ice crystal formation rate was rapid and originating from the metal plate surface rather than the PDMS walls (**Figure A2.1 A**).

The regenerated *B. mori* SF typically exhibits random coil and *β*-turn (without α-helix), termed silk I. Upon exposure to 70% (v/v) ethanol, silk I is converted to silk II due to induction of *β*-sheet crystals. After lyophilization, the lamellar constructs were subjected to ethanol treatment to induce crystallinity to ensure stability in aqueous medium. Post treatment with ethanol, conformational transition occurred to silk II as previously reported (**Figure 2.2D**)[380, 390]. Similarly, the WAXD data supported crystallinity of the lamellar constructs (**Figure 2.2C**).

SEM and fluorescent based image analysis revealed the cross-aligned and lamellar characteristics of the constructs (**Figure 2.1C, I-II** and **Figure 2.2A**). Porosity and pore size of lamellar scaffolds are mainly governed by lamellar distance and channel length. Gas perfusion and nutrient exchange during culture depend on pore size and porosity of the scaffolds and influence cell survival, proliferation and differentiation. We previously reported the effect of SF concentration on inter-lamellar distance and its porosity[380]. Electron microscopy of the transverse sections of the scaffolds revealed circular openings (44 to78 μm) of the lamellar channels. These openings were the result of longitudinal ice crystal propagation at the time of rapid freezing in liquid N_2. SEM also supported the homogeneous and aligned cell distribution throughout the lamellar channels.

The complex architecture and composition make AF an anisotropic, non-linear and viscoelastic tissue to bear mechanical loads. Although AF is subjected to various types of mechanical forces, including uniaxial and biaxial tension, shear and torsion, compressive properties were assessed for the designed multilayered angle-ply constructs. Under compressive loading, the discs become narrow in height and bulges in the outward direction, experiencing both axial and radial compressive stress. Despite of the high ductility and stiffness of silk fibers, mechanical properties of the final products depend on post processing and fabrication procedures. For the compressive study, three sets of scaffolds were used (**Figure 2.2E**). Set I scaffolds showed the highest compressive modulus (> 600 kPa) due to highly compact nature of the scaffold. However, this type of compact structure cannot be applied for disc replacement therapy as it does not contain a NP region. Set II consisted of only agarose gel (2% w/v) and showed the least compressive modulus (~ 270 kPa). Better mechanical properties were registered for set III that represented the whole disc, consisting of concentric rings of lamellar constructs surrounding the gelatinous NP substitute (agarose gel). This observation indicated the interaction between these two regions prompt mechanical response in compression that emulated native disc. This type of constructs provided a compressive modulus of 499.18 ± 86.45 kPa, a value in the range of compressive modulus of native human AF tissues (380 ± 160 kPa)[386]. Thus, at this juncture, the assessment of tensile strength, shear stress and other mechanics would be required to support final designs related to the biomechanical functionality of the disc.

Cytocompatibility of a biomaterial for tissue engineering is also key factor for its clinical success. Cellularity often depends on “form follows function” rule where scaffolds act as functional

templates to guide cellular remodeling[391]. Porous scaffolds used for AF tissue engineering supported non-uniform and reduced cell proliferation in comparison to lamellar scaffolds[239]. Silk fibroin is widely accepted for various regenerative applications due to its versatile features including high strength, biocompatibility, and biodegradability with low immunogenicity[392]. In this study, cellular compatibility of the constructs was assessed with two types of cells; porcine primary AF cells and bone marrow derived hMSCs. AF cells proliferated and formed ECM related to the vertebral disc. The potential use of AF cells in IVD tissue engineering has also been reported previously[239]. Complications in the isolation and lack of sufficient donors limit the use of primary cells for implantable scaffolds. This has stimulated interest towards alternative cell sources, such as stem cells. MSCs are multipotent stromal cells that have the ability to differentiate into various lineages including osteoblast, myocytes, adipocytes and chondrocytes. MSCs have shown significant contributions in intervertebral disc tissue engineering[393]. MSCs may be exploited either in their undifferentiated stage, allowing them to differentiate *in vivo* influenced by local stimulus, or in their differentiated stage *in vitro* prior to implantation. In the former case, unwanted differentiation may occur in the injury site, whereas differentiated MSCs are phenotypically stable and resistant to trans-differentiation when maintained in chondrogenic media[394]. In this context, bone marrow derived hMSCs were isolated and allowed to differentiate into the chondrogenic lineage post seeding into the angle-ply constructs in the present study. Cell seeded constructs were maintained for 2 weeks and cellularity was checked by DNA content (**Figure 2.3A**). Both cell sources proliferated in the construct with time, and enhanced proliferation was observed for the primary AF cells. After 2 weeks of culture in chondrogenic medium, AF cells showed ~ 2.2-fold proliferation from initial seeding ($p \leq 0.01$), whereas hMSCs showed ~ 1.7-fold increase ($p \leq 0.01$). In contrast, the AF cells, which were already differentiated, maintained their normal phenotype and proliferation rate throughout the experiment. However, cell viability using calcein AM and nuclear staining by Hoechst 33342 revealed cellularity and alignment in the constructs (**Figure 2.3B**).

A successful bioengineered construct supports cell attachment and proliferation, and also supports the deposition of ECM for functional tissue. Biochemical analysis of constructs after 2 weeks of culture in chondrogenic medium revealed significant accumulation of both collagen and sGAG, the two main ECM components of annulus fibrosus. The AF consists of ~ 67% of collagen in its dry weight, where type I collagen accounts for ~ 80% of total collagen content. Although,

proteoglycan content is as predominant in the outer AF regions, the amount gradually increases towards the central region. However, the proportion of collagen to proteoglycan changes throughout life and is also associated with disc degeneration. The developed angle-ply constructs supported both the primary AF cells and hMSCs and the AF cells secreted increased amounts of ECM components compared to the hMSCs (**Figure 2.5, A-B**). The reason for this increased level of ECM secretion by the primary AF cell might be due to their highly differentiated state. This was further confirmed by gene expression, where increased levels of col *Iα* 1 and aggrecan were observed (**Figure 2.5, C-D**). Similarly, differentiation of hMSCs in lamellar constructs was evident from the upregulated expression of col *Iα* 1, aggrecan and sox9 mRNA (early chondrogenic differentiation marker) in chondrogenic medium for 2 weeks. The chondrogenic medium consists of ITS+ (insulin, transferrin, and selenious acid), TGF-*β* and dexamethasone, the fundamental components for chondrogenic differentiation of MSCs. Previously it was reported that TGF-*β* induced new ECM synthesis in both old and degenerated discs[395]. Enhanced cell proliferation has been reported under the combined effects of ITS+ and TGF-*β*, whereas dexamethasone exerted augmentative and suppressive influence on protein and proteoglycans, respectively[396]. We observed that decreased levels of aggrecan mRNA expression were associated with increased col *Iα* 1 gene expression by hMSCs when compared to AF cells.

Cellular infiltration and their arrangement or specific ECM molecule deposition can be visualized by histological analysis of the tissue engineered constructs. H&E staining of the constructs revealed cellular infiltration and alignment in the lamellae (**Figure 2.4, A and D**). sGAG is one of the predominant ECM molecules secreted by chondrocytes or differentiated stem cells (to chondrocytic lineage). Fibrochondrocytic in nature, AF cells secreted sGAGs in the lamellar constructs and an intense and homogeneous blue color appeared throughout the scaffold section. Similarly, deposition of sGAG by differentiated hMSCs in the lamellar construct was confirmed by Alcian blue staining (**Figure 2.4, B and E**). Collagen type I, another hallmark ECM component of AF tissue was detected by immunohistochemistry. Both the primary AF cells and hMSCs secreted as corroborated by immunostaining for collagen type I (**Figure 2.4, C and F**). However, the stained color was comparatively more intense (visual observation) for the constructs seeded with primary AF cells, supporting the biochemical and gene expression studies.

While the *in vitro* experiments assist in providing an insight to the cellular interactions with the materials, *in vivo* studies are relevant to understand overall tissue responses. Any biomaterial which is non-autologous elicits some extent of foreign body response (FBR) following implantation. FBR also depends on biomaterial characteristics, including size, geometry, topology and site of implantation[397]. In this study, the constructs were subcutaneously implanted in mice and retrieved after 1 and 4 weeks followed by H&E staining (**Figure 2.6**). Although recruitment of macrophages was observed surrounding the implants after 1 week, there was a significant reduction after 4 weeks. Following 4 weeks, the implanted constructs retained structural integrity including the lamellar alignment. This observation is in line with previous studies that demonstrate lower inflammatory responses towards silk materials[380].

In the current study, recapitulation of AF internal architecture has been achieved using tissue engineering approach, but it is necessary to address other formidable challenges for the clinical implementation of the existing technologies. To move the current technology towards in vivo application, it is critically important to ensure the integration of implanted engineered disc to the surrounding tissue as well as the AF-NP confinement. The NP can be transplanted as biphasic structure (set III) or can be injected in a minimally invasive way after AF transplantation. This is important as the high mechanical properties of disc are attributed from its sealed confinement. Hence, the long term aim would be the fabrication of an entire construct comprising of AF, gelatinous NP and superior-inferior end plate. The engineered disc can be implanted as cellular or acelluar state. For cellular disc, it needs to be cultured in dynamic bioreactor system for better tissue maturation. The current study focuses on the use of two different cell types; primary cells and hMSCs. The fabricated construct was validated by both cell types in terms of biocompatibility and tissue formation. So, the biological construct, upon implantation, mimicking the internal architecture will provide the mechanical properties, whereas the cellular part will prevent the further degeneration by supporting the regenerative process. Despite of these obstacles in clinical implementation, the current work may provide a better understanding about bio-artificial disc preparation mimicking its hierarchical organization.

2.5. Significant findings

The significant findings from this chapter are as follows:

- Structural recapitulation of AF tissue is a major challenge. In this chapter, we have developed a fabrication procedure for a silk-based bioartificial disc adopting a directional freezing technique.
- The fabricated biodiscs mimicked the internal intricacy of the native disc as evaluated by electron microscopy. The mechanical properties of these biodiscs were similar to those of the native ones.
- The fabricated biodiscs supported primary annulus fibrosus or human mesenchymal stem cell proliferation, differentiation, and deposition of AF tissue specific ECM.
- A small unit of the construct was implanted subcutaneously to show its negligible immune response.

Hence, we proposed that the silk-based bioartificial discs could be a promising strategy for future direction toward disc replacement therapy.

Chapter 3

Fabrication and Characterization of a Seamless Full Thickness Disc-like Angle-ply Construct with Tailored Mechanical Properties Modulating Extracellular Matrix Secretion by Annulus Fibrosus (AF) cells

This chapter introduces a novel design to fabricate a seamless lamellar sheet possessing aligned pores at an angle of approximately ± 30° to its length, but in alternate directions akin to native AF. This improved approach may restrict the possible delamination of multiple sheets of constructs as designed in earlier chapter. Herein, the fabrication of a seamless full thickness disc-like angle-ply construct using silk fibroin (SF) protein as well as the effect of matrix alignment and mechanical properties on extracellular matrix (ECM) secretion by AF cells are investigated in details.

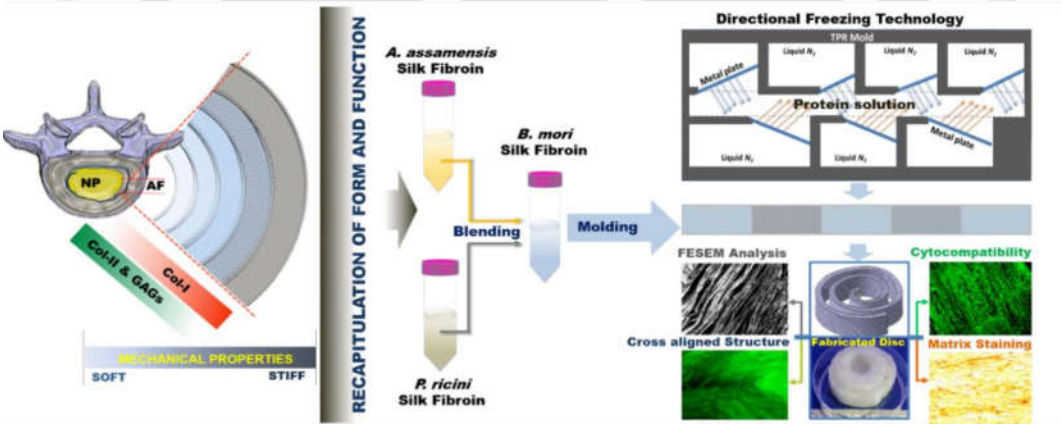

The work embodied in this chapter in published in a peer-reviewed journal as follows:

Bhunia BK, Mandal BB. Modulation of extracellular matrix by annulus fibrosus cells on tailored silk based angle-ply intervertebral disc construct. **Materials & Design**. 2018;158:74-87.

ABSTRACT

Reconstruction of native tissue's anatomical and biophysical milieu dictates the success of tissue engineered graft's cellular fate. Herein, we report a facile fabrication procedure to replicate the anatomical and biomechanical features of annulus fibrosus (AF) tissue. A seamless, full thickness disc-like angle-ply construct was fabricated using silk fibroin (SF) protein. To mimic the gradual transition of mechanical gradient from inner to outer region of native AF tissue, SF proteins from two different sources (namely *Bombyx mori*, BM SF as mulberry, and *Antheraea assamensis*, AA SF and *Philosamia ricini*, PR SF as non-mulberry) were blended that provided differential mechanical and cell binding properties. Fabricated constructs were physicochemically and biologically characterized. The seeded porcine AF cells were found to proliferate and align along the lamellar pores as visualized through staining. Gene expression study concluded higher expression of collagen-I with enhancement of mechanical properties, whereas an opposite trend was observed for both collagen-II and aggrecan. Overall, the angle-ply construct with tailored mechanical properties supported cellular alignment and proliferation, and modulated the extracellular matrix (ECM) deposition forming a functional AF tissue like construct, thus providing a robust foundation as an alternative tissue engineered strategy in intervertebral disc (IVD) regeneration for future replacement therapy.

3.1. Introduction

Intervertebral disc (IVD) consists of two morphologically and developmentally distinct regions; the multi-lamellar hierarchically arranged collagen fiber reinforced annulus fibrosus (AF) that confines the gelatinous nucleus pulposus (NP), together maintaining the intra-discal pressure upon loading[13]. AF is intrinsically complex tissue that consists of 20-25 concentric rings surrounding the NP. These rings are mainly composed of collagen nano-fibers oriented at the angle varies from ± 30°-60° (from the central NP outward to the edge of the disc) against its vertebral axis, but in successive layers forming a criss-cross structure[15]. The biochemical and biomechanical properties remarkably alter along the radial direction. The proportion and the organization of extracellular matrix (ECM) components vary with the spatial position in AF. For instance, concentration of type I collagen increases towards the outer AF layers, whereas type II collagen increases towards center. Similarly, aggrecan content is higher in the inner layers of AF (11-20%) than the outer layers (5-8%)[25]. Such variations in ECM composition are maintained by the specific cell types that reside in that spatial region and their associated cellular activities in the corresponding zone possessing different biophysical environments. This regional distinction in cellular function and ECM composition play a vital role on biomechanics of the discs. For example, the outer layers of AF resist the tensile stresses, whereas compressive loads are compensated by inner AF[398].

Static tension of different magnitudes (*i.e.,* the physico-mechanical cues of the substrate) acts as an important modulator for AF cell behavior[399]. Previous studies showed the influence of substrate stiffness on morphology and ECM gene expression of AF cells which are known to be "mechanosensitive cells"[400]. It was reported that collagen type II and aggrecan gene expression increase as the substrate stiffness decreases. Conversely, collagen type I expression increases on stiffer surfaces[399]. It is very important to choose the appropriate substrate mechanical properties for AF tissue engineering. So, an ideal tissue engineered construct should be designed in such way that it not only mimics the anatomical criss-cross structure, but also recapitulates the biomechanical, biochemical and cellular activities of the native AF. To materialize this, our recent efforts are towards approximating the anatomical features to their biomechanical properties for a successful physiologically functional engineered disc.

Recently, numerous approaches have been attempted to recapitulate the form and function of AF tissue using various biomaterials, but with limited success. This is a greater need for a strategy to mimic such complex tissue organization at the biochemical and biomechanical levels.

Silk as biomaterial is used in tissue engineering for decades due to its widespread versatility *e.g.,* biocompatibility, least immunogenicity, tunable biodegradability and mechanical properties[191]. Silk fibroin (SF) from *Bombyx mori* Linnaeus, 1758 (BM SF) is being used in tissue engineering for years[401-405]. Similarly, non-mulberry SF from *Antheraea mylitta* Drury, 1773 (AM SF) has also been extensively studied[195]. Here we studied two other non-mulberry SF sources; *Antheraea assamensis* Helfer, 1837 (AA SF) and *Philosamia ricini* Donovan, 1798 (PR SF). It is reported that non-mulberry silk fibroin possess inherent RGD-motif (arginine-glycine-aspartic acid, an integrin binding receptor) facilitating enhanced cell attachment and proliferation[406, 407]. Moreover, the unique molecular architecture (uninterrupted poly-alanine stretches) of AA SF or PR SF provides superior mechanical properties[407]. Recently, few reports suggest the potential use of non-mulberry silk (*e.g.,* AM SF, AA SF and PR SF) in various field of tissue engineering including skin, cartilage, bone, blood vessel and heart[196-198, 408-410].

In the present study, we developed and applied a novel design to fabricate a seamless lamellar sheet possessing aligned pores at an angle of approximately ± 30° to its length, but in alternate directions akin to native AF. Further through this study we thoroughly investigated the effects of structural organization and mechanical properties on extracellular matrix secretion and specific gene expression using our developed silk AF model that provided differential mechanical properties. The effect of substrate morphology and its bulk mechanical properties on growth, expression, and biochemical characteristics of AF cells were also investigated.

3.2. Materials and methods

3.2.1. Isolation of mulberry silk fibroin

Mulberry silk fibroin (SF) solution was isolated from *B. mori* cocoons following the procedure described by Kim *et al*[381]. In brief, *B. mo*ri (BM) cocoons were cut into small pieces followed by boiling for 15 min in 0.02 M Na_2CO_3 (Sigma, U.S.A.) solution to remove the glue like sericin from outer layers and then rinsed thoroughly with deionized water. The extracted silk fibers were then allowed to dry for overnight at room temperature (25 °C). The sericin free dry silk fibers were dissolved in 9.3 M LiBr (Sigma, U.S.A.) solution and kept it for 4 h at 60 °C. The liquefied silk was then extensively dialyzed against deionized water using 12 kDa molecular weight cut-off (MWCO) cellulose dialysis membrane (Sigma, U.S.A.) to remove the residual LiBr. Post dialysis, 1 mL of regenerated aqueous BM SF solution was transferred to a teflon-boat of known weight (W1) and was left to dry at 37 °C for 12-16 h. Once silk was dry, weight was measured as W2. The final concentration of the SF solution was 9-12% (w/v), determined gravimetrically using an electronic balance (Sartorius, BSA224S-CW).

3.2.2. Isolation of non-mulberry silk fibroin

Aqueous solution of non-mulberry SF was isolated from matured 5^{th} instar larvae of both muga (*A. assamensis,* AA) and eri silkworm (*P. ricini,* PR), respectively following the previously described protocol[411]. Briefly, 5^{th} instar larvae were collected from local sericulture farms of Assam, India. The silk glands of the larvae were taken out and washed with deionized water to remove the traces of water soluble sericin. The glandular tubes were squeezed with fine forceps to extrude out the protein. The extracted protein was then dissolved in 1% (w/v) sodium dodecyl sulfate (SDS, Sigma, U.S.A.). Excess surfactant was removed by extensive dialysis using dialysis membranes (Sigma, U.S.A., MWCO 12 kDa) against deionized water. The final SF (AA SF and PR SF) concentration was determined gravimetrically by weighing the remaining solid mass after drying as described in the *section 3.2.1*.

3.2.3. Preparation of BM/AA and BM/PR SF blends

Different blending ratios (**Table 3.1**) were prepared by thoroughly mixing of mulberry SF (*B. mori*. BM) to non-mulberry (*A. assamensis,* AA and *P. ricini,* PR) SF at room temperature (25

°C) before casting in specially designed mold for lamellar scaffold preparation. The final concentration of each blend was adjusted to 6% (w/v). *B. mori* SF alone was used as control.

Table 3.1 Preparation of different ratios of SF blends

Sample code	Mulberry SF % (w/v)	Non-mulberry SF % (w/v)	Final protein concentration % (w/v)
BM6.0	6.0	0	6
BM5.5/AA0.5	5.5	0.5 AA	6
BM4.0/AA2.0	4.0	2.0 AA	6
BM5.5/PR0.5	5.5	0.5 PR	6
BM4.0/PR2.0	4.0	2.0 PR	6

BM=*B. mori*, AA= *A. assamensis*, PR= *P. ricini*

3.2.4. Preparation of constructs with lamellar pores in alternate directions

The biological lamellar constructs were fabricated following a modified version of the design reported by Mandal *et al.*[380] (**Figure 3.1**). In brief, a thermoplastic rubber (TPR, Ananta Polyrubb Pvt. Ltd. India) mold was used to design the model. The mold possessed a central channel (3 mm width and 5 mm in depth) connected with a series of chambers in alternate sides. The aluminum metal plates were placed in such way that the directions of freezing maintain ~ 30° angle to the central axis, but in alternate directions. This directional freezing mimics the native architecture of AF.

To prepare lamellar scaffolds, 6% (w/v) SF solution was poured into the chambers of predesigned TPR mold. The liquid N_2 was poured on other side, directly cooling the metal plates that lead to directional freezing of SF solution. The liquid N_2 was repeatedly replenished until the whole protein was frozen. The frozen SF block was then lyophilized and threated in ethanol to induce β-sheets. The thin skin from both top and bottom side were removed by a surgical blade to open up the lamellar pores. The prepared lamellar scaffolds were stored in 70% (v/v) ethanol for further use.

3.2.5. Fabrication of disc-like angle-ply constructs

The lyophilized rectangular SF sheets possessed the lamellar pores at an angle of ~ 30° to its length, but aligned in alternate directions maintaining a certain distance (**Figure 3.1 D**). The lamellar SF sheet was then wrapped concentrically around a mold of ~ 1 cm in such way that the lamellar pores make the criss-cross alignment to its each alternate layer. The central hollow core was filled with SF hydrogel to make it a complete disc like structure.

3.2.6. Field emission scanning electron microscopy (FESEM) study

The cross-sections of lamellar scaffolds prior/post cell seeding were studied using FESEM (Zeiss, Sigma) at an operating voltage of 2-3 kV. The cell seeded scaffolds were fixed with 2.5% (v/v) glutaraldehyde for 3 h at room temperature followed by gradual dehydration with ethanol. The samples were then sputtered with gold for 3 min before analysis. Inter lamellar distance/pore size of all types of constructs were calculated by measuring random 25 pores with ImageJ 1.4 (Wayne Rasband) software.

3.2.7. Fourier transform infrared spectroscopy (FTIR)

To confirm the *β*-sheets transition in lamellar SF scaffolds after ethanol treatment, FTIR analysis was performed using an infrared spectrophotometer (Nicolet iS 10, Thermo Scientific, U.S.A.). To avoid moisture effects, samples were desiccated overnight followed by preparation of KBr disc in a ratio of 9:1 (KBr to sample). The spectra were recorded in the range of 4000 – 400 cm^{-1} with a resolution of 4 cm^{-1} averaged over 32 scans. Amide I region (1600 – 1700 cm^{-1}) was investigated to identify the secondary structure in the ethanol treated lamellar constructs following the second order derivative method using OriginPro 8.5 software and the deconvoluted spectra were curve-fitted by lorentzian peaks. The absorbance bands in the range of 1610-1635 cm^{-1}, 1635-1645 cm^{-1}, 1647-1664 cm^{-1} and 1660-1695 cm^{-1} were ascribed as β-sheets, random coil, *α*-helix and loops/*β*-turn, respectively[412].

3.2.8. Porosity measurement of lamellar scaffolds

Porosity of SF lamellar constructs was measured by hexane displacement method following a previously described method[390]. Hexane was used as it is non-solvent for silk and permeates

easily through interconnected pores without causing any swelling or shrinkage. After fabrication, lamellar constructs were immerged in a graduated cylinder containing known volume of hexane (V_1). A series of quick evacuation and depressurization cycles were performed so that the entrapped air was completely evacuated and impregnated with hexane, the volume was recorded as (V_2). After removal of hexane impregnated scaffolds, the residual hexane volume was recoded as (V_3). The porosity of scaffolds was expressed as[390]

$$Porosity = \frac{V1-V3}{V2-V3} \times 100\%$$

3.2.9. Swelling property of lamellar scaffolds

Swelling properties of SF lamellar constructs were performed by immersing them into distilled water. Briefly, dry weight of lyophilized constructs was measured as (W_d) using an electronic balance (Sartorius, BSA224S-CW) followed by immersing them into distilled water for 24 h at room temperature (25 °C). At definite time intervals, the swollen scaffolds soaked by water were carefully taken out and recorded the wet weight as (W_s). The excess water surrounding the constructs was wicked using tissue paper. The swelling ratio was expressed as[390]

$$Swelling\ ratio = \frac{Ws-Wd}{Wd}$$

3.2.10. *In vitro* enzymatic degradation

Protease XIV from *Streptomyces griseus* (Sigma, U.S.A.) with an activity of 3.5 $U.mg^{-1}$ was used for *in vitro* enzymatic degradation studies following an earlier reported protocol[390]. The SF lamellar constructs were immerged into 3 ml of phosphate buffer saline (PBS, pH 7.4) containing 2 $U.mg^{-1}$ of enzyme. The enzyme solution was replaced with freshly prepared solution at every three days. The whole experiment was performed at 37 °C to achieve the optimum result. For comparison, scaffolds were also immerged into PBS (pH 7.4) without enzyme under similar experimental condition. Constructs were taken out on every 7^{th} day, rinsed with distilled water, lyophilized, and weight was recorded to calculate the loss over the period of 28 days.

3.2.11. Mechanical properties

Mechanical characterizations *e.g.,* compressive properties of the fabricated SF lamellar constructs were determined using Instron 5944 (Norwood, MA, U.S.A.) equipped with a 100 N load cell. The SF lamellar constructs of different combinations were cut into square shape (~ 30 mm^2) and hydrated them for ~ 30 min at 37 °C before testing. All tests were accomplished with an unconfined configuration and a displacement control mode at a rate of 5 $mm.min^{-1}$. The compressive modulus was measured in both directions of the lamellar constructs *i.e.,* parallel (PD) and perpendicular to lamellae direction (PPD). After the compression tests, the stress and strain curves were plotted based on the measured cross-sectional area and sample height. The compressive modulus was calculated by drawing a line parallel to small section of strain (5%); the point where the line intersected to the stress-strain curve gave compressive modulus of the SF lamellar construct. All tests were performed following the ASTM standard D1621-04a.

3.2.12. Cell culture on lamellar SF scaffolds

3.2.12.1. Isolation and culture of annulus fibrosus (AF) cells

Porcine annulus fibrosus (AF) cells were isolated from lumber discs following a previously described protocol[413]. In brief, the lumber discs were collected from local slaughter house within 1 h of post processing. The surrounding muscle and tendons were discarded and the spine was transversely dissected to separate the discs from lower and upper vertebrae. The sterile condition was maintained to perform the whole dissection process. The isolated AF tissues were then finely minced and digested in 0.2% (w/v) protease (Sigma, U.S.A.) for 1 h at 37 °C followed by digestion in 0.03% (w/v) collagenase (Sigma, U.S.A.) for 18 h under mild shaking environment. The central nucleus pulposus (NP) gel was also processed in similar way. The digested specimens were passed through a cell strainer (70 µm pore size, Thermo Fisher Scientific, U.S.A.) to separate cells from the undigested larger particle followed by centrifugation at 235 g for 5 min to collect AF/NP cells. The cell viability was confirmed by trypan blue exclusion test.

The isolated AF and NP cell pellets were resuspended in media (DMEM/F12) and seeded at a density of 2 x 10^5 $cells.cm^{-3}$ followed by incubation at 37°C with 5% CO_2 and 85% humidity. The culture medium (DMEM/F12) supplemented with 10% (w/v) FBS, 50 $\mu g.mL^{-1}$ ascorbic acid, 100 $U.mL^{-1}$ penicillin G, and 100 $\mu g.mL^{-1}$ streptomycin (Life Technologies, U.S.A.) was changed on every 3rd day and cells were passaged up to P4 and stored at -196 °C for future applications.

3.2.12.2. Seeding and culture of AF cells within lamellar constructs

To develop *in vitro* AF-tissue like construct, porcine AF cells were seeded within the lamellar constructs of different blends and left them undisturbed for ~ 3 h in CO_2 incubator to allow cells adhered to the substrate. For biochemical analysis, the cell seeded constructs were transferred into chondrogenic medium supplemented with 10% (w/v) FBS, insulin (6.25 $\mu g.mL^{-1}$), transforming growth factor-β1 (TGF-β1; 10 $ng.mL^{-1}$), transferrin (6.25 $\mu g.mL^{-1}$), selenious acid (6.25 $mg.mL^{-1}$), ascorbic acid (50 $mg.mL^{-1}$), proline (40 $mg.mL^{-1}$), dexamethasone (100 nM), bovine serum albumin (BSA; 1.25 $mg.mL^{-1}$), and sodium pyruvate (100 $mg.mL^{-1}$), and maintained them for 21 days. For, cell proliferation study, constructs were maintained in complete DMEM/F12 (without chondrogenic components) medium for 21 days. The NP cells were seeded onto AA SF hydrogel and maintained it for 7 days. The medium was changed on every 3rd day for each case. All the media components were procured from Sigma, U.S.A.

3.2.12.3. Cell proliferation assay

Cell proliferation was monitored using Alamar blue dye reduction assay (Invitrogen, Life Technology, U.S.A.) at specified intervals of 1, 7, 14 and 21 days. Equal number of AF cells (3 x 10^4 cells per lamellar construct) was seeded within the each preconditioned construct (complete DMEM/F12 for 24 h) and incubated them at 37 °C with 5% CO_2. The medium was changed on every 3rd day. The cell proliferation was plotted in terms of percentage of alamar blue dye reduction. The absorbance was measured at 570 and 600 nm using a multiplate reader (Tecan Infinite 200 PRO series, Switzerland) and proliferation index was calculated according to the manufacturer's protocol.

3.2.12.4. Assessment of viability and alignment of seeded cells on lamellar constructs

Viability and alignment of seeded AF cells in the lamellar constructs were visualized using live/dead assay kit (Invitrogen, Life Technologies, U.S.A.). For these studies, 0.5 x 10^6 cells per construct were seeded and maintained for three weeks with periodic media changes. Cell seeded constructs were then stained with live/dead assay kit following the manufacture's protocol. The live/dead solution is a mixture of two main components: 2 mM ethidium homodimer-1 and 4 mM calcein AM. The viable cells take up calcein AM and flourish as green, whereas ethidium

homodimer-1 easily passes through the fragmented cell membrane of dead cells, bind to DNA and flourish as red. For nucleus staining, cell seeded constructs were washed in PBS (pH 7.4) and fixed in 2.5% (v/v) glutaraldehyde for 3 h at room temperature (25 °C). The samples were then incubated with 1% (w/v) bovine serum albumin (BSA) (Sigma, U.S.A.) for 30 min followed by permeabilization with 0.1% (v/v) Triton X 100 (Sigma, U.S.A.) for 5 min. The constructs were then thoroughly washed and incubated with Hoechst 33342 (Invitrogen, Life Technology, U.S.A.) for 30 min at dark. Imaging was performed under fluorescent microscopy (EVOS FL cell Imaging System, Life Technologies, U.S.A.).

3.2.12.5. Histology of lamellar constructs

For histological analysis, the cell seeded lamellar constructs were fixed in 10% (v/v) NBF (neutral buffered formalin) for overnight. The fixed constructs were then dehydrated in graded ethanol (50-100%, v/v), paraffinized and sectioned of ~ 5 µm in thickness. For the evaluation of cellular distribution throughout the constructs, sections were deparaffinized, rehydrated and staining with hematoxylin and eosin (H&E).

sGAG deposition was visualized after staining with 1% (w/v) Alcian blue (Sigma, U.S.A.) in 1 N HCl (pH 2.5) for 40 min as reported previously[413]. The immunohistochemistry was studied to evaluate the collagen (type I) secreted into the lamellar constructs. For this purpose, sections were deparaffinized, rehydrated and incubated with 1% (w/v) bovine serum albumin for 30 min at 37 °C followed by treatment with primary antibody for 2 h. The sections were then washed thoroughly to remove the non-specific binding of primary monoclonal antibody (Abcam, UK) and incubated with universal secondary antibody (Vectastain ABC kit, U.S.A.) followed by brown color development with diaminobenzidine (DAB) (Vector Laboratories, U.S.A.).

3.2.12.6. Biochemical assays for DNA, sGAG and collagen content

After culturing in chondrogenic media, the cell seeded constructs were subjected to biochemical analysis that included total DNA, sGAG and collagen content at predefined time point of day 1, 7, 14 and 21. For the estimation of total DNA and sulfated glycosaminoglycans (sGAG) content, individual constructs with and without cells (as control) were treated in papain digestion cocktail (5 mM L-cysteine, 125 mg.mL^{-1} papain, 5 mM EDTA and 100 mM Na_2HPO_4 pH 6.2) at 60 °C for 16 h under mild shaking condition. Total DNA content was measured using PicoGreen DNA

assay kit as per manufacturer's protocol (Invitrogen, U.S.A.). In brief, papain digested samples were centrifuged at 10000 rpm for 15 min and supernatant was collected. 25 µL of supernatant from each sample was placed into a 96-well plate. 75 µL of 1 x Tris-EDTA (TE) buffer and 100 µL of Quant-iT PicoGreen reagent (1:200 dilutions) were then mixed into the wells. For standard curve, different concentrations of the lambda phage DNA (0-10 $\mu g.mL^{-1}$) were used. The data were recorded using a fluorometer (Tecan Infinite 200 PRO series, Switzerland) with an excitation and emission wavelength of 480 nm and 528 nm, respectively. 1, 9-dimethylmethylene blue (DMMB) assay method was followed to measure total sulfated GAG (sGAG) content in individual construct [413]. 20 µL of aliquot from each papain digested sample was mixed with 200 µL of DMMB reagent and absorbance was measured immediately at 525 nm. Different concentrations (0-100 $\mu g.mL^{-1}$) of shark chondroitin sulfate (Sigma, U.S.A.) were used to generate the standard curve.
To estimate total collagen content, cell seeded constructs were digested in pepsin cocktail ($1mg.mL^{-1}$ pepsin, pH 3.0) at 4 °C for 48 h under mild shaking condition following previously reported protocol[413]. In brief, pepsin digested samples were centrifuged at 10000 rpm for 15 min and supernatant was collected. 100 µL of aliquots from each supernatant was placed in 96-well plates and allowed to dry at 37 °C for 24 h. 100 µL of direct red (Sigma, U.S.A.) dye solution was then added to each well and incubate it for 1 h with mild shaking. The dye solution ($1mg.mL^{-1}$, pH 3.5) was prepared in picric acid–saturated solution (1.3% (w/v); Sigma, U.S.A.) The wells were then washed 4-5 times with 0.01 N HCl and dye–sample complex was resolved after washing in 0.1 N NaOH. The absorbance was recorded at 550 nm. For standard curve, bovine collagen (Sigma, U.S.A.) was used. To avoid variations from construct size and cell numbers, sGAG and collagen contents were normalized against total scaffold weight and DNA content.

3.2.12.7. Real time PCR analysis

To understand different matrix gene expression level, total RNA from different constructs was isolated by lysing the cells using TRIzol reagent (Sigma. U.S.A.) on day 1, 7, 14, and 21 following the manufacturer's protocol. The lysate was centrifuged (12000 rpm, 4 °C, 10 min) and the obtained supernatant was transferred to new tubes followed by addition of 200 µL of chloroform and incubated for 15 min. The mixture was then centrifuged (12000 rpm, 4 °C, 15 min) and the upper aqueous layer was carefully transferred to fresh tubes. Purified total RNA was obtained after repeating washing in ethanol followed by suspending in RNase free water (Sigma, U.S.A.). The

cDNA was prepared using a high-capacity cDNA reverse transcription kit (Applied Biosystems, Invitrogen, U.S.A.) in a thermal cycler machine (TaKaRa, Japan). Power SYBR Green master mix (Applied Biosystems Invitrogen, U.S.A.) was used to quantify the level of AF specific gene expression (col *Iα* 1, col II, sox9 and aggrecan) in a real time PCR machine (Applied Biosystem 7500, ThermoFisher Scientific, U.S.A.) with the sequences as in **Table 3.2.** The comparative Ct method ($2^{-\Delta\Delta Ct}$) was applied to evaluate the differences in gene expression and the values were normalized to an endogenous housekeeping gene glyceraldehyde-3-phosphate-dehydrogenase (GAPDH).

Table 3.2: Sequence of primers for real time PCR

Gene	Sequence	NCBI Accession no.
GAPDH	F 5′-TCGGAGTGAACGGATTTGG-3′ R 5′-CCAGAGTTAAAAGCAGCCCT-3′	NM_001206359.1
col *Iα*1	F 5′ AGAAGAAGACATCCCACCAGTCA-3′ R 5′-AGATCACGTCATCGCACAACA-3′	XM_013981006.1
col II	F 5′-CAGGTGAAGGTGGGAAACCA-3′ R 5′-ACCCACGAGGCCAGGA-3′	AF201724.1
sox9	F 5′-TTCCGCGACGTGGACAT-3′ R 5′-GGCGGCAGGTACTGGTCAAACTC-3′	NM_213843.1
aggrecan	F 5′-CCCAACCAGCCTGACAACTT-3′ R 5′-CCTTCTCGTGCCAGATCATCA-3′	NM_001164652.1

3.2.12.8. *In vitro* inflammatory response study

In order to assess the immunogenic response, RAW 264.7 cells (mouse macrophages, obtained from National Center for Cell Science, NCCS, Pune) were challenged with the lamellar constructs

(BM4.0/AA2.0 and BM4.0/PR2.0; n = 3) of equal size (4 x 4 x 2 mm) for 24 h. The amount of TNF-α released in response to silk constructs or lipopolysaccharide (LPS, Sigma-Aldrich, U.S.A.) was determined using TNF-*α* ELISA kit (Invitrogen, U.S.A.) following the manufacturer's protocol. In brief, $1x10^5$ cells per well were seeded in a 24-well plate for 24 h and thereafter the constructs were placed on the seeded cells. Post 24 h incubation, the spent media were collected for TNF-*α* assessment. LPS (500 $ng.mL^{-1}$) was served as positive control, while cell seeded wells without any treatment on standard tissue culture plate (TCP) were treated as negative control. To determine TNF-*α*, biotinylated secondary antibody (50 µL) was incubated with spent media (100 µL) for 90 min followed by the addition of streptavidin-HRP solution (100 µL) for 30 min. Thereafter, 100 µL of chromogen solution was added to each well and incubated for 15 min in dark followed by the addition of stop solution. Absorbance was recorded spectrophotometrically at 450 nm using a multiplate reader (Tecan Infinite 200 PRO series, Switzerland).

3.2.13. Statistical analysis

All quantitative experiments are run at least in triplicate, and results are expressed as mean ± standard deviation for n = 3 unless specified. Statistical analysis of data was performed by one-way analysis of variance (ANOVA). Differences between groups of $*p \leq 0.05$ are considered statistically significant and $**p \leq 0.01$ as highly significant.

3.3. Results

3.3.1. Construct features

To recapitulate the gross morphology of native AF, disc-like angle-ply construct was fabricated using silk protein as a scaffolding material. For this purpose, SF solution was poured into the specially designed mold (**Figure 3.1, A and C**) followed by directional freezing of SF solution by liquid nitrogen. The mold was designed in such way that the lyophilized scaffold possessed the lamellar pores with ~ 30° angle against its length, but at a certain distance so that it could form a seamless angle-ply structure of the successive layers when wrapped concentrically surrounding the SF hydrogel mimicking the NP (**Figure 3.1, B and D**). The FESEM and fluorescence images showed the junction point where ice crystals propagated from two opposite angles met together and formed a cross-aligned morphology (**Figure 3.1, E and F**). The successive layers possessing the lamellar pores in opposite direction (~ 30°) within the gross structure of AF were confirmed by FESEM study (**Figure 3.1G**).

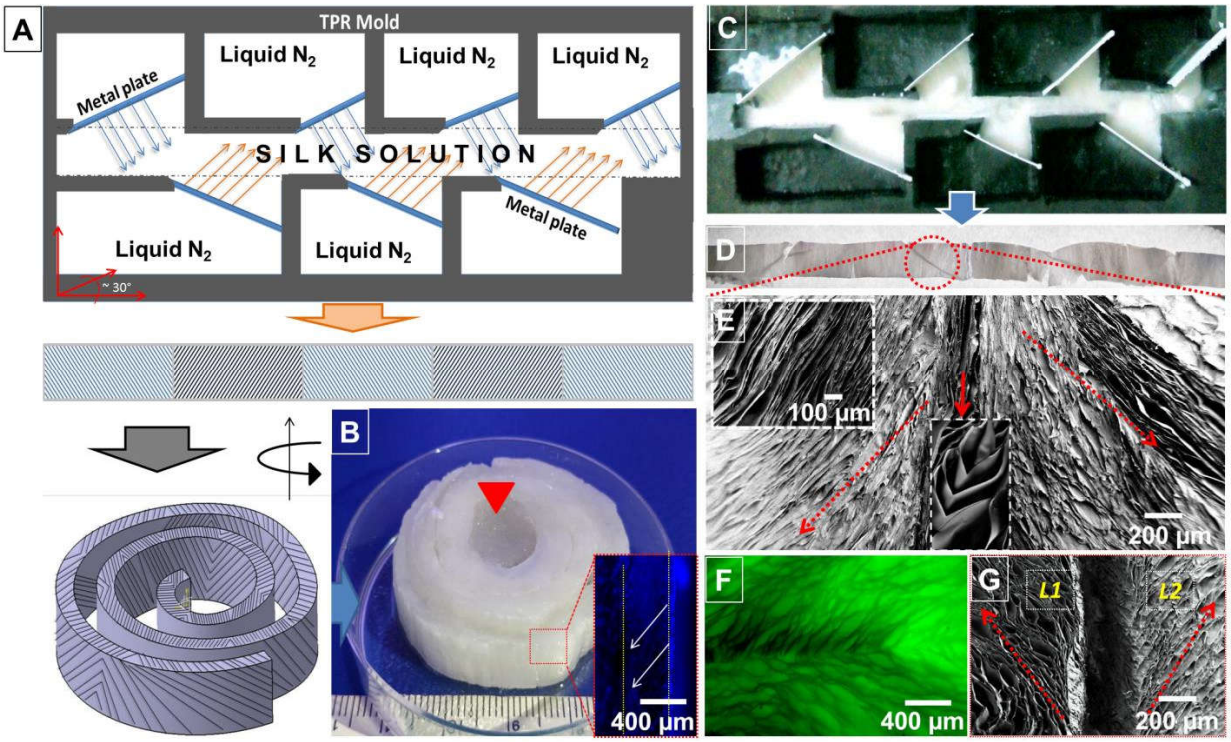

Figure 3.1. *Fabrication of disc-like angle-ply construct; (A) schematic representation of TPR mold and step-wise fabrication procedure of angle-ply lamellar construct, (B) fabricated final construct with NP resembling AA SF gel in center (red triangle), (C) the TPR mold after*

directional freezing of SF, (D) the lyophilized lamellar sheet (E) FESEM of lamellar structure and cross junction point of ice crystal propagated from two opposite diagonal directions, (F) Fluorescence of fabricated scaffold showing its criss-cross alignment, and (G) FESEM of two adjacent layers (L1 and L2) of the final fabricated disc.

To understand the effect of blends on physicochemical and biological properties of fabricated constructs, two different types of SF proteins (mulberry *B. mori* and non-mulberry *A. assamensis* and *P. ricini*) were blended together and the physicochemical or biological evaluation was performed. Individual construct of different blends with or without porcine AF cells was investigated under electron microscopy (**Figure 3.2A and 3.3E**). The inter-lamellar distance and lamellar channel length of different groups was summarized in **Table 3.3** It was seen that as the concentration of non-mulberry SF increased in the blends, the inter-lamellar distance and lamellar channel length decreased. The construct which was made of only *B. mori* SF (BM6.0) showed the maximum inter-lamellar distance and lamellar channel length ranging from 25-40 µm and 80-260 µm, respectively, whereas BM4.0/PR2.0 blends exhibited least values *i.e.,* 3-8 µm of inter-lamellar distance and 30-50 µm of channel length.

Table 3.3 Inter-lamellar distance and lamellar channel length of different constructs composed of different blending ratio of mulberry and non-mulberry SF.

Sample code	Inter-lamellar distance (µm)	Lamellar channel length (µm)
BM6.0	34.25 ± 6.11	191.12 ± 72.29
BM5.5/AA0.5	20.86 ± 3.35	102.15 ± 36.76
BM4.0/AA2.0	8.64 ± 1.21	53.13 ± 11
BM5.5/PR0.5	7.2 ± 1.95	72.66 ± 7.75
BM4.0/PR2.0	5.92 ± 2.71	41.38 ± 6.6

BM=*B. mori*, AA= *A. assamensis*, PR= *P. ricini*

It was also observed that the lamellar walls of each blend showed the spikes like protrusions whose distribution and density increased as the concentration of non-mulberry SF increased in the blends, whereas smooth wall boundaries were noticed in BM6.0 (**Figure 3.2A, II-V**).

These spikes increased the gross surface area of lamellar walls and were supposed to help in cells attachment. The lamellar constructs supported cell proliferation to form an AF-like tissue. FESEM images showed the distribution of cells in all cases after three weeks of culture (**Figure 3.3E**). The entire area of BM4.0/AA2.0 wall was covered by proliferating cells, whereas less distribution of cells was shown in case of BM4.0/PR2.0. Conversely relatively less cellular distribution was observed in BM6.0. After ethanol treatment, β-Sheet conformational transitions with the signature peaks at 1630, 1523 and 1233 cm^{-1} for amide I, II and III was confirmed by FTIR data analysis (**Figure 3.2B**). Further, different secondary conformations were determined by deconvolution of amide I region (1600-1700 cm^{-1}) which is summarized in the **Table A3.1** and **Figure A3.1.** *β*-sheet content (> 22%) was observed to be higher in all blended groups than BM6.0 (~ 15%). It was further noticed that the amount of random coil decreased with increase of non-mulberry SF within blends.

3.3.2. Porosity measurement of lamellar scaffolds

Porosity of all lamellar constructs was determined by hexane displacement method (**Figure 3.2C**). Porosity of scaffolds plays a major role in cellular migration, nutrient and gaseous exchange. It was observed that as the concentration of non-mulberry SF increased in blends, the porosity significantly decreased. The maximum porosity (65.41 ± 5.12%) was noticed in BM6.0, whereas minimum porosity (31.47 ± 3.78%) was observed in BM4.0/PR2.0 ($p \leq 0.01$). There were significant differences in porosity observed between BM5.5/AA0.5 and BM4.0/AA2.0 ($p \leq 0.05$), and also between BM5.5/PR0.5 and BM4.0/PR2.0 ($p \leq 0.01$). However, it was confirmed that the porosity was greatly affected in blends with *P. ricini* SF than the *A. assamensis* compare to BM 6.0.

3.3.3. Swelling property of lamellar constructs

Swelling ability of fabricated constructs is one of the important parameters considered for tissue engineering applications as it indirectly correlates to the water retention capacity. The degree of

swelling of different groups of lamellar constructs was determined after immersion in deionized water over period of 24 h (**Figure 3.2D**).

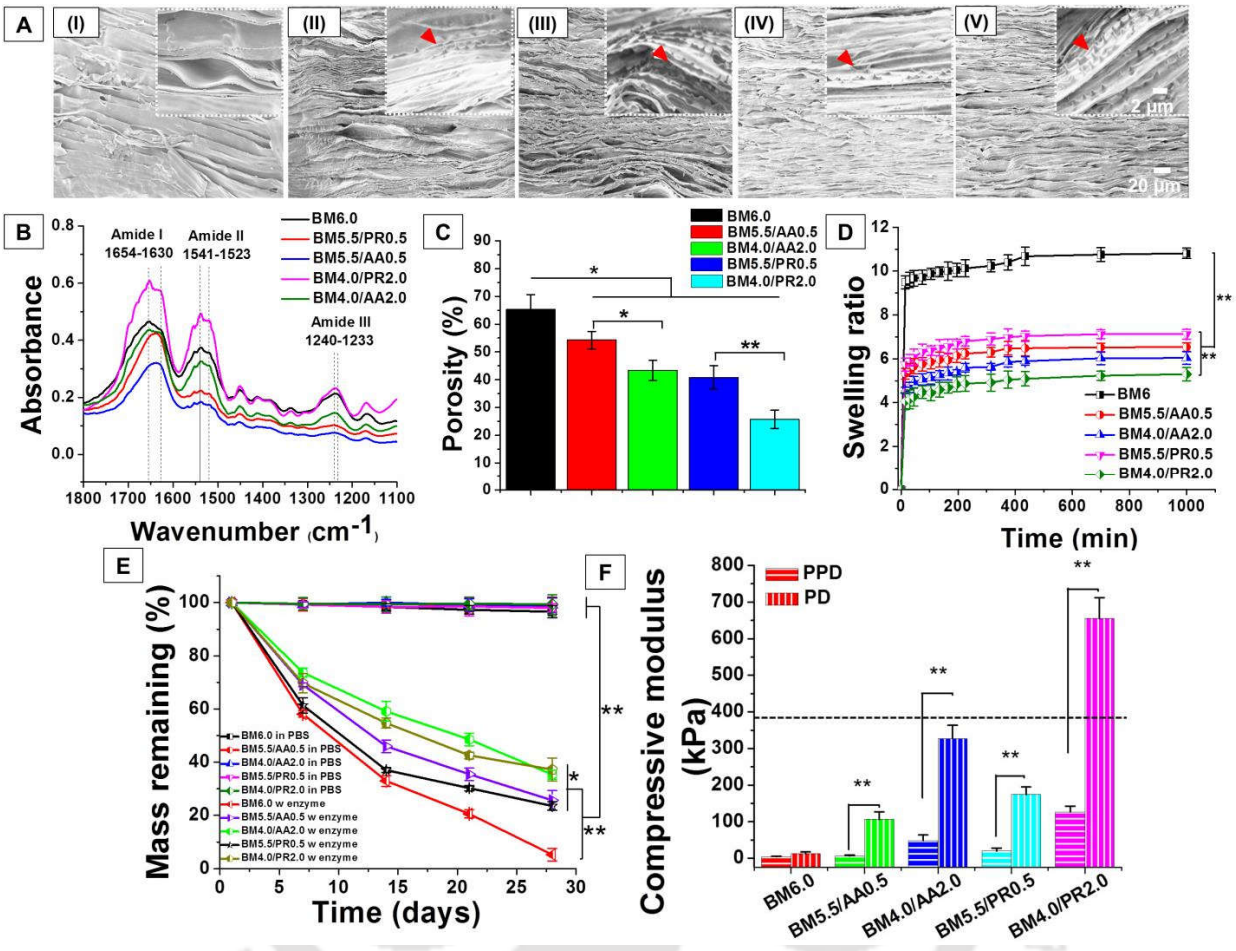

Figure 3.2. *Physicochemical characterization of fabricated lamellar constructs; (A) FESEM analysis of constructs showing lamellar pores and spike-like protrusions (red triangle) on the walls of non-mulberry bends (inset): (I) BM6.0 (II) BM5.5/AA0.5 (III) BM4.0/AA2.0 (IV) BM5.5/PR0.5, and (V) BM4.0/PR2.0. (B) FTIR analysis, (C) porosity analysis, (D) swelling ratio, (E) degradation study, and (F) mechanical properties of lamellar constructs. PD = parallel and PPD = perpendicular to the lamellae direction. The dashed line indicates native human AF benchmark[386]. Data are plotted as a mean ± standard deviation, n = 3, where ** p≤0.01 and * p≤0.05.*

A sharp increase in swelling ratio was observed within 30 min followed by a slow increase up to 225 min for all cases. As the fabricated constructs were in 3D formats, due to its high surface area

and mass content, a further increase in swelling ratio was observed after ~ 415 min. However, the maximum swelling ratio reached within 6 h and attained an equilibrium state for all cases. The swelling ratio was found to decrease with the increase in concentration of non-mulberry SF in the blends. The maximum swelling ratio was achieved by BM6.0 (10.81 ± 0.23) which was significantly higher than all blend groups ($p \leq 0.01$). Among the blends, BM4.0/PR2.0 showed the least swelling capability (5.29 ± 0.29) which was even significantly lower than BM5.5/PR0.5 ($p \leq 0.01$). However, there was no significant difference between BM5.5/AA0.5 and BM4.0/AA2.0.

3.3.4. *In vitro* enzymatic degradation

Percentage weight loss of individual lamellar construct was monitored after immersion in enzyme solution (protease XIV, 2 $U.mg^{-1}$) and in PBS (pH 7.4) as control over period of 28 days (**Figure 3.2E**). The degradation rate was significantly decreased with the increasing of non-mulberry SF in the blends ($p \leq 0.01$). The highest degradation was observed for BM6.0 *i.e.,* ~ 5% mass remained after 28 days study, whereas least degradation (~ 37% mass remaining) occurred in the blends with higher amount of non-mulberry SF (BM4.0/AA2.0 and BM4.0/PR2.0). A moderate degradation (~ 25% mass remaining) was observed for both BM5.5/AA0.5 and BM5.5/PR0.5 which was significantly higher than blends having the maximum amount of non-mulberry SF ($p \leq 0.05$).

3.3.5. Mechanical properties

Assessment of mechanical properties of fabricated constructs is critical for any load bearing tissue engineering application. For this purpose, different acellular lamellar constructs were investigated for compressive strength under universal testing machine. The compressive strength was studied in two ways; parallel (PD) and perpendicular (PPD) to the lamellae direction (**Figure 3.2F**). The compressive modulus was calculated from the stress-strain curve of each specimen. It was observed that the compressive modulus (PD) was increased drastically with the increase of non-mulberry SF within any blend ($p \leq 0.01$). The maximum value (655.05 ± 56.76 kPa) was obtained from BM4.0/PR2.0, whereas BM6.0 showed the least compressive modulus (12.53 ± 5.21 kPa). BM4.0/AA2.0 showed the compressive modulus of 326.34 ± 36.73 kPa which was in the range of native human AF (~ 380 kPa)[386]. However, there were no substantial differences in values of PPD for all groups except BM4.0/PR2.0, whereas significant differences ($p \leq 0.01$) from PD to PPD values were noticed for each group except BM6.0.

3.3.6. *In vitro* biological studies

3.3.6.1. Cells survival and proliferation on lamellar scaffolds

Assessment of cytocompatibility and cellular viability of a construct designed for tissue engineering applications is of much importance. For this purpose, isolated primary porcine AF cells were cultured in lamellar constructs and maintained in DMEM/F12 medium for 21 days.

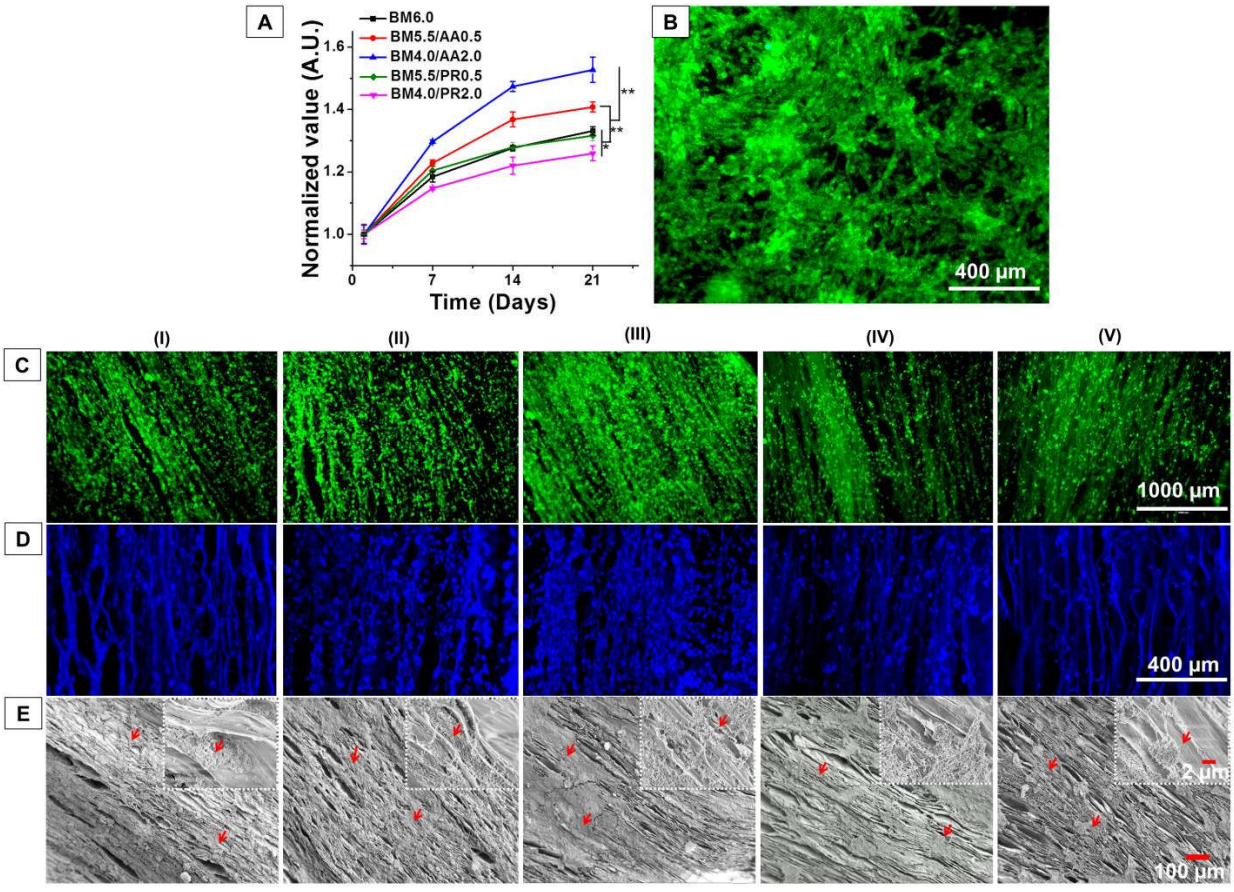

Figure 3.3. *Biological assessment of lamellar constructs over three weeks; (A) cell proliferation showing normalized values of cell growth within individual laminar silk scaffolds, (B) live NP cells on AA SF gel as a replica of central NP, (C-D) calcein-AM and Hoechst 33342 staining showing live cells and nuclear arrangement, respectively within the individual scaffold, and (E) FESEM analysis of cell-seeded lamellar constructs, red arrows indicate cells in lamellar pore (inset showing magnified images). Column representing (I) BM6.0, (II) BM5.5/AA0.5, (III) BM4.0/AA2.0, (IV) BM5.5/PR0.5, and (V) BM4.0/PR2.0. Data are plotted as a mean ± standard deviation, n = 3, where ** p≤0.01 and * p≤0.05.*

For cell proliferation study in lamellar constructs, Alamar blue reduction assay was carried out on day 1, 7, 14 and 21 (**Figure 3.3A**). Percent reduction of Alamar blue directly relates the cellular metabolism or to the cell number at a given point of time. For this purpose, equal number of AF cells was seeded in individual construct and maintained for 21 days. It was noticed that seeded AF cells proliferated with time in all cases, but the maximum proliferation was observed in BM4.0/AA2.0 ($p \leq 0.01$) followed by BM5.5/AA0.5. In BM4.0/AA2.0, the cells proliferated with the increase of ~ 1.52-fold at day 21 compared to day 1. Interestingly, it was seen that the cellular proliferation rate was enhanced as the concentration of AA SF increased in the blends. In contrast, slower cell growth was observed for the blends with higher PR SF. The maximum cell proliferations were ~ 1.33-, ~1.4-, ~ 1.31- and ~ 1.25-fold for BM6.0, BM5.5/AA0.5, BM5.5/PR0.5 and BM4.0/PR2.0, respectively on day 21 compared to the initial cell number on day 1. The least growth was noticed in BM4.0/PR2.0, whereas no significant difference was observed in between BM6.0 and BM5.5/PR0.5.

Cellular attachment and arrangement in the lamellar constructs were studied by fluorescence imaging. For the assessment of cellular viability, cell seeded constructs were treated with calcein AM that stained (green fluorescence) only the live AF cells in the constructs. Cells were viable in all constructs over period of 21 days, but variations in fluorescence signals was recorded **(Figure 3.3C, I-V**). The maximum green fluorescence signal was obtained from BM4.0/AA2.0, whereas least from BM4.0/PR2.0. The cells in BM4.0/AA2.0 were shown to be clustered, aggregated and homogeneously distributed throughout the construct discriminating it from BM6.0 or other blends. The cellular arrangement was checked by Hoechst 33342 staining for nuclei (**Figure 3.3D, I-V**). It was observed that cells were well distributed in lamellar way within all constructs, which was also observed in FESEM study (**Figure 3.3E, I-V**). The maximum blue fluorescence signal was obtained from BM4.0/AA2.0 as like calcein AM signal further confirming the high cell density. The central AA SF hydrogel also supported the NP cell viability (**Figure 3.3B**).

3.3.6.2. Histology and immunohistochemistry analysis

Cellular distribution and extracellular matrices (ECM) deposition within the fabricated constructs were visualized by H&E staining and immunohistochemistry, respectively. For this purpose, AF cells seeded constructs were maintained in chondrogenic medium for 3 weeks and sectioned for staining. From H&E, it was visualized that cells were arranged in lamellar way in all constructs

(**Figure 3.4A, I-V**). The maximum cell density and its uniform distribution were observed in BM4.0/AA2.0 followed by BM5.5/AA0.5 and least density was in BM4.0/PR2.0. The cellular infiltration was gradually decreased in blends with PR SF, whereas a relatively lesser infiltration was noticed in BM6.0.

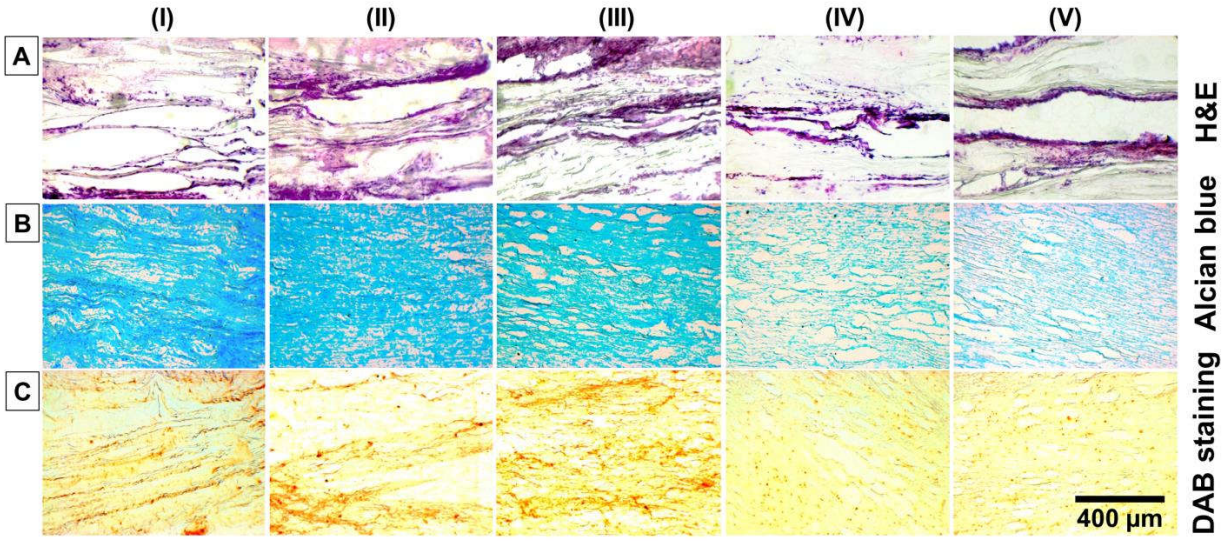

Figure 3.4. *Histology and immunohistochemistry of AF cells seeded lamellar constructs; (A) H&E staining showing cellular distribution, (B) alcian blue staining for deposited sGAG, and (C) immunohistochemistry of deposited collagen within the lamellar constructs over 3 weeks of culture in chondrogenic media: column representing (I) BM6.0, (II) BM5.5/AA0.5, (III) BM4.0/AA2.0, (IV) BM5.5/PR0.5, and (V) BM4.0/PR2.0.*

For the confirmation of sGAG deposition, alcian blue staining was performed for each type of construct (**Figure 3.4B, I-V**). The most intense blue color appeared in BM6.0 compared to other constructs supporting the maximum sGAG deposition. Sufficient amount of sGAG deposition was also found in both BM4.0/AA2.0 and BM 5.5/AA0.5, whereas deposition was considerably lower in both BM4.0/PR2.0 and BM 5.5/PR0.5. Form immunohistochemistry, unlike sGAG, it was noticed that maximum collagen type I was deposited in BM4.0/AA2.0 and sufficient amount of deposition was also found in both BM6.0 and BM5.5/AA0.5, but abruptly decreased in both BM4.0/PR2.0 and BM5.5/PR0.5 (**Figure 3.4C, I-V**).

3.3.6.3. Biochemical quantification of ECM components

The histological evaluation of collagen and sGAG deposition was further validated by biochemical quantification of cell seeded constructs on day 1, 7, 14 and 21. It was observed that total DNA content increased with time in all groups **(Figure 3.5A**).

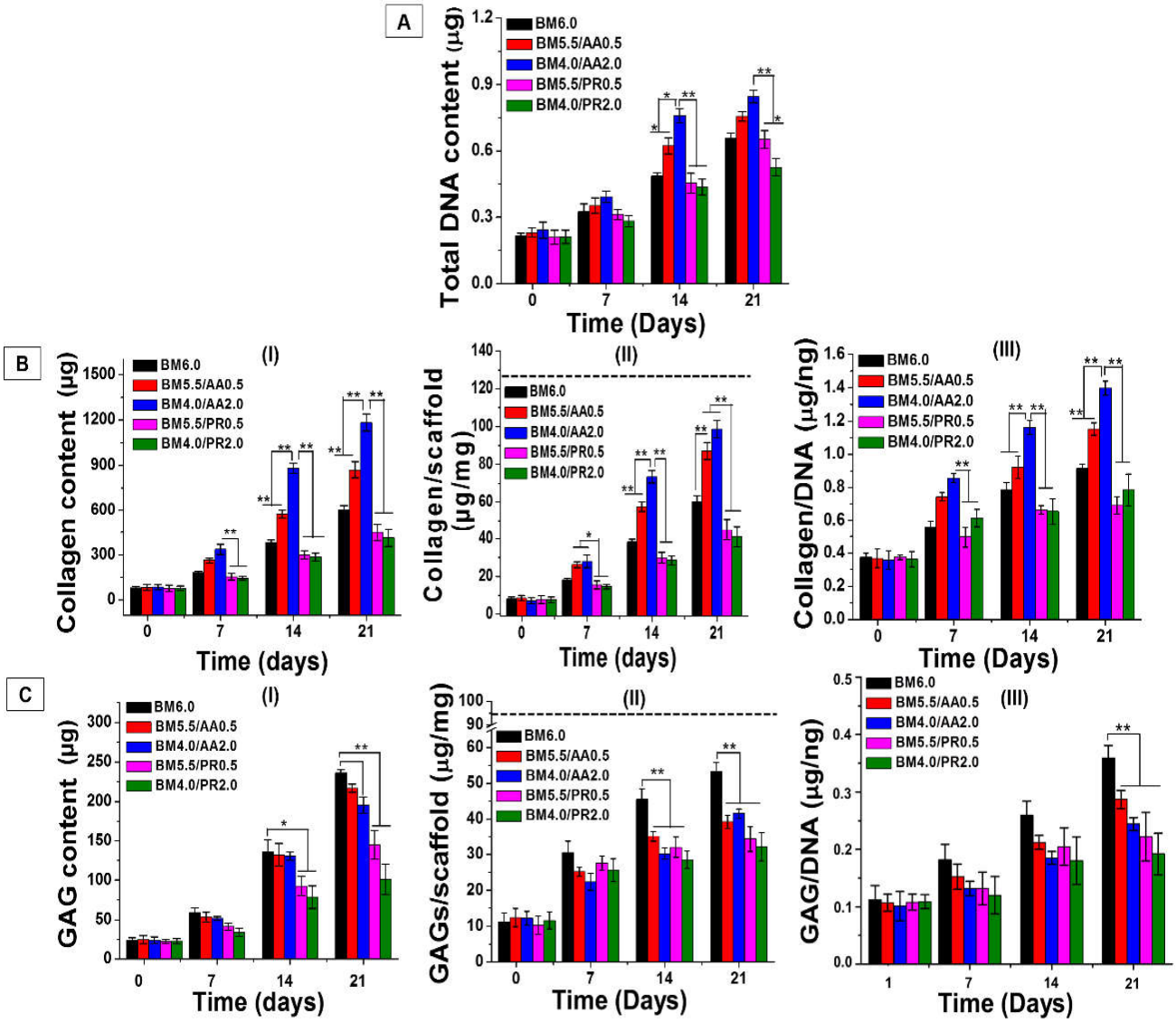

Figure 3.5. *Biochemical assessment of cell seeded constructs; (A) total DNA content, (B) collagen estimation: (I) total collagen content, (II) collagen/unit mass of construct, and (III) collagen content normalized by DNA, and (C) GAG deposition: (I) total GAG content, (II) GAG/unit mass of construct, and (III) GAG content normalized by DNA. The dashed line indicates native human*

*AF benchmark[414]. Data represent mean ± standard deviation, n = 3, where ** $p \leq 0.01$ and * $p \leq 0.05$.*

The maximum DNA content (846 ± 29 ng) was found in BM4.0/AA2.0 at day 21, whereas BM4.0/PR2.0 showed the least DNA content (526 ± 39 ng). It was noticed that total DNA content increased with the increase of AA SF in the blends as validated by Alamar blue reduction assay. Similarly, total collagen content increased with time for all groups (**Figure 3.5B, I**). It was observed that as the concentration of AA SF increased in blends, total collagen content increased. However, contrasting results were observed in PR SF blends. The maximum collagen content (1182.7 ± 56.32 µg) was found in BM4.0/AA2.0 which was ~ 13.74-fold increment as compare to day 1- and ~ 1.96-fold higher than BM6.0 (602.56 ± 32.25 µg) at 21 days ($p \leq 0.01$) The least collagen content (412.36 ± 58.52 µg) was obtained from BM4.0/PR2.0 at 21 days. To avoid the variation from scaffolds size or cell number, collagen content was normalized to DNA content. Similar trends were also observed in collagen content per mg scaffold and collagen content per ng DNA (**Figure 3.5 B II-III**). Conversely, GAGs deposition was shown to decrease with the increasing concentration of AA SF in blends (**Figure 3.5 C**). The maximum sGAG content (236.45 ± 4.26 µg) was found in BM6.0, whereas BM5.5/AA0.5 and BM4.0/AA2.0 showed the gradual decrease in total sGAG content (216.35 ± 5.36 µg and 195.56 ± 10.3 µg) at 21 days ($p \leq 0.01$) (**Figure 3.5 C, I**). However, total sGAG content drastically decreased in the blends of PR SF compared to BM6.0 at day 21 ($p \leq 0.01$). Similar trends were also noticed for sGAG/ DNA and sGAG/scaffold (**Figure 3.5 C II-III**).

3.3.6.4. Real time PCR analysis

In further support of qualitative (histology and immunohistochemistry) and quantitative (biochemical analysis) study, transcript level of AF related marker genes (col *Iα* 1, col II, aggrecan and sox9) were assessed by real time PCR and the value was normalized to the expression of GAPDH, an endogenous housekeeping gene marker (**Figure 3.6**).

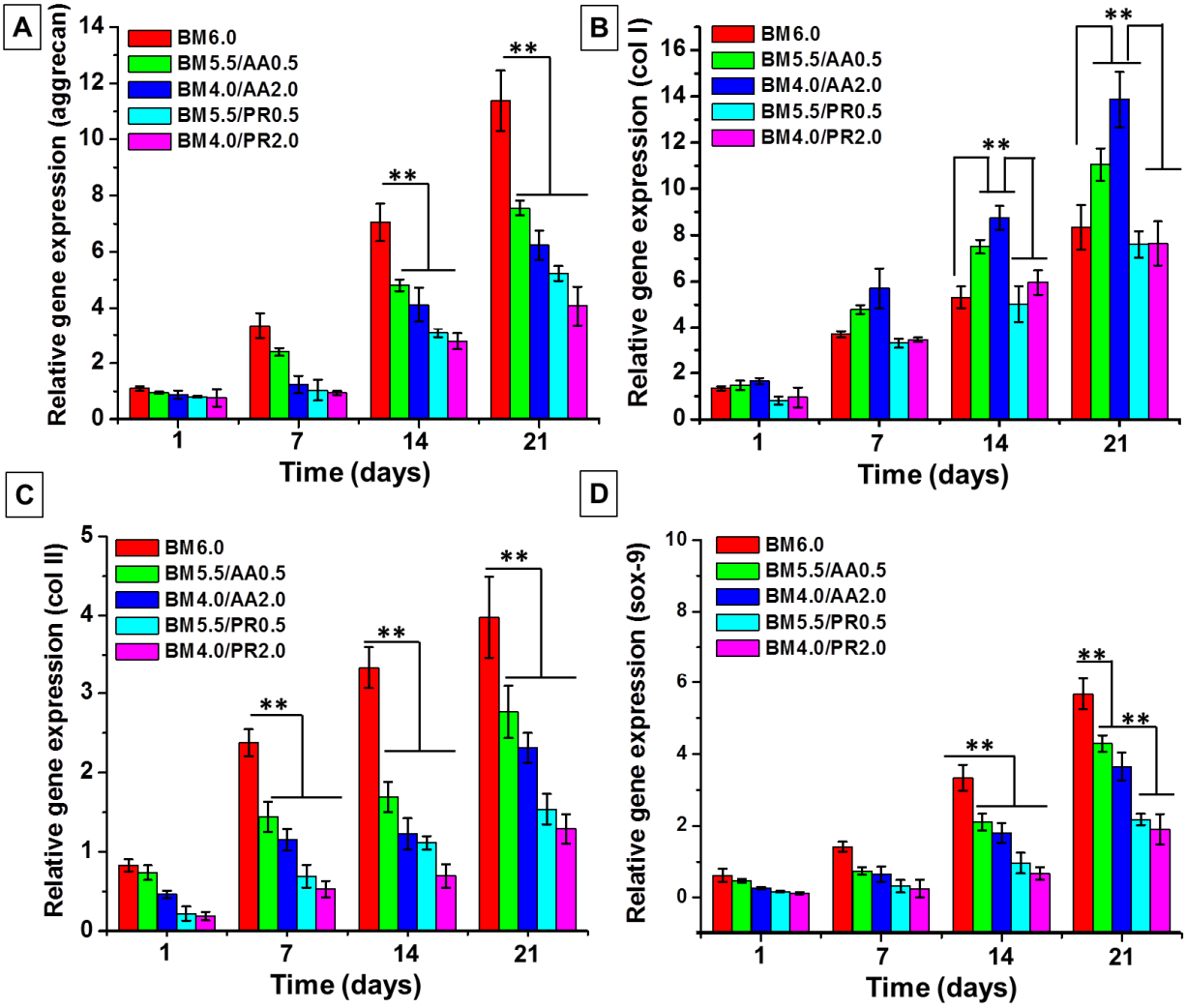

Figure 3.6. *Gene expression study for (A) aggrecan (B) col Iα 1 (C) col II, and (D) Sox9 in time points of day 1, 7, 14, and 21 days cultured in chondrogenic media. Data represent mean ± standard deviation, n = 3, where ** p≤0.01.*

For porcine AF cell, the mRNA expression level of all these four genes increased with time, but the maximum expression of col *Iα* 1 gene was observed for BM4.0/AA2.0 (~ 14-fold), whereas BM6.0 showed the maximum expression of col II (~ 4-fold) and aggrecan (~ 12-fold) after 21 days compared to day 1. Col *Iα* 1 gene expression increased as the concentration of AA SF increased in the blends. A similar pattern of sox9 expression was also noticed as like col II. However, in case of BM/PR combinations, gene expression was unrelated to the concentration of PR SF.

3.3.6.5. *In vitro* inflammatory response study

To analyze the cellular immunogenicity, lamellar constructs were subjected to sensitize the macrophages (RAW264.7) and the released TNF-α was determined using TNF-α ELISA kit.

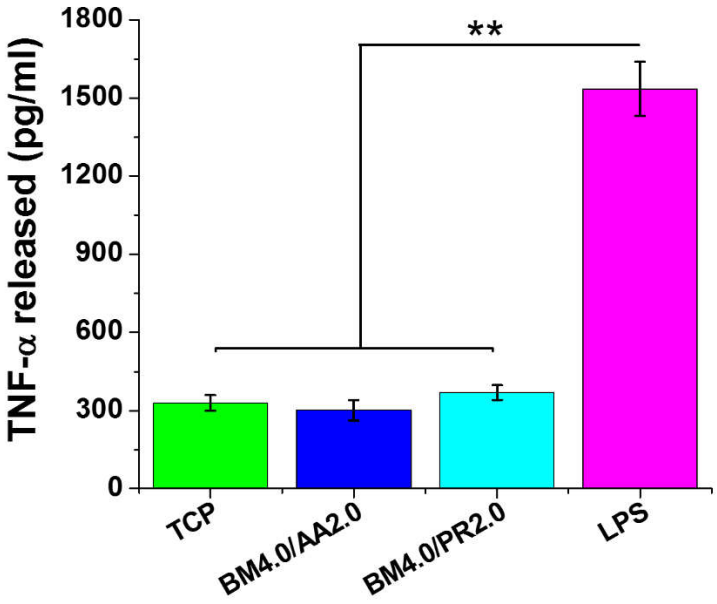

Figure 3.7. *In vitro inflammatory response study of the blended SF constructs by measuring the released TNF-α from the sensitized RAW264.7 cells. Data represent mean ± standard deviation, n = 3, where ** $p \leq 0.01$.*

The maximum amount of TNF-*α* (1535.45 ± 103.24 pg.mL^{-1}) was released by the cells treated with LPS (positive control), which was approximately 5 fold higher than the amount of TNF-α (in the range of 300-370 pg.mL^{-1}) released by the blended SF construct groups (BM4.0/AA2.0 and BM4.0/PR2.0) or TCP (negative control) ($p \leq 0.01$) (**Figure 3.7**). However, there was no significant difference between the blended SF constructs and TCP.

3.4. Discussion

To mimic the structural intricacy of AF tissue, a specially designed mold was developed using thermoplastic rubber (**Figure 3.1, A and C**). The directional freezing technique was implemented to prepare the lamellar construct following our previously reported protocol[380]. The disc-like angle-ply construct was developed using a single step process. The mold was designed in a manner that the lyophilized lamellar sheet obtained from it post lyophilization, could be circumferentially wrapped to attain the cross-aligned angle ply construct (**Figure 3.1A**). This improved approach restricted delamination effect of multiple sheets as described in our previous design (*Chapter* 2). Moreover, the design has the relaxation to vary the angles by adjusting the metal plates thus possible to mimic the angle variation (± 30-60°) from the central NP outward to the edge of the native disc. The TPR mold was used due to its flexibility and very poor thermal conductivity which facilitates rapid and directional ice crystal propagation from the surface of metal plates rather than the walls of mold (**Figure 3.1C**). The lamellar pores, the junction zone where ice crystals met propagating from two opposite diagonal directions and two adjacent layers of gross construct showing ± 30° were confirmed by FESEM study (**Figure 3.1, E-G**). The lamellar pores might overcome the limitations (*e.g.,* limited nutrition transportation and cellular infiltration) related to the previously designed constructs like nanofibrous biologic laminates or lamellar silk fibrous scaffolds[217, 240].

To mimic the zonal variations in biomechanical properties of AF tissues, two types of SF solutions were blended from different sources *i.e.,* BM SF with AA SF and BM SF with PR SF at various concentrations that provided a gradient of compressive modulus. The FESEM results showed that the pore size/porosity and inter-lamellar distance were gradually decreased with the increasing of non-mulberry SF in the blend for all cases, but substantially affected by PR SF (**Figure 3.2, A and C, and Table 3.3**). It might be due to greater hydrophobicity of non-mulberry SF. Upon blending, two proteins of different hydrophobicity interacted to each other, become aggregated (due to hydrophobic interaction) and consequently created smaller pore size. The hydrophobicity of silk protein depends on its amino acids composition, sequences and arrangement that play a fundamental role in secondary conformation which finally governs the physicochemical characteristics including pore size/porosity, swelling behavior, degradation pattern and mechanical properties of fabricated scaffolds. The primary structure BM SF consists of multiple repeats of AGSGAG which is ~ 55% of the total fibroin involved in crystalline structure formation[415]. The

rest portion consists of tyrosine residue that forms semi-crystalline structure[205, 416]. The structural changes from silk-I to silk-II occur exclusively in crystalline regions upon bio-spinning or synthetic β-sheet induction methods (*e.g.,* alcohol treatment) at laboratory conditions[390]. The BM SF consists of 30.2% alanine, 45.9% glycine, 12.1% serine and rest are 5.5% tyrosine, 1% aspartic and glutamic acid, and 2.2% isoleucine, leucine and valine[407]. On the other hand, the primary structure and repeating sequences of PR SF are considerably different from BM SF. The basic repeating unit is $(alanine)_{12\text{-}13}$ which is similar to the spider (major ampullate) silk that possesses $(alanine)_{5\text{-}6}$ as repeating unit[206]. It consists of 47.9% of alanine, 31.4% of glycine, 5.10% of serine, and 5.56% of tyrosine. Similarly, the primary structure of AA SF comprises of 42.5% alanine, 28.9% glycine, 10.2% serine and 5.5% tyrosine[407]. The secondary structure of AA SF possesses three main motifs; A-motif that mainly consists of alanine residues, G-motif that is mainly made of glycine residues and R-motif contains arginine residues. The A-motif contains poly-alanine stretches of $(alanine)_{5\text{-}15}$ and responsible for crystallinity of protein[407]. So, the presence of higher amount and larger stretches of poly-alanine in PR SF make it more hydrophobic than BM SF and even AA SF. The FESEM analysis also revealed a special characteristic feature on the lamellar walls of all blends (**Figure 3.2A, II-V**). An increasing order of spikes like protrusions were observed on the lamellar walls as the concentration of non-mulberry SF increased in the blends. The appearance of these spikes might be due to blending of two proteins of differential hydrophobicity. The rapid freezing process might differentially freeze these two proteins in the blend, consequently resulting in phase separation creating the spike like protrusions. This phase separation can also be explained on the basis of freezing point depression which is actually the difference between the freezing point of solution and pure solvent. In the freezing point depression, solvent molecules join together to make the solid phase leaving the liquid phase behind. This phenomenon is directly correlated to the molality of the solution[417, 418]. Here, the blends of different SF proteins having different molecular weight (MW) (~ 390 kDa of BM SF, ~ 460 kDa of AA SF and ~ 142kDa of PR SF[407, 419]) might possess the differential freezing points that finally caused the phase separation. Another possible reason might be the differential freezing time of the individual SF having different viscosity which was again depended on the isolation procedure and the concentration used in the blends. There is a correlation between viscosity and freezing time. The more viscous solution takes longer time to freeze than the less viscous solution. This differential freezing time of individual SF might also result in phase

separation. However, these pointed structure formed rough surface and also increased the gross surface area of lamellar walls that further helped in cellular attachment.

The aqueous stability of SF lamellar constructs was confirmed by inducing *β*-sheets after ethanol treatment. The FTIR spectra showed the conformational transition from silk I to silk II with the signature peaks of 1633, 1523 ad 1233 cm^{-1} (**Figure 3.2B**).

It is very important to assess the mechanical properties of any fabricated construct applied for load bearing tissue engineering. To recapitulate the zonal variations in mechanical properties of AF tissue, we fabricated the lamellar constructs by blending two different SF proteins in gradient ratios. The compressive modulus was found to increase as the concentration of non-mulberry SF increased in blends (**Figure 3.2F**). The maximum value (> 650 kPa) was obtained from BM4.0/PR2.0. However, the compressive modulus of BM4.0/AA2.0 was in the range of native human AF tissue (~ 380 kPa)[386]. This increasing order of compressive modulus might be related to the physicochemical properties of the fabricated constructs. The smaller pores and highly interlinked lamellar walls in the blends might support higher compressive modulus. The molecular arrangement also plays an important role in physical stability. The solid-state NMR (Nuclear magnetic resonance) study of *B. mori* SF reveals the presence of two different alanine-C*β* peaks in silk II form. It signifies that the methyl groups of alanine are located outside of the protein backbone and they are packaged with differently mode of side chain maintaining the same backbone torsion angles. This type of configuration of *B. mori* SF may provide the lesser stability than AA SF or PR SF wherein only poly-alanine residues present rather alanine-glycine repeats. The greater hydrophobicity and enhanced mechanical strength of non-mulberry SF are due to less heterogeneity and orderly arranged non-poly-alanine repeats in higher number, tighter poly-alanine *β*-crystals devoid of non-alanine residues and the lesser amount of polar residues in protein main chain[407]. In the current study, we investigated the compressive modulus in two ways; parallel (PD) and perpendicular (PPD) to the pore direction. This experiment was designed to understand the gross mechanical properties of the fabricated constructs as the vertebral discs experience the multi-axial loads. The obtained PD value was significantly higher than the PPD value for all cases except BM6.0. The walls of lamellar pores represented as fibers and the fiber orientation plays a significant role in compressive strength. It was previously reported that the mechanical properties deteriorated with increase in fiber orientation[420]. The maximum

compressive strength was obtained when the fibers orientation was parallel to the loading direction.

Besides the native structure of SF, extraction and fabrication procedures also affect the physiochemical properties of fabricated constructs. *B. mori* SF was extracted using chaotropic salt (LiBr) that might cause structural alteration finally affecting the physical properties. In contrast, non-mulberry SF was isolated from glands after dissolution in mild anionic detergent (SDS)[411]. SDS does not harshly affect the structural properties, and is relatively safer/non-toxic to both cell culture *in-vitro* and *in-vivo* tissue engineering applications[421]. So, all of these physiochemical factors about mulberry and non-mulberry SF were involved directly or indirectly in varying the pore sizes, porosity, swelling ratio, degradation properties and mechanical properties. Swelling ratio was found to decrease as the concentration of non-mulberry SF increased in blends (**Figure 3.2D**). This might be due to the increased gross hydrophobicity of constructs that repealed water molecule to interact. Moreover, the highly interconnected walls and decreased porosity/pore size (as revealed by FESEM study) of blends reduced the contact surface area and prevented water passage through pores resulting the reduced swelling ratio. A similar pattern of graph was also obtained in degradation study where the rate of degradation decreased with the increase of non-mulberry SF in blends (**Figure 3.2E**). The decreased degradation rate was associated with the lesser interaction of protein molecules to the enzyme. This might be due to the reduced pore size/porosity in blends restricting the enzyme molecules to pass through the constructs.

Cytocompatibility assessment of a biomaterial used for tissue engineering is very necessary for its clinical translation. Cell proliferation not only depends on chemical compositions of biomaterials, but "forms" that guide the cellular remodeling, where it functions as a template. This phenomenon is termed as "function follows form"[422]. It was previously reported that porous scaffolds used in AF tissue engineering supported non-uniform cell growth, though improved cell distribution was achieved under dynamic spinner flask culture condition[423, 424]. A previously reported comparative study demonstrated the non-uniform and reduced AF cell proliferation in porous scaffolds than the lamellar constructs[425]. Another report suggested the survival, alignment and differentiation of human mesenchymal stem cells (hMSCs) to different lineages in lamellar silk scaffolds[380]. The primary aim of the current study was to develop an artificial disc that could mimic the native hierarchical architecture of the AF and hence only the lamellar constructs were given preference other than the non-lamellar structure harboring its inherent disadvantages. For

this purpose, porcine AF cells were seeded within the various lamellar constructs and maintained them for 21 days. All the lamellar constructs supported AF cells growth and proliferation, but enhanced proliferation was observed for the constructs blended with AA SF (**Figure 3.3A**). This might be due to presence of RGD (arginine-glycine-aspartic acid) motif in AA SF that helped in faster cells adhesion and proliferation[407, 426]. The number of recent reports suggested this plausible effect of AA SF in various tissue engineering applications[196-198, 408, 427]. Though the constructs blended with PR SF possessed RGD sequences, no considerable effect on cellular proliferation was evidenced (GenBank: BAQ55621.1)[428]. This might be due to the adverse effects contributed by physical parameters *i.e.* less pore size/porosity and reduced swelling capacity that hinders nutrient, gas and waste exchanges, which ultimately affected cellular infiltration and proliferation.

A successful tissue engineering construct should provide the physicochemical cues that support cell proliferation and deposition of sufficient ECM for functional tissue. All types of lamellar constructs were seeded with porcine AF cells and cultured for 21 days in chondrogenic medium. Biochemical analysis showed the deposition of ECM components (collagen and sGAG content) in all type of constructs on any given time point, but there was difference in deposition in individual matrix. We found an increasing order of col *1α*I deposition in AA SF blended constructs possessing increasing order of mechanical strength, whereas an opposite trend happened for sGAG deposition (**Figure 3.4 and 3.5**). This might be due to the preferential selection and response of a specific cell population to particular matrix stiffness. Given the background, different zones of the entire AF consist of different AF cell types that differ in organization, appearance and function[429]. Moreover, there was a gradient in mechanical properties from the outer to inner layers. The cells of the outer layers (OAF) are elongated and oriented obliquely with respect to the axis (fibroblastic in nature), whereas cells of the inner layers (IAF) remain rounded and do not form distinct lamellae, possessing a more chondrocyte-like phenotype which express marker genes like collagen type II (col *2a* 1) and aggrecan, (chondrocytes in nature)[430]. Therefore, in this study, the isolated porcine cells from the entire AF tissue was a heterogeneous population having different cellular activities or ECM expression that includes different types of collagen (*viz.,* type I, II, III, V, VI and IX) and proteoglycan (aggrecan). So, the enhanced sGAG deposition in the BM6.0 possessing the least mechanical strength (12.53 ± 5.21 kPa) could be explained by the preferential selection of those IAF cells from the seeded heterogeneous population. Similarly, in gene expression study,

we observed higher level of col *1α* I expression for the constructs blended with AA SF that possessed higher mechanical strength, but col II and aggrecan mRNA expression increased as the mechanical strength decreased. For instance, maximum collagen II and aggrecan expressions were found in BM6.0 that possessed least mechanical strength and conversely, BM4.0/AA2.0 showed maximum col *1α* I expression as it was mechanically similar to native disc (**Figure 3.6**). It was clearly indicative that construct bulk stiffness or mechanical properties played key role in ECM gene regulation. Previous studies showed the influence of substrate stiffness on morphology and ECM gene expression of AF cells which are known to be "mechanosensitive cells"[399, 431]. Mechanosensing is the capacity of cells that can alter their cellular processes in response to mechanical forces applied to the cells or the variations in mechanical properties of the substrate on which cells anchor. There are several types of cells including smooth muscle cells and mesenchymal stem cells that have the capability to respond to biophysical cues such as substrate stiffness, bulk mechanical properties and surface roughness[432-434]. The matrix stiffness activates the Wnt/*β*-catenin signaling pathway in cells[435]. β-catenin expression is elevated by the activation of integrin/focal adhesion kinase (FAK) in response to stiff matrix that ultimately govern the cellular phenotypes and behaviors. In this context, mechanical properties are altered in the native AF tissue along the radial direction wherein higher stiffness is observed in outer layers than inner layers and AF cells respond (morphologically and biochemically) accordingly.

Here, our results suggested that an ideal tissue engineered construct for AF tissue could be designed with the layers possessing the increasing order of stiffness along the radial direction. Pertinent to note is that, AF cells seeded in the PR SF blended constructs did not show this mechanosensing effect though these constructs exhibited higher compressive modulus. Previously, several reports suggested that apoptosis and elevated level of catabolic gene expression might happen when the applied external mechanical stimuli exceeded the upper limit of physiological range[436]. In this study, the PR SF blended constructs showed the compressive modulus (~655 kPa) approximately twice of human native disc (~ 380 kPa), might be one of the reasons for depletion in anabolic genes expression[386]. Another possible reason might be the influence of other physical properties of constructs *e.g.,* less pore size/porosity and reduced swelling nature that ultimately created an adverse microenvironment rendering the seeded AF cells to stress. It would be interesting to assess the catabolic genes expression *e.g.,* matrix metalloproteinases (MMP)-3

and 13, and ADAMTS-5 (a disintegrin and metalloproteinase with thrombospondin motifs-5) to clarify the effect of stress microenvironment more significantly to gain more insights on the same.

An ideal biomaterial used for tissue engineering applications should possess the minimum immunogenicity to eliminate the chances of tissue rejection[437]. BM SF has already been FDA approved and few recent reports also suggested the less immunogenicity (*in vitro* or *in vivo*) of non-mulberry varieties (AA SF and PR SF) or their blends with mulberry (BM SF) variety[196, 408, 427]. In the current study, the blended constructs also showed the negligible immune responses when compared to the positive control (LPS), indicating that the constructs would not create any adverse response upon *in vivo* implantation (**Figure 3.7**).

Although, we designed a procedure to fabricate a disc-like angle-ply construct mimicking the AF structural intricacy with each blends representing the radial distribution of biomechanical and biochemical properties separately, it would be more relevant if the construct was prepared using a single lamellar sheet with a gradient of mechanical properties. Conclusively, the present study of cell viability and proliferation rate, histology and immunohistochemistry, biochemical and gene expression analysis showed that tissue maturation occurred in BM4.0/AA2.0 was superior to all other groups.

In the current study, the fabricated construct could recapitulate the intricate architecture of native AF tissue. We also looked into the mechanosensing behavior of AF cells that responded to the variations in matrix stiffness. However, it is very important to address other formidable challenges for its clinical translation. To move this technology towards clinical implementation, it is very necessary to fabricate a biphasic construct that ensures the AF-NP confinement. This is necessary as the multi-axial load can be indulged when they are in well-sealed confinement integrating to the surrounding tissue. For the clinical implementation, the engineered constructs can be used as cellular or acellular state. Upon transplantation, the construct will provide the mechanical resilience, whereas cellular entity will support ECM regulation to prevent it from further degeneration. Although there are several obstacles in clinical translation, the current study may provide a better understanding to recapitulate the form and function of an artificial disc.

3.5. Significant findings

The significant findings from this chapter are as follows:

- A silk based novel multilayered seamless *disc-like angle-ply* construct was fabricated. The developed construct consisted of concentric layers of lamellar sheets mimicking the native AF structure.
- Further, the effect of matrix alignment and mechanical properties on extracellular matrix (ECM) secretion and ECM specific gene expression were investigated.
- To provide differential physicochemical and biological cues, mulberry SF and non-mulberry SF was blended together that provided a gradient of mechanical strength.
- The developed construct supported porcine AF cells proliferation and ECM deposition.
- The mechanosensing behavior of seeded AF cells was confirmed by variation in ECM deposition in response to varied mechanical stiffness of constructs. This was further validated by gene expression study with AF tissue specific genes.

Overall, the developed constructs with varying mechanical strength supported cell proliferation, modulated ECM turnover and AF specific gene expression resulting in a functional AF tissue like construct indicating its potential as alternative strategy in IVD replacement therapy.

Chapter 4

Design and Fabrication of 3D-printed Biomimetic Construct to Recapitulate Form and Function of Intervertebral Disc (IVD)

This chapter introduces the fabrication of angle-ply AF anatomical equivalents by depositing silk-based micro-filaments in a layer-by-layer fashion using micro-extrusion based 3D printing strategy as this technique provides a precise replication and high throughput reproducibility over the manual fabrication strategy discussed in the earlier chapters.

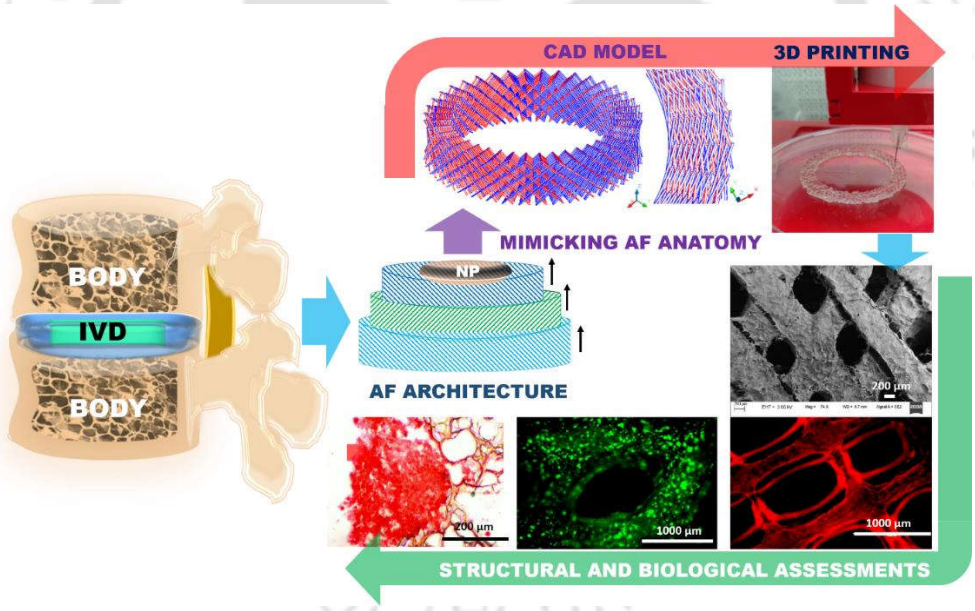

The work embodied in this chapter in published in a peer-reviewed journal as follows:

Bhunia BK, Dey S, Bandyopadhyay A, Mandal BB. 3D printing of annulus fibrosus anatomical equivalents recapitulating angle-ply architecture for intervertebral disc replacement. **Applied Materials Today**. 2021;23:101031.

ABSTRACT

Structural recapitulation is one of the prime prerequisites for the biomechanics of a complex tissue like annulus fibrosus (AF). Design and fabrication of a biomimetic AF anatomical structure has garnered immense interest among tissue engineers owing to its potential in restoration of intervertebral disc function. Three-dimensional (3D) printing technology, in recent times has demonstrated its applicability to fabricate such a complex tissue architecture. Here, we fabricated angle-ply AF anatomical equivalents by depositing silk-carrageenan filaments in a layer-by-layer fashion using micro-extrusion based 3D printing strategy. The 3D-printed constructs exhibited fiber alignment that mimics the native tissue when flipped by 90° across the periphery. The 3D printed constructs were physiochemically characterized including swelling and degradation. The cross-aligned structure was revealed by field-emission electron microscopy and fluorescence studies. Infrared spectroscopy analysis confirmed the induction of stable secondary β-sheet structure in the composite blend constructs. The 3D printed constructs exhibited higher mechanical strength (~ 78 kPa) than the native porcine AF tissue (~ 37 kPa). The constructs supported survival, growth and proliferation of both porcine primary AF cells (~ 1.43-fold) and adipose derived stem cells (ADSCs) (~ 1.32-fold) over the period of 14 days. Histological, biochemical and gene expression studies subsequently revealed the deposition of AF specific extracellular matrix on the constructs when maintained in chondrogenic medium. The developed biomaterial ink showed minimal-immunogenicity as depicted by the subcutaneous *in vivo* implantation assessment. Hence, the strategy adopted here to fabricate AF anatomical 3D printed equivalents may provide a new direction towards disc replacement therapy.

4.1. Introduction

Intervertebral disc (IVD) is a supportive avascular fibrocartilaginous tissue acting as cushion between the adjacent vertebrae. It serves as a shock-absorber as well as allows the complex spine motions in different directions such as, rotating, twisting and bending. The complicated structure of IVD is segregated mainly into two morphologically distinct areas; the central gelatinous nucleus pulposus (NP) region which is confined by multilamellar angle-ply, ring-like annulus fibrosus (AF) tissue. Any damage to the AF region due to trauma or pathophysiological conditions eventually leads to the intervertebral disc degeneration (IDD), which is one of the main reasons for low back pain (LBP)[13].

Though few manual strategies have achieved the structural and functional similarities to the native disc[217, 221, 309], precise replication and high throughput reproducibility is essential for fabricating a customized IVD construct. In this milieu, 3D printing technology can be utilized to recapitulate such a complex tissue architecture with the highest accuracy and precision in a high throughput manner. Recent advances in tissue engineering is largely due to the development of 3D printing industries. The principle of 3D printing can be described as the development of spatially defined structures with biomaterials using 3D printer technologies. It is termed as 3D bioprinting when it specially includes the encapsulation of cells within the biomaterials during printing. 3D bioprinters have made it possible to fabricate complicated heterogeneous architecture of functional tissue and organs like IVD[256].

3D printing technology has been used to print different tissues including skin, liver, heart, blood vessel, bone, cartilage[256, 438], as well as for IVD using various biomaterials. Notably, the biocompatible thermoplastic polymers such as polyurethane[280] and PCL[276] [277] [439] have been utilized to print the patient-specific AF anatomical equivalents with different internal architectures.

One of the limitations hindering the fabrication of biomimetic artificial organs using 3D printing technology is the selection of a suitable biomaterial-based ink (biomaterial ink). Ideally, a biomaterial ink is poised to be biocompatible and non-immunogenic, while being mechanically robust, possess appropriate rheological properties for printability, have controlled degradability, and preserves the bioactive molecules or cells while encapsulating[256]. A plethora of biomaterials like collagen, alginate, dextran, gelatin, Polyethylene glycol (PEG) and hyaluronic acid have been explored extensively for tissue engineering and regenerative medicine[440]. Silk fibroin (SF) from

Bombyx mori has been extensively used as biomaterial in different formats e.g., scaffolds, films, mats, micro-particle and hydrogel for decades[441]. Researchers have optimized silk fibroin based biomaterial inks for 3D printing technology[442] with enzymatic cross-linking[443], in conjunction with polyethylene glycol (PEG), polyvinylpyrrolidone (PVP)[444, 445], in methacrylate photo-crosslinking form[446], blended with gelatin with enzymatic cross-linking[447] and in a cross-linker free form, with gelatin blended, for 3D printing of various tissues[448].

Carrageenan is a type of sulphated polygalactan resembling glycosaminoglycan (GAGs) of extracellular matrix (ECM) having gel-forming, thermo reversible and viscosifying properties[449]. The negative charge of carrageenan interacts with other molecules like water and proteins forming the supramolecular assembly. Carrageenan has been extensively used in different tissue engineering applications including bone, cartilage and skin[450-452] . Carrageenan has been introduced in conjunction with calcium phosphate for encapsulating growth factors and cytokines and printing 3D bone tissue engineering constructs[453] and in photo-cross-linkable methacrylamide-modified form for adipose tissue regeneration[454].

In the present study, we developed a biomaterial ink by blending *B. mori* silk fibroin (SF) and carrageenan for the 3D printing of AF anatomical constructs, amalgamating the synergistic properties of both biopolymers. The developed biomaterial ink was thoroughly investigated for its rheological characterization and evaluated for its printability. This is the first time we reported the fabrication of a native-like-AF structural prototype using 3D printing technology. Through this study, we adopted a unique strategy where the 3D printed constructs mimicked the internal intricacy of AF tissue and the printed filaments were aligned at the angle of approximately ± 30° to the vertical plane of the construct when flipped by 90° across the periphery. Thereafter, these constructs were characterized for their physicochemical properties, mechanical behavior and cytocompatibility, followed by ECM secretion and specific gene expression *in vitro* by both porcine AF cells and adipose derived stem cells (ADSCs), and *in vivo* immunocompatibility by subcutaneous implantation.

4.2. Materials and methods

4.2.1. Isolation of *Bombyx mori* silk fibroin

For the isolation of silk fibroin (SF), *B. mori* cocoons were procured from the local silk farms (Assam, India) and an aqueous solution of SF was obtained after processing of cocoons according to the previously described procedure[381, 455]. Briefly, cocoons were finely chopped and degummed for 15 min by boiling in 0.02 M sodium carbonate (Na_2CO_3, Himedia, India) to remove the sericin. The fibers were rinsed with deionized water thoroughly, followed by drying at room temperature (25 °C). The dried fibers were dissolved in 9.3 M lithium bromide (LiBr, Sigma, U.S.A.) and kept at 60 °C for 4 hours. The obtained solution was dialyzed against distilled water in a 12 kDa cellulose membrane (Sigma-Aldrich, U.S.A.) to remove the residual LiBr with subsequent water changes at regular time intervals for 48 h. The estimation of final protein concentration (8-10%, w/v) was performed using the gravimetric method wherein the weight of remaining solid after drying of the dialyzed solution was recorded with an electronic balance (Sartorius, Germany). This regenerated aqueous SF solution was then used for biomaterial ink preparation.

4.2.2. Preparation of carrageenan solution

Stock solution of 4% (w/v) carrageenan (Sigma, U.S.A) was obtained by dissolving 4 g carrageenan powder in 100 ml of hot deionized water with continuous stirring at 80 °C for 2 h[456].

4.2.3. Formulation of silk-carrageenan based biomaterial ink

Silk-based biomaterial ink was prepared by blending 8% (w/v) regenerated *B. mori* SF (BM SF) solution and 4% (w/v) carrageenan solution in the ratio of 7:3. The blending was done with continuous stirring at a constant temperature of 60 °C for 15 minutes. After proper blending, the biomaterial ink was poured into the printing 10 CC syringe and incubated at room temperature (25 °C) until turned into gel.

4.2.4. Characterization of the silk-carrageenan based biomaterial ink

4.2.4.1. Rheological studies

A Rheometer (MCR 302, Anton Paar, Austria) with a standard steel parallel plate of 25 mm diameter was used to measure the rheological parameters of the formulated biomaterial ink. The sample holder of the rheometer was maintained at 25 °C prior to the tests. The biomaterial ink in the form of solution or suspension was dropped onto the lower plate followed by decreasing the distance between two plates to 0.5 mm and 0.1 N (Newton) force was applied for all tests. This process assured the good contact between sample and the plates. The paraffin oil was applied on the periphery to prevent the evaporation of water from the biomaterial ink during tests. The rheological test methods employed were oscillatory strain sweep (amplitude sweep test) to determine the linear visco-elastic region (LVER) of biomaterial ink, frequency sweep to understand the frequency dependent linear equilibrium modulus plateau[457], temperature sweep for temperature based gel stability and thixotropic analysis to understand structural disorganization under stress and recovery when stress is halted[458]. For amplitude sweep, the method was set up by maintaining a constant temperature (25 °C) and angular frequency (ω = 10 rad.s^{-1}) while increasing the shear strain (γ) level from 0.01% to 1000%. The change in complex viscosity (η^*) in response of strain sweep was plotted against shear strain (γ). The obtained LVER of biomaterial ink was the strain region in which storage modulus (G') and loss modulus (G'') were not dependent of strain amplitude. The biomaterial ink was further investigated for frequency sweep over a wide frequency range (ω = 0.1–1000 rad.s^{-1}) maintaining the fixed shear strain (γ = 1%) and temperature (25 °C). The temperature sweep was performed over a wide range of temperature (0-80 °C) while a fixed shear strain (γ = 1%) and angular frequency (10 rad.s^{-1}) were maintained. For thixotropic analysis, step strain sweep was applied in the range of 1-1000% in which a very high strain (1000%) was employed for 50 s followed by a low strain (1%) for 100 s and repeated for 2 cycles.

4.2.5. Computer-aided design (CAD) model of annulus fibrosus (AF)

AF has a high degree of structural complexity, wherein each lamella of the collagen fiber is aligned at a particular angle. The collagen fibers are aligned at ± 30° to the vertical plane of the spine, but in alternate direction to the successive layers. To mimic such complex architecture, a 3D CAD model of the AF tissue was developed using the AutoCAD (Autodesk). Further processing of the CAD model was done using Slic3r (1.3.0-dev, Alessandro Ranellucci), which gave the G-code

files. The G-code files were then fed to a 3D printer. The 3D CAD model developed for the AF region of the IVD consisted of multiple layers having the following dimensions (**Table 4.1**)

Table 4.1: Dimensions of the 3D CAD model developed for the AF region

Parameters	**Measurements**
Outer Diameter of the construct	40 mm
Inner Diameter of the construct	30 mm
Height of each layer	0.25 mm
Total number of layers	20
Distance between two adjacent biomaterial ink filament	0.75 mm
Angle of the biomaterial ink filaments of the odd layers	+30°
Angle of the biomaterial ink filaments of the even layers	-30 °
Printing speed	4-5 $mm.s^{-1}$
Printing pressure	30-40 psi

4.2.6. 3D printing of CAD model using silk-carrageenan biomaterial ink

The developed 3D CAD model was sliced using Slic3r software and the resultant G-codes were printed using the 3D printer (Allevi 2, U.S.A., formerly known as Biobots). 3D printing of the acellular AF construct was performed using the silk-carrageenan biomaterial ink. The biomaterial ink is extruded pneumatically through a nozzle diameter of 0.5 mm, with pressure ranging from 30 to 40 psi at room temperature (25 °C) and at a speed of 4-5 $mm.sec^{-1}$. In order to characterize the 3D printed constructs, angled grid structures with the dimension of 10 x 10 x 10 mm (height x width x thickness) were printed. Thereafter, the printed constructs were frozen at -80° C followed by lyophilization and treatment with ethanol to induce crystallinity[390, 459]. After successful printing and crosslinking, the structure was flipped by 90° across the periphery in wet condition to recapitulate the native structure of the AF.

4.2.7. Characterization of the 3D-printed constructs

4.2.7.1. Field emission scanning electron microscopy (FESEM)

Analysis of printed filament dimension and the pore size of the 3D printed acellular constructs were done using FESEM (Zeiss, Germany) at an operating voltage of 2-3 kV. The constructs were sputter coated with gold for 3 minutes before analysis. The pore size and printed filament diameter of the constructs was determined by analyzing 5 random pores and filaments, respectively, using ImageJ 1.48v software (NIH, U.S.A.).

4.2.7.2. Fourier transform infrared (FTIR) spectroscopy

To confirm the β-sheet transition, the infrared spectra of 3D-printed constructs were analyzed using FTIR (PerkinElmer, Spectrum Two, U.S.A.) in ATR (attenuated total reflection) mode. Constructs were lyophilized followed by treatment in ethanol to induce secondary structures. Lyophilized powder of untreated and ethanol treated BM SF scaffolds, and carrageenan were used as controls. For each sample, 32 scans with the resolution of 4 cm^{-1} were recorded and the spectral range was set to 4000 to 400 cm^{-1}.

4.2.7.3. Swelling behavior of the 3D printed silk based scaffolds

Conventional gravimetric method was used for analyzing the swelling behavior of the 3D-printed constructs. Briefly, the dry weight of freeze-dried constructs (n = 3) was recorded followed by immersing in MilliQ water at 37 °C for 32 h. The swelling weight of the constructs was recorded at definite time intervals, after removing the excess water surrounding the scaffold.
The swelling ratio was determined using the following equation:

$$Swelling\ ratio = \frac{W_s - W_d}{W_d}$$

where, W_s and W_d represent the swelled weight and the dry weight, respectively, of the constructs in mg.

4.2.7.4. *In vitro* enzymatic degradation

In vitro enzymatic degradation of the 3D printed constructs was performed by analyzing the weight loss post 28 days of incubation in protease *XIV* from *Streptomyces griseus* (Sigma-Aldrich, U.S.A.)

with an activity of 3.5 $U.mg^{-1}$. This assay was used to determine the biodegradability of the 3D-printed constructs under physiological conditions. The constructs (n = 3) were kept at 37 °C in phosphate buffered saline (PBS, pH 7.4) containing a final enzyme concentration of 2 $U.mL^{-1}$. The enzyme solution was replenished with fresh enzyme solution on every 3rd day for a period of 28 days. As control, scaffolds (n = 3) were kept in PBS (pH 7.4) under similar experimental conditions. 0.05% (w/v) sodium azide was used prevent any microbial growth in both the enzyme and PBS solutions. On every 7th day, the constructs were taken out, washed in deionized water, lyophilized and the dry weight was measured to calculate the percent mass remaining after degradation.

4.2.7.5. Mechanical properties

Mechanical properties were determined by using a universal testing machine (Instron 5944, Norwood, MA, U.S.A) having a 100 N load cell. The 3D printed acellular AF constructs with central hollow region, sonication induced *B. mori* hydrogels (2%, w/v) as NP substitute and 3D printed acellular AF constructs with *B. mori* hydrogel in centre as the whole bi-phasic construct were selected for mechanical testing. Compressive modulus was determined in both directions of the 3D printed angle grid constructs (10 x 10 x 10 mm); horizontal plane and vertical plane. For cyclic mechanical testing, constructs (in both planes) were subjected to ~ 30% of axial compressive strain for 50 cycles at a crosshead speed of 5 $mm.min^{-1}$. The similar parameters (except % of compressive strain which was set to ~ 20%) were also maintained for the cyclic mechanical testing of printed whole AF equivalent. The 20% axial strain was selected as it is close to the actual strain value experienced by human vertebral disc in normal physiological workload. The samples were hydrated for ~ 30 min at 37° C before testing. All tests were performed in an unconfined fashion. The stress-strain curves were plotted and compressive moduli were calculated at a small section of strain (10%).

4.2.8. Biological response study of the 3D-printed constructs

4.2.8.1. Isolation of primary porcine AF cell

AF cells were harvested from porcine lumber discs obtained from a local abattoir using a previously established protocol[413]. Briefly, the intervertebral discs (IVDs) were dissected from the lower and upper vertebral plates removing the adjacent muscle and tendon fibers. Thereafter,

the AF tissue was separated from the central NP region, minced into small fragments with a sterile scalpel blade followed by thoroughly washing with sterile PBS (pH 7.4). The whole dissection process was performed in a sterile environment. The tissue fragments were then treated with an antibiotic-antimycotic solution (100 $U.mL^{-1}$ of penicillin, 100 $\mu g.mL^{-1}$ of streptomycin and 0.25 $\mu g.mL^{-1}$ of amphotericin B; Gibco, Life Technologies, U.S.A.) followed by digestion with 0.2% (w/v) protease (Sigma, U.S.A.) for 1 h at 37 °C. After 1 h, the protease digested tissue fractions were further treated with 0.03% (w/v) collagenase for 18 h at 37 °C (Sigma, U.S.A.) under mild shaking condition. Thereafter, the digested tissue fractions were passed through a ~ 70 µm cell strainer to isolate the AF cell from the undigested tissue fraction. The cells were collected after 2 cycles of washing with sterile PBS (pH 7.4) by centrifugation (250 g for 5 min for each cycle) to remove the residual enzyme fraction. The trypan blue dye (Sigma-Aldrich, U.S.A) was used to check the viability of the isolated AF cells. The isolated AF cells were, thereafter, seeded in a monolayer at a density of 2 x 10^5 $cells.cm^{-3}$ and incubating them at 37 °C in a CO_2 incubator. For cell culture and maintenance, Dulbecco's modified eagle medium/F12 (DMEM/F12) supplemented with 10% (w/v) fetal bovine serum (FBS), 100 $unit.mL^{-1}$ penicillin G and 100 $mg.mL^{-1}$ streptomycin, and 50 $\mu g.mL^{-1}$ ascorbic acid (Gibco, Life Technologies, U.S.A.). The culture medium was changed every 3rd day and second passage (P2) AF cells were used for all in vitro experiments.

4.2.8.2. Isolation of adipose derived stem cells from porcine subcutaneous adipose tissue

Adipose derived stem cells (ADSCs) were isolated from porcine subcutaneous fat tissue following a previously described protocol [445, 460]. In brief, porcine fat tissue (from abdominal area) was procured from a local abattoir and washed thoroughly with sterile PBS (pH 7.4) followed by antibiotic-antimycotic (0.25 $\mu g.mL^{-1}$ of amphotericin B, 100 $U.mL^{-1}$ of penicillin and 100 $\mu g.mL^{-1}$ of streptomycin; Gibco, Life Technologies, U.S.A.) treatment for 30 min. Thereafter, the fat tissue was finely minced and completely digested with 0.25% (w/v) collagenase (prepared in high glucose Dulbecco's modified eagle medium (hDMEM) supplemented with 1% (w/v) FBS) for 2.5-3 h at 37 °C in a CO_2 incubator to form a viscous suspension. This suspension was then passed through a sterile cell strainer (~70 µm pore size) followed by centrifugation (1200 rpm) for 10 min to isolate the fat droplets and adipocytes in the suspension. The high density pellet, also known as stromal vascular fraction (SVF) consisting of adipose derived stem cell (ADSCs) was resuspended

in culture medium and plated for further maintenance in hDMEM, supplemented with 10% (w/v) FBS, 5 ng.mL^{-1} of b-FGF, 100 U.mL^{-1} penicillin and 100 µg.mL^{-1} streptomycin.

4.2.8.3. Cell seeding and proliferation assay within 3D-printed constructs

For cytocompatibility and cellular proliferation studies, both cell types (porcine AF cells and ADSCs) were seeded within the 3D printed constructs in separate sets. Prior to seeding, constructs (10 x 10 x 4 mm) were preconditioned in complete medium (DMEM/F12) for overnight at 37 °C in a CO_2 incubator. Thereafter, the preconditioned constructs were placed in a 24 well plate followed by seeding with AF cells (0.5 x 10^5 cells per construct). Another set of constructs were seeded with ADSCs (0.5 x 10^5 cells per construct) and incubated them at 37 °C in CO_2 incubator. Medium change was done every alternate day. Alamar Blue dye reduction assay (Invitrogen, Life Technologies, U.S.A.) was used to monitor cell proliferation after 1, 7 and 14 days of seeding. A multiplate reader (Tecan Infinite M200 PRO series) was used to measure the absorbance of reduced Alamar blue at 570 and 600 nm and the calculation of proliferation index was done as per manufacture's protocol. For the assessment of cellular distribution and infiltration inside the pores of printed filaments, cell seeded constructs were maintained in culture medium for an extended period of time (28 days). For biochemical and gene expression studies, both types of cell seeded constructs (0.8 x 10^6 cells per construct) were transferred into the chondrogenic medium (supplemented with 10% (w/v) FBS, insulin (6.25 µg.mL^{-1}), proline (40 mg.mL^{-1}), bovine serum albumin (BSA; 1.25 mg.mL^{-1}), ascorbic acid (50 mg·mL^{-1}), transferrin (6.25 µg.mL^{-1}), selenious acid (6.25 µg.mL^{-1}), transforming growth factor-β1 (TGF-β1; 10 ng.mL^{-1}), sodium pyruvate (100 mg.mL^{-1}) and dexamethasone (100 nM)), after 3 days of culture in standard medium to allow cells to acclimatize.

4.2.8.4. Cell viability study

Post 14 days of culture, the 3D printed constructs (n = 3) seeded with primary porcine AF cells and ADSCs were screened for cell viability using calcein AM live cell imaging kit (Invitrogen, Life Technologies, U.S.A.) as per manufacturer's protocol. Briefly, cell seeded constructs were incubated in calcein AM solution (4 mM) for 15 min at 37 °C followed by gentle washings with PBS (pH 7.4) to remove the excess dye bound to the constructs. The constructs were then visualized under a florescence microscope (Evos FL, Life Technologies, U.S.A.). The viable cells

took up calcein AM and could be visualized in bright green. The nuclei of seeded cells were stained with Hoechst 33342 (Invitrogen, Life Technologies, U.S.A.) following the manufacture's protocol. In brief, cell seeded constructs were fixed in 2.5% (w/v) gluteraldehyde for 3 h at room temperature (25 °C) followed by incubation with 1% bovine serum albumin (BSA) (Sigma, U.S.A.) for 30 min. The fixed samples were then permeabilized with 0.1% (v/v) Triton X 100 (Sigma, U.S.A.) for 5 min after a thorough washing with PBS (pH 7.4). Samples were then incubated with Hoechst 33342 (Invitrogen, Life Technologies, U.S.A.) staining solution for 30 min at dark. Fluorescent microscope was used to record the images.

4.2.8.5. Histological analysis

Post 14 days of culture in chondrogenic medium, cell seeded 3D printed constructs were treated in 10% (v/v) neutral buffered formalin (NBF; Sigma, U.S.A.) at room temperature (25 °C) for 24 h. For cryosectioning, the fixed samples were then transferred into 15% (w/v) sucrose solution for 1 h followed by incubation in 30% (w/v) sucrose solution for overnight at 4 °C. Thereafter, samples were placed on the top of circular cryostat block completely covered with Tissue freezing medium (Leica Biosystem Richmond, Inc. U.S.A.). Samples were sectioned at ~ 8 µm thickness using a cryomicrotome (Leica CM1860 UV, Leica Biosystem Richmond, Inc. U.S.A.). For the evaluation of cellular morphology and distribution throughout the constructs, sections were stained with hematoxylin and eosin (H&E; Sigma, U.S.A.) as well as alcian blue (1% w/v; Sigma, U.S.A.) and picrosirius red staining were performed for sGAG (sulfated glycosaminoglycan) and collagen deposition, respectively, in the matrix following previously established protocols [413, 461]. For image-based quantification of deposited sGAG, alcian blue stained images of cell-seeded and blank scaffolds were processed using ImageJ 1.52h (Wayne Rasband, National Institute of Health, U.S.A.) using color deconvolution to obtain the stained area. Thereafter, the thresholding of the images were carried out uniformly and henceforth the stained area fraction was calculated.

The immunofluorescence study was performed for the deposited collagen type I in the matrix following manufacture's protocol. In brief, sections were treated with 1% (w/v) BSA solution for 30 min followed by treatment with rabbit primary monoclonal antibody (1:200 dilution; Abcam, U.S.A.) raised against porcine collagen type I for 1 h. After a thorough washing, sections were reacted with FITC (Fluorescein isothiocyanate)-conjugated goat anti-rabbit secondary antibody

(Abcam, U.S.A.) for 1 h in dark. Images were recorded using a fluorescence microscope (Evos FL, Life Technologies, U.S.A.).

4.2.8.6. Biochemical analysis

To estimate the total collagen content within the constructs secreted by both types of cells (porcine primary AF cells and ADSCs) at day 1, 7 and 14, all cell seeded constructs were subjected to digestion in pepsin solution (1 mg.mL^{-1} pepsin, pH 3.0) at 4 °C for 48 h with gentle shaking following a previously described protocol [413]. Post digestion, samples were centrifuged (10,000 rpm*)* for 15 min to separate the undigested larger particles and the supernatant was collected for the next steps. Thereafter, 100 µL of supernatant from each sample was pipetted in 96-well plates followed by drying at 37 °C for 24 h. Post drying, 100 µL of direct red (1 mg·mL^{-1} prepared in saturated picric acid solution, pH 3.5; Sigma, U.S.A.) dye solution was added to each well and incubated at room temperature (25 °C) for 1 h under mild shaking condition followed by washing (4-5 times) with 0.01 N HCl. After washing, the dye-sample complex was dissolved in 0.1 N NaOH solution and absorbance was recorded at 550 nm using a multiplate reader (Tecan Infinite M200 PRO series). Bovine collagen (Sigma, U.S.A.) was used to generate a standard curve. As control, 3D-printed scaffolds without cells were used.

4.2.8.7. Real time PCR analysis

To isolate total RNA, individual 3D printed construct seeded with both the types of cells (porcine primary AF cells and ADSCs) cultured for different time points (day1, 7 and 14) were chopped in presence of TRIzol solution (Sigma, U.S.A.) followed by centrifugation at 12,000 rpm for 10 min at 4 °C to obtain clear supernatant (cell lysate). A 200 µL of chloroform was then mixed with the clear supernatant and incubated for 15 min. Thereafter, the mixture was centrifuged at 12,000 rpm for 15 min maintaining 4 °C and the upper aqueous layer containing RNA was carefully pipetted out followed by repeated washing in ethanol and resuspension in RNase free water (Sigma, U.S.A.) and quantification using a Nanodrop (Eppendorf, U.S.A.) as mentioned in manufacturer's instructions. A high-capacity cDNA reverse transcription kit (Applied Biosystems, Invitrogen, U.S.A.) was used to reverse-transcribe the purified RNA samples into cDNA in a thermal cycler machine (TaKaRa, Japan). Real-time PCR was conducted to quantify the level of AF specific genes (col *Iα* 1, sox9 and aggrecan (ACAN)) expression in both primary AF cells and ADSCs

using cDNA, power SYBR Green master mix (Applied Biosystems Invitrogen, U.S.A.) and, forward and reverse primers (sequences are summarized in **Table 4.2**). The whole experiment was performed in a real time PCR machine (Applied Biosystem 7500, ThermoFisher Scientific, U.S.A.) with the set conditions of holding stage (at 50 °C for 2 min and at 95 °C for 10 min) and cycling stage (40 cycles at 95 °C for 15 s and at 60 °C for 45 s) following the manufacture's protocol. The comparative Ct method ($2^{-\Delta\Delta Ct}$) was used to quantify the expression of AF specific genes and the obtained data was normalized to glyceraldehyde-3-phosphate-dehydrogenase (GAPDH), an endogenous housekeeping gene.

Table 4.2. Sequence of primers for real time PCR.

Gene	Sequence	NCBI Accession no.
GAPDH	F5′-TCGGAGTGAACGGATTTGG-3′ R 5′-CCAGAGTTAAAAGCAGCCCT-3′	NM_001206359.1
col *Iα*1	F5′AGAAGAAGACATCCCACCAGTCA-3′ R 5′-AGATCACGTCATCGCACAACA-3′	XM_013981006.1
sox9	F5′-TTCCGCGACGTGGACAT-3′ R 5′-GGCGGCAGGTACTGGTCAAACTC-3′	NM_213843.1
ACAN	F5′-CCCAACCAGCCTGACAACTT-3′ R 5′-CCTTCTCGTGCCAGATCATCA-3′	NM_001164652.1

4.2.8.8. *In vitro* inflammatory response study

For this study, RAW 264.7 cells (mouse macrophages cell line, acquired from National Center for Cell Science, NCCS, Pune, India) were allowed to react to the biomaterial ink for 24 h. The amount of released IL-1*β* and TNF-*α* in the medium secreted by activated macrophages in response to the biomaterial ink were determined using IL-1*β* and TNF-*α* ELISA kits (Thermo Fisher Scientific, U.S.A.) as mentioned in manufacturer's protocol. In brief, 10^5 cells per well were seeded in a 24-

well plate and cultured at 37 °C for 24 h in a CO_2 incubator. Post 24 h of incubation, a small block (2 x 2 x 1 mm) of biomaterial ink (BI) in combination with carrageenan (CA) and *B. mori* scaffold (BM) was placed into each cell seeded well and incubated for next 24 h maintaining the similar cell culture condition. LPS (1000 $ng.mL^{-1}$) and blank well of TCP (tissue culture plate) were treated as positive and negative controls, respectively. Thereafter, spent medium was pipetted out from each well, centrifuged and supernatant was collected for IL-1β and TNF-α assessment. For this purpose, 100 µL of spent medium was incubated with 50 µL of biotin conjugated anti-mouse IL-1 β/ TNF-α monoclonal antibody at room temperature (25 °C) for 2 h on a microplate shaker. After a thorough wash, wells were incubated with 100 µL of streptavidin-HRP (horseradish peroxidase) solution for 1 h under similar conditions followed by another round of thorough washing. Thereafter, 100 µL of TMB (tetramethyl-benzidine, a chromogen) substrate solution was added to each well and incubated at room temperature (25 °C) for 10 min in dark. Finally, 100 µL of stop solution (1 M phosphoric acid) was added to each well to terminate the enzymatic reaction. A multiplate reader (Tecan Infinite 200 PRO series, Switzerland) was used to record the data at 450 nm.

4.2.8.9. *In vivo* response to biomaterial ink

To evaluate the *in vivo* response to biomaterial ink, 8 male Sprague Dawley rats (5–7 weeks old, 200–250 g weight) were randomly allocated into two study groups; 1 week and 4 weeks. Animals were housed under standard condition (22 ± 2 °C, 55 ± 5% humidity, 12 h light-dark cycles and, food and water *ad libitum*). All the necessary pre- and postoperative care were assured. All of the experiments were conducted in accordance with the animal ethical guidelines approved by National Institute of Pharmaceutical Education and Research (NIPER), Guwahati. Before experiments, rats were anesthetized using an oxygen/isofluorane gas mixture in a closed glass chamber. After shaving and surface sterilization by wiping with 70% (w/v) isopropanol, 200 µL of sterile biomaterial ink was injected in the subcutaneous region at lower back dorsal area of each rat via a 26-gauge needle. All experiments were conducted aseptically. Rats were examined regularly for any sign of infection and their daily activity level was also monitored. No death occurred during the whole experimental time period. Post 1 week and 4 weeks, all of the experimental rats were sacrificed followed by retrieval of injected biomaterial ink including surrounding tissue to investigate its immunological response. Following retrieval, specimens were

fixed in 10% (v/v) NBF, transferred into graded sucrose solution (15-30%, w/v), covered with OCT compound followed by sectioning (~ 8 µm) using a cryomicrotome (Leica CM1860 UV, Leica Biosystem Richmond, Inc. U.S.A.). The sections were then processed for H&E staining and immunofluorescence study to investigate the macrophages infiltration surrounding the implanted area. For immunofluorescence, after blocking with 1% (w/v) BSA, sections were reacted with rabbit monoclonal primary antibody (1:200 dilutions; Abcam, U.S.A.) raised against rat CD68 (macrophage surface marker) for 1 h followed by carefully washing with PBS (pH 7.4) and reaction with FITC (Fluorescein isothiocyanate)-conjugated anti-rabbit secondary antibody (1:200 dilution; Abcam, U.S.A.) for 1 h at room temperature (25 °C). The experiment was conducted in dark to avoid any photo-bleaching related issue. The images were recorded using a fluorescence microscope (EVOS FLc; Life Technologies).

4.2.9. Statistical analysis

Quantitative analysis experiments were carried out in triplicates (n = 3) unless specified and results have been expressed in the form of mean ± standard deviation. The obtained data were statistically analyzed using one-way analysis of variance (ANOVA) in Origin Pro (OriginLab, U.S.A.). Groups were considered to possess significant statistical difference for $p \leq 0.05$ and highly significant difference was assigned for $p \leq 0.01$ and $p \leq 0.001$.

4.3. Results

4.3.1. Rheological characterization of the biomaterial ink

To prepare biomaterial ink, regenerated *B. mori* SF (8% w/v) was thoroughly mixed with 4% (w/v) carrageenan in the ratio of 7:3 at 60 °C for 15 min and kept it at room temperature (25 °C) to transform it into gel. The gel or biomaterial ink was then investigated for rheological characterization. Flow properties or deformation of the silk-based biomaterial ink at specific forces was determined by rheological analysis (**Figure 4.1, A-F**). The biomaterial ink possesses two distinct phases; viscous (or liquid) and elastic phase, and these two properties are indicated by loss (G") and storage (G') moduli, respectively. Linear visco-elastic region (LVER) of biomaterial ink was determined from amplitude sweep testing wherein G' and G" were plotted against strain value (γ). As the γ value increased, the biomaterial ink started to deform resulting declined G' value and complex viscosity (**Figure 4.1A**). The complex viscosity and G' value drastically decreased after a certain point (~ 50% of γ) and finally crossed the G" at ~ 101% of γ (**Figure 4.1, A-B**). The critical γ value (LVER) for this biomaterial ink was calculated as ~ 32% *i.e.,* below this value the biomaterial ink was intact and showed the elastic behavior. The frequency sweep of the biomaterial ink was performed to record the frequency dependent viscoelastic property at a fixed strain (γ = 1%). The biomaterial ink showed no deformation up to 200 rad.s^{-1} and both G' and G" were independent of frequency (**Figure 4.1C**).

Temperature sweep was performed to understand the temperature dependent gelling property of the biomaterial ink, while thixotropic analysis helped to determine the recoverability property of the silk based biomaterial ink. In temperature sweep, both the G' and complex viscosity were found to decrease with the increase of temperature (**Figure 4.1D**). It was observed that the biomaterial ink maintained its integrity below ~ 40 °C and gradually became fluid when temperature raised over that.

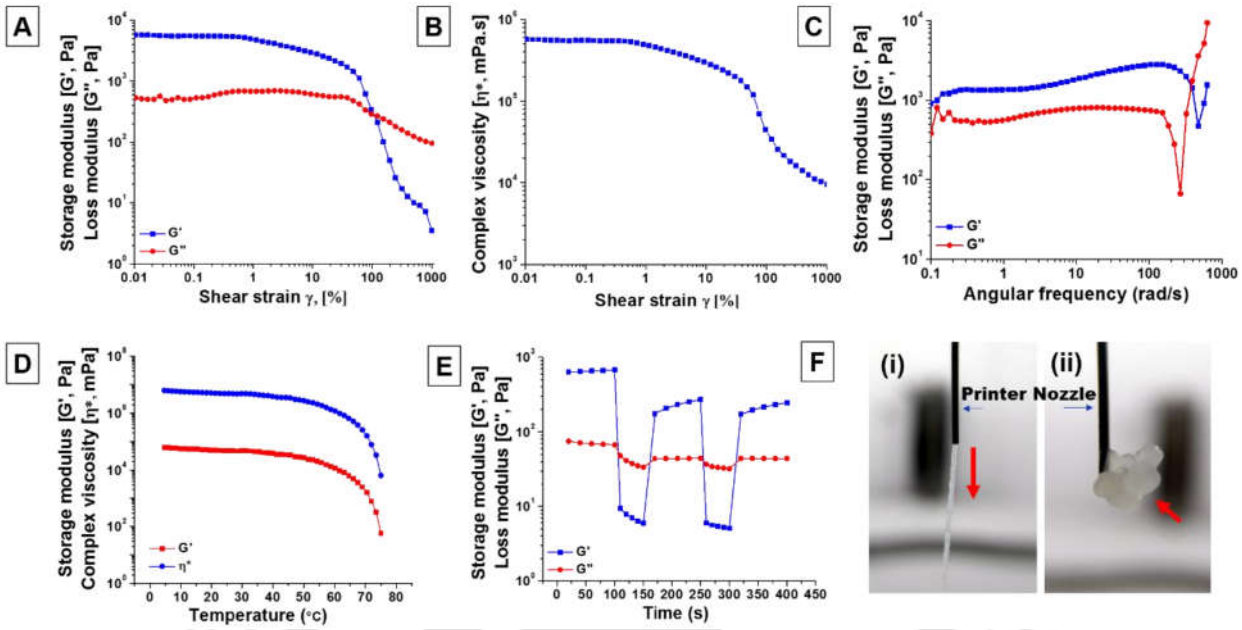

Figure 4.1. *Rheology of the silk based biomaterial ink; (A) determination of the LVER of the biomaterial ink, (B) complex viscosity vs shear strain, (C) frequency sweep, (D) temperature sweep and (E) thixotropic test, and (F) extrusion of biomaterial ink through nozzle: (i) free flowing and (ii) with a suitable G' of biomaterial ink for printing self-standing constructs.*

In thixotropic analysis, it was noted that the biomaterial ink had the recoverability property from the deformations caused by high shear strains for several times (**Figure 4.1E**).

4.3.2. Silk-carrageenan biomaterial ink based 3D printing of AF architecture

The 3D CAD model of the AF region of IVD was designed based on the native structure (**Figure 4.2, A-B**).

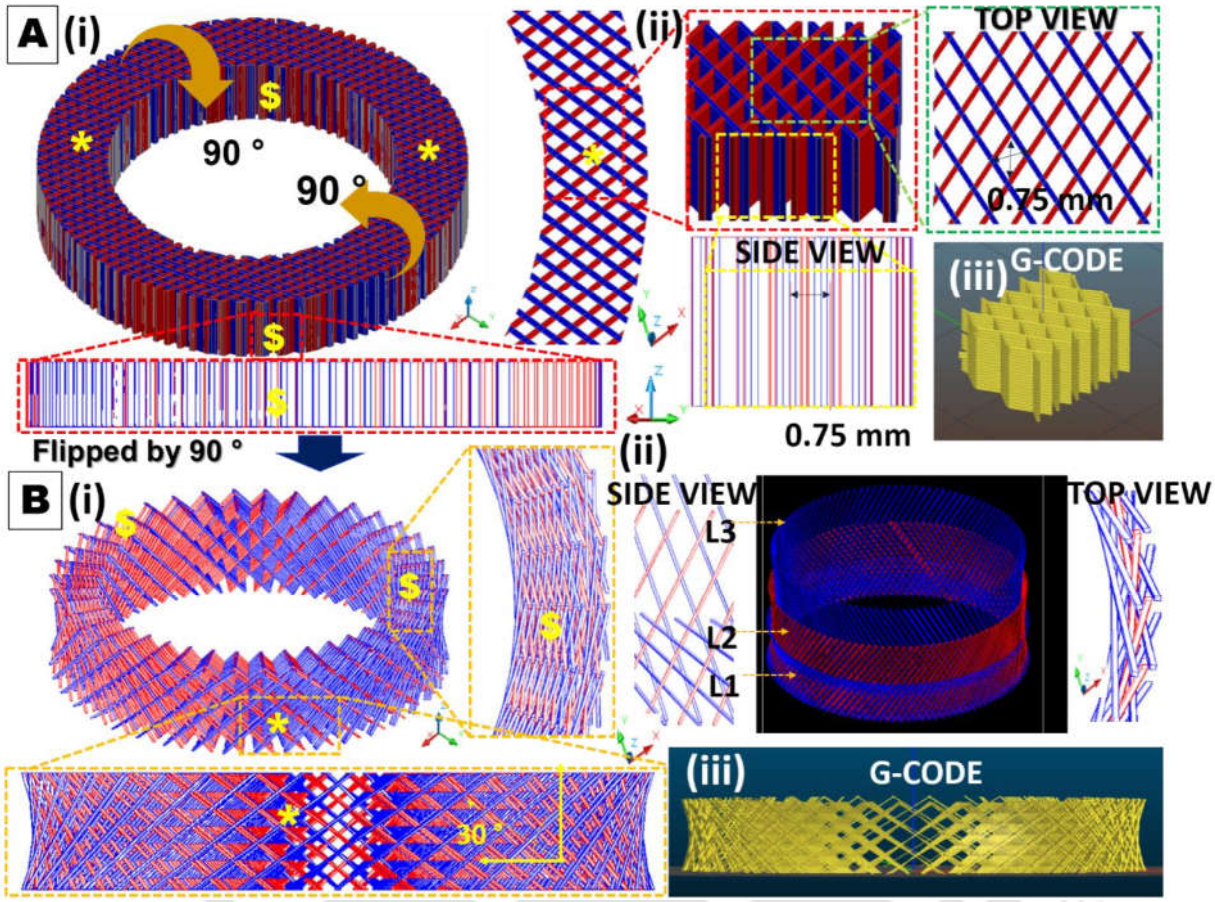

Figure 4.2. *3D CAD model of AF structure; (A) CAD model fed to the 3D bioprinter: (i) model representing the angled-grid structure (i-ii) design showing the top and side view of CAD model, (iii) showing G-code for a small section of the construct, (B) (i) prototype of the 3D CAD model with multiple layers representing the structure after flipping by 90° that would mimic the native AF architecture, (ii) CAD model of multiple layers of the filaments arranged at an angle of ± 30°, but alternate direction in each successive layer, and (iii) G-code of the full structure. Yellow star (*) represents the top view while the yellow dollar sign ($) shows the side view of the CAD design and changed their position vice-versa after twisting by 90°.*

To ascertain the printability, various shaped angle-grid structures were printed with the silk-carrageenan based biomaterial ink following the specification mentioned in **Table 4.1** (**Figure 4.3 A-C**).

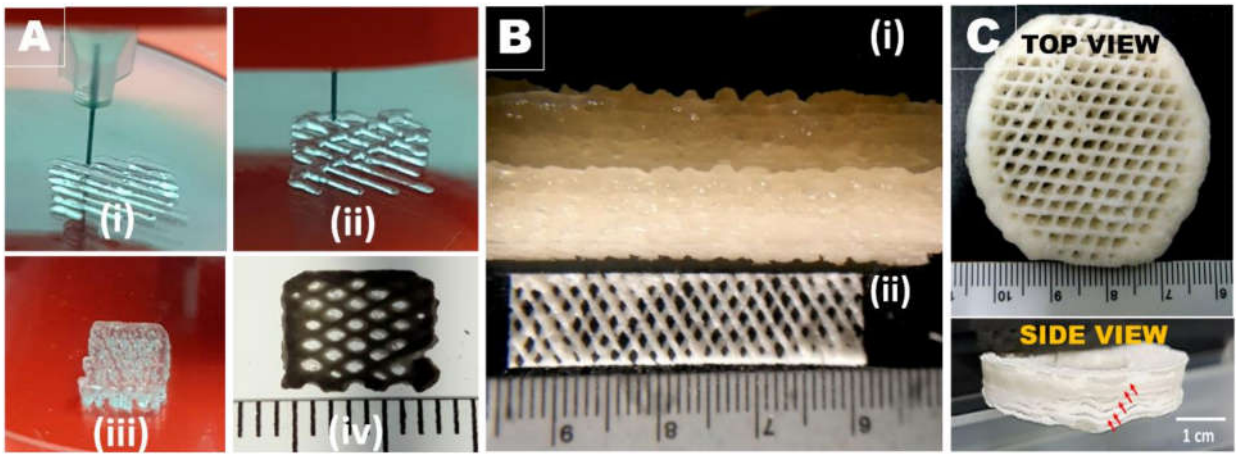

Figure 4.3. *3D printing of various constructs with the biomaterial ink; (A) step wise printing of cube-shaped angle-grid construct: (i) single layered, (ii) double layered, (iii) multiple layered, and (iv) the lyophilized constructs, (B) (i) multiple (ii) double layered 3D printed rectangular shaped constructs, and (C) disc-shaped angle-grid construct with multiple layers (up to 10 layers) (red arrow showing the layers from side view).*

The biomaterial ink showed high fidelity and requisite printability. The printed constructs were highly stable and retained their shape and size without collapsing during printing. The fiber diameter and the inter fiber spacing of the printed constructs were retained as designed in CAD model. After confirming the structural integrity and dimensional stability of smaller constructs (according to the gross morphology analysis), the larger AF anatomical constructs were printed according to the CAD model (**Figure 4.2, A-B**). The disc-like angle-grid constructs showed the printed filaments aligned in the horizontal plane. After successfully printing and crosslinking, the construct was twisted in wet condition by 90° across the periphery (inward or outward) to recapitulate the native structure of the AF (**Figure 4.4, B-C).** After twisting of the construct, the printed filaments were shown to be aligned at an angle of ~ ± 30° in alternate layers with respect to the vertical axis (**Figure 4.4C**). For further characterization, the smaller angle-grid constructs were printed maintaining the similar printing features.

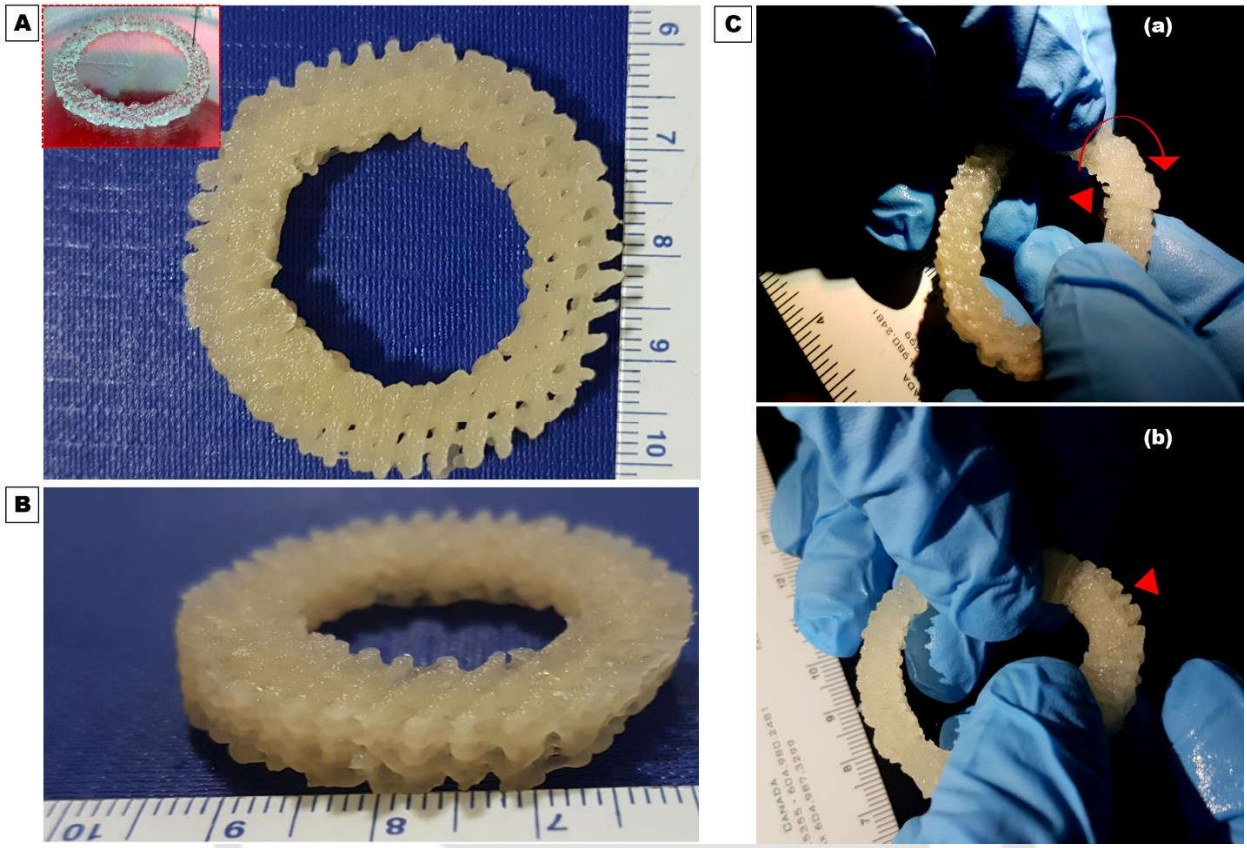

Figure 4.4. *Extrusion based 3D printing of the AF constructs; printed disc-like angle-grid AF construct (A) top view (inset: printing of construct), (B) side view, and (C) images showing the step-wise twisting of fabricated constructs by 90° across the periphery: (a) before and (b) after twisting. The red filled triangle indicates the rotated position.*

4.3.3. Physiochemical characterization of the 3D printed scaffolds

4.3.3.1. Field emission electron microscopy (FESEM) analysis

Pore size of the 3D printed scaffolds as well as their interconnectivity was evaluated by FESEM. The advantage of 3D printed scaffolds is that the pore size and the geometry can be precisely controlled. The constructs depicted uniform distribution of pores with an average diagonal length of ~ 740 µm. The average biomaterial ink filament width was ~ 500 µm and the pores had a rhombic geometry (**Figure 4.5A, i-iii**). The cross section of the printed filament portrayed highly interconnected macro- as well micro- pores (20-200 µm), which are ideal for tissue engineering scaffolds.

4.3.3.2. Furrier transform infrared spectra (FTIR) analysis

The secondary structures in the alcohol treated 3D printed AF anatomical constructs were confirmed by FTIR analysis with the signature peaks of *β*-sheets at 1620 (amide I), 1512 (amide II) and 1223 cm^{-1} (amide III) which were found to be shifted from 1650, 1542 and 1240 cm^{-1}, respectively, of the untreated BM SF scaffolds. The signature peaks of carrageenan at 1070, 930 (both for C-O of 3,6-anhydrogalactose) and 845 cm^{-1} (C–O–SO4 on C4 of galactose) were also confirmed in the printed constructs[462] (**Figure 4.5B**).

4.3.3.3. Swelling behavior

The water retention capacity was assessed by the swelling ability of the 3D printed constructs. For this study, lyophilized constructs were submerged in distilled water and at the weight was noted at various time points (**Figure 4.5C**). A rapid swelling was observed in the first 115 minutes with a swelling ratio of ~ 6.7, while in the later time points gradual swelling was noticed up to 24 h. The maximum swelling ratio at equilibrium was found to be ~ 8.4.

4.3.3.4. *In vitro* enzymatic degradation

Under ideal conditions, scaffold should degrade with time in order to allow the regeneration by formation of neo-tissue, to fill up the gap. In order to mimic the biodegradable environment at the physiological level, the 3D printed constructs were given protease treatment for 28 days (**Figure 4.5D)**.

The rate of degradation was represented as mass remaining in percentage at each time point. A significant difference was observed in the degradation rate of the 3D printed constructs treated with enzyme and the control group ($p \leq 0.001$). The percentage of mass remaining gradually decreased with time in case of the protease treated scaffolds. The enzyme treated constructs showed ~ 40% mass degradation after 7 days, ~ 55% mass degradation after 14 days followed by ~ 70% of mass reduction after 28 days while in case of the constructs kept in PBS (control group), no significant reduction in mass was observed.

4.3.3.5. Mechanical properties

Mechanical assessment is one of the vital aspects for any fabricated constructs used in load bearing applications. For this purpose, three different sets of acellular constructs were considered; set I

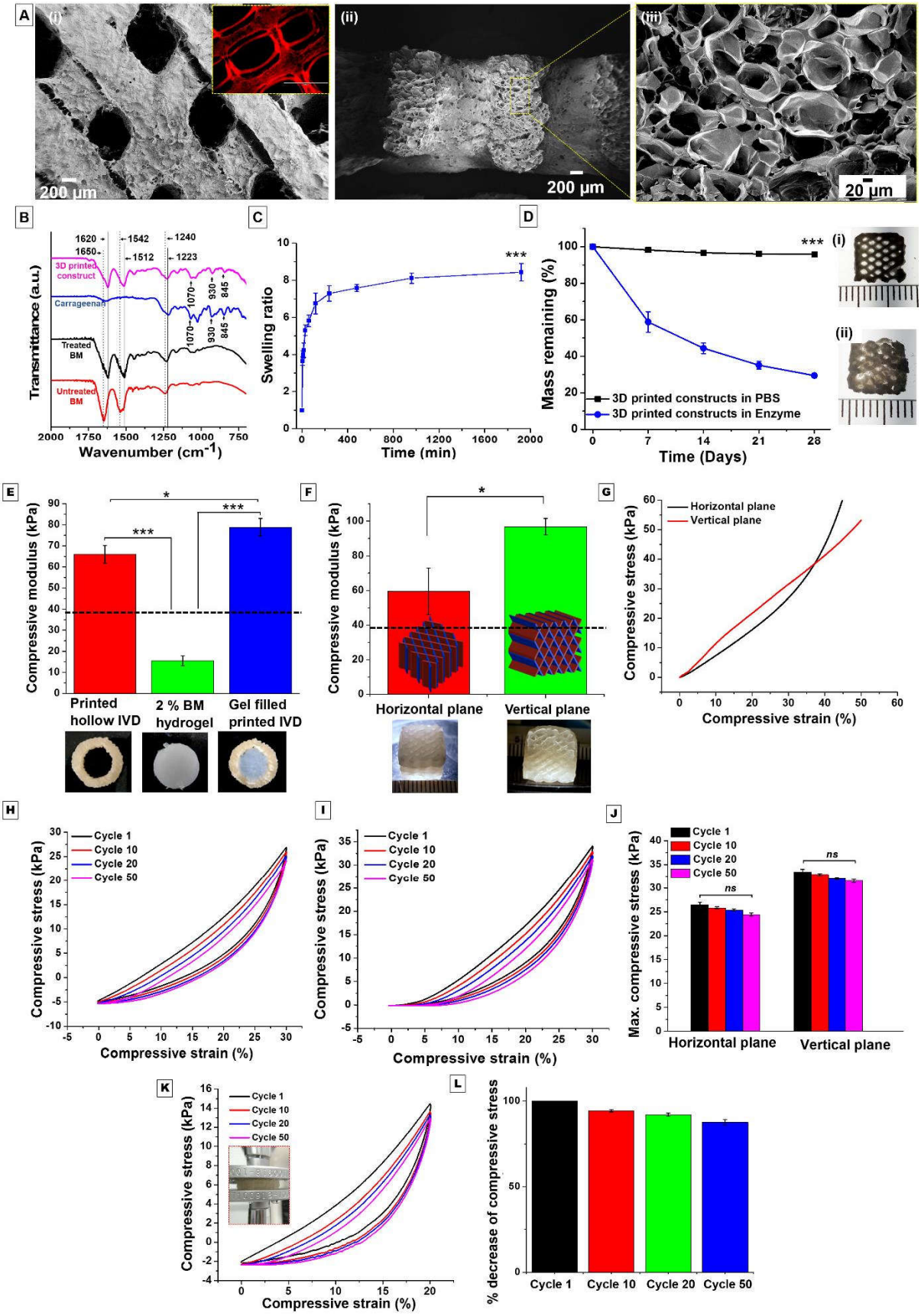

Figure 4.5. *Physicochemical characterization of 3D printed angle-grid constructs; (A) FESEM analysis, inset showing fluorescence optical microscopic image of angle-grid structure: (i) gross anatomy, (ii) cross section showing the internal pores of the constructs, and (iii) magnified image of figure (ii), (B) FTIR analysis, (C) swelling study, (D) degradation study: images showing (i) the intact construct in PBS and (ii) deformed construct in enzyme after 28 days. Mechanical properties of 3D printed constructs: (E) the compressive modulus of printed constructs (hollow IVD, B. mori hydrogel as NP substitute and the bi-phasic structure with NP substitute, (F) differential compressive properties depending on printed filament direction, (G) a typical stress-strain curve for two different plane of fiber direction, (H and I) The stress-strain curve of the cyclic mechanical testing up to 50 cycles for horizontal and vertical fiber printing directions, respectively, (J) the maximum compressive stress for both planes of printed filament direction, (K) stress-strain curve of cyclic mechanical (up to 50 cycles) testing for printed whole AF equivalent, and (L) percent decrease of maximum compressive stress after cycles. The dashed line indicates the native porcine AF benchmark. Data represent mean ± SD (n = 3), where *p≤0.05 and ***p ≤ 0.001. "ns" represents non-significant.*

consisted of 3D printed angle-grid AF anatomical construct without NP portion (hollow IVD), set II was sonication induced 2% (w/v) BM SF hydrogel as NP substitution and set III consisted of 3D printed AF anatomical construct filled with hydrogel in center as a whole intact vertebral disc (**Figure 4.5E**). The compressive modulus was calculated from the stress-strain curve of each specimen. The maximum compressive modulus (78.85 ± 4.18 kPa) was obtained from the set III construct representing as a whole disc, while set I, the hollow IVD showed significantly less compressive modulus (65.97 ± 4.11 kPa) than the set III ($p \leq 0.05$). Moreover, the obtained compressive modulus for both cases was higher than the native porcine AF tissue (represented as dotted line in **Figure 4.5, E-F**). However, the sonicated hydrogel (set II) showed the least value (15.45 ± 2.4 kPa) among all the groups ($p \leq 0.001$). The compressive modulus_was measured in both directions for the 3D printed angled grid structures *i.e.,* parallel (horizontal plane) and perpendicular (vertical plane) to 3D printed filament direction (**Figure 4.5, F-G**). Compressive modulus was significantly higher ($p \leq 0.05$) in vertical plane (96.77 ± 4.79 kPa) than horizontal plane (59.45 ± 13.38 kPa). The cyclic compressive properties were also assessed for both directions. The maximum compressive stress for both cases was calculated from stress-strain curve in different cycle *i.e.,* 1st, 10th 20th and 50th cycle. No significant change was observed in maximum

compressive stress after 50th cycle for both cases (**Figure 4.5, H-J**). Moreover, the minimal change (~ 10%) in maximum compressive stress was also observed for printed whole AF equivalent even after 50 cycles (**Figure 4.5, K-L**).

4.3.4. Biological response to 3D printed constructs

4.3.4.1. Cell viability and proliferation study

For a tissue engineering biomaterial, cytocompatibility is a vital pre-requisite towards its clinical applications. Both porcine primary AF cells and ADSCs were seeded into 3D printed constructs and cultured *in vitro* to assess cytocompatibility including cell proliferation and viability assay. Both cells were cultured for 2 weeks. Alamar blue assay was performed to observe cell proliferation. It was conducted at different time points for a period of 14 days (**Figure 4.6A**).

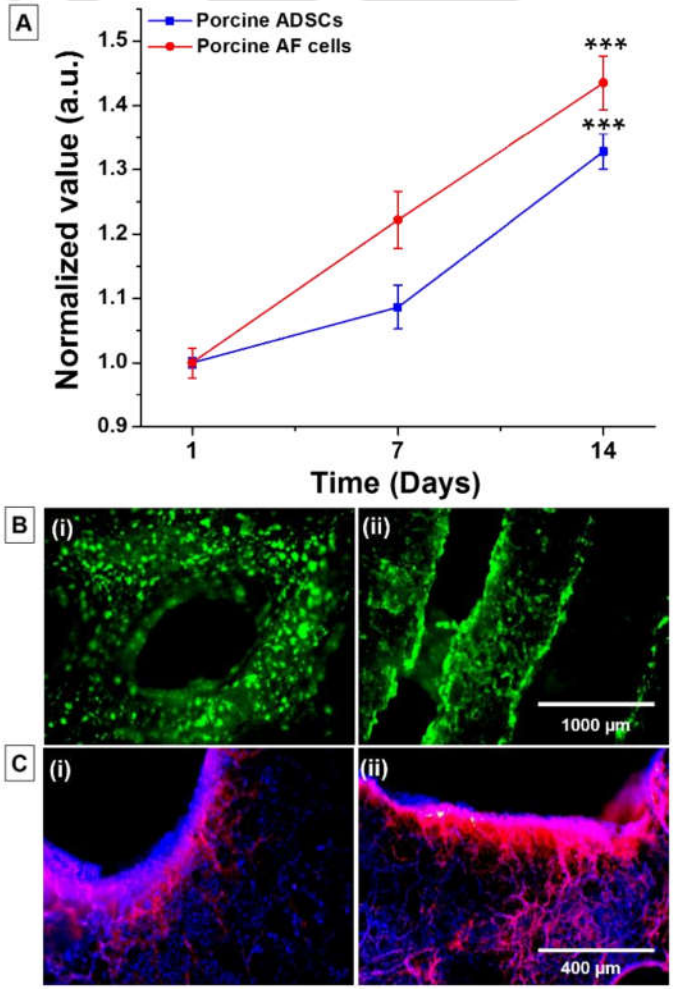

Figure 4.6. *Cell proliferation study on the 3D printed construct seeded with both porcine AF cells and ADSCs; (A) Alamar blue reduction assay for cell proliferation, (B) green fluorescent dots showing the live (i) AF cells and (ii) ADSCs on the construct, and (C) nucleus staining with Hoechst 33342 showing the cellular arrangement of (i) AF cells and (ii) ADSCs. Data represent mean ± SD (n = 3), where ***$p \leq 0.001$ with respect to day 1.*

Cell metabolism is indicated by the reduction of Alamar blue dye, which in turn correlates to the number of cells. For this assay, equal number of both AF and ADSC cells were seeded into the separate constructs. On the basis of Alamar blue reduction assay, an increase of cell proliferation was observed for both cell types. AF cells proliferated with the increased index of ~ 1.22- and ~ 1.43-fold at day 7 and 14, respectively, when compared with the initial seeding on day 1 ($p \leq 0.001$). Relatively, a slower proliferation rate was observed for ADSCs. ~ 1.08- and ~ 1.32-fold increase in proliferation index at day 7 and 14, respectively, were observed for ADSCs (**Figure 4.6A**). The fluorescent image analysis showed the attached live cells on the constructs and cells were evenly distributed along the 3D printed filaments after 14 days of culture in both cases (**Figure 4.6, B - C**).

4.3.4.2. Histological analysis

Histological analysis was performed using H&E staining and immunohistochemistry to assess the cellular distribution and AF specific ECM deposition. For this analysis, the 3D printed constructs post 14 days of culture were sectioned and stained with H&E. The H&E staining showed the cellular growth into the grooves of the cross-aligned printed filaments forming tissue for both cases (**Figure 4.7A, i-ii and 4.7B, i-ii**). Moreover, the cells were also shown to be infiltrated inside the pores of printed filaments over the time (4 weeks) (**Figure A4.1**). The intense blue color of alcian blue staining confirmed the deposition of sufficient amount of sulfated glycosaminoglycan (GAGs) by both the AF cells and differentiated ADSCs (**Figure 4.7A, iii-iv and 4.7B, iii-iv**). The deposition of collagen in the construct by both types of cells was confirmed after staining with picrosirius red (**Figure 4.7A, v-vi and 4.7B, v-vi)**. The intense red color validated the presence of collagen in the constructs. Further, the deposition of collagen type I was confirmed by immunofluorescence study (**Figure 4.7A, vii-viii and 4.7B, vii-viii)**.

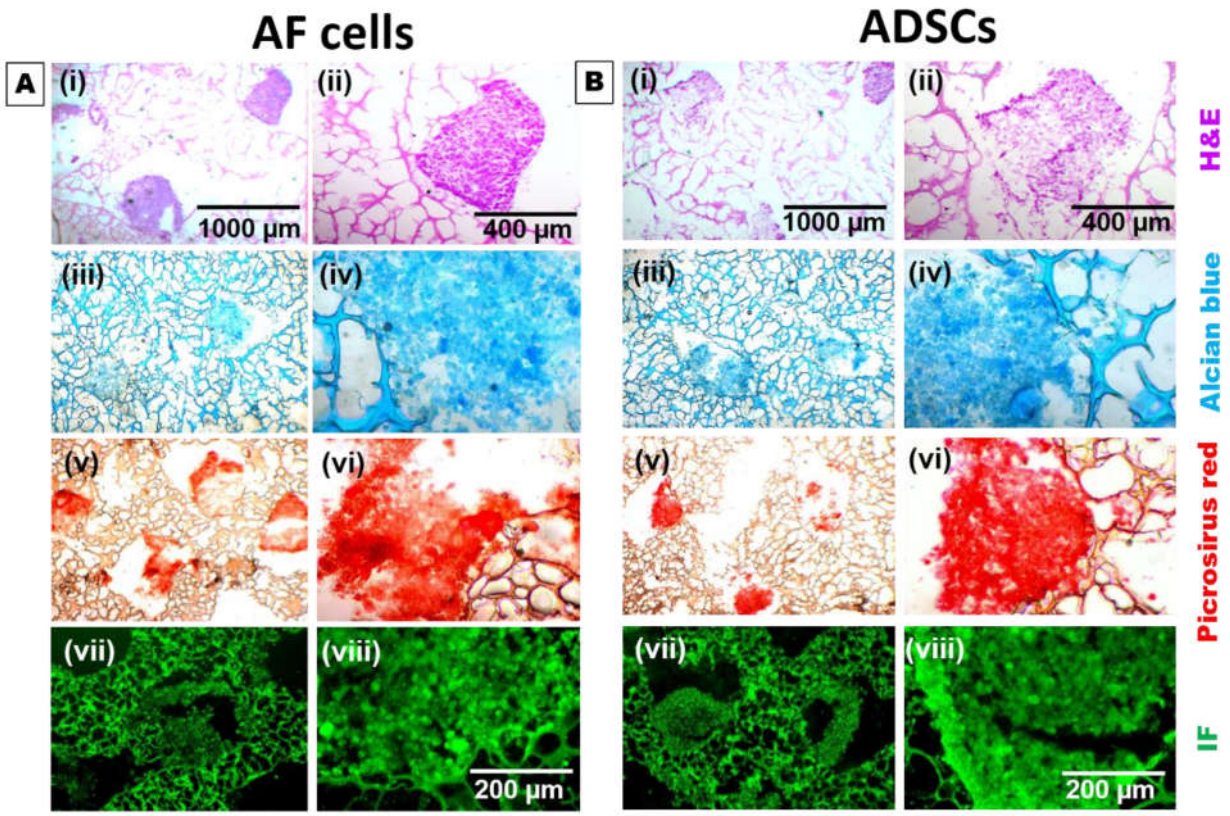

Figure 4.7. *Histological analysis of 3D printed constructs seeded with (A) AF cells and (B) ADSCs; (i) H&E staining, (iii) alcian blue staining for deposited GAGs, (v) picrosirius red staining for collagen and (vii) immunofluorescence (IF) of collagen type I. Figures of ii, iv, vi, and viii are the magnified images of i, iii, v, and vii, respectively.*

4.3.4.3. Biochemical analysis

Staining based qualitative estimation of deposited ECM was further validated by the quantitative biochemical assays. The cells seeded 3D printed constructs maintained for 14 days in chondrogenic medium were used to estimate the total collagen content, one of the predominant components of the deposited ECM. Collagen deposition increased with time for both cases (**Figure 4.8A**). The total collagen content in the AF cells seeded 3D printed constructs increased from 22.11 ± 0.84 µg.mg^{-1} of construct on day 1 to 87.11 ± 4.08 µg.mg^{-1} of construct on day 14 ($p \leq 0.001$) (~ 67% of native porcine AF tissue). Similarly, the value increased to 116.18 ± 9.08 µg.mg^{-1} of construct (the value was close to the native porcine AF) on day 14 for ADSCs when compared with the initial seeding day (17.18 ± 1.08 µg.mg^{-1} of construct) ($p \leq 0.001$). However, the deposition was relatively higher in the constructs seeded with ADSCs compared to AF cells

($p \leq 0.05$). On the other hand, the AF cell seeded scaffolds showed slightly higher presence of sGAG (~ 48.79%) as compared to ADSCs seeded scaffolds (~ 34.84%). Also, blank scaffolds retained minimal stained area (~ 0.02%) as evident from the deconvoluted images (**Figure A4.1**).

4.3.4.4. Real time PCR analysis

The qualitative (histological analysis) and quantitative (biochemical assessments) studies were further supported by real time PCR of three AF specific marker gene; col *I*α1, aggrecan (ACAN) and sox9 (**Figure 4.8, B-C**).

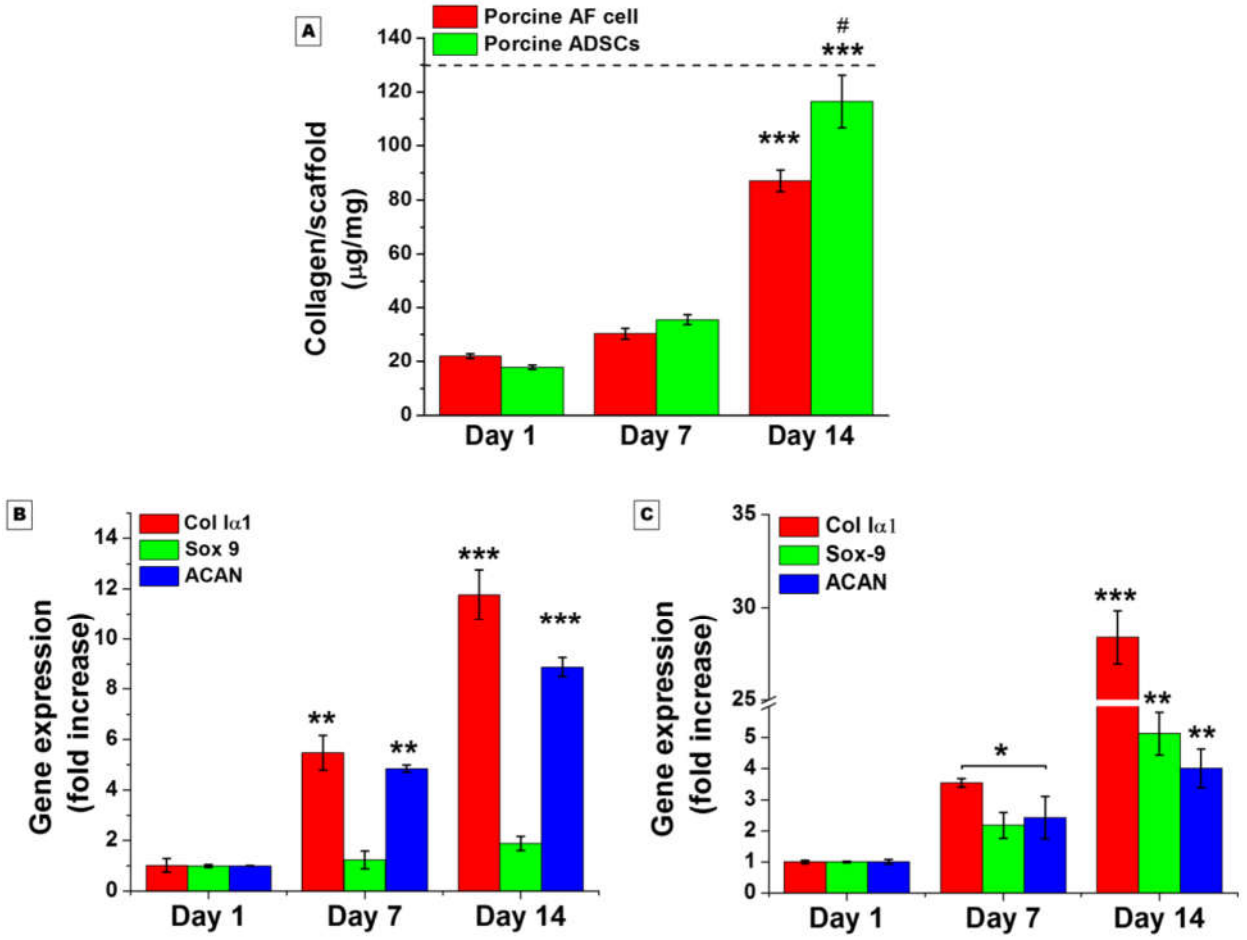

Figure 4.8. *Biochemical estimation, (A) Total collagen content deposited in the 3D printed construct by both porcine AF cells and ADSCs over a period of 14 days, Gene expression study for (B) AF cells and (C) ADSCs in time points of days 1, 7, and 14 cultured in chondrogenic media. The dashed line indicates the native porcine AF benchmark (as shown in Figure 2.5A). Data*

*represent mean ± SD (n = 3), where ***p≤0.001 **p≤0.01 and *p≤0.05 for all genes with respect to day 1 and #p≤0.05 with respect to AF cells on day 14.*

The level of mRNA expression for these three genes increased with time in both cases. For porcine AF cells, the maximum expression was observed for *col Iα1* and the value was ~ 5.4- and ~ 11.77-fold on day 7 and 14, respectively, compared with day 1 ($p \leq 0.001$). Similarly, *ACAN* gene expression increased to ~ 4.8- and ~ 8.8-fold on day 7 and 14 ($p \leq 0.001$), respectively, whereas relatively lower expression was observed for sox9 gene (~ 1.8-fold on day 14) (**Figure 4.8B**). Similar to AF cells, ADSCs showed the maximum upregulation of col *Iα*1 expression (~ 28.39 folds) on day 14 when compared with day 1($p \leq 0.001$). The level of expression for both ACAN and sox9 gene increased with time for ADSCs. The expression of ACAN gene increased to ~ 2.42- and ~ 4-fold on day 7 and 14, respectively, whereas ~ 2.17- and ~ 5.12-fold increase were observed on day 7 and 14, respectively, for sox9 gene when compared with day 1 (**Figure 4.8C**).

4.3.4.5. *In vitro* inflammatory response study

Immunocompatibility was analyzed by sensitizing the macrophages (RAW 264.7) with biomaterial ink and its components. The released IL-1*β* and TNF-*α* were quantified using the respective ELISA kits (**Figure 4.9A, i-ii**). LPS (positive control) induced the maximum release of IL-1*β* (864.44 ± 26.73 pg.mL^{-1}) which was approximately 4 folds higher than the amount (in the range of 200–270 pg.mL^{-1}) induced by biomaterial ink (BI) or associated components like BM SF (BM), carrageenan (CA) and TCP substrate ($p \leq 0.01$). A similar trend in the release of TNF-*α* was also observed. However, there was no significant difference among BM, BI and CA, and TCP which was treated as negative control.

4.3.4.6. *In vivo* response study

In vivo response study was mainly conducted by implanting the biomaterials or tissue engineered constructs into the animal model system to evaluate the biomaterial-tissue integration and immune response. For this purpose, biomaterial ink was subcutaneously injected into rats and retrieved at week 1 and 4 followed by H&E (**Figure 4.9, C-D**) and immunofluorescence staining for immune cells reactions (**Figure 4.9E**).

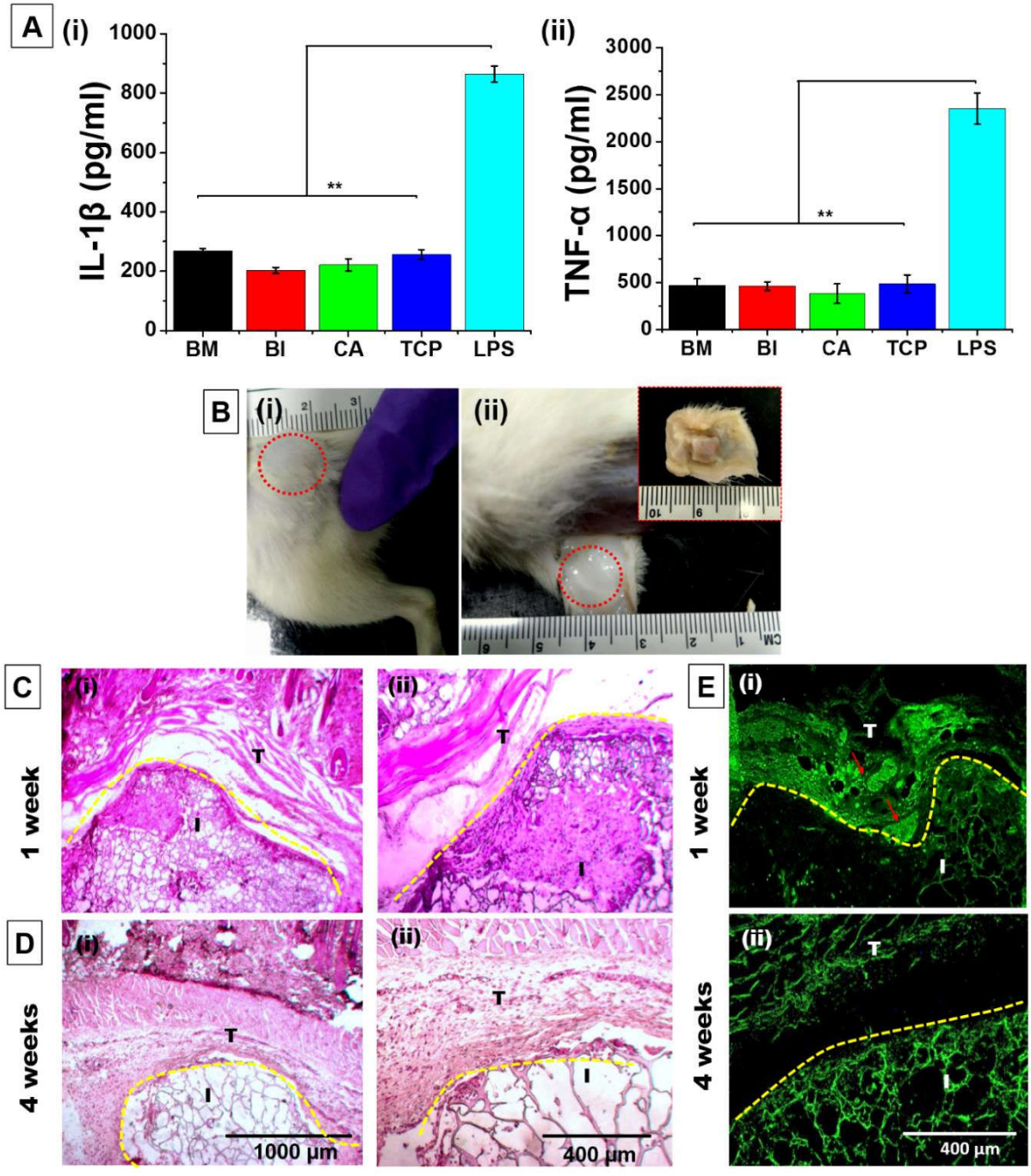

Figure 4.9. *Immunoresponse studies of biomaterial ink; (A) in vitro inflammatory study, (i) IL-1 β and (ii) TNF-α. (B-E) in vivo immunoresponse study; (B, i-ii) subcutaneous injection of biomaterial ink, inset shows the retrieved biomaterial ink, H&E staining of the sections retrieved after (C) 1 week, and (D) 4 weeks. Figure C (ii) and D (ii) are the magnified images of figure C (i) and D (i) respectively, (E) immunofluorescence of macrophage marker CD68 after (i) 1 week*

*and (ii) 4 weeks. Red arrows represent the presence of CD68 positive macrophages. BM = B. mori silk fibroin, BI = biomaterial ink, CA = carrageenan, TCP = tissue culture plate, LPS = lipopolysaccharide, I = implantation and T = tissue fraction. Data represent mean ± SD (n = 3), where **p≤0.01 with respect to LPS.*

Post 1 week of implantation, the retrieved biomaterial ink was investigated for macrophage infiltration. High macrophage infiltration was evident by immunofluorescence for CD68, a pan macrophage marker (**Figure 4.9, E-i**). Following 4 weeks, the retrieved biomaterial ink showed negligible macrophage count inside or surrounding the biomaterial ink area (**Figure 4.9, E-ii**). However, tissue-biomaterial ink integration was also visualized over 4 weeks of implantation.

4.4. Discussion

The internal architecture of annulus fibrosus (AF) tissue consists of collagen nanofibers oriented at the angle of approximately ± 30° (in alternate direction of each successive layer) against the vertical plane of spine making it a cross-aligned angle-ply construct[15]. Once damaged, it is difficult to repair due to its avascular nature and low cellularity. The cross-aligned organization of AF tissue is crucial for the biomechanical functions of the vertebral discs. In this study, we fabricated a bio-artificial disc mimicking this complex hierarchical architecture adopting 3D printing technology. In our previous studies, a manual directional freezing technique was adopted to recapitulate such complex constructs. 3D printing offers advantages over this manual process in terms of precision and high throughput reproducibility of the micro-architecture. To print tissues or organs, 3D printing prerequisites three main components; a biologically inspired CAD model, a printable biomaterial ink and the printing strategy[256]. Non-invasive medical imaging technologies *i.e.,* computer tomography (CT) and magnetic resonance imaging (MRI) can be used to generate the CAD model by collecting and digitalizing the complex tomographic information of the heterogeneous tissues. The CAD models of different tissues or organs have been made available by researchers in open source repositories and can be reproduced by software using the data available in the literature. In the current study, we designed a CAD model using software (AutoCAD, AutoDesk) that mimics the AF anatomy in details. After successful design, the model was segmented in slic3r software to generate G-codes from STL files that are finally fed to the 3D printer. The printer then deposited biomaterial ink in a layer-by-layer fashion as per instructions given in the G-code file. To print the tissue or organ, a biomaterial ink should be composed of biocompatible polymers with suitable viscoelasticity that provides shear-thinning while printing as well as self-standing property post printing.

In this study, we developed silk-carrageenan based biomaterial ink to print the AF tissue constructs. *B. mori* silk fibroin (BM SF) is a fibrous protein which not only has excellent mechanical properties but is also biodegradable, biocompatible and non-immunogenic. SF is being used as biomaterial in tissue engineering and regenerative medicine for decades[427, 463]. On the other hand, carrageenan is a type of sulphated galactan extracted from certain species of red seaweed and has been used in food industry for long time. Carrageenan, being used as an anionic polysaccharide, is composed of repeating units of D-galactose residues that are alternately linked to 3-linked-β-D-galactopyranose and 4-linked-α-D-galactopyranose units[464]. Recently,

carrageenan has been used in isolation (stabilized by Ca^{2+} ions and methyl acrylation) or in combination with other polymers *e.g.,* chitosan, alginate, gelatin and silk, for different tissue engineering applications like bone, cartilage and skin tissue engineering[450, 451, 465-469]. However, being a biocompatible viscous gel like polymer, carrageenan is also considered as a potential component of biomaterial ink in 3D printing technology[453, 470]. In our study, carrageenan was blended with silk fibroin to formulate the biomaterial ink. The biomaterial ink possesses suitable rheological properties for extrusion-based printing as depicted by rheological testing (**Figure 4.1**). The developed biomaterial ink exhibited viscoelasticity and recoverability after stress induced damages as validated by amplitude, frequency sweep and thixotropic analysis, respectively. In temperature sweep test, both the storage modulus (G') and complex viscosity were shown to decrease with the increase of temperature. Gel-like property of the biomaterial ink was maintained up to 45 °C and thereafter it transformed into fluidic viscous solution losing the G'. Carrageenan being a thermo-reversible polymer was mainly responsible for this sol-gel transition of biomaterial ink in response to temperature changes[471]. This sol-gel transition was mainly because of the conformational changes from single chain to double helix and further higher level of association among them[471].

After a successful development of biomaterial ink, it was fed to a printer. Recently, a variety of 3D printing strategies *e.g.,* inkjet, laser, micro-extrusion, acoustic droplet ejection and microwave based printing have been developed for specific applications with each having their own advantages and disadvantages[256]. Here, we utilized micro-extrusion based 3D printing strategy to recreate the AF construct. The 3D printer could successfully print the AF construct as instructed in the CAD model (**Figure 4.2 and 4.3**). The printed filaments were aligned in a criss-cross fashion within the construct, but in layer-by-layer on the top of others creating a structure with horizontal organization of fibers. However, the collagen fibers in the native AF tissue are aligned vertically to the spine axis. Printing of such complex organization wherein the fine fibers are aligned vertically with an angle of ~ ± 30° using the developed silk-carrageenan biomaterial ink and micro-extrusion based strategy was a challenging task. So, to mimic such organization of fibers, the printed construct was flipped by 90° inwards or outwards across the periphery that finally recreated the native AF architecture (**Figure 4.4**).

After fabrication, the 3D printed constructs were subjected to a series of physicochemical characterization including morphology analysis through FESEM and fluorescence imaging,

crystallinity analysis through FTIR, and the structural stability through degradation profile and the swelling behavior (**Figure 4.5**). Fluorescence and FESEM studies revealed the cross-aligned structure of printed constructs. The printed constructs consist of uniform distribution of rhombus shaped pores with average pore size of ~ 740 µm and the average biomaterial ink filament width was ~ 500 µm. The constructs portrayed interconnected macro- as well micro- pores. The macro-pores (~ 740 µm) were generated based on the distance between the printed filaments, while the micro-pores (~ 20 – 200 µm) were produced after freeze-drying process. The conformational change (from silk I to silk II) in the silk part of the biomaterial ink after ethanol treatment of the constructs was confirmed after FTIR analysis. The FTIR spectra showed the shifting of signature peaks of amide I, II and III from 1650, 1542 and 1240 cm^{-1} to 1620, 1512 and 1223 cm^{-1}, respectively indicating β-sheet induction in the constructs as previously reported [390]. The signature peaks (1070, 930 and 845 cm^{-1}) confirmed the presence of carrageenan in the biomaterial ink[462].

The nutrient exchange rate through a construct designed for tissue engineering purposes can directly be correlated with its water retention ability or swelling ratio. The fabricated 3D printed constructs showed good swelling ratio (~ 8.4 times) suitable for tissue engineering applications. Swelling of the constructs might be attributed to the fact that carrageenan is capable of binding with water molecules via both ionic and hydrogen bonding[472]. However, scaffolds made of silk fibroin are also known to have the good swelling properties[473].

The scaffolds should not only have the ability to restore the functionality of the tissues but should also degrade with time to allow the regeneration through neo-tissue formation, which will fill up the gaps. For this purpose, the 3D printed constructs were subjected to enzyme treatment mimicking the physiological conditions. The constructs showed a good rate of degradation with time when compared with the constructs kept in only PBS without any enzyme (the control system) and ~ 70% of the mass of constructs degraded over a 28 days of enzyme treatment indicating its biodegradability potential for tissue engineering applications.

Although the AF tissue of vertebral disc experiences various kinds of mechanical forces e.g., compression, tensile and torsion during our daily activities, only the unconfined compressive properties were recorded for this 3D printed constructs. In an unconfined compressive test, the constructs experienced both the axial and radial stresses. The constructs became thinner and bulged in outward direction when the compressive load was applied axially. In this study, three sets of

constructs were considered for compressive testing; set I consisted of 3D printed AF anatomical constructs devoid of central NP tissue, set II consisted of 2% (w/v) BM SF hydrogel representing the NP tissue and set III represented the whole IVD wherein both the 3D printed AF constructs and hydrogel in center as NP tissue substitute were integrated. The obtained compressive modulus from set I was ~ 65 kPa, whereas the value increased to ~ 78 kPa for set III indicating the importance of integration of both AF and NP tissue for a better mechanical response as compared to the native disc. To understand the impact of fiber direction on compressive strength, the 3D printed constructs were investigated for compressive modulus in both directions of the printed filaments; the horizontal plane wherein the printed filaments were deposited layer-by-layer on top of other, and the vertical plane when the constructs placed perpendicular to the printed filaments mimicking the actual fiber direction in the native disc. Relatively higher compressive modulus was recorded for the vertical plane indicating the importance role of fiber direction in compressive strength[420]. Moreover, the cyclic compressive testing revealed the mechanical stability of the 3D printed constructs up to 50 cycles without losing the structural integrity. Although, the compressive modulus of the 3D printed acellular constructs was much higher than the native porcine AF tissue, the value was not sufficient to reach the native human disc (~ 380 kPa)[386]. Thus, at this stage, a suitable composition of biomaterials would be required to develop the biomaterial ink that would provide the mechanical strength of the final 3D printed constructs close to the human native disc. However, the tunable mechanical properties could easily be achieved by modulating the filament density in the printed construct providing the advantage over the conventional method. Moreover, other mechanical properties like torsion and tensile testing need evaluation for supporting the mechanical functionalities towards implantation.

Cytocompatibility assessment is one of the necessary steps towards the clinical translation of a biomaterial to be used for tissue engineering applications. The developed biomaterial ink was made of silk fibroin and carrageenan; both are well investigated cytocompatible biomaterials (**Figure 4.6**). Silk based scaffolds are being used in different tissue engineering and regenerative medicine applications including AF tissue engineering for decades[441]. For cytocompatibility study of the fabricated 3D printed constructs, two types of cells were considered; primary porcine AF cells and adipose derived stem cells (ADSCs). The potential of AF cells in the field of AF tissue engineering is well explored as it is the inherent cell populace of AF tissue[239]. The potential of ADSCs has also been investigated for disc regeneration as an alternative cell source

to avoid donor related issues regarding primary cell[474-477]. The ADSCs could be used in either undifferentiated stage or AF differentiated lineage. However, there are many uncertainties in fate of undifferentiated ADSCs in physiological conditions due to the local stimulus, whereas the differentiated ADSCs are stable at AF lineage when maintained in chondrogenic medium *in vitro*. In this study, both primary porcine AF cells and ADSCs were seeded on the 3D printed constructs and maintained for two weeks. Both cells were found to proliferate throughout the experimental timeline. The cell viability and arrangement of cells on the constructs were further confirmed after calcein AM and Hoechst 33342 staining, respectively.

A successful tissue engineered construct supports both the cell proliferation and deposition of sufficient ECM forming a matured functional tissue-like construct. The histological analysis revealed the cellular proliferation, distribution and deposition of AF specific ECM components on the fabricated 3D printed constructs when maintained in chondrogenic medium over 2 weeks. The infiltration of cells inside the printed filaments from the grooves is also an important aspect to compensate the proper biomechanics of the 3D printed cross-aligned construct over the time. Cells were shown to be aligned across the filaments and eventually migrated from the grooves infiltrating the pores of printed filaments after 28 days of culture. Cellular morphology considerably varied during culture for 4 weeks. Cells were round when maintained for 2 weeks and eventually become spindle shape in long term culture (**Figure 4.7 and Figure A4.1**). The image based analysis of alcian blue staining confirmed the deposition of sGAG in both AF cells and ADSCs seeded constructs when compared to the control (**Figure 4.7 and Figure A4.2**), which was further confirmed by gene expression study. On the other hand, collagen deposition was confirmed by picrosirius stain of the histological sections. However, the deposition of type I collagen was further confirmed by immunofluorescence staining. The major ECM component of AF is collagen type I which consists of ~ 80% of total collagen content. The biochemical estimation revealed an increasing order of collagen deposition on the 3D printed constructs with time for both types of cells (primary AF and ADSCs). The biochemical estimation of the deposited collagen was further validated by the gene expression studies where an increasing order of col *Iα*1 gene expression was also noted for both cell types (**Figure 4.8**). However, relatively higher expression of sox9 gene was observed for ADSCs. A possible reason behind the elevated level of sox9 might be the use of chondrogenic medium that consists of dexamethasone, TGF-*β* and ITS+ (insulin, transferrin, and selenious acid). Previously it was reported that TGF-*β* induced new ECM

synthesis in both old and degenerated discs[395]. TGF-β binds to TGF-β RII and TGF-β RI (receptors for TGF-β) to form a heterodimeric complex that activates the smad/co-smad pathway, a transcriptional activator that regulates downstream chondrogenic responsive genes like sox9[478].

A suitable biomaterial used for implantation should not provoke the immunoresponse which leads to graft rejection. The developed biomaterial ink was composed of *B. mori* silk fibroin and carrageenan. The silk fibroin isolated from *B. mori* cocoons has already been approved by FDA (Food and Drug Administration, U.S.A.) for medical purposes, and several reports have reported the immunosuppressive properties of carrageenan [479]. In this study, the biomaterial ink (BI) along with carrageenan (CA) and silk fibroin scaffold (BM) showed negligible immunoresponse evidenced by very low detection of IL-1β and TNF-α in ELISA when compared to LPS (as positive control). While the *in vitro* inflammatory response studies provide the information about the cellular immunogenicity when macrophages interact with materials, whereas the *in vivo* experiments helps to understand the overall tissue responses (**Figure 4.9**). Any material foreign to the body provokes immunoresponse eliciting proinflammatory cytokines, the condition is known as foreign body response (FBR). To understand the overall tissue responses, the biomaterial ink was injected subcutaneously in rats and retrieved after 1 and 4 weeks followed by examination of macrophage infiltration. The tissue sections retrieved after 1 week showed several macrophages (confirmed by immunofluorescence staining of pan macrophage marker CD68) surrounding the injected area, while very negligible number of macrophages could be seen in tissue sections retrieved after 4 weeks. This indicates that the 3D printed constructs made of this biomaterial ink would not provoke any serious immunoresponse that might lead to graft rejection.

In this study, we fabricated the 3D printed disc-like angle-grid constructs using silk-carrageenan based biomaterial ink. After printing the constructs were twisted by 90° across the periphery recapitulating the native AF architecture. Although the constructs mimicked the internal intricacy of AF anatomy, it is very important to address that higher precision in thickness of printed filaments could be achieved using the advanced printing technologies and other suitable biomaterial inks. In this study, the elastic nature of the silk-carrageenan biomaterial ink was rendered to the 3D printed constructs, owing to which after flipping 90° the construct intended to recoil back. Though the elastic nature is desirable here for the AF tissue, in the current predicament it could be a limitation for surgical implantation. Hence, the printed constructs should not be too

rigid to twist or too elastic to return to its original shape after twisting. On an application stand-point, we hypothesize that when surgically implanted between intervertebral endplates and the sutured into their positions, it would restrict the subsequent recoil, giving support for the implanted acellular construct. The current work is a proof-of-concept endeavor depicting our newly developed biomaterial ink and its potency to print and materialize intricate structures by micro-extrusion printing. Moreover, the biomechanics of the printed constructs are also a matter of concern for clinical translation of the technology. Hence, the bi-phasic constructs of 3D printed AF structure integrated with gelatinous NP would be a preferable approach ensuring better biomechanics in physiological systems. However, the developed 3D printed constructs could be used in acellular or cellular form through bio-printing. It can be expected that the native cells will infiltrate and align across the printed filaments upon implantation of the acellular constructs providing a native-like platform to the cells. The printed constructs were supported by both types of cells (primary porcine AF cells and ADSC cells) in terms of cytocompatibility and tissue maturation. The printed constructs can also be matured in a bioreactor system for better ECM deposition. Although there are several complications in clinical translation, the present strategy is poised to provide a new direction in the fabrication of anatomical AF structures.

4.5. Significant findings

The significant findings from this chapter are as follows:

- 3D printed AF anatomical equivalent was fabricated using a silk-carrageenan based biomaterial ink. The developed biomaterial ink was investigated for rheological properties and also assessed for its printability using an extrusion based 3D printer.
- A CAD model for AF anatomy was designed, segmented by slicer and fed to a 3D printer that finally deposited the developed biomaterial ink in a layer-by-layer fashion as per the instruction given in G-code files.
- The printed constructs wherein the filaments were cross-aligned horizontally turned into vertical alignment mimicking the native disc architecture when twisted by 90º across the periphery.
- The compressive modulus of our fabricated constructs was higher than the native porcine AF tissue showing its potential in load bearing applications.
- The printed constructs supported proliferation of both primary AF cells and ADSCs of porcine origin and deposition of sufficient amount of ECM components forming mature tissue constructs.
- The biomaterial ink was shown to be non-immunogenic when injected subcutaneously in rat model for the *in vivo* assessment.

Overall, the strategy adopted here to print the AF mimicking constructs may provide a new direction towards disc replacement therapy.

Chapter 5

Development of an *In Situ* Formulation of Silk Hydrogel for Nucleus Pulposus (NP) Tissue Engineering

Unlike last three chapters (2, 3 and 4) which focus on recapitulating "form and function" of AF tissue, this chapter describes the formulation of biologically active in situ forming hydrogels with desirable characteristics suitable for the successful applications in central gelatinous nucleus pulposus (NP) tissue engineering to address disc degeneration. Optimization of cross-linker free gelation, physicochemical characterization and ex vivo bio-functional assessments have also been explored.

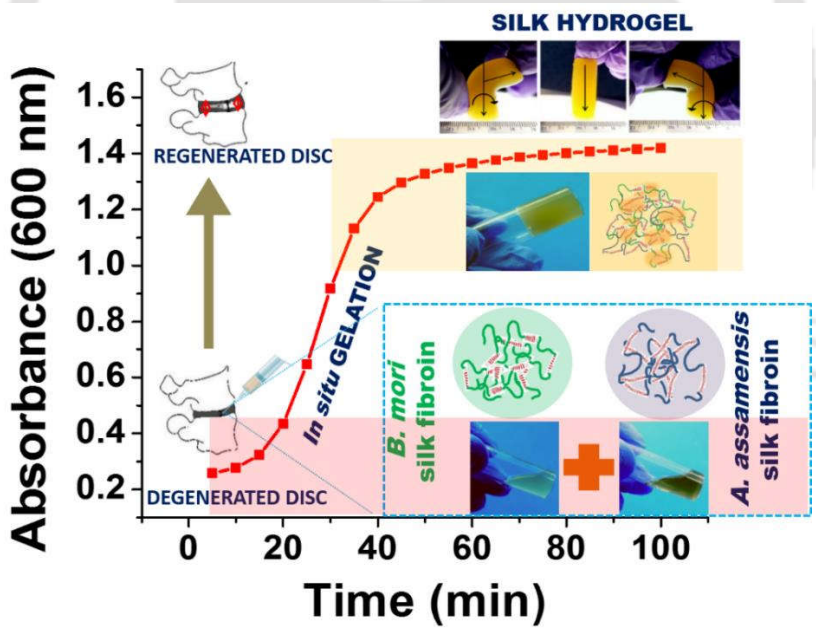

The work embodied in this chapter in published in a peer-reviewed journal as follows:

Bhunia BK, Mandal BB. Exploring gelation and physicochemical behavior of in situ bioresponsive silk hydrogels for disc degeneration therapy. ACS **Biomaterials Science & Engineering.** 2019;5(2):870-886.

ABSTRACT

Hydrogels have received considerable attention in the field of tissue engineering owing to their unique structural and compositional resemblance to the highly hydrated human tissues. In addition, controlled fabrication processes benefit them with desirable physicochemical features for injectability in minimally invasive manner and cell survival within hydrogels. Formulation of biologically active hydrogels with desirable characteristics is one of the prerequisites for successful applications like nucleus pulposus (NP) tissue engineering to address disc degeneration. To achieve such a benchmark, in this study two naturally derived silk fibroin proteins (*Bombyx mori*, BM SF and *Antheraea assamensis*, AA SF) were blended together to allow self-assembly and transformation to hydrogels in absence of any cross-linker or external stimuli. A comprehensive study on sol-gel transition of fabricated hydrogels in physiological fluid microenvironment (pH, temperature and ionic strength) was conducted using optical and fluorescence analysis. Tunable gelation time (~ 8-40 min) was achieved depending on combinations. The developed hydrogels were validated by extensive physicochemical characterizations which include confirmation of secondary structure, surface morphology, swelling and degradation. Mechanical behavior of the hydrogels was further analyzed in various *in vitro*-physiological-like conditions with varying pH, ionic strength, diameter, storage time and strain values to determine their suitability in native physiological environments. Rheological study, cytocompatibility using primary porcine NP cells and *ex-vivo* biomechanics of hydrogels were explored to validate their *in situ* applicability in minimally invasive manner towards potential disc regeneration therapy.

5.1. Introduction

Hydrogels consist of three-dimensional networks of hydrophilic polymers that either crosslink covalently or physically interact (intra- and inter-molecular attraction) with each other[480]. It has the ability to absorb large quantity of water or biological fluid and swell up to several hundred times without dissolving the polymers. In swollen state, hydrogels become semi-solid and elastic, resembling to the living tissues or extracellular matrix surrounding them that attract attention of the tissue engineers[481, 482].

Over the past few years, *in situ* gelation systems have received considerable accolades in the field of tissue engineering and regenerative medicine[483, 484]. In *in situ* gelation systems, the polymers remain in fluid state prior to administration and transform to gel under normal physiological conditions that trigger polymer-polymer or polymer-solvent interactions. These physiological conditions influence the gelation rate and the final gel strength which are often critical to their functions[485]. There are several natural and synthetic polymers that are being utilized in the recent past for *in situ* applications in tissue engineering and drug delivery systems. For instance, pectin is a natural polymer (polysaccharide) that readily forms gel in presence of calcium ions in the stomach following oral administration[486, 487]. Partially degraded xyloglucan shows thermally reversible gelation behavior by lateral stacking of chains. It forms gel under physiological conditions presenting its potential applications in ocular, intraperitoneal, oral and rectal drug delivery[488-490].

Silk fibroin (SF) is a naturally derived protein polymer that is being used as a biomaterial in various biomedical applications[198, 491-494] due to its easy processability, biocompatibility, hemocompatibility, tunable biodegradability and mechanical properties, and minimal immunogenicity[191]. SF can be isolated from both mulberry (*i.e., Bombyx mori*) and non-mulberry (*e.g., Antheraea assamensis*, *Antheraea mylitta, Philosamia ricini* etc.,) sources[411]. Aqueous solution of SF undergoes self-assembly giving rise to the formation of β-sheets which results in hydrogel formation. Silk hydrogel can be fabricated following several methods that include use of chemicals *e.g.,* salts (Ca^{2+} and K^{+} ions), organic solvents (alcohol), surfactants (sodium dodecyl sulfate), large polymeric agents (poly-ethylene glycol), low pH and high pressure CO_2 or applying physical stimulus, *e.g.,* temperature, shear force, ultrasonication and electric filed[495-499]. In a very recent study, Yang *et al.*, reported the efficiency of sodium oleate to

induce rapid gelation in SF which might be compatible with *in situ* gelation applications[500]. Similarly, Bragg *et al.,* developed an *in situ* hydrogel platform using sonicated or genipin cross-linked SF and gelatin or heparin conjugated gelatin for sustained release of growth factors[501]. The gelation time of SF solution increases in absence of these non-physiological stimuli. External stimuli like sonication or vortexing reduce the gelation time but increase the chances of shearing and contamination *in vitro*. Furthermore, these techniques require sophisticated and expensive instruments which again increases the total cost of hydrogel fabrication. In the current study, we utilized the self-gelation capability of two different varieties of SFs, when blended, as a platform for disc regeneration therapy via *in situ* gelation.

Degenerative disc disease (DDD) is often related to low back pain (LBP). The central gelatinous NP contains ~ 90% of water and rest is a composite of protein and polysaccharide in the ratio of 1:2[32]. NP tissue is not only composed of extracellular matrix (ECM) components, but also contains around 4×10^6 NP cells.mL^{-1} which is quite low than the surrounding AF tissue (~ 9×10^6 cells.mL^{-1})[20]. These cells are rounded in morphology with larger cytoplasm and more complex structure compared to AF cells[38]. Though these cells have low mitotic and regeneration capability, they can survive under certain stress conditions like low pH, hypoxia and low glucose levels. In disc degeneration, a larger portion of NP cells undergo apoptosis and senescence that finally lead to the overall loss of NP matrix followed by decrease in water content[28, 502]. In a healthy disc, NP gel releases pressure and water molecules to the surrounding AF upon compression and water molecules in turn get back to the NP upon decompression, driven by osmotic force. This pump effect is very crucial to maintain the disc biomechanics (unconfined compressive modulus of 3–6 kPa)[49, 50]. However, this load transfer mechanism gets disrupted in disc degeneration as the water content of NP gel gradually decreases resulting in declined hydrostatic pressure[51].

Currently, attempts are being made worldwide by various research groups to develop injectable hydrogels using materials such as collagen, alginate, chitosan and hyaluronic acid (HA) as scaffolds for NP gel replacement because of their similarity to the native NP tissue[43, 303, 315, 348]. Most of them are used either alone (acellular) or in combination with cells or growth factors in order to gelate in the site of NP tissue *in situ*. For instance, Jalani *et al.,* developed an *in situ* thermogel made of chitosan and HA, cross-linked with genipin and β-glycerophophate that settled

for gelation within 32 min[503]. In a very recent strategy, decellularized NP tissue was being used as *in situ* gelling platform for NP tissue replacement. The decellularized NP tissue reached the gelation point within 45 min at physiological temperature in presence of fibrillar collagen which was very much similar to the native NP tissue[504]. However, these *in situ* hydrogel systems have certain limitations like high gelation time, interference of cross-linkers or synthetic counterparts that may pose some adverse effects and weak mechanical strength which fails to provide sufficient physical support to withstand load in real situation. Moreover, these hydrogel systems display relatively faster degradation rate that cannot be well matched to the slow secretion rate of NP extracellular matrix (ECM).

To address these relevant issues, the present study illustrates the rapid gelling property of aqueous solution of SF, formed via blending of two different varieties of silk (*i.e., Bombyx mori,* BM SF and *Antheraea assamensis,* AA SF). The hydropathicity of these two types of SF is different due to their amino acid composition, sequence and arrangement[505]. The protein chains in aqueous SF solution self-assembled and transformed into gel (due to alteration of the hydrophobic-hydrophilic microenvironment) in absence of any cross-linker or given external stimulus. The purpose of this study was to design a suitable combination of these two SFs for *in situ* applications in NP replacement. The gelation process was optimized under *in vitro* physiological microenvironment (*i.e.,* physiological temperature, pH and ionic strength), thereby implying a special emphasis on gelation mechanism on the basis of optical and fluorescence studies. The hydrogels so fabricated were extensively characterized in terms of mechanical behavior, rheological properties and *ex-vivo* bio-functional assessments conducted under *in vitro* physiological conditions. Furthermore, cytocompatibility study using primary porcine NP cells validated its *in situ* applicability in disc regeneration therapy.

5.2. Materials and methods

5.2.1. Preparation of aqueous solution of silk fibroin (SF)

Aqueous solution of SF from both *B. mori* (mulberry BM SF) and *A. assamensis* (non-mulberry AA SF) were isolated following previous studies[381, 411]. In brief, *B. mori* cocoons were chopped and degummed in 0.02 M sodium carbonate (Na_2CO_3) followed by dissolution in 9.3 M lithium bromide (LiBr) and subsequent dialysis to purify the protein. Contrarily, silk glands of *A. assamensis* were collected and dissolved in 1% (w/v) sodium dodecyl sulfate (SDS) followed by dialysis at 4 °C. The protein concentration from both the sources was measured gravimetrically and stored at 4 °C for future use.

5.2.2. Formation of hydrogels

SF isolated from both silk varieties *i.e., B. mori* (BM SF) and *A. assamensis* (AA SF) were blended in different ratios maintaining the final protein concentration at 3% (w/v), as summarized in **Table 5.1.** The blended protein solution was then incubated at different physicochemical conditions (*viz.,* temperature, protein concentration, molecular weight of protein and ionic strength) for gelation pattern analysis.

Table 5.1: Preparation of different ratios of SF blends

Sample code	BM SF (w/v)	AA SF (w/v)	Final protein concentration (w/v)
BM3.0	3.0	0	3
AA3.0	0	3.0	3
BM0.5/AA2.5	0.5	2.5	3
BM1.0/AA2.0	1.0	2.0	3
BM1.5/AA1.5	1.5	1.5	3
BM2.0/AA1.0	2.0	1.0	3
BM2.5/AA0.5	2.5	0.5	3

BM = *Bombyx mori,* AA = *Antheraea assamensis*

5.2.3. Spectroscopic studies on the silk blends

5.2.3.1. Gelation kinetics by visible light spectroscopy

To study the effect of different parameters on silk blends in hydrogel formation, turbidity change during gelation process was assessed by UV-Visible spectroscopic measurements. 200 µL silk blends were taken per well in a 96 well-plate (Tarsons, India) and absorbance at 600 nm were measured using a multiplate-reader equipped with temperature control (Tecan Infinite M200, Switzerland). The effect of temperature in gelation was monitored at 25 °C, 37 °C and 42 °C for a period of ~ 70 min at an interval of 3 min. BM3.0 and AA3.0 (without blending) were used as controls. The effect of protein concentration in gelation was studied by blending SF solutions in 1:1 ratio in an increasing order from 0.5 to 2.0% w/v for the gelation pattern analysis, while keeping one type of SF protein constant (2%, w/v) and by increasing the other SF protein concentration gradually (0.5 to 3.0%, w/v). The effect of ion concentration and pH was studied on 3.0% (w/v) SF blends (BM3.0:AA3.0, 1:1) at different ion Ca^{2+}, K^{+} concentrations (1-4 mM, adjusted by 1 M aqueous stock of KCl and $CaCl_2$); at different pH (7.4 and 9.0, adjusted by 1 N HCl/NaOH). The effect of ion chelators (1-20 mM Ethylenediaminetetraacetic acid, EDTA; Sigma, U.S.A.) in reversing the effect of ion addition during gelation was studied in 4 mM $CaCl_2$ containing 3.0% (w/v) SF blends (BM3.0:AA3.0, 1:1), wherein blends without Ca^{2+}/EDTA and blends with only Ca^{2+} (4 mM) were used as positive (+*ve*) and negative (-*ve*) control, respectively.

The effect of molecular weight of BM in gelation was studied by obtaining different molecular sized BM obtained by altering the degumming time, as described previously[506]. Results obtained from turbidity, fluorescence and dynamic light scattering (DLS) analysis inferred that BM SF degummed at time points 5, 30 and 60 min were found to be as high molecular weight BM (hMWBM), medium molecular weight BM (mMWBM) and small molecular weight protein (sMWBM), respectively[506]. 3% (w/v) AA SF was blended with 3% (w/v) BM SF of different molecular weights in the ratio of 1:1 and absorbance at 600 nm was recorded (37 °C). 3.0% (w/v) each of hMWBM, mMWBM and sMWBM, and 3% (w/v) AA SF (AA3.0) were used as control. To confirm the hydrophobic interaction between two types of protein, BM SF was replaced by bovine serum albumin (BSA; Sigma, U.S.A.) in the blends. 3% (w/v) BSA was blended with 3% (w/v) AA SF in the ratio of 1:1 and absorbance at 600 nm was recorded at 37 °C. BM1.5/AA1.5

blended protein was used as positive control, whereas BSA3.0 (*i.e.,* 3% w/v BSA), AA3.0 and BM3.0 were used as negative controls.

5.2.3.2. Intrinsic fluorescence spectra of sol-gel transition

The conformational transformation in blended SF solution during the sol–gel transition was found out spectrofluorometrically (FluoroMax-4, Horiba) at 37 °C at excitation/emission wavelengths of 280/600 nm. The intrinsic tryptophan (*Trp*) residues of SF were used as probe in fluorescence measurement. Scan speed was set at 1200 nm.min^{-1} with an excitation/emission slit of 5 nm. Fluorescence emission spectra were collected at a resolution of 1 nm. The emission spectra were recorded at every 5 min up to 30 min for each sample. The maximum peak at 340 nm was normalized to compare gelation pattern among different blends. The full width half maxima (FWHM) at 340 nm of a blended SF was plotted to understand the change in fluorescence intensity per unit of time interval.

5.2.4. Physicochemical characterization of hydrogels

5.2.4.1. Field emission scanning electron microscopy (FESEM) and energy-dispersive X-ray spectroscopy (EDX)

Surface morphology of the lyophilized hydrogels was studied using FESEM (Zeiss Sigma, Carl Zeiss AG, Germany) at an operating voltage of 2 kV. Hydrogels were frozen rapidly in liquid nitrogen (-196 °C) and samples were freeze fractured for observation. The freeze fractured hydrogels were lyophilized followed by gold (Au) coating and images were captured under vacuum dried condition. Average pore size of each hydrogel was determined using ImageJ 1.4 (Wayne Rasband) software by measuring ~ 50 pores, randomly. EDX analysis of hydrogels was conducted to measure the presence of any toxic elements *e.g.,* Li/Br during silk fibroin isolation.

5.2.4.2. Fourier transform infrared spectroscopy (FTIR)

The secondary structure of the hydrogels was analyzed using FTIR (Nicolet iS 10, Thermo Scientific, U.S.A.). Briefly, the hydrogel samples were lyophilized followed by making of KBr disks in the ratio of 9:1 (KBr to sample). All absorbance spectra were recorded within the spectral range of 4000-400 cm^{-1} with a resolution of 4 cm^{-1} and 32 scans. Lyophilized powder of AA3.0 and BM3.0 were used as control. Amide I region (1600 – 1700 cm^{-1}) was examined to identify the secondary structures in the hydrogels by performing a second order derivitization of the spectra

using OriginPro 8.5 software and finally the Lorentzian curve-fitting method was applied to the deconvoluted spectra. The absorbance bands in the range of 1650-1658 cm^{-1}, 1620-1640 cm^{-1}, 1660-1680 cm^{-1} and 1670-1695 cm^{-1} were attributed as α-helix, β-sheets, loops, and anti-parallel β-sheets, respectively[507].

5.2.4.3. Wide angle x-ray diffraction (WAXD)

The X-ray diffractogram of different sets of hydrogels were recorded with a Bruker D2 Phaser diffractometer (U.S.A). Ni filtered CuKα was used as the X-ray source to investigate the changes in crystallinity upon gelation. The diffraction range (2θ) was set between 10°-60° with a scan speed of 0.5° min^{-1}. Powder forms of AA3.0 and BM3.0 were used as control.

5.2.4.4. Swelling study

Swelling behavior of hydrogels was carried out by immersing them into distilled water. Briefly, dry weight of the lyophilized hydrogels was measured as (Wd) using an electronic balance (Sartorius, BSA224S-CW) followed by aqueous immersion at room temperature (25 °C) for 24 h. At definite time intervals, the swollen hydrogels soaked with water were carefully taken out and the wet weight (Ws) was recorded. The excess water surrounding the constructs was gently wicked out using tissue paper. The swelling ratio was expressed via the following equation[390]

$$Swelling\ ratio = \frac{Ws - Wd}{Wd}$$

5.2.4.5. *In vitro* enzymatic degradation

In vitro enzymatic degradation was performed to determine the stability of hydrogels in physiological conditions. For this purpose, protease *XIV* from *Streptomyces griseus* (Sigma, U.S.A.) with an activity of 3.5 $U.mg^{-1}$ was used as described previously[390]. In brief, different sets of hydrogel were immersed in 3 ml of phosphate buffered saline (PBS, pH 7.4) containing 2 $U.mg^{-1}$ of enzyme at 37 °C to achieve the optimum enzyme activity. The enzyme solution was replaced with freshly prepared solution at every 3rd day. For control studies, hydrogels were also immersed in PBS (pH 7.4) without enzyme under similar experimental conditions. Hydrogels were taken out every 7th day, rinsed with distilled water, lyophilized, and dry weight was recorded to calculate the loss over a period of 28 days.

5.2.4.6. Mechanical behavior of hydrogels

Unconfined compressive strength of various sets of hydrogels in different physicochemical conditions (*e.g.,* various diameter of hydrogel, % of strain rate, time frame, pH and ionic strength) was determined using Instron 5944 (Norwood, MA, U.S.A.), equipped with a 100 N load cell. Hydrogels were cut into cylindrical shape (10 x 10 mm) and used for compressive test 1 h post gelation. All tests were accomplished with an unconfined configuration and a displacement control mode at a rate of 5 $mm.min^{-1}$. After the compression tests, the stress and strain curves were plotted based on the measured cross-sectional area and sample height. Compressive strain was applied up to 80% or until the construct got fractured. To mimic the native biomechanical condition of NP, compressive modulus of all hydrogels of two different diameters (12 mm and 20 mm) with same height (10 mm) was calculated for three different compressive strains *i.e.,* 10%, 20% and 30%. To determine the impact of storage time on mechanical properties, compressive modulus was also recorded after 1 h, 24 h and 14 day of gelation. All sets of hydrogels were incubated in PBS till the aforementioned time points (pH 7.4) at 37 °C before testing. To mimic different physiological conditions, hydrogels were immersed in three buffer systems having different pH (citrate buffer, pH 4.0; phosphate buffer, pH 7.4 and glycine-NaOH buffer, pH 9.0) and ionic strength (100, 500 and 1000 mM of NaCl) for 1 h prior to testing. To determine the recovery of mechanical properties, hydrogels were transferred from both pH 4.0 and pH 9.0 to pH 7.0 following 1 h of incubation in respective pH buffer systems.

A confined compressive modulus was also measured to mimic the confined NP tissue construct. A manually prepared cylindrical plunger was compressed upon the hydrogel samples using a strain rate of 5 $mm.min^{-1}$. The hydrogel was confined by a high-density polypropylene ring. The polypropylene ring was considered to be a harder body, as its modulus (approximately 10.0 GPa) is several orders of magnitude higher than that of hydrogels. Confined compressive modulus was recorded for each hydrogel at 10% compressive strain. Other sets of hydrogel were used for unconfined compressive testing as control.

For cyclic mechanical testing, hydrogels were compressed to axial strain of ~ 15% for 50 cycles at a loading and unloading rate of 5 $mm.min^{-1}$ in PBS solution (pH 7.4) at 37 °C. The axial strain of 15% was selected as it is close to the actual strain value corresponding to loading on the

complete intervertebral discs (IVD) in normal physiological conditions. The maximum compressive stress was calculated for each complete cycle.

5.2.4.7. Rheological properties of hydrogel

Dynamic oscillatory test for gelation point analysis, amplitude sweep for viscoelastic region (LVER) and frequency sweep for frequency dependent viscoelastic properties of hydrogels were performed on a Rheometer (MCR 302, Anton Paar) using a stainless steel parallel plate of 25 mm diameter and a gap distance of 0.5 mm. The normal force on the sample was set to 0.1 N during the entire experimental procedure. To determine the gelation point, blended silk solution of different ratios were placed in between two plates maintaining the temperature at 37 °C and data was collected at a low strain amplitude (γ = 1%, ω = 10 rad.s^{-1}) to prevent possible sample manipulation due to shear induced gelation in SF solution. A low viscosity mineral oil was applied surrounding the plates to minimize the evaporation rate. Complex viscosity (η^*) for each hydrogel system was plotted against time. A strain amplitude sweep (1% to 1000%) was performed to determine the LVR for each hydrogel system. The LVER of hydrogel was important for frequency sweep testing in which elastic modulus (G′) and viscous modulus (G″) were independent of strain amplitude. Frequency sweep for each hydrogel system was collected over a wide frequency range (γ = 1%, ω = 1–100 rad.s^{-1}). For thixotropic analysis, strain sweep was performed in the range of 1-1000%. Step strain was set at 1000% for 50 s followed by 1% strain for 200 s for three different sets of hydrogel systems (BM0.5/AA2.5, BM1.5/AA1.5 and BM2.5/AA0.5).

5.2.5. Biological studies on hydrogels

5.2.5.1. Isolation and culture of porcine NP cells

Nucleus pulposus (NP) cells were isolated from porcine intervertebral disc (IVD) procured from local abattoir within 1 h post processing. In brief, IVDs from lumber portion were preferred and adjacent muscle and tendons were discarded to separate the vertebral discs from the spine. The entire dissection procedure was performed under sterile condition. The central gelatinous NP was separated from the adjoining annulus fibrosus (AF) tissue. Thereafter, the isolated NP tissue was thoroughly washed with PBS (pH 7.4) followed by digestion in 0.03% (w/v) collagenase (Sigma, St. Louis, MO) in complete DMEM/F12 medium for 7-8 h. The digested slurry was then centrifuged at 235 g for 5 min followed by 1-2 times PBS washing to remove extra enzyme

fraction. The cell number and viability were determined by Trypan blue staining. NP cell pellets were resuspended and plated at a density of 2 x 10^5 cells.cm^{-3} and placed at 37 °C in an incubator with 5% CO_2 and 85% humidity. The culture medium [DMEM/F12 supplemented with 10% (v/v) Fetal bovine serum (FBS), 100 U.mL^{-1}penicillin G (Gibco, Life Technologies, U.S.A.), and 100 mg.ml^{-1} streptomycin (Gibco, Life Technologies, U.S.A.)] was changed every 3rd day. Cells were passaged up to P4 and stored at -196 °C for future use.

5.2.5.2. Cell seeding and proliferation assay

Cell proliferation was monitored using Alamar blue dye reduction assay (Invitrogen, Life Technologies, U.S.A.) at specified intervals of 1, 3 and 7 days. Equal number of NP cells (2 x 10^4 cells per hydrogel surface, 12 mm in diameter) was seeded on preconditioned hydrogels (complete DMEM/F12 for 24 h) in a 24 well plate. Three different sets of hydrogels (BM0.5/AA2.5, BM1.5/AA1.5 and BM2.5/AA0.5) were used for cell seeding purpose. Equal number of cells was encapsulated in the hydrogels. The cell seeded hydrogels were incubated at 37 °C with 5% CO_2. The medium was changed every alternative day. The cell proliferation was plotted in terms of Alamar blue dye reduction. The absorbance was measured at 570 and 600 nm using a multiplate reader (Tecan Infinite 200 PRO series) and proliferation was calculated following the manufacturer's protocol. The cell encapsulated hydrogels were further used for cell viability assessment.

5.2.5.3. Assessment of viability and arrangement of seeded cells in hydrogel

Viability of encapsulated NP cells in hydrogels was screened using live/dead assay kit (Invitrogen, Life Technologies, U.S.A.) following the manufacturer's protocol. In brief, live/dead assay reagent was added to the cell loaded hydrogels and incubated at 37 °C for 15 min. Thereafter, hydrogels were thoroughly washed with PBS (pH 7.4) and images were recorded using a florescence microscopy (Evos FL, Life Technologies, U.S.A.).

5.2.5.4. *Ex vivo* biomechanical study of hydrogel

For bio-functional assessment, blended SF solution was injected into the degenerated native disc, allowed to form hydrogel and thereafter, cyclic mechanical testing was performed. For this purpose, three different sets of native porcine lumber discs were collected from local abattoir within 1h of post processing. Set I was used as control without any treatment. Set II and III were

used as degenerative discs. To degenerate, 1 mL mixture of collagenase (0.5 $mg.mL^{-1}$) and protease (2 $U.mL^{-1}$) was injected into the central NP portion and incubated at 37 °C for 24 h in sterile condition. After 24 h of degeneration, set II was injected with PBS and set III was injected with blended SF solution (BM0.5/AA2.5) followed by 1 h incubation at 37 °C. Cyclic mechanical test was performed with all three sets. All discs were compressed to the axial strain of ~ 2% for 5 cycles at a loading and unloading rate of 1 mm/minute in PBS solution (pH 7.4) at 37 °C. The stress-strain curve was plotted for all the cases.

5.2.6. Statistical analysis

All quantitative experiments were performed in triplicates and results are expressed as mean ± standard deviation. Statistical analysis of data was performed by one-way analysis of variance (ANOVA) with Origin 6.0. Differences between groups of $p<0.05$ were considered statistically significant, and $p<0.01$ highly significant.

5.3. Results

5.3.1. Temperature effect on the gelation profile of SF

Two types of silk fibroin isolated from two different sources (*B. mori* as mulberry and *A. assamensis* as non-mulberry) were blended in five different ratios (**Table 5.1**) keeping the final protein concentration at 3% (w/v). The blended silk solutions were kept at 37 °C for at least 30 min. The preliminary confirmation of gelation was achieved by tube inversion method (**Figure 5.1, A-C**).

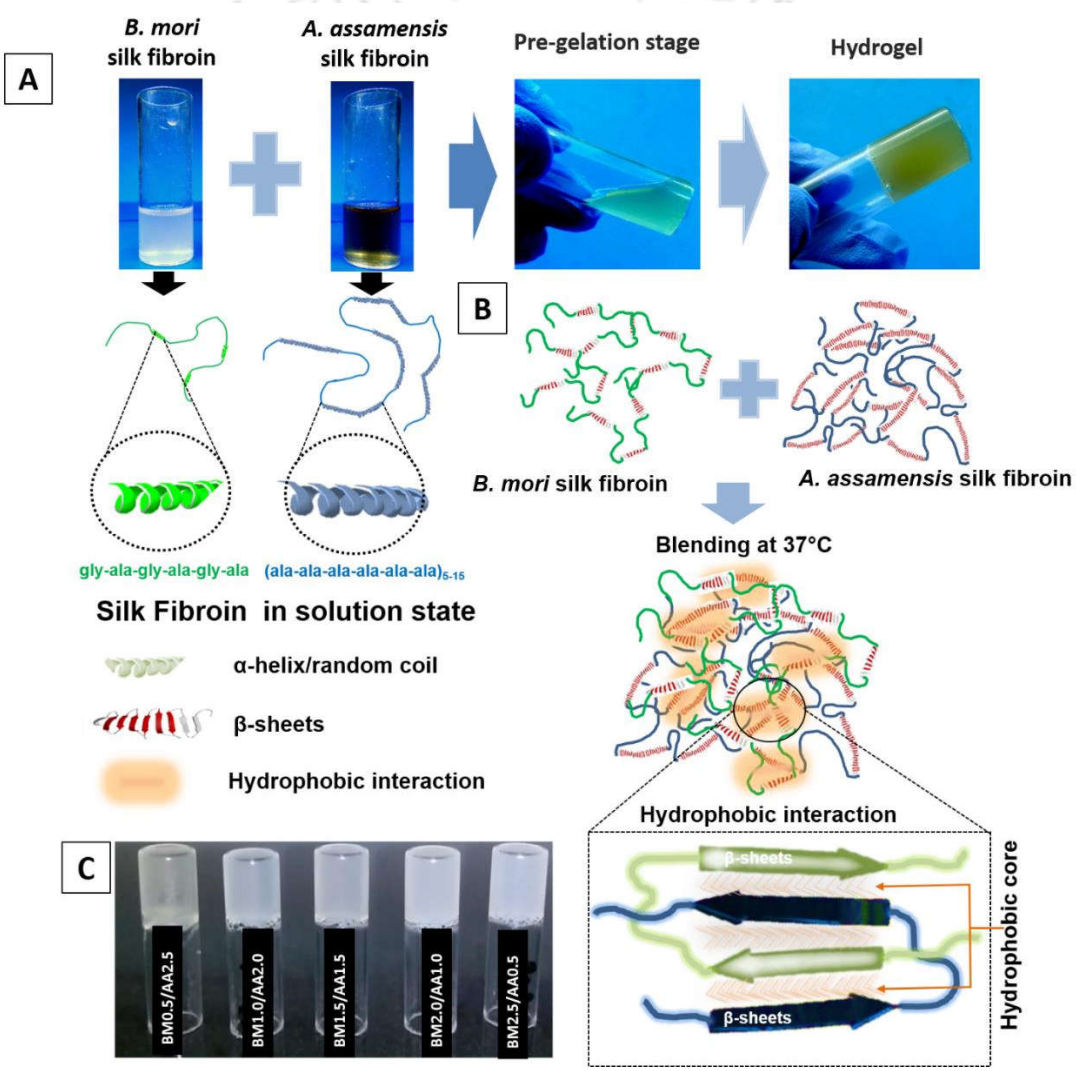

Figure 5.1. *Silk hydrogel; (A) stepwise process of hydrogel preparation (B) schematic representation of gelation mechanism, and (C) hydrogels of five different ratios (tube inversion method)*

To understand the effect of temperature on gelation, three sets of hydrogel systems were maintained in three different temperature conditions *i.e.,* 25 °C, 37 °C and 42 °C (**Figure 5.2A, I-III**). Gelation process was monitored by recoding the absorbance at 600 nm for ~ 70 min with the time interval of 3 min. It was noted that absorbance of any combination increased with time as the gelation process continued. The total sol-gel transition time was divided into three phases; translucent time (TT) referred to the initial phase of gelation, viscous time (VT) referred to the log phase of crosslinking and gelation time (GT) referred to the final gel formation. TT, VT and GT for different hydrogel systems at different temperatures are summarized in **Table A5.1.**

At a particular temperature *e.g.,* 37 °C, gelation time was dependent on the various ratios of two SF proteins (**Figure 5.2A, II**). The fastest gelation occurred in BM1.5/AA1.5 and BM1.0/AA2.0 (> 20 min) which was followed by BM2.0/AA1.0 and BM0.5/AA2.5 (< 20 min). However, no gelation was observed at 37 °C for BM2.5/AA0.5 even after 70 min. The control protein BM3.0 also did not show any sign of gelation at 37 °C, but gelation started for the control protein AA3.0 after 50 min.

It was observed that gelation pattern for all cases shifted left (faster gelation) at 42 °C, whereas it shifted right (slower gelation) at 25 °C (**Figure 5.2A, I and III**). At 42 °C, gelation occurred in AA3.0 within 40 min. However, in BM2.5/AA0.5 blends signs of gelation were observed after 60 min at 42 °C whereas no gelation was observed in case of BM3.0 throughout at any experimented temperature.

5.3.2. Effect of SF concentration and SF types on gelation

To understand the effect of total protein concentration on gelation profile, two different SF proteins were blended in an increasing order of wt % (1-4%) maintaining the same ratio (1:1). The gelation time was faster with increase in total protein concentration. The minimum gelation time was recorded for BM2.0/AA2.0, whereas maximum time was taken by BM0.5/AA0.5 at 37 °C (**Figure 5.2B, I**). It was also observed that the transparency of hydrogels decreased with the increase in total protein concentration. To confirm which SF type had more significant role in gelation initiation, two SF proteins were blended in ratios keeping one SF protein concentration constant [2% (w/v)] while increasing the other SF type [0.5 to 3.0% (w/v)]. In group-1 AA SF was kept constant (**Figure 5.2B, II**) while varying the BM SF concentration, whereas in group-2 BM SF

was kept constant (**Figure 5.2B, III**) while varying the AA SF concentration. While comparing between two groups it was observed that the combinations that consisted of higher AA showed faster gelation (**Figure A5.2**). TT, VT and GT for all the cases are summarized in **Table A5.2.**

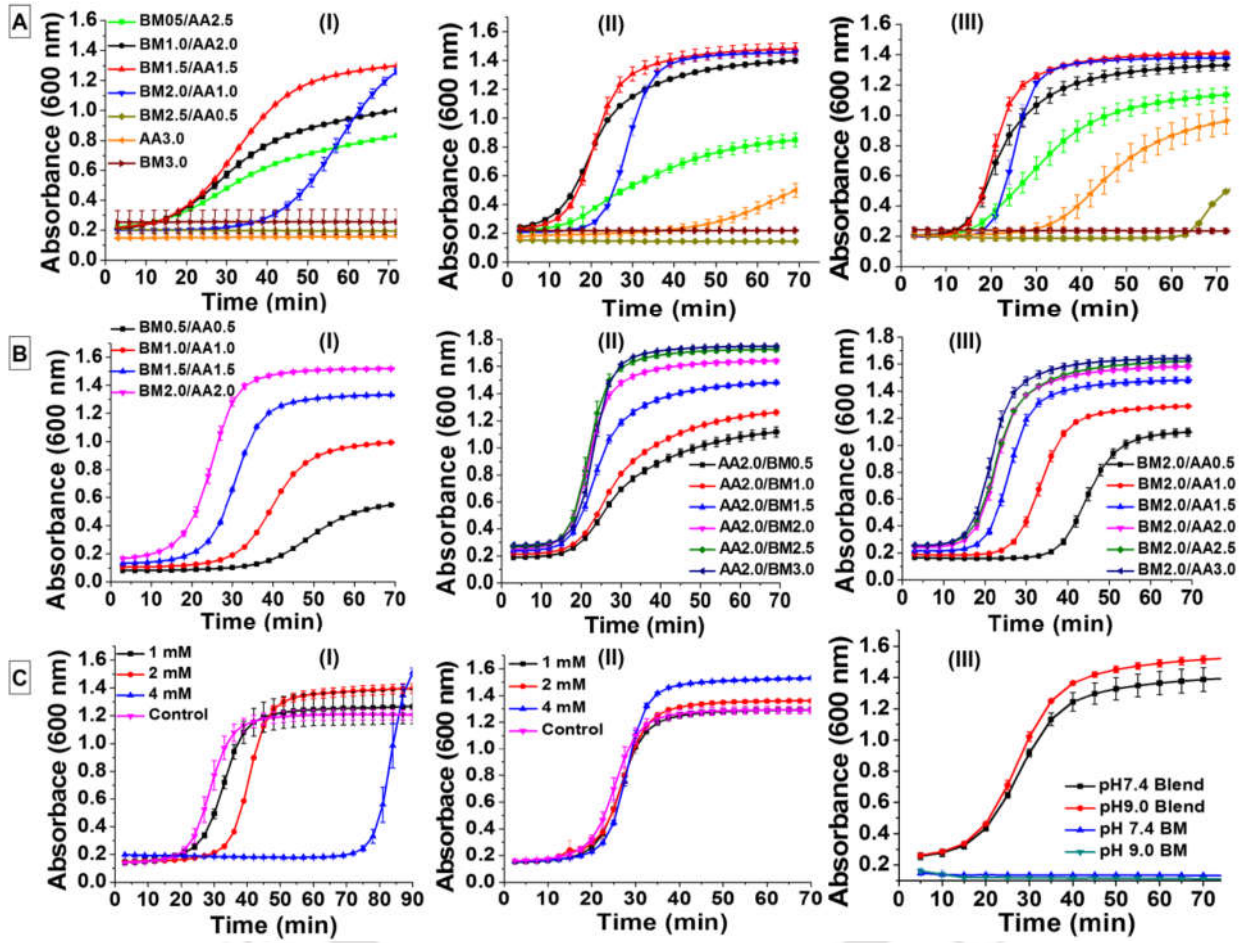

Figure 5.2. *Gelation pattern of silk hydrogel in different physiological conditions; (A) effect of temperature on gelation profile: (I) 25 °C, (II) 37 °C, and (III) 42 °C, (B) effect of SF concentration and SF types on gelation: (I) concentration dependent gelation where total SF protein concentration varies from 1-4%, w/v (II) group -1; blends of fixed AA concentration (2%, w/v) with varying BM concentration (0.5-3.0%, w/v), and (III) group-2; blends of fixed BM concentration (2%, w/v) with varying AA concentration (0.5-3.0%, w/v), and (C) effect of ionic concentrations on gelation: (I) effect of Ca^{2+} ions (II) effect of K^{+} ions and (III) effect of pH. Data represents mean ± SD (n = 3).*

5.3.3. Effect of salt concentration and pH on gelation

To understand the effect of physiological ionic conditions on gelation, two different ions (K^+ and Ca^{2+}) were selected. It was noticed that gelation time was highly affected by Ca^{2+} concentration. Slower gelation occurred compared to control when Ca^{2+} ions concentration increased in the blends (**Figure 5.2C, I**). Gelation occurred at ~ 80 min when Ca^{2+} concentration was 4 mM in the blends, whereas it took ~ 20 min for control or 1 mM Ca^{2+} containing blend. However, there was no effect of K^+ ions (0-4 mM) on gelation (**Figure 5.2C, II**). Similarly, alterations in pH (from pH 7.4 to pH 9.0) also did not show any effect on gelation process except increasing the opaqueness with the increase of pH (**Figure 5.2C, III**). The total time taken for the gelation process is summarized in detail in **Table A5.3.**

5.3.4. Reversal of Ca^{2+} effect on gelation using EDTA (Ethylenediaminetetraacetic acid)

To reverse the effect of Ca^{2+} ions on gelation, EDTA was added to the blends. Here, EDTA acts as a divalent ion chelator. Gelation was highly influenced by EDTA when it was added to the Ca^{2+} containing blends. Faster gelation occurred as the concentration of EDTA increased in the SF blends (**Figure 5.3A**). The control blend (*-Ve*) that contained only 4 mM Ca^{2+} showed the onset of gelation at ~ 80 min, whereas gelation time was gradually decreased to ~ 65, ~ 60, ~ 50 and ~ 20 min for 1 or 3, 5, 10 and 20 mM EDTA containing blends, respectively. Gelation time for SF blends containing 20 mM EDTA was almost close to the control system *(+Ve*) which did not contain EDTA or Ca^{2+}. The gelation process is as summarized in **Table A5.4.**

5.3.5. Effect of molecular weight (MW) or size of BM SF on gelation

Molecular weight of BM SF also played an important role in gelation. To produce different molecular weight of BM SF, cocoons were degummed in three different time frames *i.e.,* 5, 30 and 60 min following a previously established protocol [506]. To confirm different molecular weight by virtue of its hydrodynamic size, dynamic light scattering (DLS) and fluorescence studies were performed.

In fluorescence study, 0.1% (w/v) of BM SF aqueous solution derived from different degumming time points (5, 30 and 60 min) was excited at 280 nm and emission spectra were recorded in the range of 290-400 nm. The maximum emission peak was at 307 nm with a shoulder peak at 340 nm. The maximum fluorescent intensity at 340 nm differed for the three different samples (**Figure**

A5.4, A-B). The sample (hMWBM) degummed for 5 min showed maximum fluorescence intensity followed by those degummed for 30 min (mMWBM) and 60 min (sMWBM). The particle size distribution of BM SF was analyzed using DLS. hMWBM showed the maximum particle size (Z-average = 423 nm, 99% of particle in size of 545 nm) which was followed by mMWBM (Z-average = 373 nm, 99% of particle in size of 440 nm) and SMWBM Z-average = 190 nm, 99% of particle in size of 15 nm), respectively (**Figure A5.4 C**). In turbidity assessment, the maximum turbidity was shown by hMWBM, whereas sMWBM showed the least turbidity and moderate turbidity was recorded for mMWBM (**Figure A5.4 D**).

To understand the effect of molecular weight of BM SF on gelation, 3% (w/v) of different MW of BM SF (*i.e.,* sMWBM, mMWBM and hMWBM) was blended with 3% (w/v) AA SF in a ratio of 1:1 and absorbance was measured at 37 °C. It was observed that MW of BM SF played a vital role in gelation. Gelation time was decreased with the decrease of MW (**Figure 5.3B**). Therefore, sMWBM was found to be more efficient for gelation than others. However, there was no sign of gelation in control groups (*e.g.,* only hMWBM, mMWBM, sMWBM) except AA3.0 in which gelation started after 45 min (**Table A5.5).**

5.3.6. Confirmatory assessment of hydrophobic interaction in gelation

To confirm the hydrophobic interaction involved in gelation, BM SF was replaced by bovine serum albumin (BSA, hydrophilic protein) in the blends. AA SF was blended with equal volume of BSA rather BM SF. Gelation did not occur in BSA1.5/AA1.5 blend, whereas usual gelation profile was observed in BM1.5/AA1.5 blend. However, BSA1.5/AA1.5 exhibited gelation profile similar to AA3.0 as (**Figure 5.3C**).

5.3.7. Fluorescence analysis during sol-gel transition

The intrinsic fluorescent property of SF was utilized to study the gelation process. For this purpose, blended silk solution was excited at 280 nm and the emission spectra (290-400 nm) were recorded over a time period of 30 min. The fluorescent intensity increased with the time as the gelation process continued (**Figure 5.3D, I**). It was observed that the blends containing equal ratio of two SF proteins (BM1.5/AA1.5) showed faster increase in fluorescence intensity which was followed by BM1.0/AA2.0 and BM2.0/AA1.0, respectively.

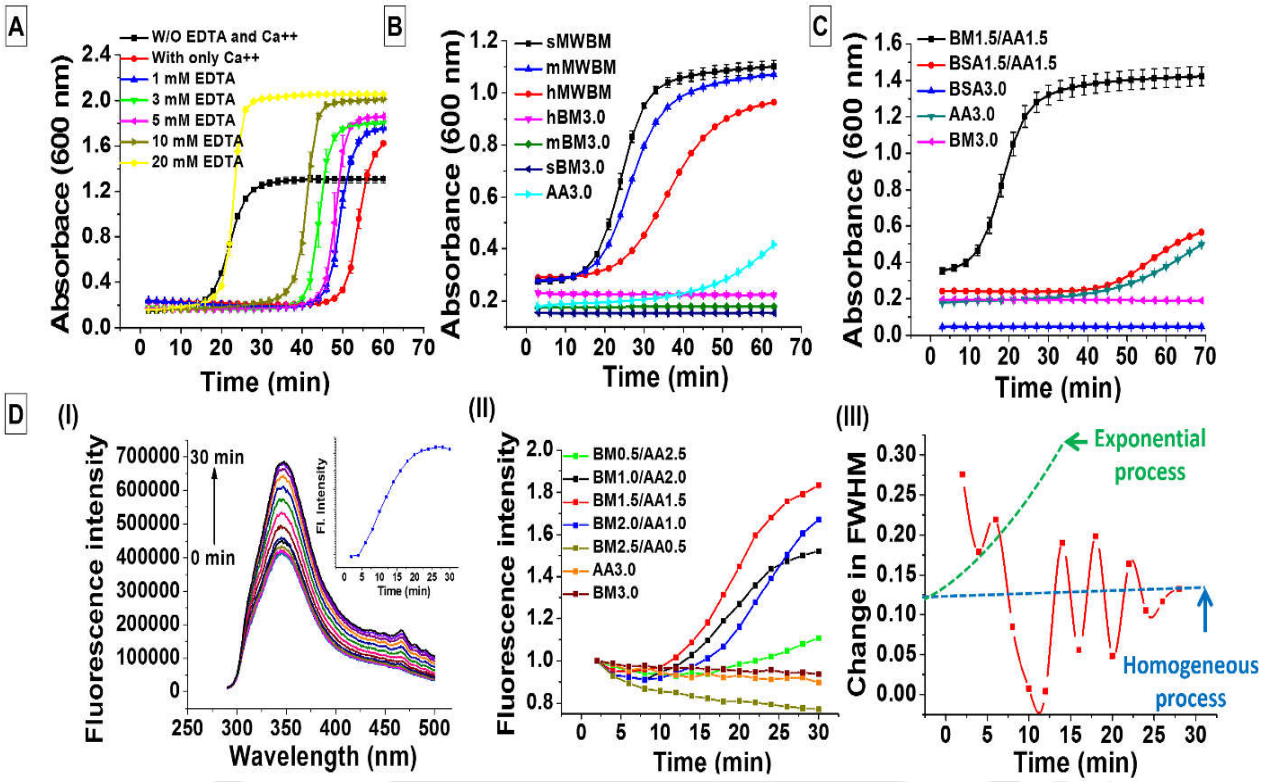

Figure 5.3. *Gelation pattern of silk hydrogel; (A) reversal of Ca^{2+} ions effect on gelation using EDTA, (B) effect of different molecular weight of BM SF on gelation, (C) confirmatory assessment of hydrophobic interaction behind gelation, and (D) intrinsic fluorescence analysis of silk hydrogel: (I) time dependent increase in fluorescence intensity of hydrogel, (II) comparative analysis of fluorescence intensity values among the blends, and (III) graph representing the changes in fluorescence intensities per unit of time: the blue and green dotted lines are the hypothetical situation of a homogeneous and exponential gelation process. Data represents mean ± SD (n = 3).*

However, there was no increase in fluorescence intensity in BM2.5/AA0.5, AA3.0 and BM 3.0 (**Figure 5.3D, II**). The results were found to be in correlation to the absorbance values obtained for gelation. The typical graph pattern (**Figure 5.3D, III**) supported randomness behind gelation as opposed to homogeneous or continuous process.

5.3.8. Physico-chemical characterization of hydrogels

Pore size and interconnectivity of hydrogels were evaluated by FESEM. It was observed that pore size of the hydrogels was gradually decreased as the concentration of BM SF increased in the

blends. The maximum pore size (10-20 µm) was obtained in BM0.5/AA2.5, whereas BM2.5/AA0.5 displayed minimum pore size (1-2 µm) (**Figure 5.4A, I-V**). Pores were found to be well interconnected in all hydrogel systems. High magnification FESEM (200 KX) images revealed formation of nanofibers (2-5 nm) during gelation (**Figure 5.4A, VI**).

The secondary structure and crystallinity in hydrogels were confirmed by FTIR and WAXD. The FTIR data showed the conformational changes with respect to β-sheets formation in hydrogel with the signature peaks at 1624, 1544 1228 cm^{-1} for amide I, II and III, respectively (**Figure 5.4B**). Further, amide I (1600-1700 cm^{-1}) region was deconvoluted to identify the different secondary structures of hydrogels and results are summarized in the supplementary information **Table A5.6** and **Figure A5.7**. It was noticed that regenerated SF solution predominantly made up of loops/turns or α-helices underwent conformational changes to obtain β-sheeted structure in the hydrogel, explain their formed hydrogel's structural stability. The maximum amount of β-sheets (~ 92%) was observed in the hydrogel prepared with the equal amount of AA SF and BM SF (*i.e.,* BM1.5/AA1.5), which was followed by BM0.5/AA2.5 (~ 83%) and BM2.5/AA0 (~ 65%). Furthermore, BM1.5/AA1.5 showed ~ 0.35% and ~ 1.44% of α-helix and loops/turn, respectively, which were the least values obtained from other hydrogels. However, total β-sheet content (65-92 %) was observed to be higher in all hydrogels than the solution of BM SF or AA SF (> 64%). Crystallinity in hydrogel was further confirmed by WAXD. Peaks at 2θ = 21° (major peak), 24° (minor peak) and a shoulder peak at 2θ = 42° confirmed the crystallinity in hydrogels (**Figure 5.4C**). However, the controls BM3.0 and AA3.0 did not show β-sheet transition. EDX was utilized to analyze the elemental or chemical compositions of the hydrogel samples under investigation. Hydrogels did not contain any residual amount of LiBr ions, used during degumming of protein fibers (**Figure A5.8**).

5.3.9. Swelling study

Swelling ability of any construct applied in tissue engineering purpose is one of most important necessities as it reveals the water retention capacity of that construct. To evaluate this intrinsic property, lyophilized hydrogels were submerged in deionized water over a period of 24 h (**Figure 5.4D**). A sharp increase in swelling ratio was observed in all types of hydrogels within 20 min except in BM2.0/AA0.5 blend which showed minimum swelling. A gradual yet slow increase was shown up to 250 min and thereafter attained an equilibrium state. Swelling ratio increased with the

increase in the concentration of AA SF blends. Maximum swelling occurred in BM0.5/AA2.5 which was significantly higher than all the groups ($p \leq 0.01$), whereas BM2.5/AA0.5 showed minimum swelling ratio. The swelling ratio of all the hydrogel groups was significantly different ($p \leq 0.01$) from each other.

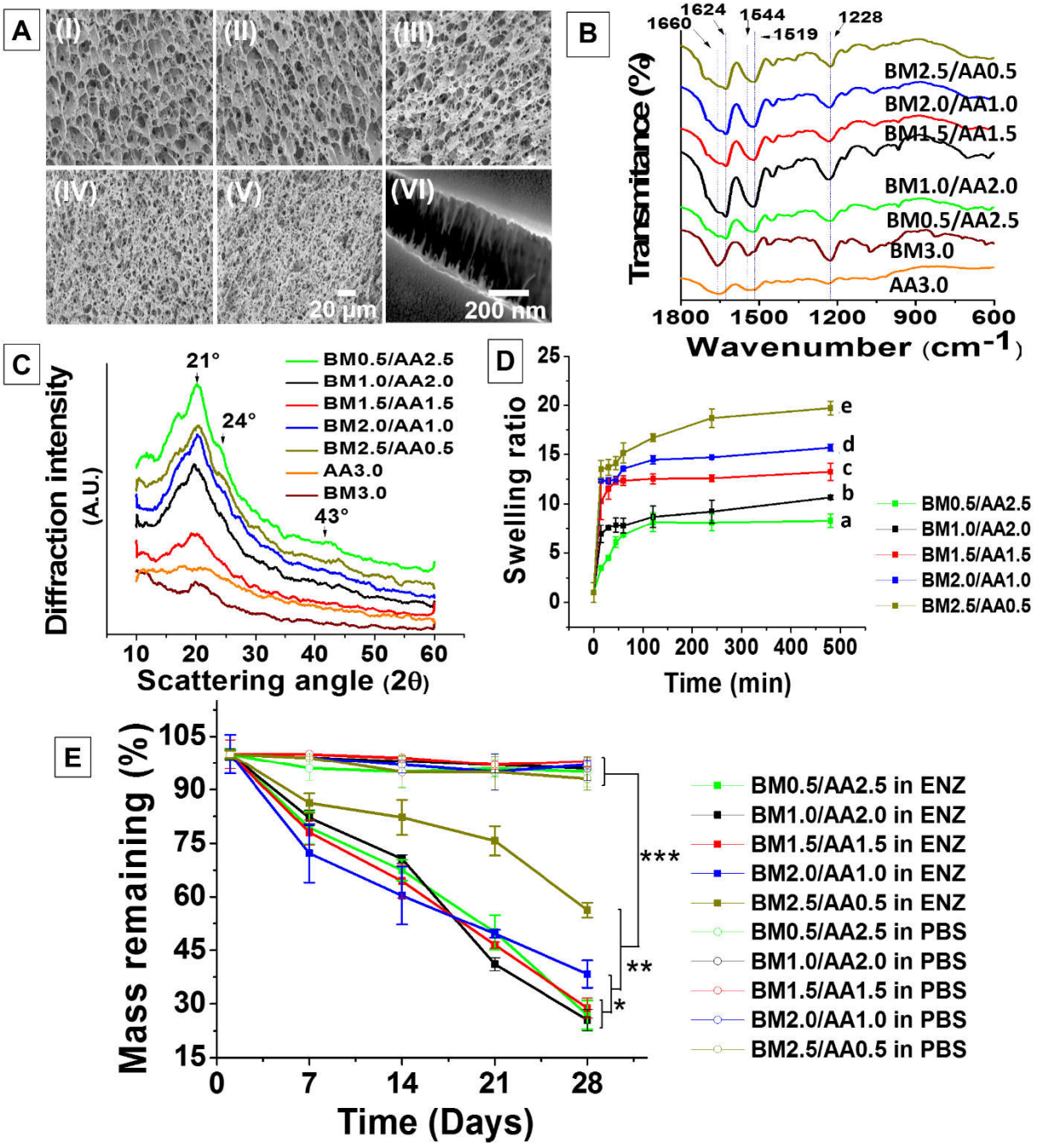

Figure 5.4. *Physicochemical characteristics of hydrogels; (A) FESEM images of hydrogels: (I) BM0.5/AA2.5, (II) BM1.0/AA2.0, (III) BM1.5/AA1.5, (IV) BM2.0/AA1.0, (V) BM2.5/AA0.5, and (VI) 200 KX magnification of hydrogel, (B) FTIR spectra, (C) WAXD analysis, (D) swelling study, and (E) degradation study; mass remaining of hydrogel. Values are plotted as mean ± standard deviation, n = 3, where *** p≤0.001, ** p≤0.01 and * p≤0.05. For swelling study; different letters (a, b, c, d, and e) represent that the groups are significantly different from each other (p≤0.01).*

5.3.10. Degradation study

In tissue engineering, the applied biomaterials should get degraded with time and regeneration of neo-tissue will seal the gap thus formed. To mimic the physiological biodegradable microenvironment, hydrogels were treated with protease solution over 28 days (**Figure 5.4E**). The degradation rate was represented as percent of mass remaining at each time point. There was a significant difference in degradation rate of the hydrogels treated with enzymes group than that of the control group ($p \leq 0.001$). It was observed that the degradation rate was decreased with the increase of BM SF in the blends. BM2.5/AA0.5 experienced minimum degradation (~ 60% mass remaining), followed by BM2.0/AA1.0 (~ 38% mass remaining) after a period of 28 days ($p \leq 0.01$). However, there was no significant difference in degradation rate among BM1.5/AA1.5, BM1.0/AA2.0 and BM0.5/AA2.5 blends, but significantly different from BM2.0/AA1.0 ($p \leq 0.05$) and BM2.5/AA0.5 ($p \leq 0.01$).

5.3.11. Mechanical properties of hydrogel

Mechanical characterization of silk hydrogel is obligatory as it would be used to study the load bearing applications like NP tissue engineering for disc degeneration therapy. The mechanical properties of the hydrogels were analyzed under different *in vitro* conditions *e.g.,* different time frames post gelation, diameters, strain value, ionic strength, pH and mechanical confinement to mimic the physiological microenvironment. The compressive modulus was calculated from stress-strain curve for each hydrogel system in unconfined method at 10% strain.

The compressive modulus of various hydrogels was calculated post 1 h of gelation. It was observed that the compressive modulus was increased to a certain limit with the increase in concentration of BM SF (**Figure 5.5A**). The maximum modulus value was obtained from BM2.0/AA1.0 (21.85 ± 0.85 kPa), followed by BM1.5/AA1.5 (17.2 ± 2.21 kPa), BM1.0/AA2.0 (11.37 ± 1.07 kPa) and

BM0.5/AA2.5 (4.7 ± 0.24 kPa). BM0.5/AA2.5 showed minimum compressive modulus which was significantly lower than any other group studied ($p \leq 0.01$). However, BM2.5/AA0.5 did not show any significant difference in compressive modulus from BM1.0/AA2.0, but showed significantly less value than both BM1.5/AA1.5 and BM2.0/AA1.0 ($p \leq 0.01$).

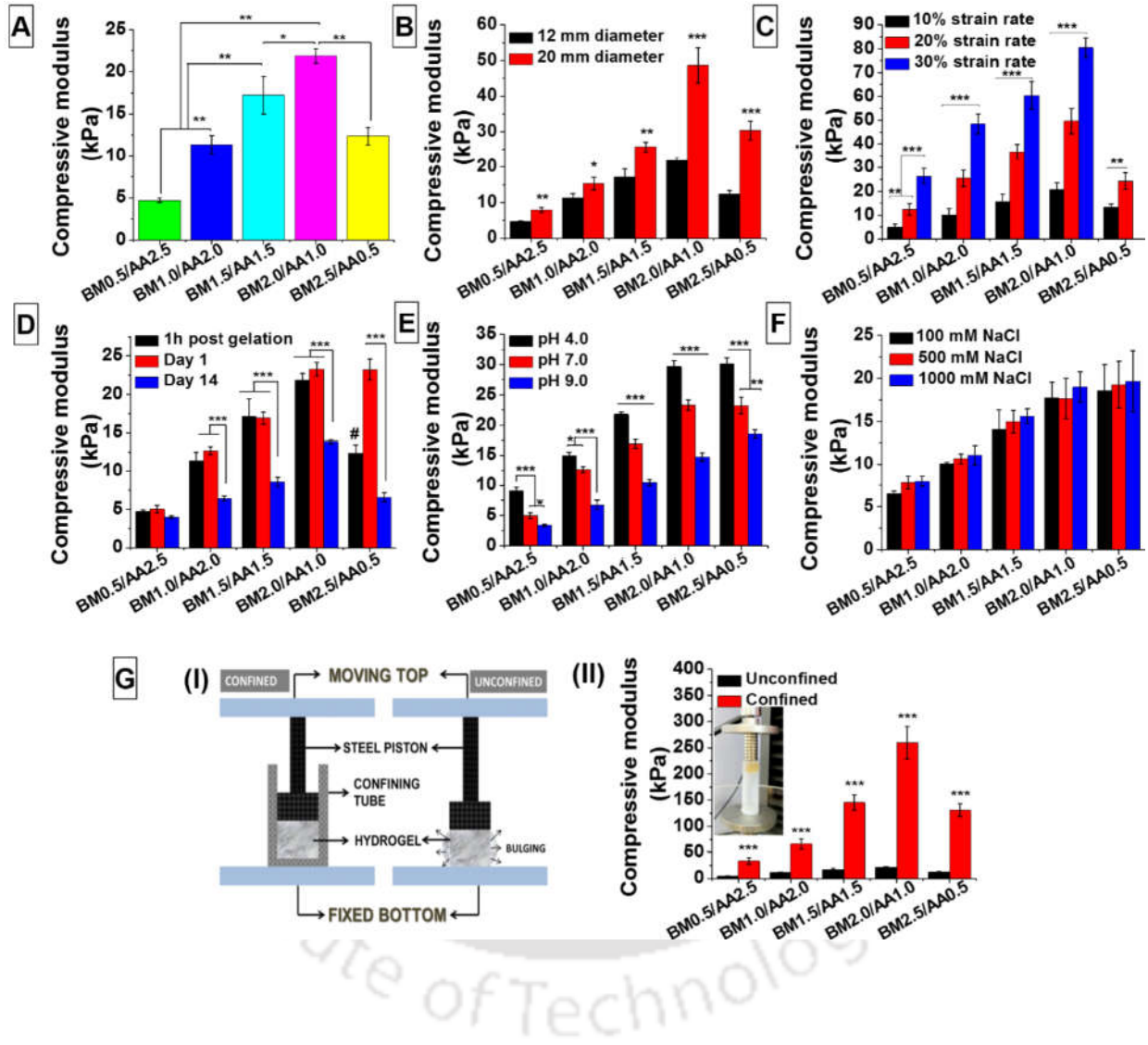

Figure 5.5. *Mechanical properties of hydrogel; (A) compressive modulus post 1 h of gelation, (B) diameter dependent compressive modulus measurement, (C) compressive modulus at different strain, and (D) time dependent compressive modulus measurement, (E) effect of pH on compressive modulus, (F) effect of salt concentration on compressive modulus, and (G) confined mechanical testing of hydrogel: (I) schematic diagram of confined-unconfined mechanical testing, and (II) comparative analysis of confined and unconfined compressive modulus of hydrogels.*

*Values are plotted as mean ± standard deviation, n = 3, where # $p \leq 0.001$ vs Day 1, *** $p \leq 0.001$, ** $p \leq 0.01$ and * $p \leq 0.05$.*

As NP diameter varies from patient to patient, we used two different diameters of hydrogels; 12 mm and 20 mm. The compressive modulus of all hydrogel systems were significantly affected by diameter. It was observed that as the diameter was increased, the compressive modulus was increased as well (**Figure 5.5B**). For instance, 20 mm diameter of BM2.0/AA1.0 resulted in compressive modulus of 48.6 ± 3.9 kPa which was ~ 2.5 times higher than that of 10 mm diameter of the same ($p \leq 0.001$).

The IVD can compress ~ 30% of its vertical axis[508]. To mimic such biomechanical conditions, the compressive modulus of the hydrogels was calculated in three different strain rates, 10%, 20% and 30%. In all cases, the value got increased as the strain rate was increased (**Figure 5.5C**). For instance, BM2.0/AA1.0 blend showed maximum compressive modulus (80.42 ± 4.21 kPa) at 30% strain which was significantly higher than 20% strain (49.61 ± 5.32 kPa) ($p \leq 0.001$) and 10% strain (20.8 ± 2.78) ($p \leq 0.01$), respectively.

The stability of hydrogels was assessed by maintaining them in PBS (pH 7.4) at three different time frames; 1 h post gelation, 1day post gelation and at day 14 (**Figure 5.5D**). The compressive modulus of all types of hydrogels (except BM2.5/AA0.5) was not affected by a short incubation time of 1 day, but significantly decreased after 14 days ($p \leq 0.001$). For instance, the obtained compressive modulus of BM2.0/AA1.0 was 23.29 ± 0.89 kPa on day 1, which was decreased to 13.83 ± 0.26 kPa on day 14. In an exceptional case, BM2.5/AA0.5 showed maximum compressive modulus of 12.42 ± 1.21 kPa following 1 h of gelation, which was significantly increased to 23.22 ± 1.35 on day 1 ($p \leq 0.001$) but decreased to 6.76 ± 1.15 kPa on day 14.

To understand the effect of physiological fluid environments on mechanical behaviors, hydrogels were treated in three different pH (4.0, 7.4 and 9.0) and salt strengths (100, 500 and 1000 mM NaCl). It was noticed that pH played a significant role on compressive modulus. In all the cases, the compressive modulus was significantly increased after transferring the hydrogels from pH 7.0 to pH 4.0, whereas the value decreased when transferred to pH 9.0 (**Figure 5.5E**). For instance, the compressive modulus of BM2.0/AA1.0 was significantly increased to 29.65 ± 0.97 kPa from 23.29 ± 0.89 kPa when transferred at pH 4.0 from pH 7.4 ($p \leq 0.001$), whereas the value decreased

to 17.77 ± 0.67 kPa after transferring at pH 9.0 ($p \leq 0.001$). However, after transferring the hydrogels from pH 7.4 to pH 4.0, compressive modulus increased by ~ 30% in all cases except BM0.5/AA2.5 that showed ~ 80% increase (**Figure A5.9 A**). Similarly, after transferring into pH 9.0, maximum % decrease of compressive modulus was recorded for BM1.0/AA2.0 (~ 45%), whereas the least value was obtained for BM2.5/AA0.5. However, > 30% decrease in compressive modulus was recorded for the rest of the hydrogel systems (**Figure A5.9 B**). To check the recoverability of mechanical properties, hydrogels were transferred from pH 9.0 to pH 7.4 and the compressive modulus was measured. All the hydrogel systems had the ability to recover their compressive modulus by > 70% (**Figure A5.9 C**). However, change in salt concentration (100-1000 mM) did not show any significant effect on compressive modulus (**Figure 5.5F**).

Gelatinous NP is confined by AF tissue. To mimic such microenvironment, compressive modulus was conducted under confined system. The results showed that compressive modulus for all the cases were significantly higher when measured under confined strategy than the unconfined way ($p \leq 0.001$) (**Figure 5.5G, II**). For instance, the unconfined compressive modulus of BM2.0/AA1.0 was 21.85 ± 0.86 kPa, whereas the confined compressive modulus was 259.94 ± 30.88 kPa ($p \leq 0.001$) which was approximately 11 fold higher than the unconfined compressive modulus.

5.3.12. Cyclic mechanical study of hydrogels

The IVD is more often experienced to display continuous compression-decompression cycles throughout life-time. Therefore, it is of utmost importance to perform the cyclic compression test with NP analog of SF hydrogels. Cyclic compression test was conducted to study the regaining of mechanical properties of all hydrogel systems (**Figure A5.10 A**). **Figure A5.10 B, I** shows the typical stress-strain curve for all types of hydrogels. BM0.5/AA2.5 and BM1.0/AA2.0 did not show any fissure even after applying 80% strain. BM1.5/AA1.5 was broken down at 70% strain, whereas BM2.0/AA1.0 and BM2.5/AA0.5 showed permanent deformation at 40% and 25% strain, respectively. From cyclic compression test, it was noticed that the area under stress-strain curve gradually decreased after each cycle for all types of hydrogels (**Figure A5.10 B, II-V**). It was observed that maximum compressive stress at any particular strain decreased faster for initial cycles and thereafter the rate of energy differences decreased slowly when 50 cycles were reached. The maximum variation in compressive stress at 15% strain from cycle 1-50 was recorded for BM2.0/AA1.0, whereas BM0.5/AA2.5 showed minimum changes. BM0.5/AA2.5 was shown to

retain the maximum compressive stress of ~ 78%, whereas this ability was gradually decreased as the concentration of BM SF increased in the blends. For instance, BM2.0/AA1.0 showed minimum recoverability of compressive stress (**Figure A5.10 B, VI**)

5.3.13. Rheological properties of hydrogel

Rheological analysis was undertaken to study the flow properties or deformation of the hydrogels at specific forces. Gelation point was determined in time sweep test of blended solutions. All the blended solutions showed a typical sol feature (G”>G’) at initial time points. However, after certain point, G’ crossed G” resulting in gel formation. It was observed that BM1.5/AA1.5 took at least (~ 270 s) time to form gel, whereas maximum time (~ 765 s) was taken by BM2.5/AA0.5. The gelation time for BM0.5/AA2.5, BM1.0/AA2.0 and BM2.0/AA1.0 was ~ 610 s, ~ 300 s and ~ 500 s, respectively (**Figure 5.6A**). These results complimented the values obtained from absorbance or fluorescence based assays for gelation study. The maximum storage modulus (~ 8686 Pa) was gained by BM1.5/AA1.5 which was related to the faster crosslinking in the blend. Gelation is directly related to the increase in complex viscosity (η*) with time. Here, η* was gradually increased with time for all cases supporting the gelation occurrence (**Figure 5.6 B**).

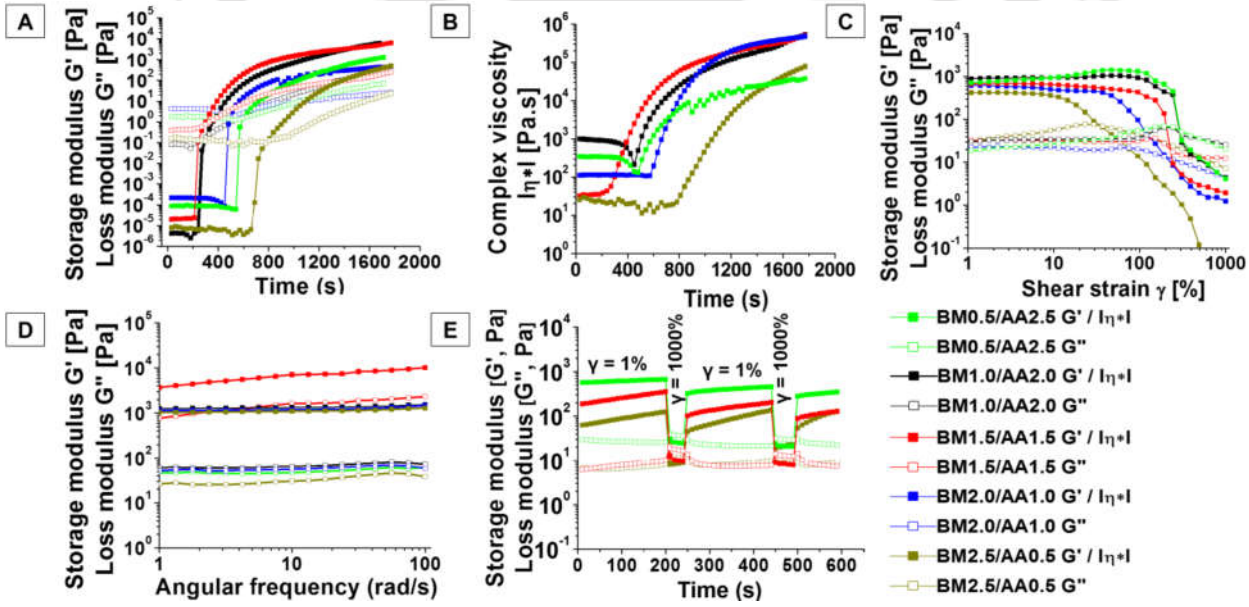

Figure 5.6. *Rheology of SF hydrogel; (A) time sweep for gelation point analysis, (B) complex viscosity vs. time, (C) determination of LVR for hydrogels, (D) frequency sweep, and (E) thixotropic test.*

In amplitude sweep, shear strain (γ) is varied while frequency is kept constant. For analysis, G' and G" were plotted against γ. At low γ, G' and G" were constant for all cases. As the γ value increased, deformation was started leading to decrease in G' value that crossed G". The slope value of G', known as linear viscoelastic region (LVR) was gradually decreased as the concentration of BM SF increased in the hydrogels (**Figure 5.6C**). BM 0.5/AA2.5 displayed the maximum value and LVER extended up to ~ 222% strain, whereas BM2.5/AA0.5 showed the least strain value (γ = ~ 14%) for LVER. A moderate value (γ = ~ 165 %) was obtained for BM1.5/AA11.5. In frequency sweep, frequency is varied while γ remains fixed. All the hydrogels showed no deformation up to 100 rad.s^{-1}. G' and G" were frequency independent for all hydrogels (**Figure 5.6D**). In the thixotropic analysis, it was observed that all the hydrogels had the recoverability property from high strain induced deformations. However, the greater recoverability was shown by BM 0.5/AA2.5 (**Figure 5.6E**).

5.3.14. Biological assessment

Cytocompatibility assessment of any biomaterial used for tissue engineering applications is one of the most important pre-requisites. For this purpose, primary NP cells, isolated from porcine source, were seeded on hydrogel surface and cultured for 7 days (**Figure 5.7A**). Alamar blue reduction assay was performed to assess the proliferation rate of the primary cells upon contact with hydrogel surface. It was observed that NP cells proliferated over 7 days on all types of hydrogels surface. However, maximum number of cell proliferation occurred on BM0.5/AA2.5 which was significantly higher than that of BM1.5/AA1.5 or BM2.5/AA0.5 on day 7 ($p \leq 0.01$) (**Figure 5.7B**).

To check the cellular viability inside hydrogel microenvironment, NP cells were encapsulated within hydrogels and maintained for 7 days in DMEM/F12 (**Figure 5.7C, I-III**). Live cells were visualized using live/dead assay kit. Cells were viable in all hydrogel systems, but enhanced green fluorescence signal was recorded for BM0.5/AA2.5.

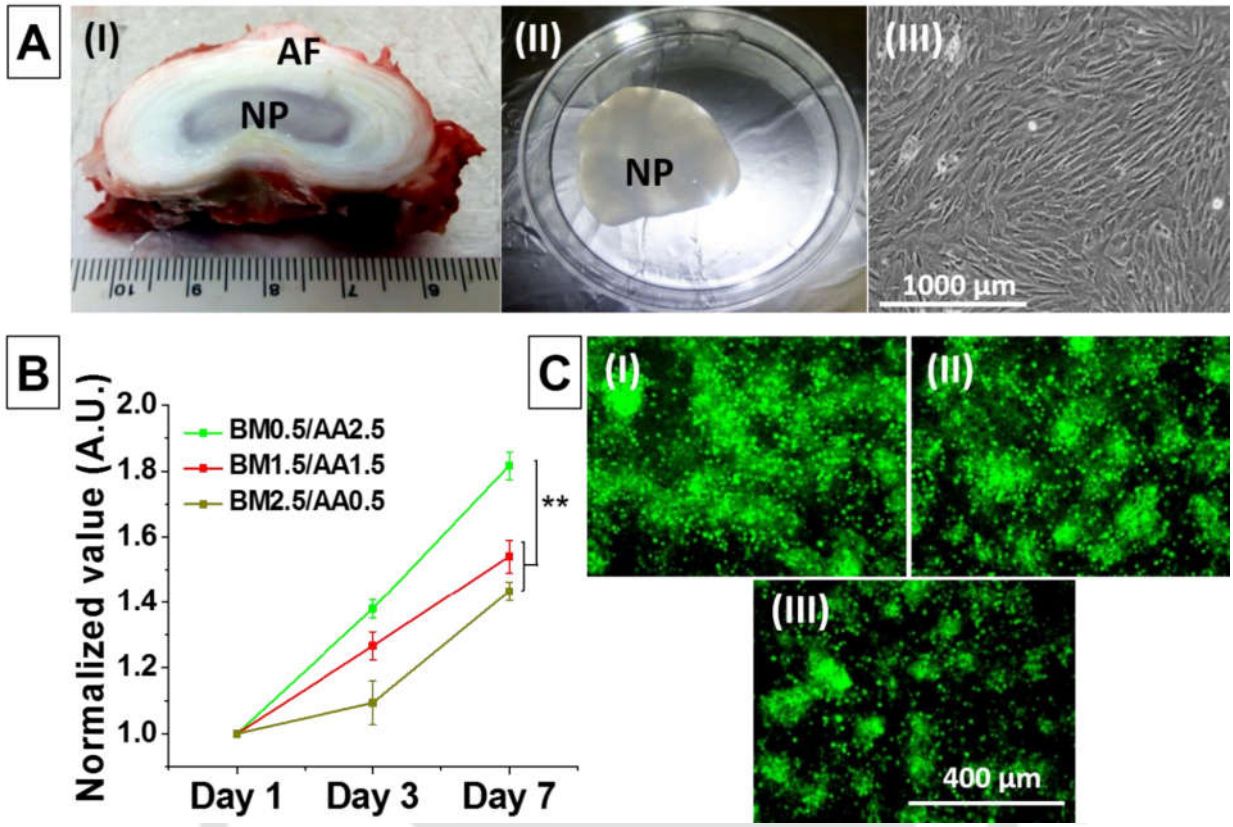

Figure 5.7. *Biological assessment of silk hydrogel; (A) isolation of NP hydrogel and NP cell form porcine vertebral disc: (I) native vertebral disc, (II) native NP gel, and (III) cultured NP cells on tissue culture plate, (B) Cell proliferation assay using Alamar blue reduction method and, (C) viable cells (green fluorescence) inside the hydrogels: (I) BM0.5/AA2.5, (II) BM1.5/AA1.5, and (III) BM2.5/AA0.5. Data are plotted as a mean ± standard deviation, n = 3, where **p≤0.01.*

5.3.15. *Ex vivo* biomechanical study of hydrogel

Ex-vivo biomechanical study was performed by injecting the blended SF solution into the degenerated NP portion of disc. Injected solution was allowed to form hydrogel inside the disc. Three sets were used for this study; normal disc (control group), degenerated disc filled with PBS and hydrogel assisted regenerated disc (**Figure 5.8, A-B**). Cyclic compression test was performed with all the three types of discs. In control group (Set I), stress-strain curve area remained unchanged throughout the cyclic process (**Figure 5.8C, I**). The PBS filled degenerated disc (Set II) showed drastic drop in maximum compressive stress after 5 cycles (**Figure 5.8C, II**). However,

the hydrogel assisted regenerated disc (Set III) maintained its compressive properties to a satisfactory level (**Figure 5.8C, III**).

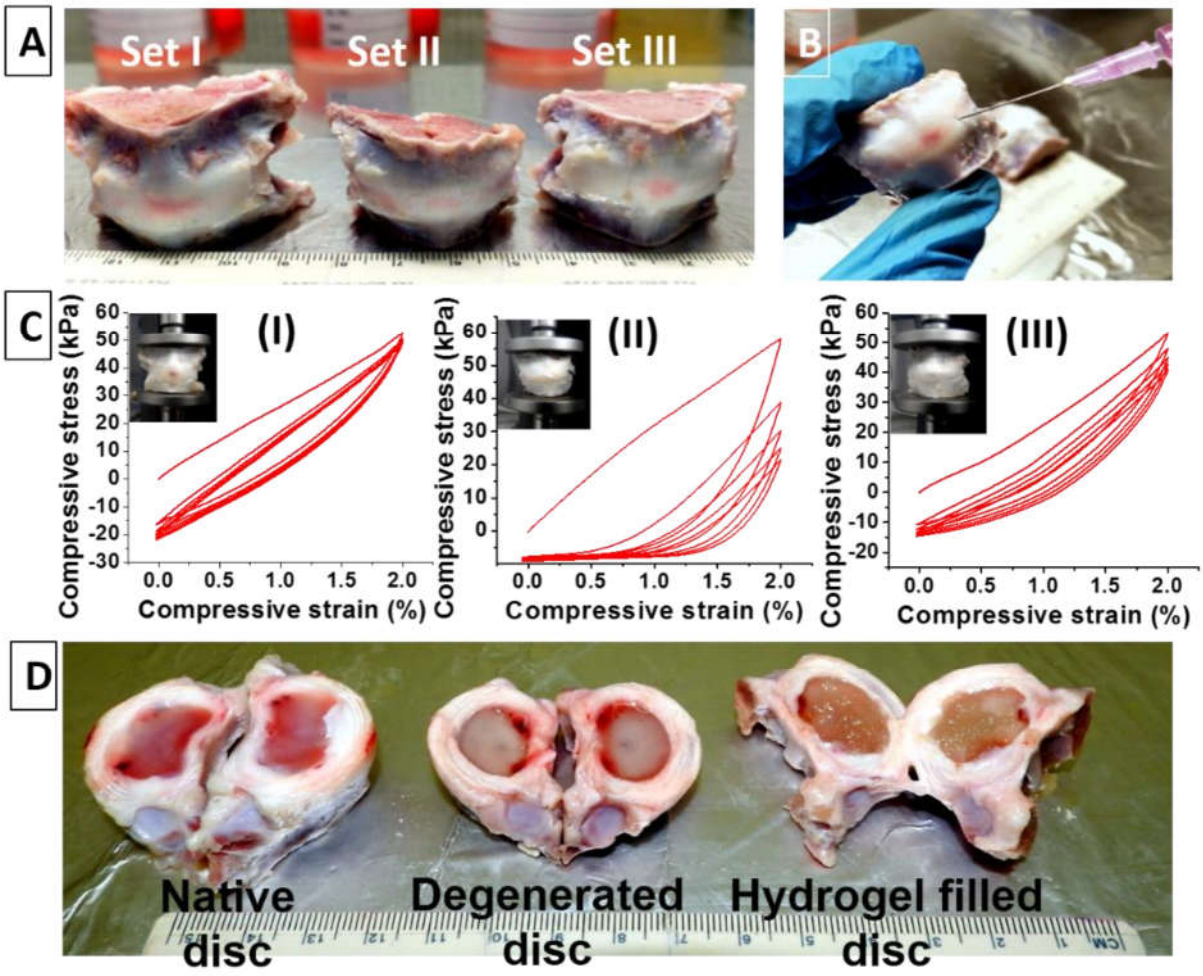

Figure 5.8. *Ex vivo biomechanical study; (A) three sets of porcine vertebral discs, (B) injection of blended SF solution into the disc, (C) cyclic compressive test: (I) native disc, (II) degenerated disc, and (III) hydrogel assisted regenerated disc, and (D) three sets of dissected discs after test.*

5.4. Discussion

Silk hydrogels have been used over the years in different tissue engineering applications including cartilage, bone, and intervertebral disc[43, 509]. The aqueous SF solution can easily be transformed into hydrogel by inducing structural transition into β-sheets utilizing several physiochemical methods. These time consuming, labor-intensive methods do not only increase the final expenditure of hydrogel fabrication, but also increase the chances of chemical toxicity. However, the mechanical properties of fabricated hydrogels are also unsatisfactory, specifically when applied in load bearing applications like NP tissue engineering. Therefore, there is an urgency need for a facile and rapid gelling technique with tunable mechanical and bioresponsive properties, avoiding the usage of any hazardous chemicals.

NP is the gelatinous central tissue of vertebral disc. It is confined by multiple sheets of AF tissue and dissipates the pressure to this surrounding AF. Once degeneration of the disc starts it fails to regenerate as it is an avascular organ. A minimally invasive way is to inject the hydrogel into the damaged disc via *in situ* gelation approach that may overcome the surgically associated treatment fallacy. In the present study, we blended two different SF (*B. mori* and *A. assamensis*) to make hydrogel independent of any external stimuli. SF from two different sources self-assembled with time forming hydrogel. This self-assembly might be due to the alteration in hydrophobic-hydrophilic microenvironment. The differential hydrophobicity that caused the proteins to interact happened because of the amino acid composition, sequence and arrangement of the protein chain. The primary structure of BM SF mainly consists of AGSGAG repeats which comprises ~ 55% of the total fibroin. These repeats are mainly involved in crystalline structure formation which in turn are primarily responsible for conformational changes of protein (silk I to silk II) when subjected to bio-spinning or under laboratory conditions (*e.g.,* alcohol treatment, sonication, pH and ionic strength variations)[415, 506, 510, 511]. The BM SF consists of 30.2% alanine, 45.9% glycine, 12.1% serine and rest are 5.5% tyrosine, 1% aspartic and glutamic acid, and 2.2% isoleucine, leucine and valine[505]. Similarly, the primary structure of AA SF consists of 42.5% alanine, 28.9 % glycine, 10.2% serine and 5.5% tyrosine[505]. There are mainly three motifs in AA SF secondary confirmations; A-motif that has only alanine residue, G-motif mainly consisting of glycine residues and R-motif containing arginine residues. Among these three motifs, A-motif is mainly responsible for crystallinity as it contains poly-alanine stretches of $(alanine)_{5\text{-}15}$.

The gelation was accelerated or decelerated when reaction occurred at high (42 °C) or low temperature (25 °C), respectively (**Figure 5.1A and 5.2A**). This could be related to the hydrophobic interaction between SF chains. It is a well-known phenomenon that hydrophobic interaction is highly influenced by temperature and the strength of hydrophobic interaction increases as the temperature raises[512]. Here, two SF proteins of different hydropathicity (due to their amino acid composition, sequence and arrangement) when blended, the protein chains were intended to interact to each other due to the hydrophobic interaction. At the initial stage of gelation, the hydrophobic regions in the protein chains began to rearrange themselves (inter-chain interaction) which was further accelerated by intra-chain interaction as the gelation continued. The ratio of two different hydrophobic chains also played a fundamental role in gelation. It was observed that when two proteins were blended at a ratio of 1:1 (BM1.5/AA1.5), faster gelation occurred than any other combinations at any given temperature. BM SF did not show any sign of gelation at any temperature, whereas gelation initiation occurred in AA SF in the later stage either at 37 °C or at a higher temperature. As AA SF itself possessed longer hydrophobic chains of poly-alanine, change in temperature lead to the formation of self-assembled chains (**Figure A5.1**). Furthermore, we conducted an experimental set up where a type of SF concentration got fixed while varying the other type. It was observed that the protein combinations containing higher amount of AA SF, showed faster onset of gelation (**Figure 5.2B, II-III and Figure A5.2**). This might be due to the presence of longer hydrophobic fragments in AA SF chain that had more potential to self-assemble, and BM SF is hypothesized to play the role of an *inducer* in gelation (**Figure A5.1**). Gelation process was also associated with total protein concentration in the blends. It was noticed that gelation time gradually decreased with the increase in total SF concentration in the blends (**Figure 5.2B, I**). Higher amount of protein corresponds to higher probability of resulting in development of hydrophobic chains which is correlated to the faster interaction that resulted in faster gelation.

To understand the effect of various ions present in physiological fluids, gelation process was conducted in presence of Ca^{2+} and K^{+} ions (1-4 mM). It was seen that gelation time gradually increased with the increase in Ca^{2+} ions in the blend (**Figure 5.2C, I**). Previously, it was reported that faster gelation occurred in presence of Ca^{2+} ions (20-200 mM) in sonication induced BM SF solution[497]. The high concentration of Ca^{2+} ions coagulated SF that finally led to the formation of gel as a result of "*salting out*" effect. In the present study, we used a low range of Ca^{2+}

concentration (1-4 mM) similar to the biological fluids. This significantly low ionic strength could not induce coagulation or precipitation in BM SF rather induces *"salting in"* effect. In contrast, AA SF was very sensitive to *"salting out"* effect even at a very less ionic strength. However, visible BM SF protein coagulation was observed at 6 mM Ca^{2+}, and therefore it could be hypothesized that coagulation might start below the ionic strength level used in this study (**Figure A5.3 A**). The hydrophobic interaction is directly correlated to salt concentration[513]. With the increase in salt concentration, it takes out the water molecule surrounding the protein molecules keeping the hydrophobic residues close together. In this study, the gelation time was increased in presence of Ca^{2+} ions. This might be due to the absence of hydrophobic chains in AA SF, required to entangle with BM SF chains during gelation, as it was already precipitated or separated from the blended solution. One possible reason behind the AA SF precipitation was the presence of high content of Lys, Arg and His (3.9%) that possess greater *relative calcium-binding strength* over other amino acids (**Figure A5.3 B**)[514]. Study conducted by a group suggested that higher Ca^{2+} ion concentrations maintain the random coil in BM SF [515]. This might be another possible reason restricting one of the SF to play the role in hydrogel formation. However, monovalent K^{+} ion did not show any effect on gelation process (**Figure 5.2C, II**). There were few contradictory reports on the effect of K^{+} ions on SF gelation[497, 516]. Therefore, it can be inferred that the presence of Ca^{2+} in the physiological fluid hinders the occurrence of *in situ* SF gelation. For a successful *in situ* gelation, EDTA was added to the blended SF solution and recoverability of gelation time was checked (**Figure 5.3A**). It was observed that EDTA chelated the Ca^{2+} ions thus setting the hydrophobic chains free for interaction.

The gelation time was also influenced by the molecular size of BM SF. The higher degumming time provided low molecular weight BM SF and *vice versa*. Molecular size by virtue of the hydrodynamic size was confirmed by conducting fluorescence and DLS analysis. It was noticed that sMWBM (~15 nm in size) showed reduced fluorescence intensity at 340 nm than mMWBM or hMWBM (**Figure A5.4**). The less degraded samples possessed higher tryptophan to tyrosine fluorescence than the highly degraded samples. This was because of less probability of fluorescence resonance energy transfer (FRET) between the two residues in smaller peptide chains of highly degraded sample[506]. However, it was observed that faster gelation occurred in the blends containing sMWBM (**Figure 5.3B**). This might be due to the ability of smaller BM SF chains to penetrate into the core and interact faster with the relatively larger entangled AA SF

chains (**Figure A5.5**). In order to confirm the hydrophobic interaction between two SF types during gelation, we replaced BM SF with BSA that does not have any hydrophobic motif (**Figure 5.3C**). It was observed that blends with BSA showed the same gelation pattern as control AA3.0, indicating a time dependent self-assembly phenomenon.

The intrinsic fluorescence of SF was also utilized to understand the gelation process. Fluorescence intensity gradually increased as gelation process continued (**Figure 5.3D**). The protein molecules were in *Brownian* motion when they were in liquid state. The gelation initiated when two protein molecules started to interact with each other through hydrophobic interaction. The enhanced fluorescence intensity with the gelation progression might be due to better fluorescence resonance energy transfer between tryptophan to tyrosine residues when it was in close association within hydrogel (cross-linked) microenvironment (**Figure A5.6**)[506]. The maximum and faster increment of fluorescence intensity was recorded for BM1.5/AA1.5 indicating faster interaction among the chains when two proteins were in equal ratio (**Figure 5.3D, II**). To understand whether gelation was an exponential/homogeneous or inhomogeneous process, we calculated the *change in FWHM* from fluorescence intensity graph for each unit time interval and plotted them against the gelation time. The zigzag pattern of *change in FWHM* depicted that the gelation progression was an inhomogeneous or discontinuous process. We hypothesized if gelation was a homogeneous process *i.e.,* same number of both molecules ($n+ n, n+ n, \ldots\ldots n+ n$) interacted with each other at each unit time, a straight line of *change in FWHM* would be obtained (blue dotted line). Similarly, if gelation was an exponential process *i.e.,* an increasing order of both molecules ($n+ n, 2n+ 2n, \ldots\ldots Nn+ Nn$) interacted to each other; a linear pattern of *change in FWHM* against time would be obtained (green dotted line). (**Figure 5.3D, III**).

From the FESEM data, it was noticed that the pore size of hydrogels gradually decreased as the percentage of BM SF increased in the blends. Maximum pore size was obtained from BM0.5/AA2.5, whereas BM2.5/AA0.5 showed minimum pore size (**Figure 5.4A**). Here, the smaller hydrophobic fragments (GSGAGG) of BM SF chains (MW ~ 390 kDa) behaved as *filler* to this hybrid polymeric network system. On the other hand, AA SF possess relatively longer chains (~ 460 kDa) with greater hydrophobicity (poly-Ala) that interacted with themselves, leaving the free spaces between the two zones of the interface. This event finally resulted in the formation of bigger pores (**Figure A5.8 A**). This type of phenomenon was also observed in freeze dried

scaffolds from *Antheraea mylitta* SF[390]. However, as the concentration of *filler* BM SF increased in the blends, it occupied the free spaces, thereby resulting in reduced pore size. The *β*-sheets transition in the hydrogels was confirmed by FTIR (**Figure 5.4B**). The maximum amount of *β*-sheets was observed in BM1.5/AA1.5. This might be due to the faster interaction between chains that finally lead to the faster conformational changes. Gelation time can be correlated with the *β*-sheets content of the hydrogels. It was evident from the *β*-sheets content (~ 83%) of BM0.5/AA2.5 which showed faster gelation than BM2.5/AA0.5 having the *β*-sheets content of ~ 65%) **(Table A5.6)**.

Swelling ability of hydrogels or scaffolds is one of the most important prerequisites for tissue engineering applications. The swelling ratio increased with the increase of BM SF in the blend **(Figure 5.4D)**. This could be possibly because of the gross hydrophobicity and cross linking density in the blends. BM0.5/AA2.5 showed minimum swelling owing to the maximum amount of hydrophobic chains it possesses as well as high amount of β-sheets content (~ 83%) that further resisted the hydrogel from swelling.

Biodegradation of implanted materials should be accompanied with the neo-tissue regeneration. For biodegradation purpose, a protease cocktail was used. It showed that blends with higher amount of AA SF were degraded relatively at a faster rate (**Figure 5.4E**). This might be due to presence of higher amount of target sites (Xaa-hydrophobic-*cut*-hydrophobic-Xaa, where Xaa is any amino acid and hydrophobic amino acid is Ala) for proteases in AA SF chains.

Mechanical behaviors of any implantable system have to be analyzed to understand its efficacy upon implantation, particularly in load bearing applications. The compressive modulus was gradually increased as the concentration of *filler* BM SF increased in blends. The minimum compressive modulus was recorded for BM0.5/AA2.5 in which longer hydrophobic chains of AA SF were predominant (**Figure 5.5A**). Basically it was a homogenous complex of same molecules that rearranged themselves in a systematic way. However, as the *filler* BM SF concentration increased, the composite became a heterogeneous polymeric network. However, reduced compressive modulus was recorded for BM2.5/AA0.5 as it became a homogeneous complex. It is a well-known fact that mechanical strength is higher in heterogeneous matrix than homogenous complex[517, 518]. If we compare between two "*close to homogenous*" complexes *i.e.,* BM2.5/AA0.5 and BM0.5/AA2.5, the later combination showed less compressive modulus. This

could be correlated to the larger pores in BM0.5/AA2.5 leaving more void spaces making it more sponge like material, whereas BM2.5/AA0.5 showed solid like construct comprising of higher mechanical strength. From the stress-strain curve, it was evident that the maximum compressive stress was gradually decreased with the increase of BM SF in the blends. Hydrogels with high amount BM SF became more brittle than the hydrogels containing high amount AA SF. To understand the deformation behavior of hydrogels, the cyclic compressive testing was performed. The hydrogels with higher amount of AA SF (*e.g.,* BM0.5/AA2.5) showed minimum loss of ultimate compressive stress and retained ~ 80% elasticity after 50 cycles (**Figure A5.10 B, VI**). The high elasticity of BM0.5/AA2.5 might be due to the longer chains of AA SF that entangled making a sponge like matrix, whereas the *filler* BM SF filled the pores and became a solid like construct.

To understand the impact of geometry on mechanical properties, two different diameters of hydrogels were selected; 12 mm and 20 mm. It was noticed that compressive modulus was increased with the increase in diameter for any hydrogel systems **(Figure 5.5B**). This might be due to the presence of more cross-linking (chemical or physical) in larger diameter group. There are various reports that indicate the impact of geometrical parameter on compressive modulus of hydrogel implants[508, 519]. Therefore, the volume of implanted hydrogel might play an important role in disc biomechanics. It could be expected that larger diameter of hydrogel might provide higher compressive modulus allowing the intervertebral discs to withstand more loads. Moreover, hydrogels in confined mechanical testing showed higher values than unconfined method for all hydrogel systems. There are several factors (*viz.,* under-filling, over-filling or line-to-line fit to the nucleus cavity with hydrogel or confinement of NP) influencing the biomechanics that could be resolved by this *in vitro* approach. To check the stability of the fabricated hydrogels, they were placed in PBS (pH 7.4) and compressive modulus was recoded on day 1 and day 14. The compressive modulus did not change significantly after day 1 of gelation for all cases, except in BM2.5/AA0.5 where the compressive modulus was significantly increased (~ 2-fold). It could be hypothesized that the gelation process in this combination was very slow and took the maximum time to form hydrogel in which relatively smaller BM SF chains interacted with each other making a highly compact construct (**Figure 5.5D**).

To understand the effect of biological fluids on compressive modulus, hydrogels were treated in solutions of different pH and ionic strength. The compressive modulus of all the hydrogels was increased in pH 4.0, whereas the value was decreased in pH 9.0 (**Figure 5.5E**). The isoelectric pH of silk fibroin is varied from pH 4.0-5.0[520]. After transferring the hydrogels into the solution of pH below the isoelectric point, intermolecular interaction increased inside the hydrogel resulting in higher compressive modulus. In contrast, the higher pH (9.0) might degenerate the protein chains that caused reduced compressive modulus. BM0.5/AA2.5 showed the maximum value of percentage increase of compressive modulus in response to pH 4.0. It was therefore confirmed that AA SF had greater pH sensitivity than BM SF. All the hydrogel systems recovered ~ 70% of compressive modulus after getting transferred from alkali pH (9.0) to neutral pH (7.4) (**Figure A5.9**). However, the compressive modulus remained unchanged in salt concentration up to 1000 mM NaCl (**Figure 5.5F**). From amplitude sweep of hydrogels, liner viscoelastic region (LVER) was determined. LVR was extended till ~ 222% of strain for BM0.5/AA2.5. This might be due to the interpenetrating network of longer and homogeneous AA SF chains (**Figure 5.6C**) in the BM0.5/AA2.5. Thixotropic test confirmed the reversibility of the hydrogel structures under very high strain (1000%).

Cytocompatibility assessment of a biomaterial used for tissue engineering applications is very much essential for its clinical translation. All the hydrogels were found to be compatible for the growth and proliferation of NP cells, enhanced proliferation being observed for the hydrogels having higher amount of AA SF (**Figure 5.7**). This might be due to presence of RGD (arginine-glycine-aspartic acid) motif in AA SF that supported faster cell-matrix adhesion and proliferation. Few reports in the recent past have suggested this plausible effect of AA SF in various tissue engineering applications[197, 491, 492, 521]. Though the NP tissue exhibits fewer number of cells, it could be expected that the high proliferation rate would provide the sufficient amount of healthy cells within a very short period of time and the healthy cells would secret adequate amount of ECM molecules to recover the discs from disease condition.

Ex vivo IVD organ culture model is a well-established technique to understand the biological and biomechanical measures of disc health and disease[522-524]. However, there are several reports on injectable hydrogel to be used as NP substitute to restore the disc biomechanics in *ex vivo* model. For instance, Showalter et al., used the degenerated human lumber discs wherein hydrogel

(20% teleostean, 3% N-carboxyethyl chitosan, and 7.5% oxidized dextran) was injected to restore the biomechanics after physiologic cyclic compressive loading in an *ex vivo* model[525]. In a similar kind of study, Malhotra et al., investigated the hyaluronic acid-gelatin based injectable hydrogel to restore the range of motion of degenerated discs upon hydrogel implantation in the ex-vivo model[526]. In the current study, an *ex vivo* model system was developed in order to speculate the feasibility of these hydrogels in NP tissue engineering applications. The hydrogel assisted regenerated disc showed good recovery of compressive modulus (**Figure 5.8**) when compared to degenerated disc. So, the previous reports and our current study may provide a solid foundation to evaluate the efficacy and reliability of *ex vivo* model for better understanding of disc biomechanics using hydrogel implants.

For *in situ* applications, the faster gelation always gets precedence. BM1.5/AA1.5 combination took lesser time than any other combinations. On the other hand, compressive modulus of BM05/AA2.5 was in the range of native NP gel (5.39 ± 2.56 kPa)[50]. Other plausible factors of BM05/AA2.5 included superior elasticity and cytocompatibility than rest of the combinations. However, BM05/AA2.5 was highly sensitive to pH changes. Therefore, it could be a novel approach to select a suitable combination of silk hydrogels in a particular physiological condition.

5.5. Significant findings

The significant findings from this chapter are as follows:

- Two naturally derived silk proteins (*B. mori* SF and *A. assamensis* SF) of different hydropathicity were self-assembled independent of external stimuli and form hydrogel. Suitable combinations of these two proteins were investigated for *in situ* applications in NP replacement.
- The gelation process could be tuned by types, concentration and molecular weight of SF, temperature, pH and ionic concentrations.
- The tunable mechanical properties *e.g.,* compressive modulus and elastic behavior were achieved by varying the silk fibroin ratios. The efficiency of the hydrogels lies in the fact that they could recover the compressive modulus from adverse conditions.
- Further, cytocompatibility study using primary porcine NP cells and the *ex vivo* study supported the possibility of hydrogels to its clinical translation.

Overall, *in situ* application of the developed silk based hydrogel system could be a novel approach in disc regeneration therapy.

Chapter 6

Development of a Minimally Invasive Injectable Bioactive Silk-hydrogel Functionalized with Human Decellularized Wharton's Jelly Extracellular Matrix (dWJECM) for Nucleus Pulposus (NP) Tissue Replacement Therapy

This chapter describes a novel cross-linker free silk fibroin and decellularized Wharton's jelly matrix-based hybrid hydrogel designed to be injectable, hence minimally invasive, possess enhanced bioactivity, and shares all the mechanical and rheological properties similar to the native NP tissue. Here, the pre-existing silk hydrogel system as discussed in chapter 5 was enriched with biological cues that came from Wharton's jelly ECM.

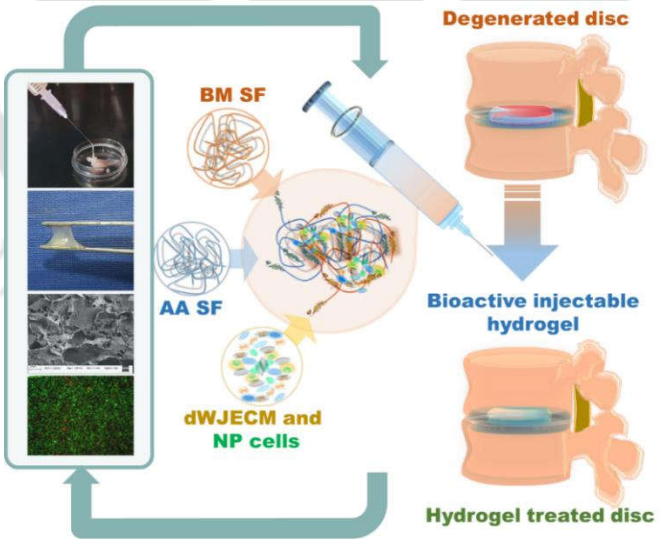

Bhunia BK, Bandyopadhyay A, Dey S, Mandal BB. Silk-hydrogel functionalized with human decellularized Wharton's jelly extracellular matrix (dWJECM) as a minimally invasive injectable hydrogel system for potential nucleus pulposus tissue replacement therapy. (**Submitted to journal**).

ABSTRACT

Intervertebral disc degeneration (IDD) is a primary cause for chronic low back pain (LBP), a common health problem with high incidence and the leading cause of disability globally, affecting performance at work. It is believed that the early stages of disc degeneration in terms of functional and anatomical abnormalities start from the central nucleus pulposus (NP) tissue of the intervertebral disc (IVD); hence the regeneration of this tissue has become a prime concern. A plethora of hydrogel systems have been investigated as NP tissue substitute over the years, yet challenges remain for their clinical translation. In the present study, we formulated a minimally invasive injectable cross-linker free bioactive silk based hybrid hydrogel system functionalized with decellularized human Wharton's jelly extracellular matrix (dWJECM) as an ampule of bioactive cues. The centrifugation based decellularization method removed > 92% of cellular components and preserved > 83% of ECM composition. The hydrogels were extensively investigated for secondary structure and surface properties through FTIR and FESEM, respectively. Notably, the developed hydrogels were found to mimic rheological and mechanical properties of the native NP tissue when the dWJECM content was 0.5% (w/v) in the base silk hydrogel. Finally, the hydrogels were found to support cell viability, proliferation, and tissue maturation offering great potential for future applications related to NP tissue engineering.

6.1. Introduction

The prime concern of nucleus pulposus (NP) tissue engineering is to fabricate a suitable hydrogel system which is mechanically and rheologically resembles the NP gel. It should retain a high amount of water for the maintenance of hydrostatic pressure as well as support the cellular growth and deposition of NP-specific extracellular matrix (ECM). It is believed that the early stages of degeneration, *i.e.,* anatomical and functional abnormalities, mainly start from the NP; hence, restoration of it may be an ideal step towards IDD (intervertebral disc degeneration) treatment.

A wide range of natural polymers like hyaluronic acid (HA), chitosan, alginate and gellan gum are being utilized as NP tissue substitute for decades because of their biocompatibility, biodegradability, and bioactivity[4, 252, 300, 323, 343]. But these are associated with some disadvantages such as impurities, long term stability, and poor mechanical performance unless a high concentration of cross-linkers are applied[282].

Despite SF scaffolds (lamellar or porous) being extensively used to fabricate AF constructs silk-based hydrogels are also being explored for NP replacement. Silk fibroin (SF) based hydrogel was used in combination with other polymers such as polyurethane or alone[239, 345, 347, 424, 508]. One remarkable study of NP repair was the clinical trial of NuCore® (Spine Wave Inc., Shelton, CT, USA), a recombinant protein co-polymer of silk and elastin[348]. However, there are several methods like use of chemicals (salts, organic solvents, and large polymeric agents)[498-500], varying the pH, applying the physical stimulus (mechanical shear force, temperature, sonication, and electric filed) and cross-linkers (horseradish peroxidase, genipin and riboflavin) that are used to fabricate the hydrogel with only silk fibroin[495, 497, 527]. The limitations of these external stimuli include the use of some sophisticated and expensive instruments as well as chances of contamination. Moreover, the cytotoxic effect of cross-linkers is a matter of concern since it adversely affects cellular viability. In the previous work (*chapter 5*), we fabricated the silk-based hydrogel without any external stimuli. The silk fibroin (SF) from two different sources (*Bombyx mori* SF as mulberry and *Antheraea assamensis* SF as non-mulberry source) were blended together. The SF solution eventually self-assembled and transformed into hydrogel due to the differences in their hydropathicity (hydrophobic-hydrophilic alteration)[207]. The tunable mechanical and rheological properties could be achieved depending on the protein combinations.

In this study, we selected a suitable combination of two SF proteins functionalized with decellularized Wharton's jelly matrix (dWJECM) that provided the mechanical and rheological properties matched to the native NP tissue (gel).

Extracellular matrix (ECM) and ECM-mimicking scaffolds could be the ideal candidates for tissue engineering applications as cells are surrounded by ECM components. The ECM functions as supporting material and regulates cell survival, proliferation, morphogenesis, and differentiation[528, 529]. Moreover, the various bioactive molecules such as growth factors and cytokines integrated inside the ECM can modulate the signal transduction[530, 531]. Ideally, the scaffolds or hydrogel systems used for tissue engineering can provide a similar microenvironment to the seeded cells mimicking the *in vivo* conditions. However, native ECMs are composed of different kinds of proteins with very intricate structures and are very difficult to emulate. Hence, decellularization of ECM and application of the same as a constituent for tissue engineering scaffolds is becoming widespread.

Several methods have been applied for decellularization, including physical, chemical, and enzymatic treatments[532, 533]. However, these methods are associated with their respective advantages and disadvantages. For instance, some of these methods can efficiently remove the cellular components that are mainly known to be immunogenic, while they also adversely affect the microstructure of ECM that eventually alters its bio-functionalities. In this study, we adopted a very simple and efficient method to decellularize the human umbilical Wharton's jelly (WJ) tissue without using any chemical or enzymatic treatment to preserve its composition and bioactivity.

WJ is a mucosal connective tissue surrounding the umbilical cord vessels and is wrapped with an amniotic epithelium layer[534]. The primary function of this tissue is to maintain and support the blood flow during fetal movements, labour, or any kind of cord abnormalities like knots. To perform such tremendous job, Wharton's jelly needs high mechanical strength, which comes from its unique biochemical composition. The WJ matrix is rich in collagen, elastin, hyaluronan, and sulfated glycosaminoglycan[534]. WJ matrix can provide several characteristic features in a scaffolding material used for different tissue engineering applications[535-538]. Although the potential of the WJ matrix in the field of IVD tissue engineering is mostly unexplored, a recent study showed the potency of decellularized WJ matrix to revert the degenerated IVD cells that lost

their chondrocyte-like phenotype[539]. In general, the 3D microenvironment of jelly potentially provides all the suitable conditions for cell proliferation and differentiation[540].

With these favorable features of Wharton's Jelly matrix, in the current study, for the first time, we reported a cross-linker free self-assembled silk based minimally invasive injectable bioactive hydrogel functionalized with decellularized Wharton's jelly matrix (dWJECM) as NP tissue substitute. In this frame, the prime goal of this study was to develop a suitable hydrogel system, which was rheologically and mechanically, similar to the native NP tissue. Therefore, the developed hydrogel was extensively investigated for its biomechanics and cytocompatibility to open up a new possible direction with the decellularized WJ matrix towards disc degeneration therapy.

6.2. Materials and methods

6.2.1. Collection of human umbilical cord

Human umbilical cords were collected from a local hospital (Guwahati Neurological Research Centre; GNRC, North Guwahati) with the due consent of pregnant mothers and/their guardians, and all the procedures were performed in accordance with the approved ethical committees of both Indian Institute Technology Guwahati and GNRC hospital. The umbilical cords were then put in PBS (phosphate buffered saline, pH 7.4) supplemented with penicillin (800 $U.mL^{-1}$), streptomycin (9.1 $mg.mL^{-1}$) and amphotericin B (0.25 $mg.mL^{-1}$), and immediately stored at -80 °C. The decellularization process was performed within 72 h of collection.

6.2.2. Isolation and decellularization of Wharton's jelly matrix (dWJECM)

Decellularization of Wharton's jelly was performed following a modified protocol described by Bakhtyar *et al.,*[541]. In brief, the umbilical cords were cut into small pieces (2-3 cm in length) followed by vigorous washing with sterile PBS supplemented with 1% (w/v) antibiotic/antimycotic to remove the remaining bloodstain. Each piece was then dissected to separate the arteries, vein, and underlying epithelium layer, followed by chopping into tiny pieces. Thereafter, the chopped pieces (10 -15 pieces) were transferred into a 50 mL conical tube with 20 mL of sterile PBS supplemented with antibiotic/antimycotic solution and incubated at 4 °C under the strong shaking condition for 48 h. Post incubation, the mixture was passed through a filter mesh to separate the larger tissue fractions, and the filtered solution was centrifuged at 5,000 (5K) and 10,000 (10K) rpm for 10 min to settle down cellular fraction. The supernatant was collected followed by lyophilization to get the decellularized Wharton's jelly extracellular matrix (dWJECM) in powder form.

6.2.3. Characterization of lyophilized dWJECM

6.2.3.1. Solubility assay

To determine the solubility, 0.1% (w/v) lyophilized dWJECM powder was dissolved in deionized water and incubated at 4 °C for 24 h with mild shaking followed by centrifugation at 10000 rpm to separate the undissolved fraction. The dissolved fraction was investigated under optical microscopy (Evos FL, life technologies), and the particle size distribution was determined by the

dynamic light scattering (DLS) method. The native WJ (before centrifugation) and the dWJECM (after centrifugation, but before lyophilization) were used as control.

6.2.3.2. Dynamic light scattering (DLS)

Particle size and distribution pattern of dWJECM were evaluated by DLS (Malvern, Zetasizer Nano ZS90). The zetasizer is equipped with a He-Ne laser of 633 nm. BSA solution (0.1%. w/v) and the centrifuged dWJECM solution (prior to lyophilization) was used as control. Data were plotted as the mean of triplicate experiments, and each experiment was run 15 times.

6.2.4. Biochemical assessment

6.2.4.1. DNA quantification

Lyophilized dWJECM powder from both fractions (5K and 10 K rpm) was digested with papain digestion cocktail (5 mM L-cysteine, 125 $mg.mL^{-1}$ papain, 5 mM EDTA, and 100 mM Na_2HPO_4 pH 6.2) at 60 °C for 16 h with mild shaking. After digestion, a PicoGreen DNA assay was performed to measure the total DNA content in the decellularized sample following the manufacturer's protocol (Invitrogen, Life Technologies). In brief, 25 µL aliquot from digested sample of both decellularized and the native cord was put into a 96-well plate followed by addition of 75 µL of 1 × Tris-EDTA buffer and 100 µL of Quant-iT PicoGreen reagent (1:200 dilutions). A standard curve was generated using λ-phage DNA. The data were recorded using a fluorescence spectrophotometer (Tecan Infinite 200 PRO series) with an excitation and emission wavelength of 480 and 528 nm, respectively.

6.2.4.2. Sulfated glycosaminoglycans (sGAG) quantification

Sulfated GAG (sGAG) content in lyophilized dWJECM (in both fractions, 5K, and 10K) was estimated using 1, 9-dimethylmethylene blue (DMMB) assay method[542]. For this assay, 200 µL of DMMB reagent was mixed with 20 µL of each papain digested sample, and absorbance was recorded immediately at 525 nm. The non-centrifuged WJECM (without decellularization) served as control. Shark chondroitin sulfate (Sigma, U.S.A.) was used to generate the standard curve.

6.2.4.3. Estimation of total collagen content

The total collagen content of both lyophilized dWJECM and non-centrifuged (without decellularization) WJECM powder was determined following a previously described protocol[542]. In brief, samples were digested in pepsin solution (1 mg·mL^{-1} pepsin, pH 3.0) at 4 °C for 48 h followed by centrifugation at 10,000 rpm for 15 min to collect the supernatant from undigested larger particles. 100 µL of each sample was pipetted in a 96-well plate and kept at 37 °C for 24 h for complete drying. Thereafter, each well was added with 100 µL direct red (1 mg·mL^{-1} in a saturated picric acid solution, pH 3.5; Sigma, U.S.A.) dye solution and incubated at room temperature (25 °C) for 1 h with the mild shaking condition. The dye-sample complex was then dissolved in 0.1 N NaOH solution after a vigorous washing with 0.01 N HCl, and absorbance was measured at 550 nm using a multiplate reader (Tecan Infinite M200 PRO series). A standard curve was generated with bovine collagen (Sigma, U.S.A.).

6.2.4.4. Staining of sGAG and collagen

Glass coverslips (200 x 200 mm) were coated with a 100 µl of aliquot from each fraction (5K and 10K rpm) of dWJECM and allowed to air dry at room temperature (RT, 25 °C) overnight, which was further followed by EDC-NHS (EDC (1-ethyl-3-(3-dimethylamino) propyl carbodiimide- N-hydroxysuccinimide, Sigma, U.S.A.) cross-linking for 24 h to stabilize the coating on the glass surface. To visualize sGAG, the coated glass coverslips were stained with 1% (w/v) alcian blue (Sigma, U.S.A.) in 1 N HCl (pH 2.5) for 40 min as reported previously[542]. Picrosirius red staining was performed to visualize collagen in dWJECM following the previously described protocol[543]. In brief, coated coverslips were incubated with 0.1% (w/v) picrosirius red (Sigma, U.S.A.) solution prepared in saturated picric acid (Himedia, India) for 1 h followed by washing with acidified water, air drying, and imaging under microscopy (Evos FL, life technologies). Native Wharton's jelly (prior to decellularization by centrifugation) coated glass coverslips were treated as control.

6.2.5. Fabrication of hydrogel

6.2.5.1. Isolation of silk fibroin (SF)

The aqueous solution of silk fibroin (SF) was isolated from both *B. mori* (mulberry SF) and *A. assamensis* (non-mulberry SF) following the previously described protocols[200]. In brief, for

mulberry SF, *B. mori* cocoons were chopped into small pieces followed by degumming in 0.02 M sodium carbonate (Na_2CO_3) to remove the glue-like sericin protein covering the fibroin fibers. The dried degummed fibers were then dissolved in 9.3 M lithium bromide (LiBr, Sigma, U.S.A.) and kept at 60 °C for 4 h followed by subsequent dialysis to remove the residual LiBr molecules. On the other hand, to isolate non-mulberry SF, silk glands from *A. assamensis* were dissolved in ice-cold 1% (w/v) sodium dodecyl sulfate (SDS) solution followed by dialysis against deionized water at 4 °C. Both types of isolated proteins were measured gravimetrically and stored at 4 °C for future use.

6.2.5.2. Formulation of dWJECM functionalized hydrogel

The isolated mulberry and non-mulberry SF were blended in a ratio of 0.5:1.0 (w/v), wherein dWJECM was mixed in the range of 0.1 to 1% (w/v) summarized in **Table 6.1**. The blended solutions were then incubated at 37 °C for polymerization.

Table 6.1. Preparation of SF-dWJECM blends

Types of silk fibroin (SF)		dWJECM (% w/v)	Sample code
Mulberry SF (% w/v)	**Non-mulberry SF (% w/v)**		
0.5	1.0	0.1	SH with 0.1% dWJECM
0.5	1.0	0.5	SH with 0.5% dWJECM
0.5	1.0	1.0	SH with 1% dWJECM
0.5	1.0	-	Control gel (SH)
0.5	-		BM0.5
-	1.0		AA1.0
-	-	1.0	dWJECM1.0

SH = silk hydrogel, BM = *Bombyx mori,* AA = *Antheraea assamensis*

6.2.6. Physicochemical characterization of hydrogel

6.2.6.1. Gelation kinetics by visible light spectroscopy

To understand the gelation kinetics, the blended solution was investigated using a spectrophotometer (Multiskan SkyHigh, ThermoFisher Scientific, U.S.A.) that recorded the turbidity change (as the polymerization continued with time) at 600 nm of the blended solution. For this assay, 200 µL of each blended solution was kept into a 96-well plate followed by recording the data at every 3 min interval at 37 °C. BM0.5, AA1.0, and dWJECM1.0 were used as control.

6.2.6.2. Protein release assay

To confirm the entrapment of water-soluble dWJECM into the silk fibroin polymeric network, a protein release assay was performed using Bradford assay. In brief, the blended hydrogels were incubated in 3 mL of PBS (phosphate-buffered saline, pH 7.4) at room temperature (RT, 25 °C) with gentle shaking. 20 µL of an aliquot from each group in a definite interval time was mixed with 200 µL of Bradford reagent (Sigma, U.S.A.) followed by incubation for 10 min at dark. BSA (bovine serum albumin, Himedia, Sigma) was used to generate the standard curve. The data was measured using a spectrophotometer (MultiSkan SkyHigh, ThermoFisher Scientific, U.S.A.) at 595 nm.

6.2.6.3. Field Emission scanning electron microscopy (FESEM)

Surface morphology, pore size, and interconnectivity of the lyophilized dWJECM blended silk hydrogels were investigated using FESEM (Zeiss Sigma, Carl Zeiss AG, Germany) at an operating voltage of 3 kV. Hydrogels were subjected to freeze fractured in liquid nitrogen (-196 °C) followed by lyophilization. The lyophilized samples were then sputtered with gold that provided the conductivity to the samples. The average pore size of each hydrogel was determined using ImageJ 1.4 (Wayne Rasband) software by measuring ~ 50 pores randomly.

6.2.6.4. Fourier transform infrared spectroscopy (FTIR)

FTIR (Spectrum Two, PerkinElmer, U.K.) was used to analyze the secondary structure in the lyophilized hydrogel systems. Briefly, the lyophilized hydrogels from each group were placed on the measuring window and analyzed using ATR mode. All transmitted spectra were measured within the spectral range of 4000-400 cm^{-1} with a resolution of 4 cm^{-1} and 32 scans. Lyophilized

powder of AA1.0, BM0.5, and dWJECM0.1 served as control. The absorbance bands in the range of 1650-1620 cm^{-1}, 1544-1514 cm^{-1} and 1236-1220 cm^{-1} were attributed as amide I, amide II and amide III, respectively.

6.2.6.5. Mechanical behavior of hydrogels

Different mechanical properties, including peel test, injectability, and compressive behavior in the confined mode, were determined using a universal testing machine (Instron 5944, Norwood, MA, U.S.A.) equipped with a 100 N load cell. All the mechanical tests were conducted 2 h post gelation. For the peel test, a custom-designed mold was fabricated wherein hydrogel was placed between two PDMS (Polydimethylsiloxane) sheets in a sandwich model. A standard 90° peeling test was performed for each hydrogel system with a constant peeling speed of 5 $mm.min^{-1}$. The peeling strength was measured from the stress-strain curve at 5% strain.

The injectability test was performed to determine the maximum force required to inject the hydrogel through a standard 23-gauge needle (inner diameter, ~ 337 µm). For this purpose, the hydrogel filled 2 mL syringe was placed in a 25 mL empty glass cylinder. The barrel flange helped the syringe to hang inside the glass cylinder from its mouth. The plunger flange of the syringe was attached to the upper compression platen connected to the load cell. All the tests were performed with the cross-head displacement speed of 1, 30, and 100 $mm.min^{-1}$. The stress-strain curve was plotted for each cross-head displacement speed from the load-displacement measurement.

For confined compressive testing, the hydrogel was placed inside a manually prepared polypropylene cylindrical tube that provided the confinement to the hydrogel. The diameter of the metal plunger (connected to the upper compression platen) perfectly matched the diameter of the polypropylene tube that stopped leakage of hydrogel during the compression. The cross-head speed was adjusted to 5 $mm.min^{-1}$. The compressive modulus was calculated from the stress-strain curve at 5% strain.

6.2.6.6. Rheological properties of hydrogels

In order to study the rheological properties, hydrogels were subjected to amplitude sweep test, frequency sweep test, and thixotropic analysis using a rheometer (MCR 302, Anton Paar) equipped with a steel parallel plate of 25 mm in diameter. All the tests were performed at 37 °C with a gap distance of 500 µm and 0.1 N of sample force. The amplitude sweep test with a dynamic shear

strain (γ) varied from 0.1-1000% was carried out to determine the linear viscoelastic regime (LVER). The frequency sweep test was conducted over a wide frequency range (1 to 100 rad.s^{-1}) within the LVER (γ = 1%) of hydrogels. The change in complex viscosity (η*) in response to amplitude sweep was plotted against shear strain (γ). The tan δ (G"/G') was measured for all hydrogels after plotting against shear strain (γ) and angular frequency (ω). For the thixotropic study, hydrogels were applied with step strain, set at 1000% for 25 seconds, followed by 1% for 100 seconds at a constant angular frequency (ω = 10 rad.s^{-1}).

6.2.7. Biological assessments

6.2.7.1. Nucleus pulposus (NP) cells isolation and culture

NP cells from porcine lumbar discs were isolated and cultured for cytocompatibility assessments with the fabricated hydrogels. Porcine lumbar portions were collected from a local abattoir, followed by dissecting the attached muscle and tendon and separating the gelatinous NP tissue from the adjoining annulus fibrosus (AF) rings. The isolated NP gel was then thoroughly washed with sterile PBS (pH 7.4) and kept for digestion with collagenase (0.03%, w/v; Sigma, U.S.A.) for 7-8 h at 37 °C. The digested sample was then passed through the cell strainer (pore size, 70 µm) followed by centrifugation (250 g for 10 min) and washing with sterile PBS to remove the enzyme traces. The NP cell pellet was resuspended, plated and cultured in high glucose DMEM supplemented with 10% (v/v) FBS (fetal bovine serum) and 1% (v/v) penicillin-streptomycin at 37 °C in a humidified (85%) CO_2 (5%) incubator. The culture media was replaced with fresh media every 3rd day. All the cell culture grade chemicals were purchased from Gibco, Life Technologies, ThermoFisher Scientific, U.S.A.

6.2.7.2. Cell viability assay

Cell viability was checked at two stages - just after injection, passing through a 23-gauge needle, and post 7 days of incubation. Cell encapsulated hydrogel (SH with 0.5% dWJECM) was passed through the needle (23-gauge), and the cell viability was immediately checked using Calcein-AM-ethidium homodimer dye (Gibco, life technologies, ThermoFisher, U.S.A.). To assess the long-term cell viability, a custom-designed mold was used wherein two glass coverslips (11 x 25 x 0.4 mm) were fixed on top of each other with spacers. The gap between the two coverslips was adjusted to 0.4 mm (a coverslip thickness). This gap was then filled with the cell encapsulated

solution (at pre-gelation state), which was eventually transformed into hydrogel upon incubation at 37 °C. The solution was evenly spread throughout the space due to the capillary action. Post gelation, the total setup was incubated with complete cell culture medium (high glucose DMEM with 10% (w/v) FBS) in a humidified CO_2 incubator for 7 days, and cell viability was assessed using Calcein-AM-ethidium homodimer dye under a fluorescence microscope (Evos FL, Life technologies, U.S.A.).

6.2.7.3. Cell proliferation assay

Cell proliferation assay was conducted through the DNA quantification estimation. A custom-designed *gel-in gel* device was fabricated for all the biological experiments, including DNA quantification, histological analysis, and gene expression study. The device was agarose (Sigma, U.S.A) based solid cylinder (10 x 10 mm) wherein a groove (6 x 4 mm) was made in the center using a 6 mm biopsy punch. The groove was filled with cell encapsulated hydrogel (100 µL) for the biological experiments. The cell proliferation was measured in terms of DNA quantification using PicoGreen dsDNA quantification assay following the manufacture's protocol. The NP cell encapsulated (1 x 10^5 cell per hydrogel, SH with 0.5% dWJECM) *gel-in-gel* devices were incubated with high glucose DMEM for 7 days with periodic media changes. The same amount of cells was also encapsulated in a control gel (SH). Post incubation, hydrogels were digested with papain digestion solution (125 mg·mL^{-1} papain, 5 mM EDTA, 100 mM Na_2HPO_4, and 5 mM L-cysteine, pH 6.2; Sigma, U.S.A.) at 60 °C for 16 h. The digested hydrogels were then centrifuged at 10,000 rpm for 15 min, followed by the collection of supernatant containing DNA. The DNA quantification was performed using the method as discussed in *section 6.2.4.1.*

6.2.7.4. Gene expression study

To isolate RNA, 1, 7, and 14 days post cultured NP cell encapsulated hydrogels (SH with 0.5% dWJECM) were chopped in TRIzol solution (Sigma, U.S.A.) followed by the centrifugation at 12,000 rpm for 10 min at 4 °C. The clear supernatant (cell lysate) was mixed with 200 µL of chloroform and incubated for 20 min, followed by centrifugation at 12,000 rpm for 10 min at 4 °C. Post centrifugation, the upper transparent layer containing RNA was carefully pipetted out and put in a separate centrifuge tube, followed by precipitation using chilled isopropanol for 20 min. The RNA was pelleted down by centrifugation at 12000 rpm for 15 min and repeatedly washed

with ice-cold DNA diluent to achieve better purity. The final RNA pellet was resuspended in RNase free water for quantification using a spectrophotometer MultiSkan Sky (Thermofisher Scientific, U.S.A.). A thermal recycler Veriti (Applied Biosystems, Thermofisher Scientific, U.S.A.) was used to reverse-transcribe the purified RNA into cDNA using the cDNA reverse-transcription kit (Applied Biosystems, Thermofisher Scientific, U.S.A.). NP specific gene expression (col II, sox9, and aggrecan) was evaluated through real-time PCR (RT-PCR) using the 20 µL reaction of cDNA, Power SYBR Green master mix (Applied Biosystems, Invitrogen, U.S.A.) and, forward/reverse primers (sequences in **Table 6.2**). The QuantStudio 3 PCR system was used (Applied Biosystem 7500, ThermoFisher Scientific, U.S.A.) for RT-PCR. GAPDH (Glyceraldehyde 3-phosphate dehydrogenase) gene expression was used as an internal control to normalize the obtained delta values over the background, and the comparative Ct method ($2^{-\Delta\Delta Ct}$) was followed for the relative gene expression.

Table 6.2: Sequences of the primers for real time PCR

Gene	Sequence	NCBI Accession no.
GAPDH	F5′-TCGGAGTGAACGGATTTGG-3′ R 5′-CCAGAGTTAAAAGCAGCCCT-3′	NM_001206359.1
Col *II*	F5’-CAGGTGAAGGTGGGAAACCA-3′ R 5′-ACCCACGAGGCCAGGA-3′	AF201724.1
Sox9	F5′-TTCCGCGACGTGGACAT-3′ R 5′-GGCGGCAGGTACTGGTCAAACTC-3′	NM_213843.1
ACAN	F5′-CCCAACCAGCCTGACAACTT-3′ R 5′-CCTTCTCGTGCCAGATCATCA-3′	NM_001164652.1

6.2.7.5. Histological analysis

For histological studies like H&E and immunofluorescence staining, the *gel-in-gel* devices with encapsulated NP cells were maintained in chondrogenic media [insulin (6.25 µg.mL^{-1}), proline (40

mg.mL^{-1}), bovine serum albumin (BSA; 1.25 mg.mL^{-1}), transforming growth factor-β1 (TGF-β1; 10 ng.mL^{-1}), ascorbic acid (50 mg.mL^{-1}), transferrin (6.25 µg.mL^{-1}), selenious acid (6.25 µg.mL^{-1}), sodium pyruvate (100 mg.mL^{-1}) and dexamethasone (100 nM)] for two weeks. Both the cell-free and cell encapsulated hydrogels (SH with 0.5% (w/v) dWJECM) were fixed in 10% (v/v) NBF (neutral buffered solution; Sigma, U.S.A.) for 24 h at room temperature (25 °C). Hydrogels were then incubated with 15% (w/v) sucrose solution for 6 h, followed by transferring to 30% (w/v) sucrose solution for the next 12 h at 4 °C. Thereafter, hydrogels were placed on the cryostat block, completely covering with tissue freezing medium (PolyFreeze, Sigma, U.S.A) followed by micro-sectioning (8 µm) using a cryomicrotome (Leica CM1860 UV, Leica Biosystem Richmond, Inc. U.S.A). To study cellular morphology, distribution, and arrangement, micro-sections were stained with hematoxylin-eosin (Sigma, U.S.A.) and examined under the microscope (Evos FL, Life Technologies, U.S.A.). Cell-free hydrogel micro-sections were stained with alcian blue and picrosirius red (as described in *section 6.2.4.4*) for sGAG and collagen, respectively. The native NP gel was treated as a control system.

6.2.8. Statistical analysis

Quantitative analysis experiments were carried out in triplicates (n = 3) unless specified, and results have been expressed in the form of mean ± standard deviation. The obtained data were statistically analyzed using one-way analysis of variance (ANOVA) in Origin Pro (OriginLab, U.S.A.). Groups were considered to possess significant statistical differences for $p \leq 0.05$, and a highly significant difference was assigned for $p \leq 0.01$ and $p \leq 0.001$.

6.3. Results

6.3.1. Decellularization and characterization of Wharton's jelly matrix

A simple method was adopted to remove the cellular components of Wharton's jelly (WJ) matrix without using any harsh chemical treatment, avoiding the risk of adverse effects on biological cues like growth factors. The WJ portion was isolated and purified from the umbilical cord after the careful dissection and removal of vein/arteries and the underlying epithelial layers of it (**Figure 6.1**). The WJ was chopped into small pieces and incubated with the sterile PBS at 4 °C for 48 h under vigorous agitation. The water-soluble WJ fraction was collected upon filtering through a mesh separating the larger tissue particles. To perform the decellularization, the water-soluble WJ fraction was centrifuged at two different rpm: 5K and 10 K. The supernatant was lyophilized, and the obtained white powder was investigated for further studies, including the solubility assessment through particle size analysis, DNA and biochemical quantification. It was estimated that approximately 70 mg of decellularized WJECM (dWJECM) powder could be obtained from 4-5 inches of the umbilical cord.

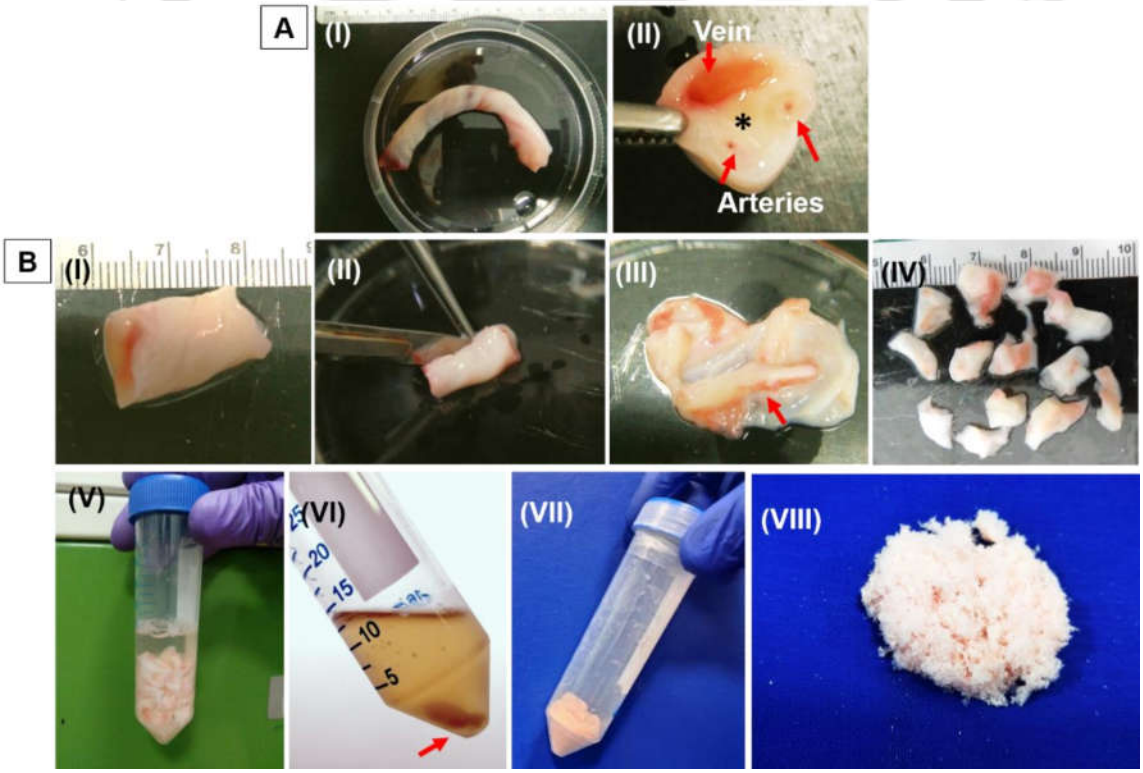

Figure 6.1. *Isolation and decellularization of human Wharton's jelly; (A, I-II)) the gross anatomy of the human umbilical cord and the cross-section showing the vein, arteries (red arrow), and red asterisk sign (*) indicating the Wharton's jelly part of the cord (B, I-VIII) stepwise decellularization process of Wharton's jelly and the lyophilized powder after decellularization.*

6.3.2. Physical and biochemical characterization of dWJECM

6.3.2.1. The solubility of lyophilized dWJECM and particle size distribution

A small fraction of lyophilized dWJECM powder (0.1%, w/v) was dissolved in deionized water, and solubility was checked on the basis of its particle size and distribution pattern. In an optical microscopy study, very few and tiny particles were noticed after centrifugation (decellularization) (**Figure 6.2A, I**), whereas relatively larger particles were observed for non-centrifuged WJECM (**Figure 6.2A, II**). However, very tiny discrete fibrillar particles were also observed in the case of lyophilized dWJECM (**Figure 6.2A, III**).

The particle size and distribution pattern were analyzed through the DLS (**Figure 6.2B**). The Z-average value of centrifuged WJECM particles (or dWJECM- before lyophilization) was 214.8 d.nm with a PDI (polydispersity index) of 0.482 and the value increased to 453.0 d.nm (PDI = 0.554) when lyophilized dWJECM was dissolved in water (**Figure 6.2B, I-IV**). The centrifuged WJECM (dWJECM- before lyophilization) was composed of three distinct populations in particle size that included 332.5 ± 220.5 d.nm (86.6%), 4219 ± 1018 d.nm (7.9%), and 29.92 ± 1.25 d.nm (5.6%). In contrast, two distinct populations (82.6% of 932.8 ± 349.9 d.nm and 17.4% of 151.8 ± 36 d.nm) of particles were obtained for lyophilized dWJECM. However, the particle size for both cases (lyophilized dWJECM and before lyophilization) was far greater than a control soluble protein (BSA) that showed the Z-average value of 10.52 d.nm with a PDI of 0.293.

6.3.2.2. Biochemical estimation

To evaluate the efficiency of the decellularization process using the centrifugation method, DNA content in both native (non-centrifuged) and centrifuged WJECM (5K and 10K fraction, designated as dWJECM) was measured using the PicoGreen DNA assay method. The mean DNA content of native tissue (non-centrifuged) was measured as 930.62 ± 46.79 $ng.mg^{-1}$ of dry tissue. In contrast, the decellularized matrix showed the values of 75.84 ± 1.43 $ng.mg^{-1}$ and 72.99 ± 1.17

ng.mg^{-1} for 5K and 10K group, respectively, which were a ~ 92% reduction of DNA content from the native tissue ($p \leq 0.001$) (**Figure 6.2C, I**).

To understand the effect of centrifugation on the biochemical status of dWJECM, both the qualitative (staining based method) and quantitative estimation were performed. The sGAG, one of the most predominant components in ECM, was estimated using the DMMB method. The sGAG content was measured as 395.44 ± 6.31 ng.mg^{-1} of dry native WJ (non-centrifuged), while the values were 324.10 ± 7.34 ng.mg^{-1} and 330.85 ± 4.22 ng.mg^{-1} for 5K and 10K dWJECM, respectively (**Figure 6.2C, II**). Similarly, the collagen content was measured using picrosirius assay method. The total collagen content of native WJECM was shown to be 27.72 ± 5.1 µg.mg^{-1} of dry weight, and the values were 31.43 ± 2.58 µg.mg^{-1} and 29.21 ± 3.35 µg.mg^{-1} for 5K and 10K dWJECM, respectively (**Figure 6.2C, III**).

The sGAG and collagen were further stained with alcian blue and picrosirius red, respectively (**Figure 6.2D, I-VI**). It was noticed that all groups, including the centrifuged (5K and 10K) and non-centrifuged showed a similar intensity of staining for both of alcian blue and picrosirius red.

6.3.3. Hydrogel formation, gelation kinetics, and injectability

To fabricate a minimally invasive injectable hydrogel with the desirable characteristics for NP tissue substitute, dWJECM was blended with an established silk hydrogel system (**Figure 6.3A, I-II**). The silk hydrogel (SH) was formulated by blending of silk fibroin from two different sources (mulberry *B. mori*; BM and non-mulberry *A. assamensis;* AA). 0.5% (w/v) of BM and 1.0% (w/v) of AA were blended to make a final silk protein of 1.5% (w/v) in the control hydrogel (SH). For gelation kinetic study, blended silk protein was mixed with three concentrations of dWJECM (0.1, 0.5 and 1%, w/v), and polymerization was measured with time (in terms of turbidity changes) using a spectrophotometer at 600 nm. It was observed that the presence of dWJECM did not interfere in gelation kinetics except for the variation in optical opacity. The gelation time for all combinations was in the range of 20-30 min.

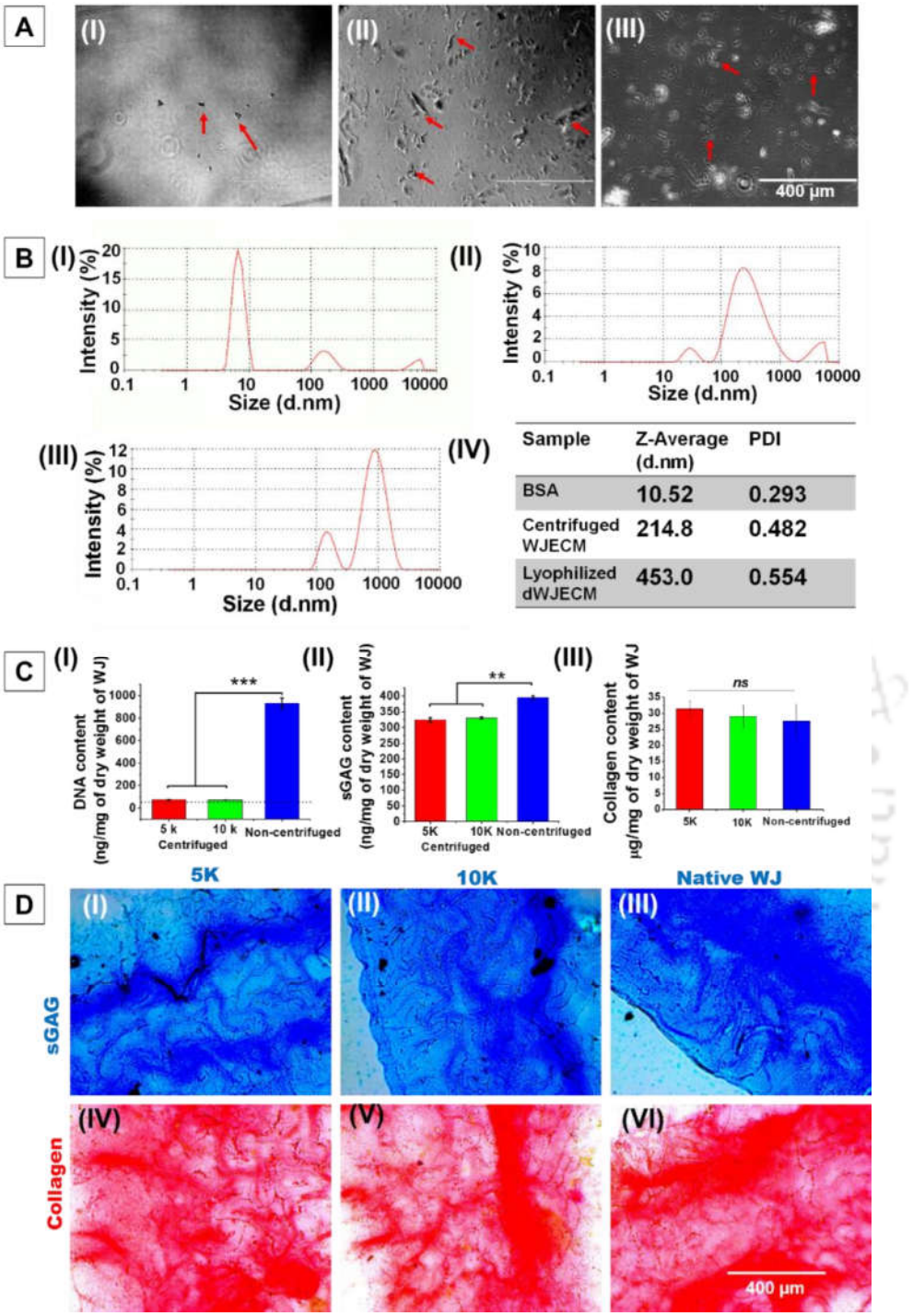

Figure 6.2. *Physical and biochemical characterization of decellularized Wharton's jelly extracellular matrix (dWJECM); (A) digital images of WJ particles under an optical microscope: (I) WJ after decellularization (dWJECM), (II) WJ prior decellularization, and (III) lyophilized dWJECM dissolved in water, (B) DLS analysis of dWJECM: (I) BSA, (II) dWJECM, (III)*

*lyophilized dWJECM after dissolving in water, and (IV) figure showing the z-average and PDI values of dWJECM particles, (C) biochemical estimation of (I) DNA, (II) sGAG, and (III) collagen of WJ before (non-centrifuged) and after decellularization (centrifuged at 5K and 10K), and (D) alcian blue staining for sGAG (I-III) and picrosirius staining for collagen (IV-VI), (I and IV) for dWJECM at 5K, (II and V) for dWJECM at 10K, (III and VI) for native WJ (before decellularization or centrifugation). Data represent mean ± SD (n = 3), where ***P≤0.001, **P≤0.01 and "ns" = non-significant. The dotted line represents the permissible limit of DNA in decellularized ECM.*

Prior to gelation, the solution mixture was optically transparent, which gradually transformed into opaque hydrogel upon gelation **(Figure 6.3A, I**). However, the control systems like BM, AA, and ECM alone did not show any sign of gelation within the experimental duration (**Figure 6.3B, I**). For the injectability test, the hydrogel was prepared in a 2 mL syringe and extruded through the 23-gauge needle. A smooth and easy extrusion of hydrogel against a low force was noticed during the injection process (detailed studies are in the "mechanical properties" section) (**Figure 6.3A, II**).

6.3.4. Physicochemical characterization

6.3.4.1. Protein leaching assay

To understand the entrapment of water-soluble dWJECM in the silk polymeric network, 1% (w/v) dWJECM was blended with the silk solution containing BM and AA silk fibroin, and the release study was performed after gel formation. It was observed that the cumulative released protein from SH with 1% dWJECM group (~ 2300 $\mu g.ml^{-1}$) was similar to the control group (~ 2400 $\mu g.ml^{-1}$) (control gel, SH) after 30 h.

6.3.4.2. Fourier transform infrared spectroscopy (FTIR) analysis

The induction of secondary structure in the hydrogel was confirmed by FTIR analysis (**Figure 6.3B, III**). The signature peaks of amide I, II, and III were shown to be shifted from 1650, 1544, and 1236 cm^{-1} to 1620, 1514, and 1220 cm^{-1} for the control gel (SH) and SH with 1% dWJECM upon gelation. However, the shifting of signature peaks was not evident in all control systems, including AA1.0, BM0.5, SH with 1% dWJECM before gelation and ECM1.0.

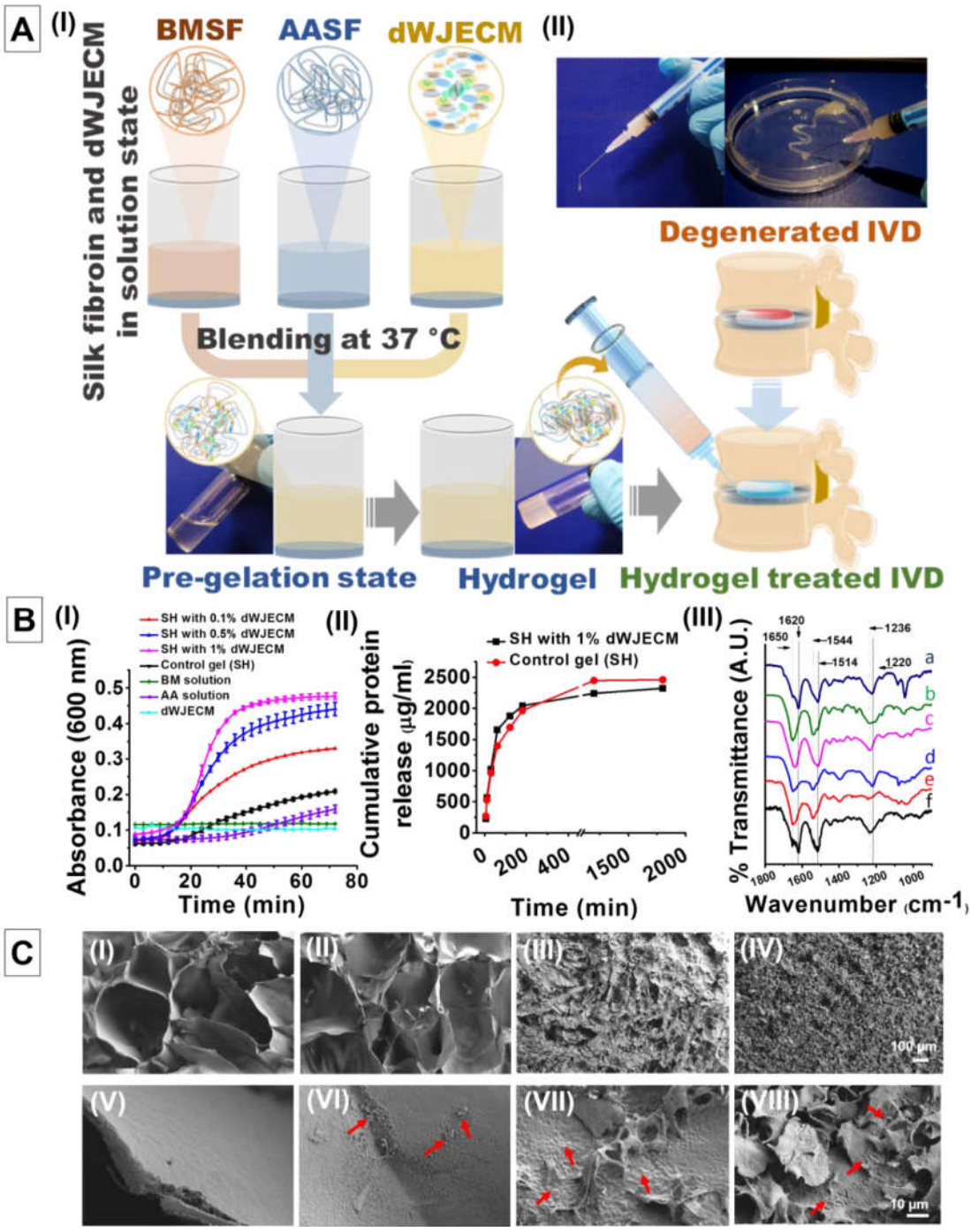

Figure 6.3. *Hydrogel formulation and physicochemical characterization; (A) (I) scheme presenting the hydrogel formulation and its application, and (II) digital images showing the injectability of the formulated hydrogel, (B) physicochemical characterization: (I) gelation kinetics, (II) protein release assay, and (III) FTIR analysis: (a) SH with 1% dWJECM, (b) AA 1.0,*

(c) BM 0.5, (d) SH with 1% dWJECM before gelation (e) ECM1.0, and (f) control gel (SH), and (C) FESEM study: (I) control gel (SH), (II) SH with 0.1% dWJECM, (III) SH with 0.5% dWJECM, (IV) SH with 1% dWJECM. Figure V, VI, VII, and VIII are the magnified images of I, II, III and IV, respectively. Red arrows are indicating the presence of dWJECM particles.

6.3.4.3. Field emission electron microscopy (FESEM) study

FESEM study was performed to analyze the surface properties like morphology, pore size, and interconnectivity of the fabricated silk-dWJECM hydrogel (**Figure 6.3C**). It was observed that the pore size decreased with the increase of dWJECM concentration in the hydrogel. The control gel (SH) and the SH with 0.1% dWJECM possessed the pore size in the range of 300-350 μm (**Figure 6.3C, I and IV, II and IV**), whereas the value radically decreased to ~10 μm for SH with 0.5% dWJECM (**Figure 6.3C, III and VII**) and > 5 μm for SH with 1.0% dWJECM (**Figure 6.3C, IV and VIII**). Interestingly, the spherical particles (300-500 nm) were observed on the surface of struts of hydrogels with dWJECM, while a cleaner surface was observed for the control gel (SH). The number of particles increased as the concentration of dWJECM increased in the hydrogel.

6.3.4.4. Mechanical properties

The mechanical property of the formulated hydrogel is one of the most important characteristics that need to be analyzed to evaluate its efficacy upon implantation, owing to its load-bearing applications. A series of mechanical testing, including peeling test, injectability efficiency, and confined compressive tests, were conducted with the formulated hydrogels. The adhesive property of the hydrogel was checked through a standard 90° peeling test method (**Figure 6.4A, I-IV**). A custom-designed PDMS mold was fabricated for the peeling test (**Figure 6.4A, I, a-b**). It was measured that Young's modulus gradually increased as the amount of dWJECM increased in the hydrogel (**Figure 6.4A, III-IV**). The maximum value (1.03 ± 0.33 MPa) was obtained from the SH with 1% dWJECM group, which significantly decreased to 0.51 ± 0.07 MPa and 0.37 ± 0.04 MPa for SH with 0.5% dWJECM group and SH with 0.1% dWJECM group, respectively ($p \leq 0.05$). The minimum Young's modulus (0.21 ± 0.02 MPa) was recorded for the control gel (SH). However, it was also observed that Young's modulus of the native NP gel (0.56 ± 0.07 MPa) was similar to the SH with 0.5% dWJECM group. The consistency of hydrogels was manually checked using round head serrated tweezers, wherein hydrogel was placed, and the repeated press-pull

process was followed (**Figure 6.4A, II**). A similar kind of hydrogel consistency was observed for both the native NP gel (**Figure 6.4A, II, a-b**) and SF with 0.5% dWJECM (**Figure 6.4A, II, c-d**). For the injectability test, the hydrogel was made in a 2 mL syringe and allowed to extrude through the 23-gauge needle using the UTM (**Figure 6.4B, I**). The stress-strain curve was plotted for all hydrogel groups. A minimum or hindrance free extrusion was observed for control gel (SH) as depicted from the smooth stress-strain curve, whereas the gradually increased hindrance was observed as the amount of dWJECM increased in the hydrogel (**Figure 6.4B, II**).

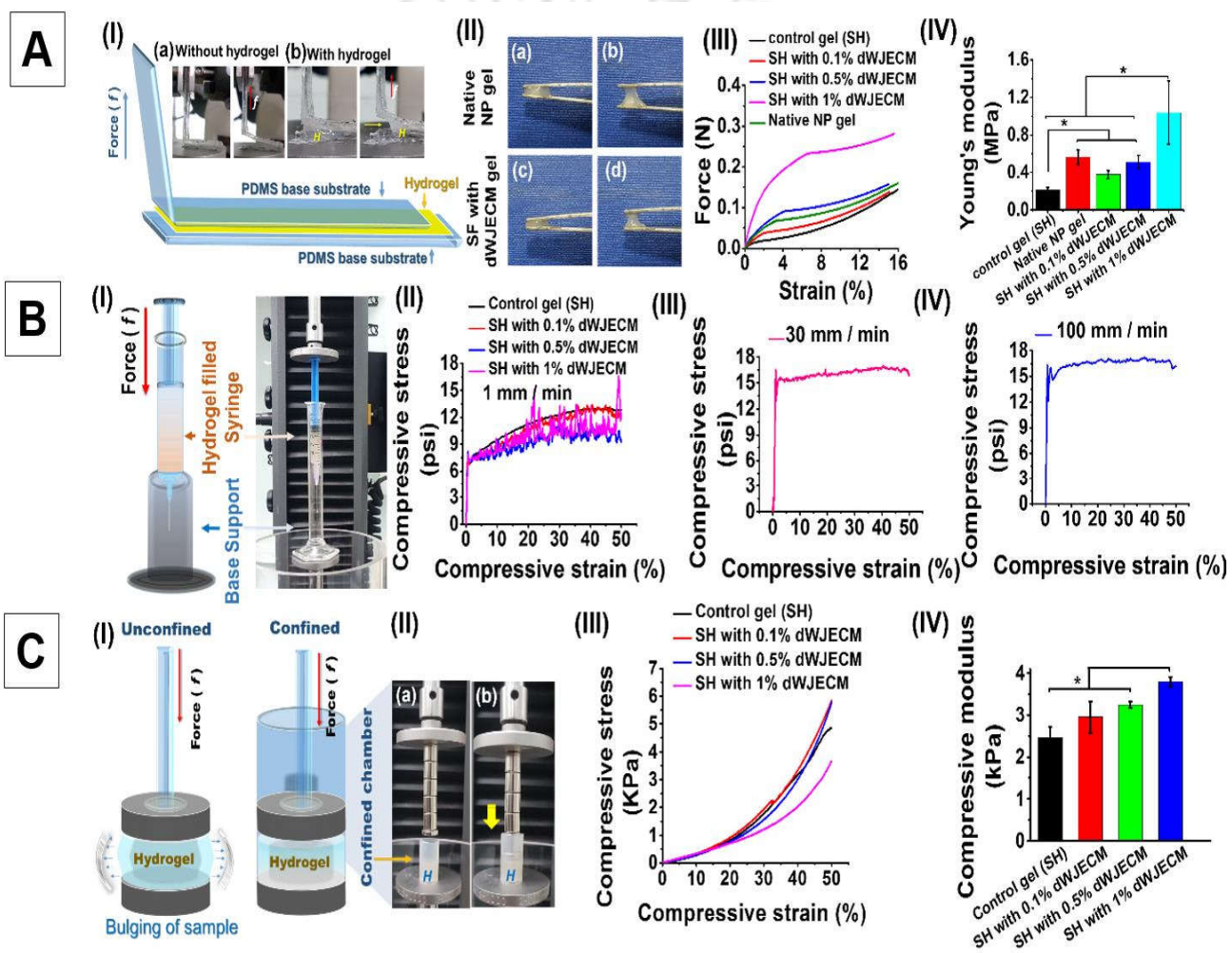

Figure 6.4. *Mechanical studies; (A) peel test: (I) diagram representing the device fabricated for peel test; fabricated device made of PDMS, (a) without hydrogel, (b) with hydrogel, red and yellow arrows representing the direction of applied force and hydrogel, respectively. "H" representing hydrogel in the device (II) digital images showing the adhesiveness of hydrogel, (a-b) for native*

*NP gel and (c-d) fabricated hydrogel (SH with 0.5% dWJECM), (III) the stress-strain curve of the peel test, and (IV) Young's modulus derived from the stress-strain curve of peel test, (B) injectability assessment: (I) the diagram and the digital image is representing the test procedure, (II) a typical stress-strain curve of the injectability test with a cross-head speed at 1 mm.min^{-1}, (II) 30 mm.min^{-1}, and (III) 100 mm.min^{-1}, and (C) confined compressive mechanical testing: (I) diagram representing the confined and unconfined compressive testing, (II) the digital images showing the apparatus set up for the confined compressive testing, (a) open and (b) compressed condition. "H" representing the hydrogel confined by the Teflon mold, (III) the stress-strain curve of the confined compressive test, and (IV) compressive modulus derived from stress-strain curve. Data represent mean ± SD (n = 3), where *p≤0.05.*

However, the smooth extrusion was achieved when the injection speed (cross-head displacement speed) was increased to 30 mm.min^{-1} or 100 mm.min^{-1} even for the hydrogel consisting of the maximum amount of dWJECM (SH with 1% dWJECM) (**Figure 6.4B, III and IV**). The maximum compressive stress during the extrusion process was in the range of 15 to 18 psi for all cases.

To mimic the native NP environment, the compressive mechanical testing was performed in the confined mode using a custom-designed mold (**Figure 6.4C, I**). The mold was a cylindrical tube (made of polypropylene) wherein hydrogel was placed, and the metal plunger compressed the hydrogel at a cross-head speed of 5 mm.min^{-1} (**Figure 6.4C, II, a-b**). It was observed that the compressive modulus was gradually increased as the concentration of dWJECM increased in the hydrogel. The minimum compressive modulus (2.46 ± 0.24 kPa) was measured for control gel (SH), whereas SH with 1% dWJECM group showed the maximum (3.8 ± 0.11 kPa) compressive modulus (**Figure 6.4C, III and IV**).

6.3.4.5. Rheological properties

An exclusive comparative rheological study was performed between the fabricated silk-dWJECM hydrogel groups and the native NP gel. The effect of shear strain (γ) and angular frequency (ω) on the storage (G') and loss modulus (G") were analyzed for all hydrogel groups, including the native NP gel (**Figure 6.5**). It was observed that the G' for all cases gradually decreased as the shear strain (γ) increased towards 1000% and crossed G" after a certain point. The hydrogel containing the maximum amount of dWJECM (SH with 1% dWJECM) showed the cross–over point at ~ 70%

of shear strain (γ), and the value increased to ~ 130% of shear strain (γ) for both of SH with 0.1% dWJECM and SH with 0.5% dWJECM.

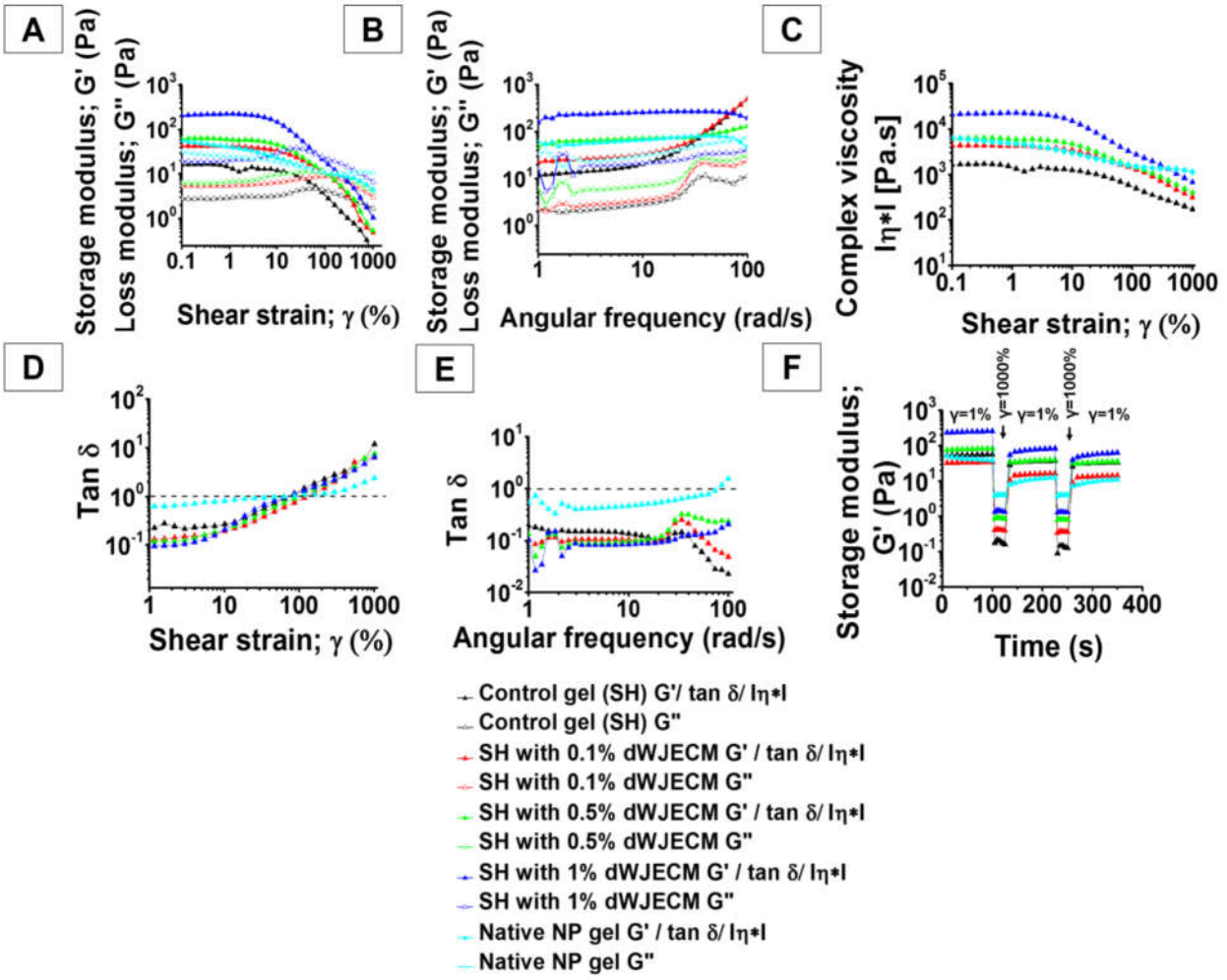

Figure 6.5. *Rheological characterization of hydrogel; (A) amplitude sweep, (B) frequency sweep, (C) behavior of complex viscosity and (D) tan δ in response to shear strain, (E) changes in tan δ in response to frequency sweep, and (F) thixotropic test.*

The cross-over point for the native NP gel was also in a similar range of shear strain (γ) (~ 135 %). The maximum G' (~ 200 Pa) was recorded for SH with 1% dWJECM at 1% of shear strain (γ), whereas the value decreased to a range of 45 to 60 Pa for SH with 0.1% dWJECM, SH with 0.5% dWJECM and even for native NP gel. In contrast, the control gel (SH) showed the minimum G' value (~ 15 Pa) at 1% shear strain (γ) (**Figure 6.5A**). A frequency sweep was performed to

understand the effect of frequency on the viscoelastic properties of hydrogels at a fixed strain (γ = 1%). The storage modulus (G') was shown to be independent of frequency for SH with 0.5% dWJECM, SH with 1% dWJECM, and native NP gel up to 60 rad.s^{-1}, whereas an increasing order of G' was observed for both of SH with 0.1% dWJECM and control gel (SH) after 5 rad.s^{-1} (**Figure 6.5B**). The complex viscosity (η*) for all cases gradually decreased after 5% shear strain (γ). The maximum complex viscosity (η* = ~ 22460 Pa.s) was recoded for SH with 1% dWJECM, whereas the values were ~ 4247 Pa.s and ~ 5914 Pa.s for SH with 0.1% dWJECM and SH with 0.5% dWJECM, respectively at 1 % shear strain (γ) . However, the complex viscosity (η* = ~ 4729 Pa.s) of native NP gel lied between SH with 0.1% dWJECM and SH with 0.5% dWJECM, while the control gel (SH) showed the minimum value (η* = ~ 1347 Pa.s) at the same shear strain (γ = 1%) (**Figure 6.5C**). The tan δ (G"/G') was measured in the response of shear strain (γ) and frequency (ω). The tan δ increased gradually as the shear strain (γ) increased, and tan δ > 1 was recorded for all cases close to 100% shear strain (γ) (**Figure 6.5D**). However, tan δ < 1 was observed for all hydrogels in response to frequency (ω) except native NP gel, which was shown to cross the value of 1 (tan δ > 1) after 80 rad.s^{-1} (**Figure 6.5E).** In the thixotropic analysis, it was observed that all types of hydrogels had the potential to recover from the high strain-induced deformation (**Figure 6.5F)**.

6.3.5. Biological assessment

6.3.5.1. Cell viability study

Cells were isolated from porcine NP tissue after the collagenase digestion. Cell viability was checked in two stages, just after injection and on 7th day. The NP cells encapsulated hydrogel (SH with 0.5% dWJECM and control gel) was passed through a 23-gauge needle, and cell viability was checked using calcein-AM – ethidium homodimer dye. > 99% of the population were visually estimated as live cells for both cases just after the injection (**Figure 6.6B, I-III**). To check the long term cell viability, a custom-designed mold was fabricated wherein calls encapsulated hydrogel was maintained for 7 days (**Figure 6.6A and 6.6C, I-III**). An enhanced green fluorescence (live cells) was recorded for the SH with 0.5% dWJECM, whereas few dead cells (red fluorescence) were observed for the control gel (SH) after 7 days of culture (**Figure 6.6C, IV-V**).

For other biological experiments like cell proliferation assay, histological, and gene expression studies, a custom made *gel-in gel* system was developed (**Figure 6.6, A and D**).

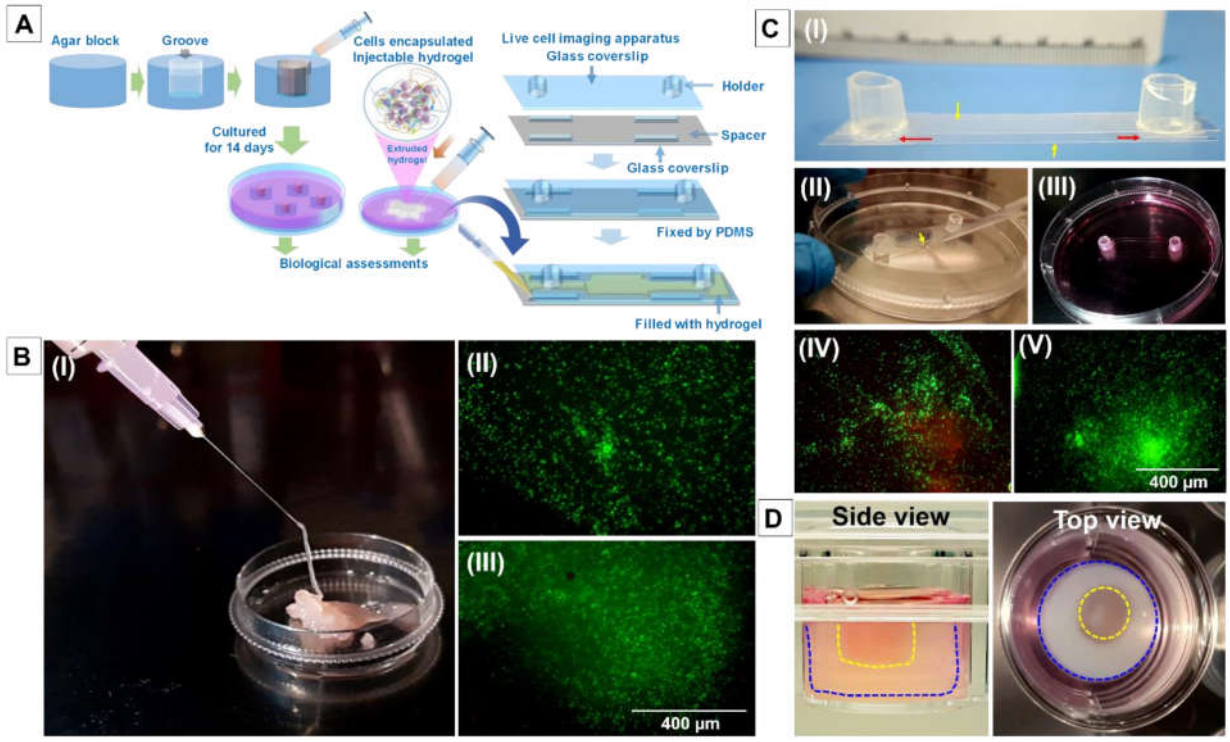

Figure 6.6. *Biological assessment of hydrogel; (A) the scheme showing the experimental procedure for biological studies, (B) (I) the digital image showing the injectability of cell encapsulated hydrogel, cell viability study just after injection (II) control gel (SH), and (III) SH with 0.5% dWJECM, (C) (I) a custom made cell imaging apparatus, the red arrows indicating the spacer between two glass coverslips indicated by yellow arrows, (II) loading of cell encapsulated hydrogel, (III) incubation with cell culture media. Cell viability assessment after 7 days of culture, (IV) control gel (SH), and (IV) SH with 0.5% dWJECM, and (D) a custom made gel-in-gel device for biological assessment.*

6.3.5.2. Cell proliferation

Cell proliferation was checked through DNA quantification on days 1 and 7 using the PicoGreen dsDNA assay method. The equal number of NP cells were encapsulated in both SH with 0.5% dWJECM and control gel (SH). Based on DNA quantification, cells were found to proliferate in

both types of hydrogels, but a significantly enhanced proliferation was observed for the SH with 0.5% dWJECM group.

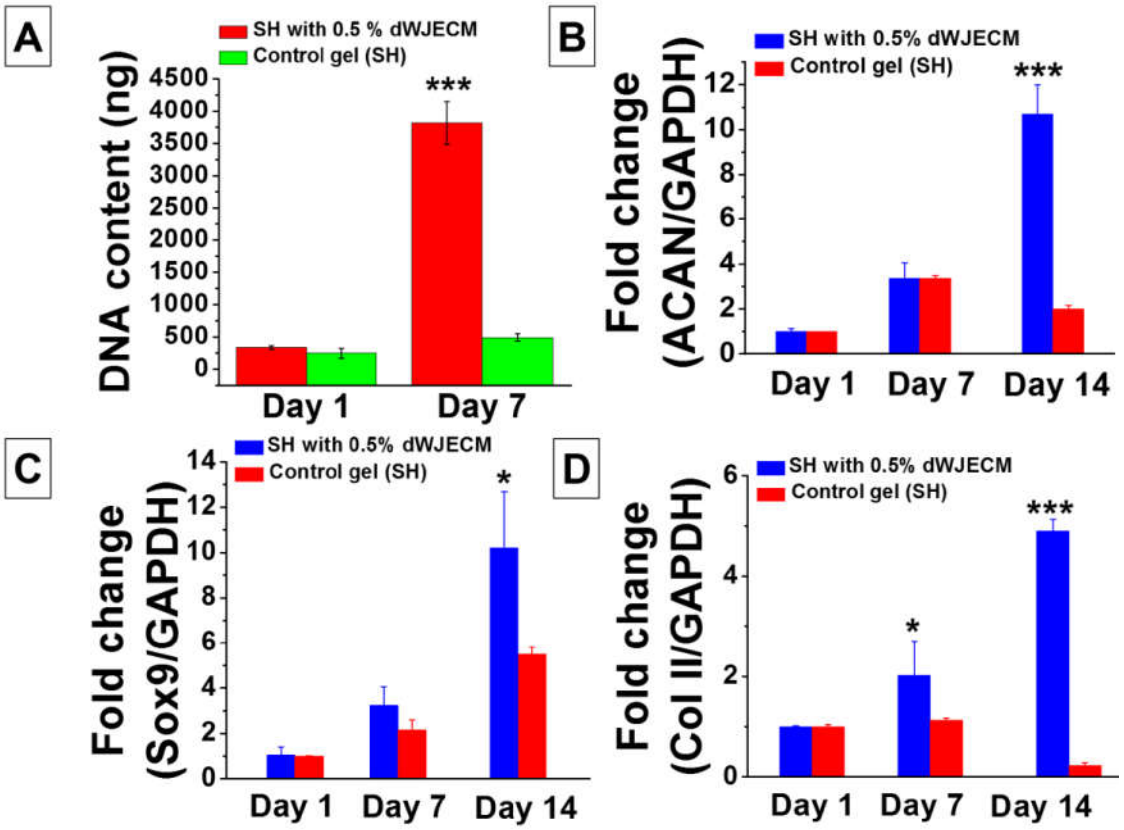

Figure 6.7. *Cell proliferation and gene expression study; (A) DNA quantification for cell proliferation, and the relative fold-changes in gene expression for (B) aggrecan (ACAN), (C) Sox9, and (D) col II on day1, 7 and 14. Data represent mean ± SD (n = 3), where *P≤0.05 and ***P≤0.001.*

The NP cells encapsulated in SH with 0.5% dWJECM proliferated with a ~ 10-fold increase compared with the initial seeding day, whereas the control gel (SH) showed a ~ 2-fold cell proliferation. The maximum DNA content estimated for the SH with 0.5% dWJECM was 3812.30 ± 327.96 ng, which was significantly higher ($p \leq 0.001$) than the control gel (SH) (490.95 ± 55.1 ng) after 7 days of culture (**Figure 6.7A**).

6.3.5.3. Real time PCR

The maintenance of chondrogenic behavior of encapsulated NP cells within the control SH gel and SH with 0.5% dWJECM gel was assessed by the expression profile of sox9, aggrecan, and collagen II genes. The aggrecan expression was found to increase to ~ 4-fold after 7 days successively and > 10 folds after 14 days for the cells encapsulated within 0.5% dWJECM SH gels. However, the aggrecan expression was found to increase to ~ 4-fold within the SH control gel after 7 days and thereafter decreased below 0.5-fold post 14 days **(Figure 6.7B)**. A similar trend was observed in the case of collagen II gene expression profile where the NP cells within SH with 0.5% dWJECM gel increased to ~ 2-fold and ~ 6-fold after 7 and 14 days, the NP cells encapsulated within the control gel (SH) showed no change in expression after 7 days and a less than 0.5-fold expression past 14 days. These changes may be a result of the higher beta-sheet content and hence increase matrix stiffness and nutrient deficiency of the control gel (SH) as compared to the SH with 0.5% dWJECM gel. The expression of the sox9 gene was found to increase in both SH control gel as well as SH with 0.5% dWJECM gel. However, the sox9 expression was significantly higher for NP cells within SH with 0.5% dWJECM gel, *i.e.,* ~ 4-fold after 7 days and ~ 10-fold after 14 days whereas, the expression profile within SH control gels increased gently, *i.e.,* ~ 3-fold after 7 days and ~ 5-fold after 14 days **(Figure 6.7, C-D)**. The different profile of expression of aggrecan and collagen II is a precursor to higher NP-specific ECM synthesis profile of the cells within SH with 0.5% dWJECM gels.

6.3.5.4. Histological analysis

Both the cell-free and cell-encapsulated hydrogels were subjected to histological analysis to evaluate the cellular distribution and presence of specific ECM molecules in the hydrogels (**Figure 6.8**). The micro-sections of cell-free hydrogels were stained with alcian blue and picrosirius red for sGAG and collagen, respectively. The cell-free SH with 0.5% dWJECM showed a more intense blue and red color than the cell-free control gel (SH) group due to sGAG and collagen in the dWJECM component (**Figure 6.8A, I-II and B, I-II**). A similar trend was observed in the micro-sections of native NP tissue, which demonstrated a high-intensity blue color for sGAG and red color for collagen (**Figure 6.8A, III and B, III**). From H&E staining, it was observed that cells were well distributed throughout the hydrogels of both groups, but denser cellular distribution was observed for SH with 0.5% dWJECM (**Figure 6.8C, I-II)**

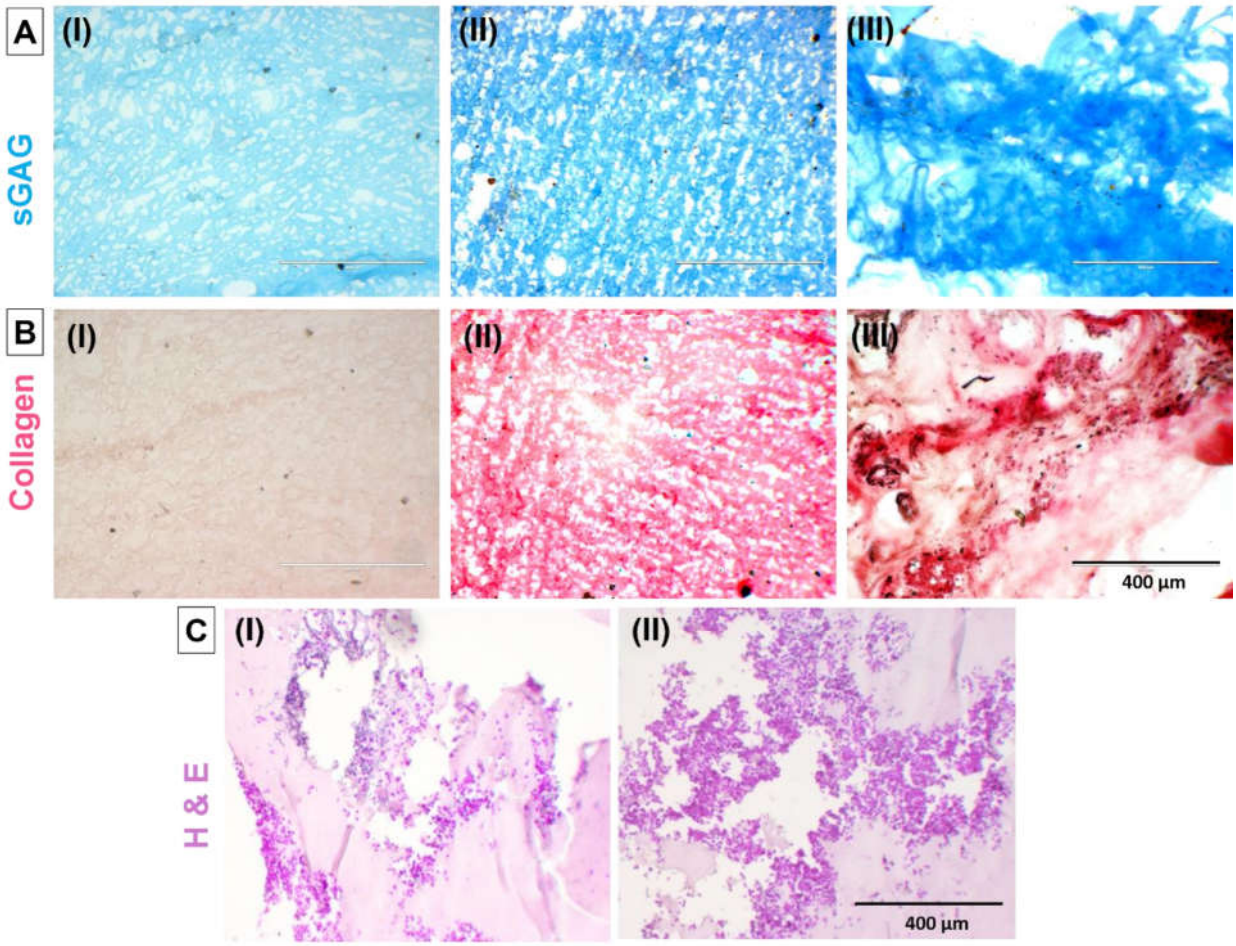

Figure 6.8. *Histological analysis; (A) alcian blue staining for sGAG, (B) picrosirius staining for collagen of (I) cell-free control gel (SH), (II) cell-free SH with 0.5% dWJECM, and (III) native NP tissue, and (C) H&E staining for cell distribution in cell encapsulated hydrogel system of both (I) control gel (SH) and (II) SH with 0.5% dWJECM.*

6.4. Discussion

The term "decellularization" refers to the removal of cells, including the cellular components, *e.g.,* lipids, nuclear membrane, and DNA fragments, which are mainly responsible for immunogenicity or tissue rejection during organ transplantation[544, 545]. However, decellularization is not only the removal of cells or their components but retaining the extracellular matrix (ECM) composition and microarchitecture[544]. The ECM is mainly composed of structural protein (*e.g.,* collagen and elastin), specific protein (*e.g.,* fibrin, fibronectin, and laminin), some proteoglycans (*e.g.,* chondroitin sulfate, keratin sulfate, and sulfated glycosaminoglycan, and heparin sulfate), and growth factors. Decellularized ECM provides a unique inductive platform for constructive cellular remodelling when incorporated into an artificial scaffolding system[546]. Therefore, integrating such decellularized ECM components into scaffolds or hydrogels opens up a huge potential for tissue engineering approaches. There are several well-established decellularization processes including physical methods (*e.g.,* agitation, sonication, and freezing, and thawing), chemical methods (*e.g.,* use of acids, alkali, detergents, hypo-hypertonic solution and organic solvents) and enzymatic methods (*e.g.,* protease and nuclease)[547]. However, these methods are tissue-specific and have their own pros and cons.

In this study, decellularized Wharton's jelly extracellular matrix (dWJECM) was utilized to make an NP tissue-specific hydrogel applicable towards disc-degeneration therapy. Nowadays, there is an increasing demand for natural scaffold materials, and the WJECM has desirable features since it is an easily available naturally derived material (can be considered as "medical waste") with a potential source of hyaluronan and several growth factors, *e.g.,* insulin-like growth factor-1 (IGF-1) and platelet-derived growth factor (PDGF) promoting cell adherence and proliferation[540].

A simple strategy was adopted to decellularize the Wharton's jelly (WJ), avoiding the use of harsh chemicals or a multistep enzymatic digestion process. The decellularization was performed solely using centrifugation steps, and its efficiency was checked through the DNA quantification assay. It was estimated that ~ 92% of DNA content could be removed by centrifugation compared to the non-centrifuged native Wharton's jelly matrix. Previous studies claimed that 100% removal of cells or cellular components is challenging as they are tightly integrated within the ECM components[545]. Some studies also suggested that the decellularized ECM should contain ~ 50 $ng.mg^{-1}$ of dry tissue or DNA > 200 bp that does not elicit any significant inflammatory

reaction[548, 549]. However, the residual amount of DNA helps in tissue remodelling by recruiting the M2 macrophages.

Efficient decellularization is not only the removal of cellular components but also retention of ECM composition. Two major ECM components (collagen and sGAG) were preserved after the decellularization process (centrifugation). Though there was a significant difference in sGAG content between the centrifuged and non-centrifuged group ($p \leq 0.01$), the value for dWJECM was ~ 83% of the native WJ (non-centrifuged) supporting the ECM preservation. However, the high amount of sGAG in native WJ might be due to larger tissue chunks during the WJ isolation. The solubility of a biological component is one of the important factors that determine its bioavailability to the cells. However, solubility also determines the homogeneous distribution of a component throughout a solvent system. Here, the dWJECM was blended with an established silk hydrogel system as described in previous chapter. To understand its solubility and homogeneity in the silk hydrogel system, we analyzed the particle size and distribution by optical microscopy and DLS system. Under optical microscopy, few tiny particles were observed after centrifugation (dWJECM), whereas larger tissue chunks were seen in the non-centrifuged WJ. The centrifugation process removed most of the particles that might include cells, cellular fraction, and tissue chunks very efficiently. To determine the particle size, lyophilized dWJECM powder was resuspended in water and examined under optical microscopy and the DLS system. The fiber shaped particles of sub-micron range in size was noticed under the optical microscope, which was further analyzed by DLS. However, the average particle size of lyophilized dWJECM after resuspending in water was below 0.5 μm.

After successful decellularization, dWJECM was incorporated into an established silk-based hydrogel system wherein silk fibroins from two different sources (BM as mulberry and AA as non-mulberry) were blended at a certain ratio. The blended silk solution transformed into hydrogel gradually (self-polymerized) in the absence of any cross-linker or external stimuli. The gelation time was dependent on various factors like the concentration of silk fibroin, incubation temperature, and ionic strength. In this study, the ratio (BM/AA = 0.5:1.0, wt%) was selected to match the mechanical properties of the fabricated hydrogel to the native NP tissue (3-6 kPa)[49]. The dWJECM was incorporated in this established hydrogel system as an additive providing the biological cues. It was hypothesized that the differences in hydropathicity (hydrophilic-hydrophobic interaction) of silk fibroin isolated from two different sources were responsible for

this self-polymerization resulting from hydrogel formation, and the dWJECM molecules were entrapped inside this polymeric network system. The entrapment of dWJECM was further confirmed by protein release assay where it (SH with 1% dWJECM) did not show any significant change in protein release profile compared with the control hydrogel system (SH). The unbound protein fraction of both hydrogel systems was estimated as 8-10% of the total protein content in hydrogel. Induction of β-sheets in the hydrogel was confirmed by FTIR analysis, and FESEM study showed the presence of dWJECM particles (0.3-0.5 μm in size) on the surface of hydrogel (SH with dWJECM groups) pore walls as evident from the DLS analysis.

The main focus of this study was to formulate a minimally invasive injectable hydrogel system which was mechanically and rheologically equivalent to the native NP tissue. The peeling test was performed to investigate the adhesive property of the fabricated hydrogels. The incorporation of dWJECM provided the adhesiveness and stickiness consistency to the silk-based hydrogel similar to the native NP gel compared to the control gel (SH). The enhanced adhesiveness of the SH with dWJECM hydrogel system over the control gel (SH) was mainly due to the presence of ECM components, *e.g.,* hyaluronan, collagen, and fibrinogen[550-553]. However, these adhesive properties might help the hydrogel stick to the upper and lower vertebral endplate and prevent leakage upon injection.

It is an important aspect to measure the pressure to extrude a cell-encapsulated hydrogel through a needle with a specific diameter as the cell viability depends on the applied pressure. It was reported that the cell viability decreased as the needle diameter decreased, and the applied pressure increased. Nearly 50% cell viability was recorded when HepG2 cells-encapsulated alginate-based hydrogel was dispensed through the needle with a diameter of 400 μm applying the dispensing pressure of 40 psi[554]. In this study, all the hydrogels were shown to be easily extruded through a 23-gauge needle (~ 337 μm in diameter) when the applied dispensing pressure was in the range of 15-18 psi. However, the hindrance free injection could be obtained if the speed of the injection increased. Compressive mechanical testing was conducted in confined mode to mimic the native NP environment surrounded by AF tissue and the upper-lower vertebral endplates. The compressive modulus was shown to gradually increase as the concentration of the dWJECM increased in the hydrogel. The enhanced compressive modulus might be due to the presence of dWJECM molecules that filled the pores resulting in a compact structure, as evident from the

FESEM study. However, the compressive modulus of all hydrogels containing dWJECM was in the range of compressive modulus of native NP tissue (3-6 kPa)[49].

The viscoelastic behavior of hydrogels was determined through a series of rheological testing, including amplitude sweep, frequency sweep, and thixotropic test. In the amplitude sweep test, all hydrogels showed shear-thinning property as the storage modulus (G') for all cases decreased after a certain point of applied shear strain (γ). The shear-thinning property of hydrogels was further confirmed as depicted by the decreasing order of complex viscosity in response to shear strain. The maximum storage modulus (G') was recorded for the SH with 1% dWJECM hydrogel group that comprised of the highest amount of ECM molecules interpenetrating the silk fibroin chains enhancing its gel-strength. However, relatively softer and more viscoelastic hydrogels with G' value and cross-over points were similar to the native NP gel were obtained when dWJECM content was in the range of 0.1-0.5%. The frequency sweep was performed to understand the time-dependent behavior and inner structure of polymers in the linear viscoelastic region (non-destructive deformation range). The frequency-independent behavior was recorded for SH with 0.5% dWJECM, SH with 1% dWJECM hydrogel, and native NP gel. Minimal structural deformation was observed in both of SH with 0.1% dWJECM and control gel (SH) as the G" did not cross the G' in the given angular frequency (ω) range. The structural stability might be due to the entanglement of ECM molecules to the silk fibroin chains that provided enough strength to the hydrogels preventing their deformation. The internal friction in the response of shear strain (γ) and angular frequency (ω) was measured as tan δ, which is the ratio of loss modulus (G") and storage modulus (G') (G"/G'). The tan δ of all hydrogels was shown to be frequency independent, but shear strain-dependent. After a certain point of shear strain, all hydrogels lost the elastic property and behaved like viscous fluids as depicted from the tan δ value where tan $\delta > 1$. However, all hydrogels maintained the elastic nature in the response of angular frequency (ω) where tan $\delta < 1$. The thixotropic analysis showed the recoverability of hydrogels from the deformation induced by a strong shear strain ($\gamma = 1000\%$).

The biological assessment of any biomaterial used in tissue engineering is very important for its clinical translation. For the biological assessment, the SH with 0.5% dWJECM hydrogel was selected as it shared all the mechanical and rheological features close to the native NP tissue. In this study, cell viability was checked at two stages; just after the extrusion and after 7 days of

culture. The viability of cells encapsulated in a hydrogel depends on a few factors like mechanical-rheological properties of the hydrogel, needle diameter through which hydrogel is going to be injected, and the injection pressure[554]. Here, the SH with 0.5% dWJECM possessing a similar gel consistency equivalent to the native NP tissue was extruded through a 23-gauge (~ 337 µm) needle applying the force below 20 psi. The cell viability was not affected by the applied conditions in both control gel as well as hydrogel with dWJECM just after the extrusion. However, less viable cells were found in the control gel (SH) when compared to the SH with 0.5% dWJECM hydrogel group after 7 days of culture. The DNA content analysis revealed that the SH with 0.5% dWJECM hydrogel not only supported cell viability but also helped in cell proliferation, as evident from increased DNA amount. This cell supportive nature of SH with 0.5% dWJECM hydrogel might be attributed to the presence of ECM components like hyaluronan (HA) and growth factors. HA has an important role in cell and tissue hydrodynamics as it possesses a high water-retention and ion exchange capacity helping in microcirculation. The HA also regulates biological responses through its interaction with cell-associated receptors like CD44[555, 556]. Moreover, the growth factors like insulin-like growth factors-1 (IGF-1) and platelet-derived growth factors (PDGF) of the dWJECM also play a significant role in cell signalling that controls the cell proliferation, differentiation, tissue maturation, and ECM remodeling[557, 558].

The Wharton's jelly ECM contains several types of collagen except collagen II, while NP cells majorly secrete collagen II as a part of ECM components[540]. Here, we investigated the ability of encapsulated cells to express the NP-specific genes, including ACAN, sox9, and col II. The SH with dWJECM supported an increased order of expression for all these three genes, whereas a decreased expression was observed for control gel (SH) on 14^{th} day. This decreased expression in control gel (SH) might be due to the unfavorable gel microenvironment that could be correlated with cell proliferation and cell viability studies. Moreover, silk-based hydrogels have the tendency to become stiffer with time as beta-sheet content increases and more cross-linking occurs, whereas the presence of dWJECM limited the time-dependent cross-linking among the silk fibroin chains and maintained the softness and favorable hydrated microenvironment throughout the experimental duration.

In the current study, we developed minimally invasive silk based injectable hydrogel, which was further functionalized with decellularized human Wharton's jelly extracellular matrix providing

the additive biological cues like growth factors. Although the developed hydrogel showed the rheological and mechanical properties similar to the native NP tissue and supported cell viability and deposition of NP tissue-specific ECM molecules, it is imperative to address post-injection integration before its clinical implementation. It is critically important to integrate the developed hydrogel to the surrounding AF tissue upon *in vivo* injection into the central NP portion of the IVD. The long-term stability and regenerative properties of the developed dWJECM functionalized hydrogel in *in vivo* system could be further explored in future for its clinical translation for treatment of disc degeneration therapy.

6.5. Significant findings

The significant findings from this chapter are as follows:

- A pre-established cross-linker free self-assembled silk based hybrid hydrogel system was enriched with bioactive cues that came from dWJECM. The minimal invasive nature of this injectable hydrogel system was investigated for NP replacement therapy.
- The WJECM was isolated from the human umbilical cord, and the decellularization was performed solely through the centrifugation process. The biochemical analysis confirmed the efficient decellularization and preservation of ECM components of the WJECM.
- The protein release assay confirmed the entrapment of dWJECM molecules inside the silk hydrogel.
- The tunable rheological and mechanical properties were achieved by varying the dWJECM components in the base silk hydrogel system. The developed hydrogel possessed the rheological and mechanical properties similar to the native NP tissue.
- The hydrogel system supported NP cell viability, cell proliferation, and tissue maturation.

Overall, the developed cytocompatible hydrogel sharing the biomechanical and rheological properties similar to the native NP tissue open up a new possible direction towards NP tissue regeneration therapy

SUMMARY AND FUTURE PERSPECTIVES

SUMMARY AND FUTURE PERSPECTIVES

One of the major causes of low back pain (LBP) is intervertebral disc degeneration (IDD) which is characterized by the gradual dehydration of central nucleus pulposus (NP) tissue followed by radial tears in surrounding multilamellar annulus fibrosus (AF) tissue. As the conventional therapies are not much effective in regeneration of the discs, issue engineering technology may provide a promising alternative strategy to treat IDD. In IVD tissue engineering, structural recapitulation, particularly the AF anatomy, is important as it reflects the cellular physiology, hence the biomechanical properties. In this thesis, we tried to develop the biomimetic IVD constructs that included AF anatomical equivalents and the suitable hydrogel systems as NP substitute using silk fibroin as biomaterial. The significant achievements of this study (**Figure S1**) and the future prospects associated with it are described in the following sections:

- The multilamellar disc-like angle-ply construct was developed using directional freezing technique. The developed constructs mimicked the complex architecture of native AF tissue and supported primary AF cells and hMSCs viability, proliferation and deposition of AF specific ECM components with time.
- An improved design was considered in fabricating AF anatomical construct restricting the possible delamination of multiple lamellar sheets upon implantation. Further, the mechanosensing behavior of AF cells responding to the variation in matrix stiffness was investigated. This variable matrix stiffness was achieved upon blending of silk fibroin isolated from two different sources (mulberry and non-mulberry).
- Further, for precise replication and high throughput reproducibility, the 3D printing technology was adopted wherein silk-carrageenan based biomaterial ink was deposited in layer-by-layer pattern mimicking the native AF anatomy. This AF cells/ADSCs compatible 3D printed construct possessed a good compressive modulus showing its potential in load bearing applications.
- For *in situ* application in NP tissue replacement, the self-gelling properties of silk fibroin isolated from two different varieties was thoroughly investigated under several

- physiological conditions. SF chains were self-assembled and transformed into hydrogel when blended without using any cross-linker or external stimuli. This NP cells compatible hydrogel system showed good recovery of compressive modulus when tested in an *ex vivo* model.
- This silk based hydrogel system was further enriched with dWJECM that provided the ampule of biological cues. The developed NP cells compatible hydrogel showed the rheological and mechanical properties similar to the native NP tissue, hence used as minimally invasive injectable hydrogel as NP substitute.

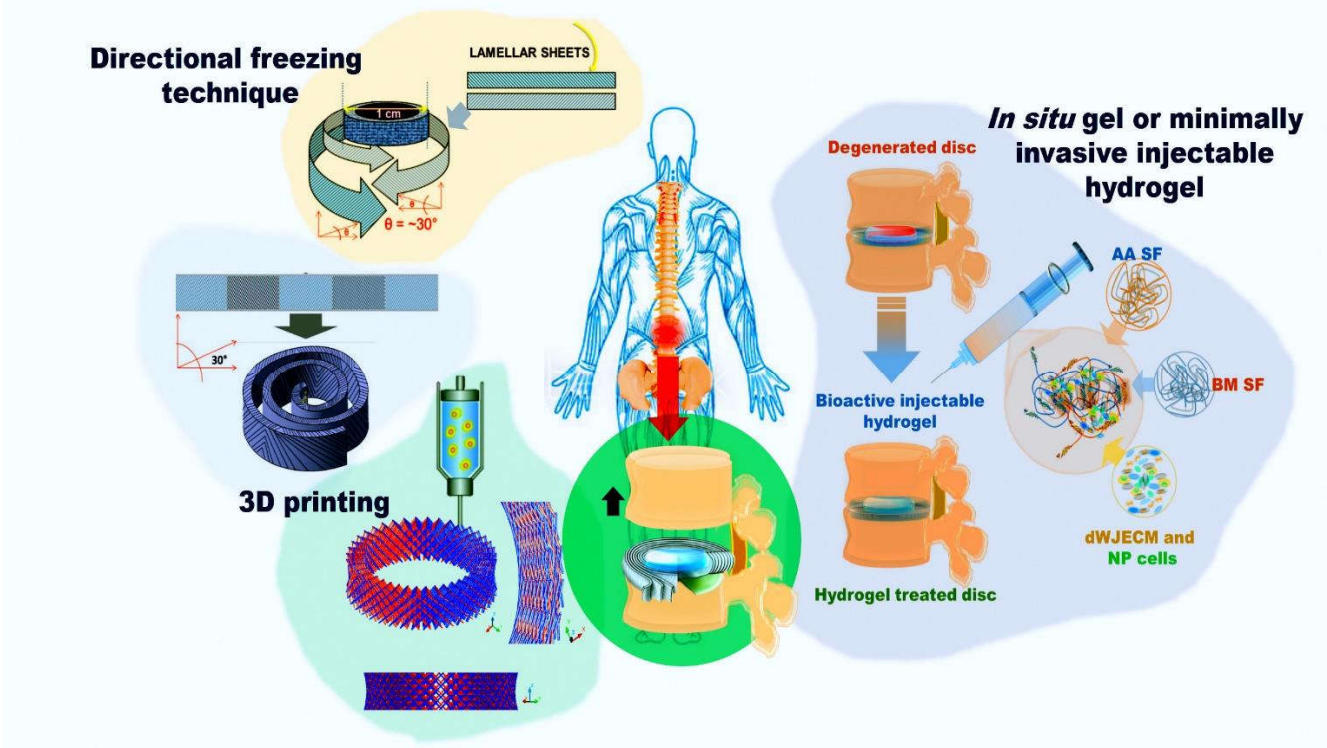

Figure S1. *Image illustrating various adopted tissue engineering strategies to treat damaged IVD*

In this thesis work, we tried to mimic the AF anatomy and a suitable hydrogel system for NP tissue replacement individually. In future studies, a biphasic construct consisting of both the AF and NP will provide a better understanding of tissue integration, hence biomechanics. The use of a dynamic bioreactor system in tissue maturation will provide additional advantages. The developed lamellar scaffolds can be used in another aligned tissue engineering like a muscle, cardiac, tendon, etc. Though the silk-carrageenan based biomaterial ink provided a suitable microenvironment for cells, it can be augmented with several biological cues like growth factors for better cell studies.

The self-assembled silk hydrogel can further be functionalized with bioactive molecules for a faster and better regeneration process Finally, one of the future studies would be the validation of the construct in larger animal model prior to its clinical translation.

Bibliography

[1] Silva-Correia J, Correia SI, Oliveira JM, Reis RL. Tissue engineering strategies applied in the regeneration of the human intervertebral disk. Biotechnology advances. 2013;31:1514-31.

[2] Lucas J. QuickStats: Percentage* of Adults Aged≥ 18 Years Who Had Lower Back Pain in the Past 3 Months,† by Sex and Age Group—National Health Interview Survey, § United States, 2018. 2020.

[3] Bindra S, Sinha A, Benjamin A. Epidemiology of low back pain in Indian population: a review. Int J Basic Appl Med Sci. 2015;5:166-79.

[4] Chung T-W, Chen W-P, Tai P-W, Lo H-Y, Wu T-Y. Roles of Silk Fibroin on Characteristics of Hyaluronic Acid/Silk Fibroin Hydrogels for Tissue Engineering of Nucleus Pulposus. Materials. 2020;13:2750.

[5] Ahdhi GS, Subramanian R, Saya GK, Yamuna TV. Prevalence of low back pain and its relation to quality of life and disability among women in rural area of Puducherry, India. Indian Journal of Pain. 2016;30:111.

[6] Gupta G, Nandini N. Prevalence of low back pain in non working rural housewives of Kanpur, India. Int J Occup Med Environ Health. 2015;28:313-20.

[7] Ganesan S, Acharya AS, Chauhan R, Acharya S. Prevalence and risk factors for low back pain in 1,355 young adults: a cross-sectional study. Asian spine journal. 2017;11:610.

[8] Haldiya K, Mathur M, Mathur N, Mathur A. Epidemiology of musculoskeletal conditions in India. Dr SN Medical College, Jodhpur Annual Report. 2010.

[9] Sidhu A, Sidhu G, Jindal R, Banga A, Nishat S. Sociodemographic profile of low back pain-Saharanpur spine. Pb J Orthop. 2012;8:1.

[10] Bandyopadhyay L, Baur B, Basu G, Haldar A. Musculoskeletal and other health problems in workers of small scale garment industry–an experience from an urban slum, Kolkata. IOSR Journal of Dental and Medical Sciences. 2012;2:23-8.

[11] Kim LH, Vail D, Azad TD, Bentley JP, Zhang Y, Ho AL, et al. Expenditures and health care utilization among adults with newly diagnosed low back and lower extremity pain. JAMA network open. 2019;2:e193676-e.

[12] Wilke HJ, Neef P, Caimi M, Hoogland T, Claes LE. New in vivo measurements of pressures in the intervertebral disc in daily life. Spine. 1999;24:755-62.

[13] Shankar H, Scarlett JA, Abram SE. Anatomy and pathophysiology of intervertebral disc disease. Techniques in Regional Anesthesia and Pain Management. 2009;13:67-75.

[14] Coventry MB, Ghormley RK, Kernohan JW. The intervertebral disc: Its microscopic anatomy and pathology: Part I. Anatomy, development, and physiology. JBJS. 1945;27:105-12.

[15] Cassidy J, Hiltner A, Baer E. Hierarchical structure of the intervertebral disc. Connective tissue research. 1989;23:75-88.

[16] Kurtz SM, Edidin A. Spine technology handbook: Elsevier; 2006.

[17] Peacock A. Observations on the pre-natal development of the intervertebral disc in man. Journal of anatomy. 1951;85:260.

[18] Beckett M, Ralphs JR, Caterson B, Hayes AJ. The transmembrane heparan sulphate proteoglycan syndecan-4 is involved in establishment of the lamellar structure of the annulus fibrosus of the intervertebral disc. Eur Cell Mater. 2015;30:69-88.

[19] Yu J, Fairbank JC, Roberts S, Urban JP. The elastic fiber network of the anulus fibrosus of the normal and scoliotic human intervertebral disc. Spine. 2005;30:1815-20.

[20] Cassinelli EH, Kang JD. Current understanding of lumbar disc degeneration. Operative techniques in orthopaedics. 2000;10:254-62.

[21] Buckwalter JA, Smith K, Kazarien L, Rosenberg LC, Ungar R. Articular cartilage and intervertebral disc proteoglycans differ in structure: an electron microscopic study. Journal of orthopaedic research. 1989;7:146-51.

[22] Whatley BR, Wen X. Intervertebral disc (IVD): Structure, degeneration, repair and regeneration. Materials Science and Engineering: C. 2012;32:61-77.

[23] Yu J. Elastic tissues of the intervertebral disc. Biochemical Society Transactions. 2002;30:848-52.

[24] Nosikova Y, Santerre J, Grynpas M, Gibson G, Kandel R. Characterization of the annulus fibrosus–vertebral body interface: identification of new structural features. Journal of anatomy. 2012;221:577-89.

[25] Feng H, Danfelter M, Strömqvist B, Heinegård D. Extracellular matrix in disc degeneration. JBJS. 2006;88:25-9.

[26] McNally D, Adams MA. Internal intervertebral disc mechanics as revealed by stress profilometry. Spine. 1992;17:66-73.

[27] Vonk LA, Kroeze RJ, Doulabi BZ, Hoogendoorn RJ, Huang C, Helder MN, et al. Caprine articular, meniscus and intervertebral disc cartilage: an integral analysis of collagen network and chondrocytes. Matrix Biology. 2010;29:209-18.

[28] Zhao C-Q, Wang L-M, Jiang L-S, Dai L-Y. The cell biology of intervertebral disc aging and degeneration. Ageing research reviews. 2007;6:247-61.

[29] Melrose J, Smith SM, Appleyard RC, Little CB. Aggrecan, versican and type VI collagen are components of annular translamellar crossbridges in the intervertebral disc. European Spine Journal. 2008;17:314-24.

[30] Errington R, Puustjarvi K, White I, Roberts S, Urban J. Characterisation of cytoplasm-filled processes in cells of the intervertebral disc. Journal of anatomy. 1998;192:369-78.

[31] Ashton IK, Walsh DA, Polak JM, Eisenstein SM. Substance P in intervertebral discs: binding sites on vascular endothelium of the human annulus fibrosus. Acta Orthopaedica Scandinavica. 1994;65:635-9.

[32] Iatridis JC, Weidenbaum M, Setton LA, Mow VC. Is the nucleus pulposus a solid or a fluid? Mechanical behaviors of the nucleus pulposus of the human intervertebral disc. Spine. 1996;21:1174-84.

[33] Chen J, Jing L, Gilchrist CL, Richardson WJ, Fitch RD, Setton LA. Expression of laminin isoforms, receptors, and binding proteins unique to nucleus pulposus cells of immature intervertebral disc. Connective tissue research. 2009;50:294-306.

[34] Joshi A, Fussell G, Thomas J, Hsuan A, Lowman A, Karduna A, et al. Functional compressive mechanics of a PVA/PVP nucleus pulposus replacement. Biomaterials. 2006;27:176-84.

[35] Kraemer J. Natural course and prognosis of intervertebral disc diseases. International Society for the Study of the Lumbar Spine Seattle, Washington, June 1994. Spine. 1995;20:635-9.

[36] Urban J, Roberts S, Ralphs J. The nucleus of the intervertebral disc from development to degeneration. American Zoologist. 2000;40:53-061.

[37] Singh K, Masuda K, Thonar EJA, An HS, Cs-Szabo G. Age-related changes in the extracellular matrix of nucleus pulposus and anulus fibrosus of human intervertebral disc. Spine. 2009;34:10.

[38] Fujita N, Miyamoto T, Imai J-i, Hosogane N, Suzuki T, Yagi M, et al. CD24 is expressed specifically in the nucleus pulposus of intervertebral discs. Biochemical and biophysical research communications. 2005;338:1890-6.

[39] Kim K-W, Ha K-Y, Lee J-S, Nam S-W, Woo Y-K, Lim T-H, et al. Notochordal cells stimulate migration of cartilage end plate chondrocytes of the intervertebral disc in in vitro cell migration assays. The Spine Journal. 2009;9:323-9.

[40] Kim K-W, Lim T-H, Kim JG, Jeong S-T, Masuda K, An HS. The origin of chondrocytes in the nucleus pulposus and histologic findings associated with the transition of a notochordal nucleus pulposus to a fibrocartilaginous nucleus pulposus in intact rabbit intervertebral discs. Spine. 2003;28:982-90.

[41] Weiler C, Nerlich AG, Schaaf R, Bachmeier BE, Wuertz K, Boos N. Immunohistochemical identification of notochordal markers in cells in the aging human lumbar intervertebral disc. European Spine Journal. 2010;19:1761-70.

[42] Le Maitre CL, Freemont AJ, Hoyland JA. Accelerated cellular senescence in degenerate intervertebral discs: a possible role in the pathogenesis of intervertebral disc degeneration. Arthritis research & therapy. 2007;9:1-12.

[43] Park S-H, Cho H, Gil ES, Mandal BB, Min B-H, Kaplan DL. Silk-fibrin/hyaluronic acid composite gels for nucleus pulposus tissue regeneration. Tissue Engineering Part A. 2011;17:2999-3009.

[44] Minogue BM, Richardson SM, Zeef LA, Freemont AJ, Hoyland JA. Transcriptional profiling of bovine intervertebral disc cells: implications for identification of normal and degenerate human intervertebral disc cell phenotypes. Arthritis research & therapy. 2010;12:1-20.

[45] Rutges J, Creemers L, Dhert W, Milz S, Sakai D, Mochida J, et al. Variations in gene and protein expression in human nucleus pulposus in comparison with annulus fibrosus and cartilage cells: potential associations with aging and degeneration. Osteoarthritis and Cartilage. 2010;18:416-23.

[46] Shamji MF, Setton LA, Jarvis W, So S, Chen J, Jing L, et al. Proinflammatory cytokine expression profile in degenerated and herniated human intervertebral disc tissues. Arthritis & rheumatism. 2010;62:1974-82.

[47] Purmessur D, Freemont AJ, Hoyland JA. Expression and regulation of neurotrophins in the nondegenerate and degenerate human intervertebral disc. Arthritis research & therapy. 2008;10:1-9.

[48] Nerlich AG, Weiler C, Zipperer J, Narozny M, Boos N. Immunolocalization of phagocytic cells in normal and degenerated intervertebral discs. Spine. 2002;27:2484-90.

[49] Nerurkar NL, Elliott DM, Mauck RL. Mechanical design criteria for intervertebral disc tissue engineering. Journal of biomechanics. 2010;43:1017-30.

[50] Cloyd JM, Malhotra NR, Weng L, Chen W, Mauck RL, Elliott DM. Material properties in unconfined compression of human nucleus pulposus, injectable hyaluronic acid-based hydrogels and tissue engineering scaffolds. European Spine Journal. 2007;16:1892-8.

[51] Inoue N, Orías AAE. Biomechanics of intervertebral disk degeneration. Orthopedic Clinics. 2011;42:487-99.

[52] Moore RJ. The vertebral endplate: disc degeneration, disc regeneration. European Spine Journal. 2006;15:333-7.

[53] Roberts S, McCall I, Menage J, Haddaway M, Eisenstein S. Does the thickness of the vertebral subchondral bone reflect the composition of the intervertebral disc? European Spine Journal. 1997;6:385-9.

[54] Roberts S, Menage J, Urban J. Biochemical and structural properties of the cartilage end-plate and its relation to the intervertebral disc. Spine. 1989;14:166-74.

[55] Raj PP. Intervertebral disc: anatomy-physiology-pathophysiology-treatment. Pain Practice. 2008;8:18-44.

[56] Herbert C, Lindberg K, Jayson M, Bailey A. Proceedings: Intervertebral disc collagen in degenerative disc disease. Annals of the rheumatic diseases. 1975;34:467.

[57] Freemont A. The cellular pathobiology of the degenerate intervertebral disc and discogenic back pain. Rheumatology. 2009;48:5-10.

[58] Choi SH, Adsul N, Kim HS, Jang J-S, Jang I-T, Oh S-H. Magnetic Resonance Imaging Undetectable Epiduroscopic Hotspot in Chronic Diskogenic Back Pain—Does Sinuvertebral Neuropathy Actually Exist? World neurosurgery. 2018;110:354-8.

[59] Kang JD, Georgescu HI, McIntyre-Larkin L, Stefanovic-Racic M, Donaldson III WF, Evans CH. Herniated lumbar intervertebral discs spontaneously produce matrix metalloproteinases, nitric oxide, interleukin-6, and prostaglandin E2. Spine. 1996;21:271-7.

[60] Visse R, Nagase H. Matrix metalloproteinases and tissue inhibitors of metalloproteinases: structure, function, and biochemistry. Circulation research. 2003;92:827-39.

[61] Bachmeier BE, Nerlich A, Mittermaier N, Weiler C, Lumenta C, Wuertz K, et al. Matrix metalloproteinase expression levels suggest distinct enzyme roles during lumbar disc herniation and degeneration. European Spine Journal. 2009;18:1573-86.

[62] Vo NV, Hartman RA, Yurube T, Jacobs LJ, Sowa GA, Kang JD. Expression and regulation of metalloproteinases and their inhibitors in intervertebral disc aging and degeneration. The Spine Journal. 2013;13:331-41.

[63] Le Maitre CL, Freemont AJ, Hoyland JA. The role of interleukin-1 in the pathogenesis of human intervertebral disc degeneration. Arthritis research & therapy. 2005;7:1-14.

[64] Le Maitre CL, Hoyland JA, Freemont AJ. Catabolic cytokine expression in degenerate and herniated human intervertebral discs: IL-1β and TNFα expression profile. Arthritis research & therapy. 2007;9:1-11.

[65] Wang C, Yu X, Yan Y, Yang W, Zhang S, Xiang Y, et al. Tumor necrosis factor-α: a key contributor to intervertebral disc degeneration. Acta biochimica et biophysica Sinica. 2017;49:1-13.

[66] Millward-Sadler SJ, Costello PW, Freemont AJ, Hoyland JA. Regulation of catabolic gene expression in normal and degenerate human intervertebral disc cells: implications for the pathogenesis of intervertebral disc degeneration. Arthritis research & therapy. 2009;11:1-10.

[67] Krock E, Rosenzweig DH, Chabot-Doré AJ, Jarzem P, Weber MH, Ouellet JA, et al. Painful, degenerating intervertebral discs up-regulate neurite sprouting and CGRP through nociceptive factors. Journal of cellular and molecular medicine. 2014;18:1213-25.

[68] Gilbert HT, Hodson N, Baird P, Richardson SM, Hoyland JA. Acidic pH promotes intervertebral disc degeneration: Acid-sensing ion channel-3 as a potential therapeutic target. Scientific reports. 2016;6:1-12.

[69] Sélard É, Shirazi-Adl A, Urban JP. Finite element study of nutrient diffusion in the human intervertebral disc. Spine. 2003;28:1945-53.

[70] Lee RS, Kayser MV, Ali SY. Calcium phosphate microcrystal deposition in the human intervertebral disc. Journal of anatomy. 2006;208:13-9.

[71] Grant M, Epure L, Bokhari R, Roughley P, Antoniou J, Mwale F. Human cartilaginous endplate degeneration is induced by calcium and the extracellular calcium-sensing receptor in the intervertebral disc. Eur Cell Mater. 2016;32:137-51.

[72] Bartels EM, Fairbank JC, Winlove CP, Urban JP. Oxygen and lactate concentrations measured in vivo in the intervertebral discs of patients with scoliosis and back pain. Spine. 1998;23:1-7.

[73] Holm S, Maroudas A, Urban J, Selstam G, Nachemson A. Nutrition of the intervertebral disc: solute transport and metabolism. Connective tissue research. 1981;8:101-19.

[74] Pluijm S, Van Essen H, Bravenboer N, Uitterlinden A, Smit J, Pols H, et al. Collagen type I α1 Sp1 polymorphism, osteoporosis, and intervertebral disc degeneration in older men and women. Annals of the rheumatic diseases. 2004;63:71-7.

[75] Kalichman L, Hunter DJ. The genetics of intervertebral disc degeneration. Associated genes. Joint Bone Spine. 2008;75:388-96.

[76] Boyd LM, Richardson WJ, Allen KD, Flahiff C, Jing L, Li Y, et al. Early-onset degeneration of the intervertebral disc and vertebral end plate in mice deficient in type IX collagen. Arthritis & rheumatism. 2008;58:164-71.

[77] Annunen S, Paassilta P, Lohiniva J, Perälä M, Pihlajamaa T, Karppinen J, et al. An allele of COL9A2 associated with intervertebral disc disease. Science. 1999;285:409-12.

[78] Roughley P, Martens D, Rantakokko J, Alini M, Mwale F, Antoniou J. The involvement of aggrecan polymorphism in degeneration of human intervertebral disc and articular cartilage. Eur Cell Mater. 2006;11:1-7.

[79] Solovieva S, Kouhia S, Leino-Arjas P, Ala-Kokko L, Luoma K, Raininko R, et al. Interleukin 1 polymorphisms and intervertebral disc degeneration. Epidemiology. 2004:626-33.

[80] Noponen-Hietala N, Virtanen I, Karttunen R, Schwenke S, Jakkula E, Li H, et al. Genetic variations in IL6 associate with intervertebral disc disease characterized by sciatica. Pain. 2005;114:186-94.

[81] Takahashi M, Haro H, Wakabayashi Y, Kawa-Uchi T, Komori H, Shinomiya K. The association of degeneration of the intervertebral disc with 5a/6a polymorphism in the promoter of the human matrix metalloproteinase-3 gene. The Journal of bone and joint surgery British volume. 2001;83:491-5.

[82] Cheung KM, Chan D, Karppinen J, Chen Y, Jim JJ, Yip S-P, et al. Association of the Taq I allele in vitamin D receptor with degenerative disc disease and disc bulge in a Chinese population. Spine. 2006;31:1143-8.

[83] Suthar P, Patel R, Mehta C, Patel N. MRI evaluation of lumbar disc degenerative disease. Journal of clinical and diagnostic research: JCDR. 2015;9:TC04.

[84] Wu PH, Kim HS, Jang I-T. Intervertebral disc diseases PART 2: a review of the current diagnostic and treatment strategies for intervertebral disc disease. International journal of molecular sciences. 2020;21:2135.

[85] Oikawa Y, Eguchi Y, Inoue G, Yamauchi K, Orita S, Kamoda H, et al. Diffusion tensor imaging of lumbar spinal nerve in subjects with degenerative lumbar disorders. Magnetic resonance imaging. 2015;33:956-61.

[86] Murata K, Akeda K, Takegami N, Cheng K, Masuda K, Sudo A. Morphology of intervertebral disc ruptures evaluated by vacuum phenomenon using multi-detector computed tomography: association with lumbar disc degeneration and canal stenosis. BMC musculoskeletal disorders. 2018;19:1-13.

[87] Modic MT, Masaryk TJ, Ross JS, Carter JR. Imaging of degenerative disk disease. Radiology. 1988;168:177-86.

[88] Pfirrmann CW, Metzdorf A, Zanetti M, Hodler J, Boos N. Magnetic resonance classification of lumbar intervertebral disc degeneration. Spine. 2001;26:1873-8.

[89] Griffith JF, Wang Y-XJ, Antonio GE, Choi KC, Yu A, Ahuja AT, et al. Modified Pfirrmann grading system for lumbar intervertebral disc degeneration. Spine. 2007;32:E708-E12.

[90] Hayden J, Van Tulder MW, Malmivaara A, Koes BW. Exercise therapy for treatment of non-specific low back pain. Cochrane database of systematic reviews. 2005.

[91] Karppinen J, Shen FH, Luk KD, Andersson GB, Cheung KM, Samartzis D. Management of degenerative disk disease and chronic low back pain. Orthopedic Clinics. 2011;42:513-28.

[92] Wieland LS, Skoetz N, Pilkington K, Vempati R, D'Adamo CR, Berman BM. Yoga treatment for chronic non-specific low back pain. Cochrane database of systematic reviews. 2017.

[93] Koes BW, Van Tulder M, Lin C-WC, Macedo LG, McAuley J, Maher C. An updated overview of clinical guidelines for the management of non-specific low back pain in primary care. European Spine Journal. 2010;19:2075-94.

[94] Yang S, Kim W, Kong HH, Do KH, Choi KH. Epidural steroid injection versus conservative treatment for patients with lumbosacral radicular pain: A meta-analysis of randomized controlled trials. Medicine. 2020;99.

[95] Kelekis AD, Filippiadis DK, Martin J-B, Brountzos E. Standards of practice: quality assurance guidelines for percutaneous treatments of intervertebral discs. Cardiovascular and interventional radiology. 2010;33:909-13.

[96] Masala S, Salimei F, Lacchè A, Marcia S, Massari F. Overview on Percutaneous Therapies of Disc Diseases. Medicina. 2019;55:471.

[97] Erginousakis D, Filippiadis DK, Malagari A, Kostakos A, Brountzos E, Kelekis NL, et al. Comparative prospective randomized study comparing conservative treatment and percutaneous disk decompression for treatment of intervertebral disk herniation. Radiology. 2011;260:487-93.

[98] Buy X, Gangi A, Guth S, Guermazi A. Percutaneous treatment of intervertebral disc herniation. Imaging in percutaneous musculoskeletal interventions. 2009:93-118.

[99] Murphy K, Elias G, Steppan J, Boxley C, Balagurunathan K, Victor X, et al. Percutaneous treatment of herniated lumbar discs with ozone: investigation of the mechanisms of action. Journal of Vascular and Interventional Radiology. 2016;27:1242-50. e3.

[100] Stagni S, De Santis F, Cirillo L, Dall'Olio M, Princiotta C, Simonetti L, et al. A minimally invasive treatment for lumbar disc herniation: DiscoGel® chemonucleolysis in patients unresponsive to chemonucleolysis with oxygen-ozone. Interventional Neuroradiology. 2012;18:97-104.

[101] Beack JY, Chun HJ, Bak KH, Choi K-S, Bae I-S, Kim KD. Risk factors of secondary lumbar discectomy of a herniated lumbar disc after lumbar discectomy. Journal of Korean Neurosurgical Society. 2019;62:586.

[102] Parker SL, Mendenhall SK, Godil SS, Sivasubramanian P, Cahill K, Ziewacz J, et al. Incidence of Low Back Pain After Lumbar Discectomy for Herniated Disc and Its Effect on Patient-reported Outcomes. Clinical Orthopaedics and Related Research®. 2015;473:1988-99.

[103] Bohlman H, Emery S, Goodfellow D, Jones P. Robinson anterior cervical discectomy and arthrodesis for cervical. J Bone Joint Surg Am. 1993;75:1298-307.

[104] Endler P, Ekman P, Berglund I, Möller H, Gerdhem P. Long-term outcome of fusion for degenerative disc disease in the lumbar spine. The bone & joint journal. 2019;101:1526-33.

[105] Link HD. History, design and biomechanics of the LINK SB Charite artificial disc. Arthroplasty of the Spine: Springer; 2004. p. 36-43.

[106] Bertagnoli R, Habbicht H. The ProDisc-L lumbar prosthesis. Interactive surgery. 2008;3:209-13.

[107] Mattei TA, Beer J, Teles AR, Rehman AA, Aldag J, Dinh D. Clinical outcomes of total disc replacement versus anterior lumbar interbody fusion for surgical treatment of lumbar degenerative disc disease. Global spine journal. 2017;7:452-9.

[108] Bono CM, Garfin SR. History and evolution of disc replacement. The Spine Journal. 2004;4:S145-S50.

[109] Mathews HH, LeHuec J-C, Friesem T, Zdeblick T, Eisermann L. Design rationale and biomechanics of Maverick Total Disc arthroplasty with early clinical results. The Spine Journal. 2004;4:S268-S75.

[110] Valdevit A, Errico TJ. Design and evaluation of the FlexiCore metal-on-metal intervertebral disc prosthesis. The Spine Journal. 2004;4:S276-S88.

[111] axiomed. Biocompatibility of the Freedom® Lumbar Disc and Freedom® Cervical Disc. 2012.

[112] spinalkinetics. M6-L Overview. 2019.

[113] Goins ML, Wimberley DW, Yuan PS, Fitzhenry LN, Vaccaro AR. Nucleus pulposus replacement: an emerging technology. The Spine Journal. 2005;5:S317-S24.

[114] Ahrens M, Tsantrizos A, Donkersloot P, Martens F, Lauweryns P, Le Huec JC, et al. Nucleus replacement with the DASCOR disc arthroplasty device: interim two-year efficacy and safety results from two prospective, non-randomized multicenter European studies. Spine. 2009;34:1376-84.

[115] Bertagnoli R, Sabatino CT, Edwards JT, Gontarz GA, Prewett A, Parsons JR. Mechanical testing of a novel hydrogel nucleus replacement implant. Elsevier; 2005.

[116] Ju DG, Kanim LE, Bae HW. Intervertebral Disc Repair: Current Concepts. Global spine journal. 2020;10:130S-6S.

[117] Balsano M, Zachos A, Ruggiu A, Barca F, Tranquilli-Leali P, Doria C. Nucleus disc arthroplasty with the NUBAC™ device: 2-year clinical experience. European Spine Journal. 2011;20:36-40.

[118] Wave S. Spine Wave Announces Start of NuCore® RPXL Injectable Nucleus

Study in Europe. 2011.

[119] Marotta N, Cosar M, Pimenta L, Khoo LT. A novel minimally invasive presacral approach and instrumentation technique for anterior L5–S1 intervertebral discectomy and fusion: Technical note and case presentations. Neurosurgical focus. 2006;20:1-8.

[120] Trans1. Axialif+. 2019.

[121] Cryolife. CryoLife Announces First Human Implants of BioDisc(TM) Spinal Disc Repair System. 2005.

[122] Thompson JP, Oegema Jr T, Bradford D. Stimulation of mature canine intervertebral disc by growth factors. Spine. 1991;16:253-60.

[123] Gilbertson L, Ahn S-H, Teng P-N, Studer RK, Niyibizi C, Kang JD. The effects of recombinant human bone morphogenetic protein-2, recombinant human bone morphogenetic protein-12, and adenoviral bone morphogenetic protein-12 on matrix synthesis in human annulus fibrosis and nucleus pulposus cells. The Spine Journal. 2008;8:449-56.

[124] Kim D-J, Moon S-H, Kim H, Kwon U-H, Park M-S, Han K-J, et al. Bone morphogenetic protein-2 facilitates expression of chondrogenic, not osteogenic, phenotype of human intervertebral disc cells. Spine. 2003;28:2679-84.

[125] Kuh SU, Zhu Y, Li J, Tsai K-J, Fei Q, Hutton WC, et al. Can TGF-β 1 and rhBMP-2 act in synergy to transform bone marrow stem cells to discogenic-type cells? Acta neurochirurgica. 2008;150:1073-9.

[126] Gandhi SD, Maerz T, Mitchell S, Bachison C, Park DK, Fischgrund JS, et al. Intradiscal Delivery of Anabolic Growth Factors and a Metalloproteinase Inhibitor in a Rabbit Acute Lumbar Disc Injury Model. International Journal of Spine Surgery. 2020;14:585-93.

[127] Hayes AJ, Ralphs JR. The response of foetal annulus fibrosus cells to growth factors: modulation of matrix synthesis by TGF-β1 and IGF-1. Histochemistry and cell biology. 2011;136:163-75.

[128] Akyuva Y, Kaplan N, Yılmaz İ, Özbek H, Yaşar Şirin D, Karaaslan N, et al. Delivering growth factors through a polymeric scaffold to cell cultures containing both nucleus pulposus and annulus fibrosus. 2019.

[129] Li Z, Lang G, Karfeld-Sulzer LS, Mader KT, Richards RG, Weber FE, et al. Heterodimeric BMP-2/7 for nucleus pulposus regeneration—In vitro and ex vivo studies. Journal of Orthopaedic Research. 2017;35:51-60.

[130] Wei A, Williams LA, Bhargav D, Shen B, Kishen T, Duffy N, et al. BMP13 prevents the effects of annular injury in an ovine model. International journal of biological sciences. 2009;5:388.

[131] Imai Y, Okuma M, An HS, Nakagawa K, Yamada M, Muehleman C, et al. Restoration of disc height loss by recombinant human osteogenic protein-1 injection into intervertebral discs

undergoing degeneration induced by an intradiscal injection of chondroitinase ABC. Spine. 2007;32:1197-205.

[132] Liu H, Lin G, Li P, Lin Z, Huang Y, Chen G, et al. The influence of osteogenic protein-1 on histologic changes of rabbit lumbar disc induced by aspirating the nucleus pulposus. Chinese J Spine Spinal Cord. 2013;1:013.

[133] Li X, Leo BM, Beck G, Balian G, Anderson GD. Collagen and proteoglycan abnormalities in the GDF-5-deficient mice and molecular changes when treating disk cells with recombinant growth factor. Spine. 2004;29:2229-34.

[134] Chujo T, An HS, Akeda K, Miyamoto K, Muehleman C, Attawia M, et al. Effects of growth differentiation factor-5 on the intervertebral disc− in vitro bovine study and in vivo rabbit disc degeneration model study. Spine. 2006;31:2909-17.

[135] Yan J, Yang S, Sun H, Guo D, Wu B, Ji F, et al. Effects of releasing recombinant human growth and differentiation factor-5 from poly (lactic-co-glycolic acid) microspheres for repair of the rat degenerated intervertebral disc. Journal of biomaterials applications. 2014;29:72-80.

[136] Zhu J, Xia K, Yu W, Wang Y, Hua J, Liu B, et al. Sustained release of GDF5 from a designed coacervate attenuates disc degeneration in a rat model. Acta biomaterialia. 2019;86:300-11.

[137] Akeda K, An HS, Pichika R, Attawia M, Eugene J-MT, Lenz ME, et al. Platelet-rich plasma (PRP) stimulates the extracellular matrix metabolism of porcine nucleus pulposus and anulus fibrosus cells cultured in alginate beads. Spine. 2006;31:959-66.

[138] Obata S, Akeda K, Imanishi T, Masuda K, Bae W, Morimoto R, et al. Effect of autologous platelet-rich plasma-releasate on intervertebral disc degeneration in the rabbit anular puncture model: a preclinical study. Arthritis research & therapy. 2012;14:1-11.

[139] Comella K, Silbert R, Parlo M. Effects of the intradiscal implantation of stromal vascular fraction plus platelet rich plasma in patients with degenerative disc disease. Journal of translational medicine. 2017;15:1-8.

[140] Michalek AJ, Buckley MR, Bonassar LJ, Cohen I, Iatridis JC. The effects of needle puncture injury on microscale shear strain in the intervertebral disc annulus fibrosus. The Spine Journal. 2010;10:1098-105.

[141] Mwale F, Masuda K, Pichika R, Epure LM, Yoshikawa T, Hemmad A, et al. The efficacy of Link N as a mediator of repair in a rabbit model of intervertebral disc degeneration. Arthritis research & therapy. 2011;13:1-9.

[142] Ma K, Wu Y, Wang B, Yang S, Wei Y, Shao Z. Effect of a synthetic link N peptide nanofiber scaffold on the matrix deposition of aggrecan and type II collagen in rabbit notochordal cells. Journal of Materials Science: Materials in Medicine. 2013;24:405-15.

[143] Gawri R, Antoniou J, Ouellet J, Awwad W, Steffen T, Roughley P, et al. Best paper NASS 2013: link-N can stimulate proteoglycan synthesis in the degenerated human intervertebral discs. European cells & materials. 2013;26:107-19; discussion 19.

[144] Yeh C-H, Chen D, Aghdasi B, Xiao L, Ding M, Jin L, et al. Link protein N-terminal peptide and fullerol promote matrix production and decrease degradation enzymes in rabbit annulus cells. Connective tissue research. 2018;59:191-200.

[145] Mwale F, Masuda K, Grant MP, Epure LM, Kato K, Miyazaki S, et al. Short Link N promotes disc repair in a rabbit model of disc degeneration. Arthritis research & therapy. 2018;20:1-8.

[146] Wang Z, Weitzmann MN, Sangadala S, Hutton WC, Yoon ST. Link protein N-terminal peptide binds to bone morphogenetic protein (BMP) type II receptor and drives matrix protein expression in rabbit intervertebral disc cells. Journal of Biological Chemistry. 2013;288:28243-53.

[147] Rajasekaran S, Soundararajan DCR, Tangavel C, Nayagam SM, KS SV, Sunmathi R, et al. Uncovering molecular targets for regenerative therapy in degenerative disc disease: do small leucine-rich proteoglycans hold the key? The Spine Journal. 2021;21:5-19.

[148] Cho H, Lee S, Park S-H, Huang J, Hasty KA, Kim S-J. Synergistic effect of combined growth factors in porcine intervertebral disc degeneration. Connective tissue research. 2013;54:181-6.

[149] Le Maitre CL, Hoyland JA, Freemont AJ. Interleukin-1 receptor antagonist delivered directly and by gene therapy inhibits matrix degradation in the intact degenerate human intervertebral disc: an in situ zymographic and gene therapy study. Arthritis research & therapy. 2007;9:1-12.

[150] Tobinick E, Davoodifar S. Efficacy of etanercept delivered by perispinal administration for chronic back and/or neck disc-related pain: a study of clinical observations in 143 patients. Current medical research and opinion. 2004;20:1075-85.

[151] Friedmann T, Roblin R. Gene therapy for human genetic disease? Science. 1972;175:949-55.

[152] Woods BI, Vo N, Sowa G, Kang JD. Gene therapy for intervertebral disk degeneration. Orthopedic Clinics. 2011;42:563-74.

[153] Fontana G, See E, Pandit A. Current trends in biologics delivery to restore intervertebral disc anabolism. Advanced drug delivery reviews. 2015;84:146-58.

[154] Takeoka Y, Yurube T, Nishida K. Gene therapy approach for intervertebral disc degeneration: An update. Neurospine. 2020;17:3.

[155] Nishida K, Kang JD, Gilbertson LG, Moon SH, Suh JK, Vogt MT, et al. Modulation of the biologic activity of the rabbit intervertebral disc by gene therapy: An in vivo study of adenovirus-mediated transfer of the human transforming growth factor beta 1 encoding gene. Spine. 1999;24:2419-25.

[156] Moon S-H, Nishida K, Gilbertson LG, Lee H-M, Kim H, Hall RA, et al. Biologic response of human intervertebral disc cells to gene therapy cocktail. Spine. 2008;33:1850.

[157] Kuh S, Zhu Y, Li J, Tsai K-J, Fei Q, Hutton W, et al. The AdLMP-1 transfection in two different cells; AF cells, chondrocytes as potential cell therapy candidates for disc degeneration. Acta neurochirurgica. 2008;150:803-10.

[158] Paul R, Haydon RC, Cheng H, Ishikawa A, Nenadovich N, Jiang W, et al. Potential use of Sox9 gene therapy for intervertebral degenerative disc disease. Spine. 2003;28:755.

[159] Le Maitre CL, Freemont AJ, Hoyland JA. A preliminary in vitro study into the use of IL-1Ra gene therapy for the inhibition of intervertebral disc degeneration. International journal of experimental pathology. 2006;87:17-28.

[160] Wehling P, Schulitz K-P, Robbins PD, Evans CH, Reinecke JA. Transfer of genes to chondrocytic cells of the lumbar spine: proposal for a treatment strategy of spinal disorders by local gene therapy. Spine. 1997;22:1092-7.

[161] Wallach CJ, Sobajima S, Watanabe Y, Kim JS, Georgescu HI, Robbins P, et al. Gene transfer of the catabolic inhibitor TIMP-1 increases measured proteoglycans in cells from degenerated human intervertebral discs. Spine. 2003;28:2331-7.

[162] Ren S, Liu Y, Ma J, Liu Y, Diao Z, Yang D, et al. Treatment of rabbit intervertebral disc degeneration with co-transfection by adeno-associated virus-mediated SOX9 and osteogenic protein-1 double genes in vivo. International journal of molecular medicine. 2013;32:1063-8.

[163] Liu X, Li K, Song J, Liang C, Wang X, Chen X. Efficient and stable gene expression in rabbit intervertebral disc cells transduced with a recombinant baculovirus vector. Spine. 2006;31:732-5.

[164] Liu Y, Yu T, Ma XX, Xiang HF, Hu YG, Chen BH. Lentivirus-mediated TGF-β3, CTGF and TIMP1 gene transduction as a gene therapy for intervertebral disc degeneration in an in vivo rabbit model. Experimental and therapeutic medicine. 2016;11:1399-404.

[165] Nishida K, Doita M, Takada T, Kakutani K-i, Miyamoto H, Shimomura T, et al. Sustained transgene expression in intervertebral disc cells in vivo mediated by microbubble-enhanced ultrasound gene therapy. Spine. 2006;31:1415-9.

[166] Feng G, Zha Z, Huang Y, Li J, Wang Y, Ke W, et al. Sustained and bioresponsive two-stage delivery of therapeutic miRNA via polyplex micelle-loaded injectable hydrogels for inhibition of intervertebral disc fibrosis. Advanced healthcare materials. 2018;7:1800623.

[167] Kakutani K, Nishida K, Uno K, Takada T, Shimomura T, Maeno K, et al. Prolonged down regulation of specific gene expression in nucleus pulposus cell mediated by RNA interference in vitro. Journal of Orthopaedic Research. 2006;24:1271-8.

[168] Seki S, Asanuma-Abe Y, Masuda K, Kawaguchi Y, Asanuma K, Muehleman C, et al. Effect of small interference RNA (siRNA) for ADAMTS5 on intervertebral disc degeneration in the rabbit anular needle-puncture model. Arthritis research & therapy. 2009;11:1-10.

[169] Yamada K, Sudo H, Iwasaki K, Sasaki N, Higashi H, Kameda Y, et al. Caspase 3 silencing inhibits biomechanical overload–induced intervertebral disk degeneration. The American journal of pathology. 2014;184:753-64.

[170] Farhang N, Ginley-Hidinger M, Berrett KC, Gertz J, Lawrence B, Bowles RD. Lentiviral CRISPR epigenome editing of inflammatory receptors as a gene therapy strategy for disc degeneration. Human gene therapy. 2019;30:1161-75.

[171] Rodrigues-Pinto R, Ward L, Humphreys M, Zeef LA, Berry A, Hanley KP, et al. Human notochordal cell transcriptome unveils potential regulators of cell function in the developing intervertebral disc. Scientific reports. 2018;8:1-13.

[172] Cappello R, Bird JL, Pfeiffer D, Bayliss MT, Dudhia J. Notochordal cell produce and assemble extracellular matrix in a distinct manner, which may be responsible for the maintenance of healthy nucleus pulposus. Spine. 2006;31:873-82.

[173] Sheyn D, Ben-David S, Tawackoli W, Zhou Z, Salehi K, Bez M, et al. Human iPSCs can be differentiated into notochordal cells that reduce intervertebral disc degeneration in a porcine model. Theranostics. 2019;9:7506.

[174] Li D, Zeng Q, Jiang Z, Ding L, Lu W, Bian M, et al. Induction of notochordal differentiation of bone marrow mesenchymal‐derived stem cells via the stimulation of notochordal cell‐rich nucleus pulposus tissue. Molecular Medicine Reports. 2021;23:1-.

[175] de Vries S, Doeselaar Mv, Meij B, Tryfonidou M, Ito K. Notochordal cell matrix as a therapeutic agent for intervertebral disc regeneration. Tissue engineering Part A. 2019;25:830-41.

[176] Meisel HJ, Ganey T, Hutton WC, Libera J, Minkus Y, Alasevic O. Clinical experience in cell-based therapeutics: intervention and outcome. European Spine Journal. 2006;15:397-405.

[177] Serigano K, Sakai D, Hiyama A, Tamura F, Tanaka M, Mochida J. Effect of cell number on mesenchymal stem cell transplantation in a canine disc degeneration model. Journal of Orthopaedic Research. 2010;28:1267-75.

[178] Hegewald AA, Endres M, Abbushi A, Cabraja M, Woiciechowsky C, Schmieder K, et al. Adequacy of herniated disc tissue as a cell source for nucleus pulposus regeneration. Journal of Neurosurgery: Spine. 2011;14:273-80.

[179] Lee JW, Kim YH, Kim SH, Han SH, Hahn SB. Chondrogenic differentiation of mesenchymal stem cells and its clinical applications. Yonsei medical journal. 2004;45:41-7.

[180] Shen H, Lin H, Sun AX, Song S, Wang B, Yang Y, et al. Acceleration of chondrogenic differentiation of human mesenchymal stem cells by sustained growth factor release in 3D graphene oxide incorporated hydrogels. Acta biomaterialia. 2020;105:44-55.

[181] Salzig D, Schmiermund A, Gebauer E, Fuchsbauer H-L, Czermak P. Influence of porcine intervertebral disc matrix on stem cell differentiation. Journal of functional biomaterials. 2011;2:155-72.

[182] Kamali A, Ziadlou R, Lang G, Pfannkuche J, Cui S, Li Z, et al. Small molecule-based treatment approaches for intervertebral disc degeneration: Current options and future directions. Theranostics. 2021;11:27.

[183] Sandborn WJ. New targets for small molecules in inflammatory bowel disease. Gastroenterology & hepatology. 2015;11:338.

[184] Hua W, Zhang Y, Wu X, Kang L, Tu J, Zhao K, et al. Icariin attenuates interleukin-1β-induced inflammatory response in human nucleus pulposus cells. Current pharmaceutical design. 2017;23:6071-8.

[185] Cao L, Chen X, Xiao X, Ma Q, Li W. Resveratrol inhibits hyperglycemia-driven ROS-induced invasion and migration of pancreatic cancer cells via suppression of the ERK and p38 MAPK signaling pathways. International journal of oncology. 2016;49:735-43.

[186] Lu L, Hu J, Wu Q, An Y, Cui W, Wang J, et al. Berberine prevents human nucleus pulposus cells from IL-1β-induced extracellular matrix degradation and apoptosis by inhibiting the NF-κB pathway. International journal of molecular medicine. 2019;43:1679-86.

[187] Kakiuchi Y, Yurube T, Kakutani K, Takada T, Ito M, Takeoka Y, et al. Pharmacological inhibition of mTORC1 but not mTORC2 protects against human disc cellular apoptosis, senescence, and extracellular matrix catabolism through Akt and autophagy induction. Osteoarthritis and cartilage. 2019;27:965-76.

[188] Barroga C, Deshmukh V, Kc S, Dellamary L, Hood J, Steward J, et al. Discovery of a small molecule inhibitor of the Wnt pathway (SM04690) as a potential treatment for degenerative disc disease. Osteoarthritis and cartilage. 2017;25:S400.

[189] Lanza R, Langer R, Vacanti JP, Atala A. Principles of tissue engineering: Academic press; 2020.

[190] Bowles RD, Setton LA. Biomaterials for intervertebral disc regeneration and repair. Biomaterials. 2017;129:54-67.

[191] Altman GH, Diaz F, Jakuba C, Calabro T, Horan RL, Chen J, et al. Silk-based biomaterials. Biomaterials. 2003;24:401-16.

[192] Neubauer VJ, Döbl A, Scheibel T. Silk-Based Materials for Hard Tissue Engineering. Materials. 2021;14:674.

[193] Wang Y, Kim H-J, Vunjak-Novakovic G, Kaplan DL. Stem cell-based tissue engineering with silk biomaterials. Biomaterials. 2006;27:6064-82.

[194] Sah M, Pramanik K. Regenerated silk fibroin from B. mori silkcocoon for tissue engineering applications. International journal of environmental science and development. 2010;1:404.

[195] Kundu S, Kundu B, Talukdar S, Bano S, Nayak S, Kundu J, et al. Nonmulberry silk biopolymers. Biopolymers. 2012;97:455-67.

[196] Gupta P, Kumar M, Bhardwaj N, Kumar JP, Krishnamurthy C, Nandi SK, et al. Mimicking form and function of native small diameter vascular conduits using mulberry and non-mulberry patterned silk films. ACS applied materials & interfaces. 2016;8:15874-88.

[197] Singh YP, Bhardwaj N, Mandal BB. Potential of agarose/silk fibroin blended hydrogel for in vitro cartilage tissue engineering. ACS applied materials & interfaces. 2016;8:21236-49.

[198] Mehrotra S, Nandi SK, Mandal BB. Stacked silk-cell monolayers as a biomimetic three dimensional construct for cardiac tissue reconstruction. Journal of Materials Chemistry B. 2017;5:6325-38.

[199] Reardon P, Konwarh R, Knowles JC, Mandal BB. Mimicking hierarchical complexity of the osteochondral interface using electrospun silk-bioactive glass composites. ACS applied materials & interfaces. 2017;9:8000-13.

[200] Gupta P, Lorentz KL, Haskett DG, Cunnane EM, Ramaswamy AK, Weinbaum JS, et al. Bioresorbable silk grafts for small diameter vascular tissue engineering applications: In vitro and in vivo functional analysis. Acta biomaterialia. 2020;105:146-58.

[201] Ramachandran C, Gupta P, Hazra S, Mandal BB. In vitro culture of human corneal endothelium on non-mulberry silk fibroin films for tissue regeneration. Translational Vision Science & Technology. 2020;9:12-.

[202] Mehrotra S, de Melo BA, Hirano M, Keung W, Li RA, Mandal BB, et al. Nonmulberry Silk Based Ink for Fabricating Mechanically Robust Cardiac Patches and Endothelialized Myocardium-on-a-Chip Application. Advanced functional materials. 2020;30:1907436.

[203] Chae SK, Kang E, Khademhosseini A, Lee SH. Micro/Nanometer-Scale Fiber with Highly Ordered Structures by Mimicking the Spinning Process of Silkworm. Advanced materials. 2013;25:3071-8.

[204] Inoue S, Tanaka K, Arisaka F, Kimura S, Ohtomo K, Mizuno S. Silk fibroin of Bombyx mori is secreted, assembling a high molecular mass elementary unit consisting of H-chain, L-chain, and P25, with a 6: 6: 1 molar ratio. Journal of Biological Chemistry. 2000;275:40517-28.

[205] Zhou CZ, Confalonieri F, Jacquet M, Perasso R, Li ZG, Janin J. Silk fibroin: structural implications of a remarkable amino acid sequence. Proteins: Structure, Function, and Bioinformatics. 2001;44:119-22.

[206] Nakazawa Y, Bamba M, Nishio S, Asakura T. Tightly winding structure of sequential model peptide for repeated helical region in Samia cynthia ricini silk fibroin studied with solid-state NMR. Protein science. 2003;12:666-71.

[207] Gupta A, Mita K, Arunkumar KP, Nagaraju J. Molecular architecture of silk fibroin of Indian golden silkmoth, Antheraea assama. Scientific reports. 2015;5:1-17.

[208] Datta A, Ghosh AK, Kundu SC. Purification and characterization of fibroin from the tropical Saturniid silkworm, Antheraea mylitta. Insect biochemistry and molecular biology. 2001;31:1013-8.

[209] Bhardwaj N, Kundu SC. Electrospinning: a fascinating fiber fabrication technique. Biotechnology advances. 2010;28:325-47.

[210] Xue J, Wu T, Dai Y, Xia Y. Electrospinning and electrospun nanofibers: Methods, materials, and applications. Chemical reviews. 2019;119:5298-415.

[211] Liang D, Hsiao BS, Chu B. Functional electrospun nanofibrous scaffolds for biomedical applications. Advanced drug delivery reviews. 2007;59:1392-412.

[212] Sun B, Long Y, Zhang H, Li M, Duvail J, Jiang X, et al. Advances in three-dimensional nanofibrous macrostructures via electrospinning. Progress in Polymer Science. 2014;39:862-90.

[213] Haider A, Haider S, Kang I-K. A comprehensive review summarizing the effect of electrospinning parameters and potential applications of nanofibers in biomedical and biotechnology. Arabian Journal of Chemistry. 2018;11:1165-88.

[214] Parham S, Kharazi AZ, Bakhsheshi-Rad HR, Ghayour H, Ismail AF, Nur H, et al. Electrospun nano-fibers for biomedical and tissue engineering applications: A comprehensive review. Materials. 2020;13:2153.

[215] Liu W, Thomopoulos S, Xia Y. Electrospun nanofibers for regenerative medicine. Advanced healthcare materials. 2012;1:10-25.

[216] Li WJ, Laurencin CT, Caterson EJ, Tuan RS, Ko FK. Electrospun nanofibrous structure: a novel scaffold for tissue engineering. Journal of Biomedical Materials Research: An Official Journal of The Society for Biomaterials, The Japanese Society for Biomaterials, and The Australian Society for Biomaterials and the Korean Society for Biomaterials. 2002;60:613-21.

[217] Nerurkar NL, Baker BM, Sen S, Wible EE, Elliott DM, Mauck RL. Nanofibrous biologic laminates replicate the form and function of the annulus fibrosus. Nature materials. 2009;8:986-92.

[218] Shamsah AH, Cartmell SH, Richardson SM, Bosworth LA. Mimicking the annulus fibrosus using electrospun polyester blended scaffolds. Nanomaterials. 2019;9:537.

[219] Nerurkar NL, Sen S, Huang AH, Elliott DM, Mauck RL. Engineered disc-like angle-ply structures for intervertebral disc replacement. Spine. 2010;35:867.

[220] Martin JT, Kim DH, Milby AH, Pfeifer CG, Smith LJ, Elliott DM, et al. In vivo performance of an acellular disc-like angle ply structure (DAPS) for total disc replacement in a small animal model. Journal of Orthopaedic Research. 2017;35:23-31.

[221] Martin J, Gullbrand S, Kim D, Ikuta K, Pfeifer C, Ashinsky B, et al. In vitro maturation and in vivo integration and function of an engineered cell-seeded disc-like angle ply structure (DAPS) for total disc arthroplasty. Scientific reports. 2017;7:1-13.

[222] Vadalà G, Mozetic P, Rainer A, Centola M, Loppini M, Trombetta M, et al. Bioactive electrospun scaffold for annulus fibrosus repair and regeneration. European Spine Journal. 2012;21:20-6.

[223] Bao J, Lv W, Sun Y, Deng Y. Electrospun antimicrobial microfibrous scaffold for annulus fibrosus tissue engineering. Journal of Materials Science. 2013;48:4223-32.

[224] Tsai T-L, Nelson BC, Anderson PA, Zdeblick TA, Li W-J. Intervertebral disc and stem cells cocultured in biomimetic extracellular matrix stimulated by cyclic compression in perfusion bioreactor. The Spine Journal. 2014;14:2127-40.

[225] Liu C, Zhu C, Li J, Zhou P, Chen M, Yang H, et al. The effect of the fibre orientation of electrospun scaffolds on the matrix production of rabbit annulus fibrosus-derived stem cells. Bone research. 2015;3:1-9.

[226] Gluais M, Clouet J, Fusellier M, Decante C, Moraru C, Dutilleul M, et al. In vitro and in vivo evaluation of an electrospun-aligned microfibrous implant for Annulus fibrosus repair. Biomaterials. 2019;205:81-93.

[227] Shamsah AH, Cartmell SH, Richardson SM, Bosworth LA. Tissue engineering the annulus fibrosus using 3D rings of electrospun PCL: PLLA angle-ply nanofiber sheets. Frontiers in bioengineering and biotechnology. 2020;7:437.

[228] Zheng K, Du D. Recent advances of hydrogel-based biomaterials for intervertebral disc tissue treatment: A literature review. Journal of Tissue Engineering and Regenerative Medicine. 2021.

[229] Günay B, Isa I, Conrad C, Scarcelli G, Grad S, Li Z, et al. A HYALURONAN-BASED HYDROGEL SYSTEM FOR ANNULUS FIBROSUS REPAIR. Orthopaedic Proceedings: The British Editorial Society of Bone & Joint Surgery; 2018. p. 119-.

[230] Tang G, Zhou B, Li F, Wang W, Liu Y, Wang X, et al. Advances of Naturally Derived and Synthetic Hydrogels for Intervertebral Disk Regeneration. Frontiers in Bioengineering and Biotechnology. 2020;8.

[231] Grunert P, Borde BH, Towne SB, Moriguchi Y, Hudson KD, Bonassar LJ, et al. Riboflavin crosslinked high-density collagen gel for the repair of annular defects in intervertebral discs: An in vivo study. Acta biomaterialia. 2015;26:215-24.

[232] Liu C, Jin Z, Ge X, Zhang Y, Xu H. Decellularized annulus fibrosus matrix/chitosan hybrid hydrogels with basic fibroblast growth factor for annulus fibrosus tissue engineering. Tissue Engineering Part A. 2019;25:1605-13.

[233] Scheibler A-G, Götschi T, Widmer J, Holenstein C, Steffen T, Camenzind RS, et al. Feasibility of the annulus fibrosus repair with in situ gelating hydrogels–A biomechanical study. PloS one. 2018;13:e0208460.

[234] Frauchiger DA, May RD, Bakirci E, Tekari A, Chan SC, Wöltje M, et al. Genipin-enhanced fibrin hydrogel and novel silk for intervertebral disc repair in a loaded bovine organ culture model. Journal of functional biomaterials. 2018;9:40.

[235] Doench I, Ahn Tran T, David L, Montembault A, Viguier E, Gorzelanny C, et al. Cellulose nanofiber-reinforced chitosan hydrogel composites for intervertebral disc tissue repair. Biomimetics. 2019;4:19.

[236] Tavakoli J. Tissue engineering of the intervertebral disc's annulus fibrosus: a scaffold-based review study. Tissue engineering and regenerative medicine. 2017;14:81-91.

[237] Helen W, Merry CL, Blaker JJ, Gough JE. Three-dimensional culture of annulus fibrosus cells within PDLLA/Bioglass® composite foam scaffolds: Assessment of cell attachment, proliferation and extracellular matrix production. Biomaterials. 2007;28:2010-20.

[238] Cabraja M, Endres M, Hegewald AA, Vetterlein S, Thomé C, Woiciechowsky C, et al. A 3D environment for anulus fibrosus regeneration. Journal of Neurosurgery: Spine. 2012;17:177-83.

[239] Park SH, Gil ES, Mandal BB, Cho H, Kluge JA, Min BH, et al. Annulus fibrosus tissue engineering using lamellar silk scaffolds. Journal of tissue engineering and regenerative medicine. 2012;6:s24-s33.

[240] Bhattacharjee M, Miot S, Gorecka A, Singha K, Loparic M, Dickinson S, et al. Oriented lamellar silk fibrous scaffolds to drive cartilage matrix orientation: towards annulus fibrosus tissue engineering. Acta biomaterialia. 2012;8:3313-25.

[241] Guillaume O, Naqvi SM, Lennon K, Buckley CT. Enhancing cell migration in shape-memory alginate–collagen composite scaffolds: In vitro and ex vivo assessment for intervertebral disc repair. Journal of biomaterials applications. 2015;29:1230-46.

[242] McGuire R, Borem R, Mercuri J. The fabrication and characterization of a multi-laminate, angle-ply collagen patch for annulus fibrosus repair. Journal of tissue engineering and regenerative medicine. 2017;11:3488-93.

[243] Chan LK, Leung VY, Tam V, Lu WW, Sze K, Cheung KM. Decellularized bovine intervertebral disc as a natural scaffold for xenogenic cell studies. Acta biomaterialia. 2013;9:5262-72.

[244] Pirvu T, Blanquer SB, Benneker LM, Grijpma DW, Richards RG, Alini M, et al. A combined biomaterial and cellular approach for annulus fibrosus rupture repair. Biomaterials. 2015;42:11-9.

[245] Frost BA, Foster EJ. Replication of annulus fibrosus through fabrication and characterization of polyurethane and cellulose nanocrystal composite scaffolds. Nanocomposites. 2019;5:13-27.

[246] Du J, Long R, Nakai T, Sakai D, Benneker LM, Zhou G, et al. Functional cell phenotype induction with TGF-β1 and collagen-polyurethane scaffold for annulus fibrosus rupture repair. European cells & materials. 2020;39:1.

[247] Gullbrand SE, Smith LJ, Smith HE, Mauck RL. Promise, progress, and problems in whole disc tissue engineering. JOR spine. 2018;1:e1015.

[248] Bowles RD, Gebhard HH, Dyke JP, Ballon DJ, Tomasino A, Cunningham ME, et al. Image-based tissue engineering of a total intervertebral disc implant for restoration of function to the rat lumbar spine. NMR in Biomedicine. 2012;25:443-51.

[249] Park S-H, Gil ES, Cho H, Mandal BB, Tien LW, Min B-H, et al. Intervertebral disk tissue engineering using biphasic silk composite scaffolds. Tissue Engineering Part A. 2012;18:447-58.

[250] Du L, Zhu M, Yang Q, Zhang J, Ma X, Kong D, et al. A novel integrated biphasic silk fibroin scaffold for intervertebral disc tissue engineering. Materials Letters. 2014;117:237-40.

[251] Xu B, Xu H, Wu Y, Li X, Zhang Y, Ma X, et al. Intervertebral disc tissue engineering with natural extracellular matrix-derived biphasic composite scaffolds. PLoS One. 2015;10:e0124774.

[252] Hudson KD, Mozia RI, Bonassar LJ. Dose-dependent response of tissue-engineered intervertebral discs to dynamic unconfined compressive loading. Tissue Engineering Part A. 2015;21:564-72.

[253] Choy ATH, Chan BP. A structurally and functionally biomimetic biphasic scaffold for intervertebral disc tissue engineering. PLoS One. 2015;10:e0131827.

[254] Moriguchi Y, Mojica-Santiago J, Grunert P, Pennicooke B, Berlin C, Khair T, et al. Total disc replacement using tissue-engineered intervertebral discs in the canine cervical spine. PLoS One. 2017;12:e0185716.

[255] Du L, Yang Q, Zhang J, Zhu M, Ma X, Zhang Y, et al. Engineering a biomimetic integrated scaffold for intervertebral disc replacement. Materials Science and Engineering: C. 2019;96:522-9.

[256] Mehrotra S, Moses JC, Bandyopadhyay A, Mandal BB. 3D printing/bioprinting based tailoring of in vitro tissue models: Recent advances and challenges. ACS Applied Bio Materials. 2019;2:1385-405.

[257] Murphy SV, Atala A. 3D bioprinting of tissues and organs. Nature biotechnology. 2014;32:773-85.

[258] Moses JC, Saha T, Mandal BB. Chondroprotective and osteogenic effects of silk-based bioinks in developing 3D bioprinted osteochondral interface. Bioprinting. 2020;17:e00067.

[259] Groll J, Burdick JA, Cho D-W, Derby B, Gelinsky M, Heilshorn SC, et al. A definition of bioinks and their distinction from biomaterial inks. Biofabrication. 2018;11:013001.

[260] Mota C, Camarero-Espinosa S, Baker MB, Wieringa P, Moroni L. Bioprinting: from tissue and organ development to in vitro models. Chemical reviews. 2020;120:10547-607.

[261] Saunders RE, Gough JE, Derby B. Delivery of human fibroblast cells by piezoelectric drop-on-demand inkjet printing. Biomaterials. 2008;29:193-203.

[262] Lorber B, Hsiao W-K, Hutchings IM, Martin KR. Adult rat retinal ganglion cells and glia can be printed by piezoelectric inkjet printing. Biofabrication. 2013;6:015001.

[263] Guo F, Mao Z, Chen Y, Xie Z, Lata JP, Li P, et al. Three-dimensional manipulation of single cells using surface acoustic waves. Proceedings of the National Academy of Sciences. 2016;113:1522-7.

[264] Foresti D, Kroll KT, Amissah R, Sillani F, Homan KA, Poulikakos D, et al. Acoustophoretic printing. Science advances. 2018;4:eaat1659.

[265] Ma X, Qu X, Zhu W, Li Y-S, Yuan S, Zhang H, et al. Deterministically patterned biomimetic human iPSC-derived hepatic model via rapid 3D bioprinting. Proceedings of the National Academy of Sciences. 2016;113:2206-11.

[266] Mota C, Puppi D, Chiellini F, Chiellini E. Additive manufacturing techniques for the production of tissue engineering constructs. Journal of tissue engineering and regenerative medicine. 2015;9:174-90.

[267] Michael S, Sorg H, Peck C-T, Koch L, Deiwick A, Chichkov B, et al. Tissue engineered skin substitutes created by laser-assisted bioprinting form skin-like structures in the dorsal skin fold chamber in mice. PloS one. 2013;8:e57741.

[268] Xing J-F, Zheng M-L, Duan X-M. Two-photon polymerization microfabrication of hydrogels: an advanced 3D printing technology for tissue engineering and drug delivery. Chemical Society Reviews. 2015;44:5031-9.

[269] Kelly BE, Bhattacharya I, Heidari H, Shusteff M, Spadaccini CM, Taylor HK. Volumetric additive manufacturing via tomographic reconstruction. Science. 2019;363:1075-9.

[270] Bernal PN, Delrot P, Loterie D, Li Y, Malda J, Moser C, et al. Volumetric bioprinting of complex living-tissue constructs within seconds. Advanced materials. 2019;31:1904209.

[271] Zhao H, Chen Y, Shao L, Xie M, Nie J, Qiu J, et al. Airflow-Assisted 3D bioprinting of human heterogeneous microspheroidal organoids with microfluidic Nozzle. Small. 2018;14:1802630.

[272] Costantini M, Testa S, Mozetic P, Barbetta A, Fuoco C, Fornetti E, et al. Microfluidic-enhanced 3D bioprinting of aligned myoblast-laden hydrogels leads to functionally organized myofibers in vitro and in vivo. Biomaterials. 2017;131:98-110.

[273] Colosi C, Shin SR, Manoharan V, Massa S, Costantini M, Barbetta A, et al. Microfluidic bioprinting of heterogeneous 3D tissue constructs using low-viscosity bioink. Advanced materials. 2016;28:677-84.

[274] Snyder J, Son AR, Hamid Q, Wu H, Sun W. Hetero-cellular prototyping by synchronized multi-material bioprinting for rotary cell culture system. Biofabrication. 2015;8:015002.

[275] Costa JB, Silva-Correia J, Ribeiro VP, da Silva Morais A, Oliveira JM, Reis RL. Engineering patient-specific bioprinted constructs for treatment of degenerated intervertebral disc. Materials Today Communications. 2019;19:506-12.

[276] Oner T, Cengiz I, Pitikakis M, Cesario L, Parascandolo P, Vosilla L, et al. 3D segmentation of intervertebral discs: from concept to the fabrication of patient-specific scaffolds. Journal of 3D printing in medicine. 2017;1:91-101.

[277] Van Uden S, Silva-Correia J, Correlo V, Oliveira J, Reis R. Custom-tailored tissue engineered polycaprolactone scaffolds for total disc replacement. Biofabrication. 2015;7:015008.

[278] Christiani TR, Baroncini E, Stanzione J, Vernengo AJ. In vitro evaluation of 3D printed polycaprolactone scaffolds with angle-ply architecture for annulus fibrosus tissue engineering. Regenerative biomaterials. 2019;6:175-84.

[279] Hu D, Wu D, Huang L, Jiao Y, Li L, Lu L, et al. 3D bioprinting of cell-laden scaffolds for intervertebral disc regeneration. Materials Letters. 2018;223:219-22.

[280] Whatley BR, Kuo J, Shuai C, Damon BJ, Wen X. Fabrication of a biomimetic elastic intervertebral disk scaffold using additive manufacturing. Biofabrication. 2011;3:015004.

[281] Sun B, Lian M, Han Y, Mo X, Jiang W, Qiao Z, et al. A 3D-Bioprinted dual growth factor-releasing intervertebral disc scaffold induces nucleus pulposus and annulus fibrosus reconstruction. Bioactive materials. 2021;6:179-90.

[282] van Uden S, Silva-Correia J, Oliveira JM, Reis RL. Current strategies for treatment of intervertebral disc degeneration: substitution and regeneration possibilities. Biomaterials research. 2017;21:1-19.

[283] Isa ILM, Abbah SA, Kilcoyne M, Sakai D, Dockery P, Finn DP, et al. Implantation of hyaluronic acid hydrogel prevents the pain phenotype in a rat model of intervertebral disc injury. Science advances. 2018;4:eaaq0597.

[284] Yang SH, Chen PQ, Chen YF, Lin FH. An in-vitro study on regeneration of human nucleus pulposus by using gelatin/chondroitin-6-sulfate/hyaluronan tri-copolymer scaffold. Artificial organs. 2005;29:806-14.

[285] Revell P, Damien E, Di Silvio L, Gurav N, Longinotti C, Ambrosio L. Tissue engineered intervertebral disc repair in the pig using injectable polymers. Journal of Materials Science: Materials in Medicine. 2007;18:303-8.

[286] Abbushi A, Endres M, Cabraja M, Kroppenstedt SN, Thomale UW, Sittinger M, et al. Regeneration of intervertebral disc tissue by resorbable cell-free polyglycolic acid-based implants in a rabbit model of disc degeneration. Spine. 2008;33:1527-32.

[287] Nesti LJ, Li W-J, Shanti RM, Jiang YJ, Jackson W, Freedman BA, et al. Intervertebral disc tissue engineering using a novel hyaluronic acid–nanofibrous scaffold (HANFS) amalgam. Tissue Engineering Part A. 2008;14:1527-37.

[288] Kim DH, Martin JT, Elliott DM, Smith LJ, Mauck RL. Phenotypic stability, matrix elaboration and functional maturation of nucleus pulposus cells encapsulated in photocrosslinkable hyaluronic acid hydrogels. Acta biomaterialia. 2015;12:21-9.

[289] Calderon L, Collin E, Murphy M, O'Halloran D, Pandit A. Type II collagen-hyaluronan hydrogel-a step towards a scaffold for intervertebral disc tissue engineering. 2010.

[290] Tsaryk R, Gloria A, Russo T, Anspach L, De Santis R, Ghanaati S, et al. Collagen-low molecular weight hyaluronic acid semi-interpenetrating network loaded with gelatin microspheres for cell and growth factor delivery for nucleus pulposus regeneration. Acta biomaterialia. 2015;20:10-21.

[291] Moss IL, Gordon L, Woodhouse KA, Whyne CM, Yee AJ. A novel thiol-modified hyaluronan and elastin-like polypetide composite material for tissue engineering of the nucleus pulposus of the intervertebral disc. Spine. 2011;36:1022-9.

[292] Chen Y-C, Su W-Y, Yang S-H, Gefen A, Lin F-H. In situ forming hydrogels composed of oxidized high molecular weight hyaluronic acid and gelatin for nucleus pulposus regeneration. Acta biomaterialia. 2013;9:5181-93.

[293] Frith JE, Menzies DJ, Cameron AR, Ghosh P, Whitehead DL, Gronthos S, et al. Effects of bound versus soluble pentosan polysulphate in PEG/HA-based hydrogels tailored for intervertebral disc regeneration. Biomaterials. 2014;35:1150-62.

[294] Peroglio M, Grad S, Mortisen D, Sprecher CM, Illien-Jünger S, Alini M, et al. Injectable thermoreversible hyaluronan-based hydrogels for nucleus pulposus cell encapsulation. European Spine Journal. 2012;21:839-49.

[295] Gansau J, Buckley CT. Incorporation of collagen and hyaluronic acid to enhance the bioactivity of fibrin-based hydrogels for nucleus pulposus regeneration. Journal of functional biomaterials. 2018;9:43.

[296] Chen P, Ning L, Qiu P, Mo J, Mei S, Xia C, et al. Photo-crosslinked gelatin-hyaluronic acid methacrylate hydrogel-committed nucleus pulposus-like differentiation of adipose stromal cells for intervertebral disc repair. Journal of Tissue Engineering and Regenerative Medicine. 2019;13:682-93.

[297] Zhang F, Liu X, Li B, Li Z, Grad S, Chen D, et al. The effect of hyaluronic acid on nucleus pulposus extracellular matrix production through hypoxia-inducible factor-1α transcriptional activation of CD44 under hypoxia. European Cells & Materials. 2021;41:142-52.

[298] Liu M, Zeng X, Ma C, Yi H, Ali Z, Mou X, et al. Injectable hydrogels for cartilage and bone tissue engineering. Bone research. 2017;5:1-20.

[299] Mwale F, Iordanova M, Demers CN, Steffen T, Roughley P, Antoniou J. Biological evaluation of chitosan salts cross-linked to genipin as a cell scaffold for disk tissue engineering. Tissue Engineering. 2005;11:130-40.

[300] Richardson SM, Hughes N, Hunt JA, Freemont AJ, Hoyland JA. Human mesenchymal stem cell differentiation to NP-like cells in chitosan–glycerophosphate hydrogels. Biomaterials. 2008;29:85-93.

[301] Smith LJ, Gorth DJ, Showalter BL, Chiaro JA, Beattie EE, Elliott DM, et al. In vitro characterization of a stem-cell-seeded triple-interpenetrating-network hydrogel for functional regeneration of the nucleus pulposus. Tissue Engineering Part A. 2014;20:1841-9.

[302] Zhang C, Gullbrand SE, Schaer TP, Boorman S, Elliott DM, Chen W, et al. Combined Hydrogel and Mesenchymal Stem Cell Therapy for Moderate-Severity Disc Degeneration in Goats. Tissue Engineering Part A. 2021;27:117-28.

[303] Nair MB, Baranwal G, Vijayan P, Keyan KS, Jayakumar R. Composite hydrogel of chitosan–poly (hydroxybutyrate-co-valerate) with chondroitin sulfate nanoparticles for nucleus pulposus tissue engineering. Colloids and Surfaces B: Biointerfaces. 2015;136:84-92.

[304] Zhu Y, Tan J, Zhu H, Lin G, Yin F, Wang L, et al. Development of kartogenin-conjugated chitosan–hyaluronic acid hydrogel for nucleus pulposus regeneration. Biomaterials science. 2017;5:784-91.

[305] Kuang W, Liu C, Xu H. The application of decellularized nucleus pulposus matrix/chitosan with transforming growth factor β3 for nucleus pulposus tissue engineering. Cytotechnology. 2021:1-10.

[306] Lee JY, Hall R, Pelinkovic D, Cassinelli E, Usas A, Gilbertson L, et al. New use of a three-dimensional pellet culture system for human intervertebral disc cells: initial characterization and potential use for tissue engineering. Spine. 2001;26:2316-22.

[307] Gaetani P, Torre ML, Klinger M, Faustini M, Crovato F, Bucco M, et al. Adipose-derived stem cell therapy for intervertebral disc regeneration: an in vitro reconstructed tissue in alginate capsules. Tissue Engineering Part A. 2008;14:1415-23.

[308] Mizuno H, Roy AK, Vacanti CA, Kojima K, Ueda M, Bonassar LJ. Tissue-engineered composites of anulus fibrosus and nucleus pulposus for intervertebral disc replacement. Spine. 2004;29:1290-7.

[309] Yang J, Yang X, Wang L, Zhang W, Yu W, Wang N, et al. Biomimetic nanofibers can construct effective tissue-engineered intervertebral discs for therapeutic implantation. Nanoscale. 2017;9:13095-103.

[310] Mwale F, Ciobanu I, Giannitsios D, Roughley P, Steffen T, Antoniou J. Effect of oxygen levels on proteoglycan synthesis by intervertebral disc cells. Spine. 2011;36:E131-E8.

[311] McCanless JD, Cole JA, Slack SM, Bumgardner JD, Zamora PO, Haggard WO. Modeling nucleus pulposus regeneration in vitro: mesenchymal stem cells, alginate beads, hypoxia, bone morphogenetic protein-2, and synthetic peptide B2A. Spine. 2011;36:2275-85.

[312] Abbott RD, Purmessur D, Monsey RD, Brigstock DR, Laudier DM, Iatridis JC. Degenerative grade affects the responses of human nucleus pulposus cells to link-N, CTGF, and TGFβ3. Journal of spinal disorders & techniques. 2013;26:E86.

[313] Gantenbein-Ritter B, Chan SC. The evolutionary importance of cell ratio between notochordal and nucleus pulposus cells: an experimental 3-D co-culture study. European Spine Journal. 2012;21:819-25.

[314] Bron JL, Vonk LA, Smit TH, Koenderink GH. Engineering alginate for intervertebral disc repair. Journal of the mechanical behavior of biomedical materials. 2011;4:1196-205.

[315] Kalaf EAG, Flores R, Bledsoe JG, Sell SA. Characterization of slow-gelling alginate hydrogels for intervertebral disc tissue-engineering applications. Materials Science and Engineering: C. 2016;63:198-210.

[316] Kalaf EAG, Pendyala M, Bledsoe JG, Sell SA. Characterization and restoration of degenerated IVD function with an injectable, in situ gelling alginate hydrogel: An in vitro and ex vivo study. Journal of the mechanical behavior of biomedical materials. 2017;72:229-40.

[317] Chou AI, Nicoll SB. Characterization of photocrosslinked alginate hydrogels for nucleus pulposus cell encapsulation. Journal of Biomedical Materials Research Part A: An Official Journal of The Society for Biomaterials, The Japanese Society for Biomaterials, and The Australian Society for Biomaterials and the Korean Society for Biomaterials. 2009;91:187-94.

[318] Guillaume O, Daly A, Lennon K, Gansau J, Buckley SF, Buckley CT. Shape-memory porous alginate scaffolds for regeneration of the annulus fibrosus: effect of TGF-β3 supplementation and oxygen culture conditions. Acta biomaterialia. 2014;10:1985-95.

[319] Foss BL, Maxwell TW, Deng Y. Chondroprotective supplementation promotes the mechanical properties of injectable scaffold for human nucleus pulposus tissue engineering. Journal of the mechanical behavior of biomedical materials. 2014;29:56-67.

[320] Strange DG, Tonsomboon K, Oyen ML. Mechanical behaviour of electrospun fibre-reinforced hydrogels. Journal of Materials Science: Materials in Medicine. 2014;25:681-90.

[321] Zeng Y, Chen C, Liu W, Fu Q, Han Z, Li Y, et al. Injectable microcryogels reinforced alginate encapsulation of mesenchymal stromal cells for leak-proof delivery and alleviation of canine disc degeneration. Biomaterials. 2015;59:53-65.

[322] Tsujimoto T, Sudo H, Todoh M, Yamada K, Iwasaki K, Ohnishi T, et al. An acellular bioresorbable ultra-purified alginate gel promotes intervertebral disc repair: A preclinical proof-of-concept study. EBioMedicine. 2018;37:521-34.

[323] Silva-Correia J, Miranda-Gonçalves V, Salgado AJ, Sousa N, Oliveira JM, Reis RM, et al. Angiogenic potential of gellan-gum-based hydrogels for application in nucleus pulposus regeneration: in vivo study. Tissue Engineering Part A. 2012;18:1203-12.

[324] Khang G, Lee S, Kim H, Silva-Correia J, Gomes ME, Viegas C, et al. Biological evaluation of intervertebral disc cells in different formulations of gellan gum-based hydrogels. Journal of Tissue Engineering and Regenerative Medicine. 2015;9:265-75.

[325] Tsaryk R, Silva-Correia J, Oliveira JM, Unger RE, Landes C, Brochhausen C, et al. Biological performance of cell-encapsulated methacrylated gellan gum-based hydrogels for nucleus pulposus regeneration. Journal of Tissue Engineering and Regenerative Medicine. 2017;11:637-48.

[326] Raheem HM, Rochefort SE, Bay BK. Developing a novel functional disc emulator to investigate the nucleus pulposus replacement. Journal of Materials Science: Materials in Medicine. 2021;32:1-7.

[327] Gruber HE, Leslie K, Ingram J, Norton HJ, Hanley Jr EN. Cell-based tissue engineering for the intervertebral disc: in vitro studies of human disc cell gene expression and matrix production within selected cell carriers. The spine journal. 2004;4:44-55.

[328] Lee K-I, Moon S-H, Kim H, Kwon U-H, Kim H-J, Park S-N, et al. Tissue engineering of the intervertebral disc with cultured nucleus pulposus cells using atelocollagen scaffold and growth factors. Spine. 2012;37:452-8.

[329] Yuan M, Leong KW, Chan BP. Three-dimensional culture of rabbit nucleus pulposus cells in collagen microspheres. The spine journal. 2011;11:947-60.

[330] Zhou X, Tao Y, Chen E, Wang J, Fang W, Zhao T, et al. Genipin-cross-linked type II collagen scaffold promotes the differentiation of adipose-derived stem cells into nucleus pulposus-like cells. Journal of biomedical materials research Part A. 2018;106:1258-68.

[331] Huang B, Li CQ, Zhou Y, Luo G, Zhang CZ. Collagen II/hyaluronan/chondroitin-6-sulfate tri-copolymer scaffold for nucleus pulposus tissue engineering. Journal of Biomedical Materials Research Part B: Applied Biomaterials: An Official Journal of The Society for Biomaterials, The Japanese Society for Biomaterials, and The Australian Society for Biomaterials and the Korean Society for Biomaterials. 2010;92:322-31.

[332] Collin EC, Grad S, Zeugolis DI, Vinatier CS, Clouet JR, Guicheux JJ, et al. An injectable vehicle for nucleus pulposus cell-based therapy. Biomaterials. 2011;32:2862-70.

[333] Strange DG, Oyen ML. Composite hydrogels for nucleus pulposus tissue engineering. Journal of the mechanical behavior of biomedical materials. 2012;11:16-26.

[334] Charron PN, Blatt SE, McKenzie C, Oldinski RA. Dynamic mechanical response of polyvinyl alcohol-gelatin theta-gels for nucleus pulposus tissue replacement. Biointerphases. 2017;12:02C409.

[335] Gan Y, Li P, Wang L, Mo X, Song L, Xu Y, et al. An interpenetrating network-strengthened and toughened hydrogel that supports cell-based nucleus pulposus regeneration. Biomaterials. 2017;136:12-28.

[336] Nichol JW, Koshy ST, Bae H, Hwang CM, Yamanlar S, Khademhosseini A. Cell-laden microengineered gelatin methacrylate hydrogels. Biomaterials. 2010;31:5536-44.

[337] Bahney C, Lujan T, Hsu C, Bottlang M, West J, Johnstone B. Visible light photoinitiation of mesenchymal stem cell-laden bioresponsive hydrogels. European Cells & Materials. 2011;22:43.

[338] Chen YC, Lin RZ, Qi H, Yang Y, Bae H, Melero-Martin JM, et al. Functional human vascular network generated in photocrosslinkable gelatin methacrylate hydrogels. Advanced functional materials. 2012;22:2027-39.

[339] Xu P, Guan J, Chen Y, Xiao H, Yang T, Sun H, et al. Stiffness of photocrosslinkable gelatin hydrogel influences nucleus pulposus cell propertiesin vitro. Journal of Cellular and Molecular Medicine. 2021;25:880-91.

[340] Buser Z, Kuelling F, Liu J, Liebenberg E, Thorne KJ, Coughlin D, et al. Biological and biomechanical effects of fibrin injection into porcine intervertebral discs. Spine. 2011;36:E1201-E9.

[341] Allon AA, Aurouer N, Yoo BB, Liebenberg EC, Buser Z, Lotz JC. Structured coculture of stem cells and disc cells prevent disc degeneration in a rat model. The spine journal. 2010;10:1089-97.

[342] Li Z, Kaplan KM, Wertzel A, Peroglio M, Amit B, Alini M, et al. Biomimetic fibrin–hyaluronan hydrogels for nucleus pulposus regeneration. Regenerative medicine. 2014;9:309-26.

[343] Häckel S, Zolfaghar M, Du J, Hoppe S, Benneker LM, Garstka N, et al. Fibrin-hyaluronic acid hydrogel (RegenoGel) with fibroblast growth factor-18 for in vitro 3D culture of human and bovine nucleus pulposus cells. International journal of molecular sciences. 2019;20:5036.

[344] Zeng C, Yang Q, Zhu M, Du L, Zhang J, Ma X, et al. Silk fibroin porous scaffolds for nucleus pulposus tissue engineering. Materials Science and Engineering: C. 2014;37:232-40.

[345] Hu J, Chen B, Guo F, Du J, Gu P, Lin X, et al. Injectable silk fibroin/polyurethane composite hydrogel for nucleus pulposus replacement. Journal of Materials Science: Materials in Medicine. 2012;23:711-22.

[346] Neo PY, Shi P, Goh JC-H, Toh SL. Characterization and mechanical performance study of silk/PVA cryogels: towards nucleus pulposus tissue engineering. Biomedical Materials. 2014;9:065002.

[347] Murab S, Samal J, Shrivastava A, Ray AR, Pandit A, Ghosh S. Glucosamine loaded injectable silk-in-silk integrated system modulate mechanical properties in bovine ex-vivo degenerated intervertebral disc model. Biomaterials. 2015;55:64-83.

[348] Boyd LM, Carter AJ. Injectable biomaterials and vertebral endplate treatment for repair and regeneration of the intervertebral disc. European Spine Journal. 2006;15:414-21.

[349] Berlemann U, Schwarzenbach O. An injectable nucleus replacement as an adjunct to microdiscectomy: 2 year follow-up in a pilot clinical study. European Spine Journal. 2009;18:1706-12.

[350] Kia C, Baldino J, Bell R, Ramji A, Uyeki C, Mazzocca A. Platelet-rich plasma: review of current literature on its use for tendon and ligament pathology. Current reviews in musculoskeletal medicine. 2018;11:566-72.

[351] Muchedzi TA, Roberts SB. A systematic review of the effects of platelet rich plasma on outcomes for patients with knee osteoarthritis and following total knee arthroplasty. The Surgeon. 2018;16:250-8.

[352] Lubkowska A, Dolegowska B, Banfi G. Growth factor content in PRP and their applicability in medicine. J Biol Regul Homeost Agents. 2012;26:3S-22S.

[353] Zhang Z, Ma J, Ren D, Li F. A possible injectable tissue engineered nucleus pulposus constructed with platelet-rich plasma and ADSCs in vitro. Journal of Orthopaedic Surgery and Research. 2020;15:1-8.

[354] Tao H, Zhang Y, Wang C-f, Zhang C, Wang X-m, Wang D-l, et al. Biological evaluation of human degenerated nucleus pulposus cells in functionalized self-assembling peptide nanofiber hydrogel scaffold. Tissue Engineering Part A. 2014;20:1621-31.

[355] Ligorio C, O'Brien M, Hodson NW, Mironov A, Iliut M, Miller AF, et al. TGF-β3-loaded Graphene Oxide-Self-assembling Peptide Hybrid Hydrogels as Functional 3D Scaffolds for the Regeneration of the Nucleus Pulposus. Acta biomaterialia. 2021.

[356] Barcellona MN, Speer JE, Jing L, Gupta MC, Buchowski JM, Kelly MP, et al. Engineered Peptide-Functionalized Hydrogels Modulate the RNA Transcriptome of Human Nucleus Pulposus Cells In Vitro. bioRxiv. 2021.

[357] Borges AC, Eyholzer C, Duc F, Bourban P-E, Tingaut P, Zimmermann T, et al. Nanofibrillated cellulose composite hydrogel for the replacement of the nucleus pulposus. Acta biomaterialia. 2011;7:3412-21.

[358] Eyholzer C, Borges de Couraça A, Duc F, Bourban P, Tingaut P, Zimmermann T, et al. Biocomposite hydrogels with carboxymethylated, nanofibrillated cellulose powder for replacement of the nucleus pulposus. Biomacromolecules. 2011;12:1419-27.

[359] Gupta MS, Cooper ES, Nicoll SB. Transforming growth factor-beta 3 stimulates cartilage matrix elaboration by human marrow-derived stromal cells encapsulated in photocrosslinked

carboxymethylcellulose hydrogels: potential for nucleus pulposus replacement. Tissue Engineering Part A. 2011;17:2903-10.

[360] Varma DM, DiNicolas MS, Nicoll SB. Injectable, redox-polymerized carboxymethylcellulose hydrogels promote nucleus pulposus-like extracellular matrix elaboration by human MSCs in a cell density-dependent manner. Journal of biomaterials applications. 2018;33:576-89.

[361] Leone G, Consumi M, Lamponi S, Bonechi C, Tamasi G, Donati A, et al. Thixotropic PVA hydrogel enclosing a hydrophilic PVP core as nucleus pulposus substitute. Materials Science and Engineering: C. 2019;98:696-704.

[362] Leone G, Consumi M, Lamponi S, Bonechi C, Tamasi G, Donati A, et al. Hybrid PVA-xanthan gum hydrogels as nucleus pulposus substitutes. International Journal of Polymeric Materials and Polymeric Biomaterials. 2019;68:681-90.

[363] Liang C, Li H, Tao Y, Zhou X, Yang Z, Xiao Y, et al. Dual delivery for stem cell differentiation using dexamethasone and bFGF in/on polymeric microspheres as a cell carrier for nucleus pulposus regeneration. Journal of Materials Science: Materials in Medicine. 2012;23:1097-107.

[364] Christiani TR, Toomer K, Sheehan J, Nitzl A, Branda A, England E, et al. Synthesis of thermogelling poly (N-isopropylacrylamide)-graft-chondroitin sulfate composites with alginate microparticles for tissue engineering. JoVE (Journal of Visualized Experiments). 2016:e53704.

[365] Christiani T, Mys K, Dyer K, Kadlowec J, Iftode C, Vernengo A. Using embedded alginate microparticles to tune the properties of in situ forming poly (N-isopropylacrylamide)-graft-chondroitin sulfate bioadhesive hydrogels for replacement and repair of the nucleus pulposus of the intervertebral disc. bioRxiv. 2021.

[366] Vernengo J, Fussell G, Smith N, Lowman A. Evaluation of novel injectable hydrogels for nucleus pulposus replacement. Journal of Biomedical Materials Research Part B: Applied Biomaterials. 2008;84:64-9.

[367] Vernengo J, Fussell G, Smith N, Lowman A. Synthesis and characterization of injectable bioadhesive hydrogels for nucleus pulposus replacement and repair of the damaged intervertebral disc. Journal of Biomedical Materials Research Part B: Applied Biomaterials. 2010;93:309-17.

[368] Malonzo C, Chan SC, Kabiri A, Eglin D, Grad S, Bonel HM, et al. A papain-induced disc degeneration model for the assessment of thermo-reversible hydrogel–cells therapeutic approach. Journal of Tissue Engineering and Regenerative Medicine. 2015;9:E167-E76.

[369] Varma D, Lin H, Long R, Gold G, Hecht A, Iatridis J, et al. Thermoresponsive, redox-polymerized cellulosic hydrogels undergo in situ gelation and restore intervertebral disc biomechanics post discectomy. European Cells & Materials. 2018;35:300.

[370] McKee C, Beeravolu N, Brown C, Perez-Cruet M, Chaudhry GR. Mesenchymal stem cells transplanted with self-assembling scaffolds differentiated to regenerate nucleus pulposus in an ex vivo model of degenerative disc disease. Applied Materials Today. 2020;18:100474.

[371] Kumar D, Gerges I, Tamplenizza M, Lenardi C, Forsyth NR, Liu Y. Three-dimensional hypoxic culture of human mesenchymal stem cells encapsulated in a photocurable, biodegradable polymer hydrogel: a potential injectable cellular product for nucleus pulposus regeneration. Acta biomaterialia. 2014;10:3463-74.

[372] Guterl CC, See EY, Blanquer SB, Pandit A, Ferguson SJ, Benneker LM, et al. Challenges and strategies in the repair of ruptured annulus fibrosus. European cells & materials. 2013;25:1.

[373] Shao X, Hunter CJ. Developing an alginate/chitosan hybrid fiber scaffold for annulus fibrosus cells. Journal of Biomedical Materials Research Part A: An Official Journal of The Society for Biomaterials, The Japanese Society for Biomaterials, and The Australian Society for Biomaterials and the Korean Society for Biomaterials. 2007;82:701-10.

[374] Wan Y, Feng G, Shen FH, Laurencin CT, Li X. Biphasic scaffold for annulus fibrosus tissue regeneration. Biomaterials. 2008;29:643-52.

[375] Bhattacharjee M, Chameettachal S, Pahwa S, Ray AR, Ghosh S. Strategies for replicating anatomical cartilaginous tissue gradient in engineered intervertebral disc. ACS applied materials & interfaces. 2014;6:183-93.

[376] Bhattacharjee M, Chawla S, Chameettachal S, Murab S, Bhavesh NS, Ghosh S. Role of chondroitin sulphate tethered silk scaffold in cartilaginous disc tissue regeneration. Biomedical Materials. 2016;11:025014.

[377] Arai T, Freddi G, Innocenti R, Tsukada M. Biodegradation of Bombyx mori silk fibroin fibers and films. Journal of Applied Polymer Science. 2004;91:2383-90.

[378] Liu B, Song Y-w, Jin L, Wang Z-j, Pu D-y, Lin S-q, et al. Silk structure and degradation. Colloids and Surfaces B: Biointerfaces. 2015;131:122-8.

[379] Baker BM, Gee AO, Metter RB, Nathan AS, Marklein RA, Burdick JA, et al. The potential to improve cell infiltration in composite fiber-aligned electrospun scaffolds by the selective removal of sacrificial fibers. Biomaterials. 2008;29:2348-58.

[380] Mandal BB, Gil ES, Panilaitis B, Kaplan DL. Laminar silk scaffolds for aligned tissue fabrication. Macromolecular bioscience. 2013;13:48-58.

[381] Kim U-J, Park J, Kim HJ, Wada M, Kaplan DL. Three-dimensional aqueous-derived biomaterial scaffolds from silk fibroin. Biomaterials. 2005;26:2775-85.

[382] Mandal BB, Park S-H, Gil ES, Kaplan DL. Stem cell-based meniscus tissue engineering. Tissue Engineering Part A. 2011;17:2749-61.

[383] Moore P. A rapid, pH insensitive, two color fluorescence viability (cytotoxicity) assay. J Cell Biol. 1990;111:58a.

[384] Whitley CB, Ridnour M, Draper K, Dutton C, Neglia JP. Diagnostic test for mucopolysaccharidosis. I. Direct method for quantifying excessive urinary glycosaminoglycan excretion. Clinical chemistry. 1989;35:374-9.

[385] Tullberg-Reinert H, Jundt G. In situ measurement of collagen synthesis by human bone cells with a Sirius Red-based colorimetric microassay: effects of transforming growth factor β2 and ascorbic acid 2-phosphate. Histochemistry and cell biology. 1999;112:271-6.

[386] Best BA, Guilak F, Setton LA, Zhu W, Saed-Nejad F, Ratcliffe A, et al. Compressive mechanical properties of the human anulus fibrosus and their relationship to biochemical composition. Spine. 1994;19:212-21.

[387] Yao H, Justiz M-A, Flagler D, Gu WY. Effects of swelling pressure and hydraulic permeability on dynamic compressive behavior of lumbar annulus fibrosus. Annals of biomedical engineering. 2002;30:1234-41.

[388] Antoniou J, Steffen T, Nelson F, Winterbottom N, Hollander AP, Poole RA, et al. The human lumbar intervertebral disc: evidence for changes in the biosynthesis and denaturation of the extracellular matrix with growth, maturation, ageing, and degeneration. The Journal of clinical investigation. 1996;98:996-1003.

[389] Wu J, Cao W, Wen W, Chang DC, Sheng P. Polydimethylsiloxane microfluidic chip with integrated microheater and thermal sensor. Biomicrofluidics. 2009;3:012005.

[390] Mandal BB, Kundu SC. Non-bioengineered silk fibroin protein 3D scaffolds for potential biotechnological and tissue engineering applications. Macromolecular bioscience. 2008;8:807-18.

[391] Iatridis JC. Function follows form. Nature materials. 2009;8:923-4.

[392] Mandal BB, Grinberg A, Gil ES, Panilaitis B, Kaplan DL. High-strength silk protein scaffolds for bone repair. Proceedings of the National Academy of Sciences. 2012;109:7699-704.

[393] Wei A, Shen B, Williams L, Diwan A. Mesenchymal stem cells: potential application in intervertebral disc regeneration. Translational pediatrics. 2014;3:71.

[394] Mehlhorn A, Schmal H, Kaiser S, Lepski G, Finkenzeller G, Stark G, et al. Mesenchymal stem cells maintain TGF-β-mediated chondrogenic phenotype in alginate bead culture. Tissue engineering. 2006;12:1393-403.

[395] Gruber HE, Fisher Jr EC, Desai B, Stasky AA, Hoelscher G, Hanley Jr EN. Human intervertebral disc cells from the annulus: three-dimensional culture in agarose or alginate and responsiveness to TGF-β1. Experimental cell research. 1997;235:13-21.

[396] Awad HA, Halvorsen Y-DC, Gimble JM, Guilak F. Effects of transforming growth factor β 1 and dexamethasone on the growth and chondrogenic differentiation of adipose-derived stromal cells. Tissue engineering. 2003;9:1301-12.

[397] Anderson J. Biomaterials Science: Inflammation, wound healing, and the foreign-body response. San Diego: Elsevier Academic Press; 2004.

[398] McNally D, Adams M. Internal intervertebral disc mechanics as revealed by stress profilometry. Spine. 1992;17:66-73.

[399] Zhu C, Li J, Liu C, Zhou P, Yang H, Li B. Modulation of the gene expression of annulus fibrosus-derived stem cells using poly (ether carbonate urethane) urea scaffolds of tunable elasticity. Acta biomaterialia. 2016;29:228-38.

[400] Zhang Y-H, Zhao C-Q, Jiang L-S, Dai L-Y. Substrate stiffness regulates apoptosis and the mRNA expression of extracellular matrix regulatory genes in the rat annular cells. Matrix Biology. 2011;30:135-44.

[401] Xue C, Zhu H, Tan D, Ren H, Gu X, Zhao Y, et al. Electrospun silk fibroin-based neural scaffold for bridging a long sciatic nerve gap in dogs. Journal of tissue engineering and regenerative medicine. 2018;12:e1143-e53.

[402] Qi Y, Wang H, Wei K, Yang Y, Zheng R-Y, Kim IS, et al. A review of structure construction of silk fibroin biomaterials from single structures to multi-level structures. International journal of molecular sciences. 2017;18:237.

[403] Han H, Ning H, Liu S, Lu Q, Fan Z, Lu H, et al. Silk biomaterials with vascularization capacity. Advanced functional materials. 2016;26:421-32.

[404] Midha S, Murab S, Ghosh S. Osteogenic signaling on silk-based matrices. Biomaterials. 2016;97:133-53.

[405] Ribeiro VP, Pina S, Oliveira JM, Reis RL. Silk Fibroin-Based Hydrogels and Scaffolds for Osteochondral Repair and Regeneration. Osteochondral Tissue Engineering: Nanotechnology, Scaffolding-Related Developments and Translation. 2018:305-25.

[406] Mandal BB, Das S, Choudhury K, Kundu SC. Implication of silk film RGD availability and surface roughness on cytoskeletal organization and proliferation of primary rat bone marrow cells. Tissue Engineering Part A. 2010;16:2391-403.

[407] Adarsh Gupta K, Mita K, Arunkumar KP, Nagaraju J. Molecular architecture of silk fibroin of Indian golden silkmoth. Antheraea assama, Scientific Reports. 2015;5.

[408] Reardon PJ, Konwarh R, Knowles JC, Mandal BB. Mimicking Hierarchical Complexity of the Osteochondral Interface Using Electrospun Silk–Bioactive Glass Composites. ACS applied materials & interfaces. 2017;9:8000-13.

[409] Behera S, Naskar D, Sapru S, Bhattacharjee P, Dey T, Ghosh AK, et al. Hydroxyapatite reinforced inherent RGD containing silk fibroin composite scaffolds: Promising platform for bone tissue engineering. Nanomedicine: Nanotechnology, Biology and Medicine. 2017;13:1745-59.

[410] Darshan G, Kong D, Gautrot J, Vootla S. Physico-chemical characterization of Antheraea mylitta silk mats for wound healing applications. Scientific reports. 2017;7:10344.

[411] Mandal BB, Kundu S. A novel method for dissolution and stabilization of non-mulberry silk gland protein fibroin using anionic surfactant sodium dodecyl sulfate. Biotechnology and bioengineering. 2008;99:1482-9.

[412] Hu X, Kaplan D, Cebe P. Determining beta-sheet crystallinity in fibrous proteins by thermal analysis and infrared spectroscopy. Macromolecules. 2006;39:6161-70.

[413] Park S-H, Gil ES, Cho H, Mandal BB, Tien LW, Min B-H, et al. Intervertebral disk tissue engineering using biphasic silk composite scaffolds. Tissue Engineering Part A. 2011;18:447-58.

[414] Antoniou J, Steffen T, Nelson F, Winterbottom N, Hollander AP, Poole RA, et al. The human lumbar intervertebral disc: evidence for changes in the biosynthesis and denaturation of the extracellular matrix with growth, maturation, ageing, and degeneration. Journal of Clinical Investigation. 1996;98:996.

[415] Levy M, Slobodian E. Sequences of amino acid residues in silk fibroin. J Biol Chem. 1952;199:563-72.

[416] Asakura T, Yamane T, Nakazawa Y, Kameda T, Ando K. Structure of Bombyx mori silk fibroin before spinning in solid state studied with wide angle x-ray scattering and 13C cross-polarization/magic angle spinning NMR. Biopolymers. 2001;58:521-5.

[417] Kawai T. Freezing point depression of polymer solutions and gels. Journal of Polymer Science Part A: Polymer Chemistry. 1958;32:425-44.

[418] Davenport V, Stimson E, Scheraga H. Determination of molecular weights by differential cryoscopy on small volumes of dilute solutions of oligopeptides. Analytical biochemistry. 1984;142:400-5.

[419] Ahmad R, Kamra A, Hasnain SE. Fibroin silk proteins from the nonmulberry silkworm Philosamia ricini are biochemically and immunochemically distinct from those of the mulberry silkworm Bombyx mori. DNA and cell biology. 2004;23:149-54.

[420] Rasheva Z, Zhang G, Burkhart T. A correlation between the tribological and mechanical properties of short carbon fibers reinforced PEEK materials with different fiber orientations. Tribology International. 2010;43:1430-7.

[421] Amako K, Yasunaka K. Effects of sodium dodecyl sulphate on the structure of purified pyocin sheaths. Microbiology. 1974;80:443-50.

[422] Iatridis JC. Tissue engineering: Function follows form. Nature materials. 2009;8:923-4.

[423] Chang G, Kim HJ, Vunjak-Novakovic G, Kaplan DL, Kandel R. Enhancing annulus fibrosus tissue formation in porous silk scaffolds. Journal of biomedical materials research Part A. 2010;92:43-51.

[424] Chang G, Kim H-J, Kaplan D, Vunjak-Novakovic G, Kandel R. Porous silk scaffolds can be used for tissue engineering annulus fibrosus. European Spine Journal. 2007;16:1848-57.

[425] Park SH, Gil ES, Mandal BB, Cho H, Kluge JA, Min BH, et al. Annulus fibrosus tissue engineering using lamellar silk scaffolds. Journal of tissue engineering and regenerative medicine. 2012;6.

[426] D'Souza SE, Ginsberg MH, Plow EF. Arginyl-glycyl-aspartic acid (RGD): a cell adhesion motif. Trends in biochemical sciences. 1991;16:246-50.

[427] Janani G, Nandi SK, Mandal BB. Functional hepatocyte clusters on bioactive blend silk matrices towards generating bioartificial liver constructs. Acta biomaterialia. 2017.

[428] Sezutsu H, Yukuhiro K. The complete nucleotide sequence of the Eri-silkworm (Samia cynthia ricini) fibroin gene. Journal of Insect Biotechnology and Sericology. 2014;83:3_059-3_70.

[429] Horner HA, Roberts S, Bielby RC, Menage J, Evans H, Urban JP. Cells from different regions of the intervertebral disc: effect of culture system on matrix expression and cell phenotype. Spine. 2002;27:1018-28.

[430] Bruehlmann SB, B Rattner J, R Matyas J, A Duncan N. Regional variations in the cellular matrix of the annulus fibrosus of the intervertebral disc. Journal of anatomy. 2002;201:159-71.

[431] Sanz-Ramos P, Mora G, Vicente-Pascual M, Ochoa I, Alcaine C, Moreno R, et al. Response of sheep chondrocytes to changes in substrate stiffness from 2 to 20 Pa: effect of cell passaging. Connective tissue research. 2013;54:159-66.

[432] Park JS, Chu JS, Tsou AD, Diop R, Tang Z, Wang A, et al. The effect of matrix stiffness on the differentiation of mesenchymal stem cells in response to TGF-β. Biomaterials. 2011;32:3921-30.

[433] Discher DE, Janmey P, Wang Y-l. Tissue cells feel and respond to the stiffness of their substrate. Science. 2005;310:1139-43.

[434] Peyton SR, Putnam AJ. Extracellular matrix rigidity governs smooth muscle cell motility in a biphasic fashion. Journal of cellular physiology. 2005;204:198-209.

[435] Du J, Zu Y, Li J, Du S, Xu Y, Zhang L, et al. Extracellular matrix stiffness dictates Wnt expression through integrin pathway. Scientific reports. 2016;6.

[436] MacLean JJ, Lee CR, Alini M, Iatridis JC. Anabolic and catabolic mRNA levels of the intervertebral disc vary with the magnitude and frequency of in vivo dynamic compression. Journal of Orthopaedic Research. 2004;22:1193-200.

[437] Vishwakarma A, Bhise NS, Evangelista MB, Rouwkema J, Dokmeci MR, Ghaemmaghami AM, et al. Engineering immunomodulatory biomaterials to tune the inflammatory response. Trends in biotechnology. 2016;34:470-82.

[438] Murphy SV, Atala A. 3D bioprinting of tissues and organs. Nature biotechnology. 2014;32:773.

[439] Christiani T, Baroncini E, Stanzione J, Vernengo A. In vitro evaluation of 3D printed polycaprolactone scaffolds with angle-ply architecture for annulus fibrosus tissue engineering. Regenerative Biomaterials. 2019;6:175-84.

[440] Rahmati M, Pennisi CP, Budd E, Mobasheri A, Mozafari M. Biomaterials for Regenerative Medicine: Historical Perspectives and Current Trends. Cell Biology and Translational Medicine, Volume 4: Springer; 2018. p. 1-19.

[441] Bandyopadhyay A, Chowdhury SK, Dey S, Moses JC, Mandal BB. Silk: A Promising Biomaterial Opening New Vistas Towards Affordable Healthcare Solutions. Journal of the Indian Institute of Science. 2019:1-43.

[442] Chawla S, Midha S, Sharma A, Ghosh S. Silk-based bioinks for 3D bioprinting. Advanced healthcare materials. 2018;7:1701204.

[443] Costa JB, Silva-Correia J, Oliveira JM, Reis RL. Fast Setting Silk Fibroin Bioink for Bioprinting of Patient-Specific Memory-Shape Implants. Advanced healthcare materials. 2017;6:1701021.

[444] Zheng Z, Wu J, Liu M, Wang H, Li C, Rodriguez MJ, et al. 3D bioprinting of self-standing silk-based bioink. Advanced healthcare materials. 2018;7.

[445] Moses JC, Saha T, Mandal BB. Chondroprotective and osteogenic effects of silk-based bioinks in developing 3D bioprinted osteochondral interface. Bioprinting. 2019:e00067.

[446] Kim SH, Yeon YK, Lee JM, Chao JR, Lee YJ, Seo YB, et al. Precisely printable and biocompatible silk fibroin bioink for digital light processing 3D printing. Nature communications. 2018;9:1620.

[447] Bandyopadhyay A, Mandal BB. 3D printed silk-based biomimetic tri-layered meniscus for potential patient specific implantation. Biofabrication. 2019.

[448] Singh YP, Bandyopadhyay A, Mandal BB. 3D Bioprinting using Cross-Linker Free Silk-Gelatin Bioink for Cartilage Tissue Engineering. ACS applied materials & interfaces. 2019.

[449] Piculell L. Gelling carrageenans. Food polysaccharides and their applications. 2006;239.

[450] Yegappan R, Selvaprithiviraj V, Amirthalingam S, Mohandas A, Hwang NS, Jayakumar R. Injectable angiogenic and osteogenic carrageenan nanocomposite hydrogel for bone tissue engineering. International journal of biological macromolecules. 2019;122:320-8.

[451] Rode MP, Batti Angulski AB, Gomes FA, da Silva MM, Jeremias TdS, de Carvalho RG, et al. Carrageenan hydrogel as a scaffold for skin-derived multipotent stromal cells delivery. Journal of Biomaterials Applications. 2018;33:422-34.

[452] Popa EG, Caridade SG, Mano JF, Reis RL, Gomes ME. Chondrogenic potential of injectable κ-carrageenan hydrogel with encapsulated adipose stem cells for cartilage tissue-engineering applications. Journal of tissue engineering and regenerative medicine. 2015;9:550-63.

[453] Kelder C, Bakker A, Klein-Nulend J, Wismeijer D. The 3D printing of calcium phosphate with K-carrageenan under conditions permitting the incorporation of biological components—a method. Journal of functional biomaterials. 2018;9:57.

[454] Tytgat L, Van Damme L, Arevalo MdPO, Declercq H, Thienpont H, Otteveare H, et al. Extrusion-based 3D printing of photo-crosslinkable gelatin and κ-carrageenan hydrogel blends for adipose tissue regeneration. International journal of biological macromolecules. 2019;140:929-38.

[455] Rockwood DN, Preda RC, Yücel T, Wang X, Lovett ML, Kaplan DL. Materials fabrication from Bombyx mori silk fibroin. Nature protocols. 2011;6:1612.

[456] Thrimawithana T, Young S, Dunstan D, Alany R. Texture and rheological characterization of kappa and iota carrageenan in the presence of counter ions. Carbohydrate Polymers. 2010;82:69-77.

[457] Zuidema JM, Rivet CJ, Gilbert RJ, Morrison FA. A protocol for rheological characterization of hydrogels for tissue engineering strategies. Journal of Biomedical Materials Research Part B: Applied Biomaterials. 2014;102:1063-73.

[458] Larson RG, Wei Y. A review of thixotropy and its rheological modeling. Journal of Rheology. 2019;63:477-501.

[459] Lin Y, Xia X, Shang K, Elia R, Huang W, Cebe P, et al. Tuning chemical and physical cross-links in silk electrogels for morphological analysis and mechanical reinforcement. Biomacromolecules. 2013;14:2629-35.

[460] Niada S, Ferreira LM, Arrigoni E, Addis A, Campagnol M, Broccaioli E, et al. Porcine adipose-derived stem cells from buccal fat pad and subcutaneous adipose tissue for future preclinical studies in oral surgery. Stem cell research & therapy. 2013;4:148.

[461] Segnani C, Ippolito C, Antonioli L, Pellegrini C, Blandizzi C, Dolfi A, et al. Histochemical detection of collagen fibers by Sirius Red/Fast Green is more sensitive than van Gieson or Sirius Red alone in normal and inflamed rat colon. PloS one. 2015;10.

[462] Pereira L, Amado AM, Critchley AT, Van de Velde F, Ribeiro-Claro PJ. Identification of selected seaweed polysaccharides (phycocolloids) by vibrational spectroscopy (FTIR-ATR and FT-Raman). Food Hydrocolloids. 2009;23:1903-9.

[463] Vepari C, Kaplan DL. Silk as a biomaterial. Progress in polymer science. 2007;32:991-1007.

[464] Li L, Ni R, Shao Y, Mao S. Carrageenan and its applications in drug delivery. Carbohydrate Polymers. 2014;103:1-11.

[465] Goonoo N, Khanbabaee B, Steuber M, Bhaw-Luximon A, Jonas U, Pietsch U, et al. κ-carrageenan enhances the biomineralization and osteogenic differentiation of electrospun polyhydroxybutyrate and polyhydroxybutyrate valerate fibers. Biomacromolecules. 2017;18:1563-73.

[466] Li J, Yang B, Qian Y, Wang Q, Han R, Hao T, et al. Iota-carrageenan/chitosan/gelatin scaffold for the osteogenic differentiation of adipose-derived MSCs in vitro. Journal of Biomedical Materials Research Part B: Applied Biomaterials. 2015;103:1498-510.

[467] Tytgat L, Vagenende M, Declercq H, Martins J, Thienpont H, Ottevaere H, et al. Synergistic effect of κ-carrageenan and gelatin blends towards adipose tissue engineering. Carbohydrate polymers. 2018;189:1-9.

[468] Pourjavadi A, Doroudian M, Ahadpour A, Azari S. Injectable chitosan/κ-carrageenan hydrogel designed with au nanoparticles: A conductive scaffold for tissue engineering demands. International journal of biological macromolecules. 2019;126:310-7.

[469] Tavakoli S, Kharaziha M, Kermanpur A, Mokhtari H. Sprayable and injectable visible-light Kappa-carrageenan hydrogel for in-situ soft tissue engineering. International journal of biological macromolecules. 2019;138:590-601.

[470] Tytgat L, Van Damme L, Arevalo MdPO, Declercq H, Thienpont H, Otteveare H, et al. Extrusion-based 3D printing of photo-crosslinkable gelatin and κ-carrageenan hydrogel blends for adipose tissue regeneration. International journal of biological macromolecules. 2019.

[471] Yuguchi Y, Thuy TTT, Urakawa H, Kajiwara K. Structural characteristics of carrageenan gels: temperature and concentration dependence. Food Hydrocolloids. 2002;16:515-22.

[472] Hikichi K. Sol-gel transition of κ-carrageenan as viewed through NMR. Polymer Gels and Networks. 1993;1:19-31.

[473] Singh SK, Bhunia BK, Bhardwaj N, Gilotra S, Mandal BB. Reloadable silk-hydrogel hybrid scaffolds for sustained and targeted delivery of molecules. Molecular pharmaceutics. 2016;13:4066-81.

[474] Jeong JH, Lee JH, Jin ES, Min JK, Jeon SR, Choi KH. Regeneration of intervertebral discs in a rat disc degeneration model by implanted adipose-tissue-derived stromal cells. Acta neurochirurgica. 2010;152:1771-7.

[475] Ganey T, Hutton WC, Moseley T, Hedrick M, Meisel H-J. Intervertebral disc repair using adipose tissue-derived stem and regenerative cells: experiments in a canine model. Spine. 2009;34:2297-304.

[476] Zhou Y, Hu X, Zheng X, Wu Y, Tian N, Xu H, et al. Differentiation potential of mesenchymal stem cells derived from adipose tissue vs bone marrow toward annulus fibrosus cells in vitro. Current stem cell research & therapy. 2017;12:432-9.

[477] Blanquer SB, Gebraad AW, Miettinen S, Poot AA, Grijpma DW, Haimi SP. Differentiation of adipose stem cells seeded towards annulus fibrosus cells on a designed poly (trimethylene carbonate) scaffold prepared by stereolithography. Journal of tissue engineering and regenerative medicine. 2017;11:2752-62.

[478] Furumatsu T, Ozaki T, Asahara H. Smad3 activates the Sox9-dependent transcription on chromatin. The international journal of biochemistry & cell biology. 2009;41:1198-204.

[479] Thomson A, Fowler E. Carrageenan: a review of its effects on the immune system. Agents and Actions. 1981;11:265-73.

[480] Kopeček J. Hydrogel biomaterials: a smart future? Biomaterials. 2007;28:5185-92.

[481] El-Sherbiny IM, Yacoub MH. Hydrogel scaffolds for tissue engineering: Progress and challenges. Global Cardiology Science and Practice. 2013;2013:38.

[482] Zhu J, Marchant RE. Design properties of hydrogel tissue-engineering scaffolds. Expert review of medical devices. 2011;8:607-26.

[483] Destruel P-L, Zeng N, Maury M, Mignet N, Boudy V. In vitro and in vivo evaluation of in situ gelling systems for sustained topical ophthalmic delivery: state of the art and beyond. Drug discovery today. 2017;22:638-51.

[484] Peppas NA, Langer R. New challenges in biomaterials. Science. 1994;263:1715-20.

[485] Madan M, Bajaj A, Lewis S, Udupa N, Baig J. In situ forming polymeric drug delivery systems. Indian journal of pharmaceutical sciences. 2009;71:242.

[486] Ni Y, Yates KM. In-situ gel formation of pectin. Google Patents; 2004.

[487] Dumitriu S, Vidal PF, Chornet E. Hydrogels based on polysaccharides. Polysaccharides in medicinal applications. 1996:125-262.

[488] Miyazaki S, Suzuki S, Kawasaki N, Endo K, Takahashi A, Attwood D. In situ gelling xyloglucan formulations for sustained release ocular delivery of pilocarpine hydrochloride. International journal of pharmaceutics. 2001;229:29-36.

[489] Miyazaki S, Suisha F, Kawasaki N, Shirakawa M, Yamatoya K, Attwood D. Thermally reversible xyloglucan gels as vehicles for rectal drug delivery. Journal of Controlled Release. 1998;56:75-83.

[490] Kawasaki N, Ohkura R, Miyazaki S, Uno Y, Sugimoto S, Attwood D. Thermally reversible xyloglucan gels as vehicles for oral drug delivery. International journal of pharmaceutics. 1999;181:227-34.

[491] Janani G, Nandi SK, Mandal BB. Functional hepatocyte clusters on bioactive blend silk matrices towards generating bioartificial liver constructs. Acta biomaterialia. 2018;67:167-82.

[492] Moses JC, Nandi SK, Mandal BB. Multifunctional cell instructive silk-bioactive glass composite reinforced scaffolds toward osteoinductive, proangiogenic, and resorbable bone grafts. Advanced healthcare materials. 2018;7:1701418.

[493] Chouhan D, Janani G, Chakraborty B, Nandi SK, Mandal BB. Functionalized PVA–silk blended nanofibrous mats promote diabetic wound healing via regulation of extracellular matrix and tissue remodelling. Journal of tissue engineering and regenerative medicine. 2018;12:e1559-e70.

[494] Darshan G, Kong D, Gautrot J, Vootla S. Physico-chemical characterization of Antheraea mylitta silk mats for wound healing applications. Scientific reports. 2017;7:1-11.

[495] Yucel T, Cebe P, Kaplan DL. Vortex-induced injectable silk fibroin hydrogels. Biophysical journal. 2009;97:2044-50.

[496] Numata K, Katashima T, Sakai T. State of water, molecular structure, and cytotoxicity of silk hydrogels. Biomacromolecules. 2011;12:2137-44.

[497] Wang X, Kluge JA, Leisk GG, Kaplan DL. Sonication-induced gelation of silk fibroin for cell encapsulation. Biomaterials. 2008;29:1054-64.

[498] Matsumoto A, Chen J, Collette AL, Kim U-J, Altman GH, Cebe P, et al. Mechanisms of silk fibroin sol− gel transitions. The Journal of Physical Chemistry B. 2006;110:21630-8.

[499] Floren M, Migliaresi C, Motta A. Processing techniques and applications of silk hydrogels in bioengineering. Journal of functional biomaterials. 2016;7:26.

[500] Yang Y, Chen J, Bonani W, Chen B, Eccheli S, Maniglio D, et al. Sodium oleate induced rapid gelation of silk fibroin. Journal of Biomaterials science, Polymer edition. 2018;29:1219-31.

[501] Bragg JC, Kweon H, Jo Y, Lee KG, Lin C-C. In situ formation of silk-gelatin hybrid hydrogels for affinity-based growth factor sequestration and release. RSC advances. 2016;6:114353-60.

[502] Le Maitre CL, Freemont AJ, Hoyland JA. Accelerated cellular senescence in degenerate intervertebral discs: a possible role in the pathogenesis of intervertebral disc degeneration. Arthritis research & therapy. 2007;9:R45.

[503] Jalani G, Rosenzweig DH, Makhoul G, Abdalla S, Cecere R, Vetrone F, et al. Tough, In-Situ Thermogelling, Injectable Hydrogels for Biomedical Applications. Macromolecular bioscience. 2015;15:473-80.

[504] Wachs RA, Hoogenboezem EN, Huda HI, Xin S, Porvasnik SL, Schmidt CE. Creation of an injectable in situ gelling native extracellular matrix for nucleus pulposus tissue engineering. The Spine Journal. 2017;17:435-44.

[505] Gupta A, Mita K, Arunkumar KP, Nagaraju J. Molecular architecture of silk fibroin of Indian golden silkmoth, Antheraea assama. Scientific reports. 2015;5:12706.

[506] Wray LS, Hu X, Gallego J, Georgakoudi I, Omenetto FG, Schmidt D, et al. Effect of processing on silk-based biomaterials: Reproducibility and biocompatibility. Journal of Biomedical Materials Research Part B: Applied Biomaterials. 2011;99:89-101.

[507] Garidel P, Schott H. Fourier-transform midinfrared spectroscopy for analysis and screening of liquid protein formulations. Bioprocess international. 2006;4:48-55.

[508] Hu J, Lu Y, Cai L, Owusu-Ansah KG, Xu G, Han F, et al. Functional compressive mechanics and tissue biocompatibility of an injectable SF/PU hydrogel for nucleus pulposus replacement. Scientific reports. 2017;7:1-8.

[509] Kapoor S, Kundu SC. Silk protein-based hydrogels: promising advanced materials for biomedical applications. Acta biomaterialia. 2016;31:17-32.

[510] Zhou C-Z, Confalonieri F, Esnault C, Zivanovic Y, Jacquet M, Janin J, et al. The 62-kb upstream region of Bombyx mori fibroin heavy chain gene is clustered of repetitive elements and candidate matrix association regions. Gene. 2003;312:189-95.

[511] Asakura T, Ohgo K, Ishida T, Taddei P, Monti P, Kishore R. Possible Implications of Serine and Tyrosine Residues and Intermolecular Interactions on the Appearance of Silk I Structure of

Bombyx m ori Silk Fibroin-Derived Synthetic Peptides: High-Resolution 13C Cross-Polarization/Magic-Angle Spinning NMR Study. Biomacromolecules. 2005;6:468-74.

[512] Schellman JA. Temperature, stability, and the hydrophobic interaction. Biophysical journal. 1997;73:2960-4.

[513] Melander W, Horváth C. Salt effects on hydrophobic interactions in precipitation and chromatography of proteins: an interpretation of the lyotropic series. Archives of biochemistry and biophysics. 1977;183:200-15.

[514] Ho YP, Yang MW, Chen LT, Yang YC. Relative calcium-binding strengths of amino acids determined using the kinetic method. Rapid Communications in Mass Spectrometry: An International Journal Devoted to the Rapid Dissemination of Up-to-the-Minute Research in Mass Spectrometry. 2007;21:1083-9.

[515] Zhou P, Xie X, Knight DP, Zong X-H, Deng F, Yao W-H. Effects of pH and calcium ions on the conformational transitions in silk fibroin using 2D Raman correlation spectroscopy and 13C solid-state NMR. Biochemistry. 2004;43:11302-11.

[516] Kim U-J, Park J, Li C, Jin H-J, Valluzzi R, Kaplan DL. Structure and properties of silk hydrogels. Biomacromolecules. 2004;5:786-92.

[517] Wu X, Zhu Y. Heterogeneous materials: a new class of materials with unprecedented mechanical properties. Materials Research Letters. 2017;5:527-32.

[518] Elder RM, Neupane MR, Chantawansri TL. Mechanical properties of homogeneous and heterogeneous layered 2D materials. 2015 International Conference on Simulation of Semiconductor Processes and Devices (SISPAD): IEEE; 2015. p. 471-4.

[519] Carthy JM, Luo Z, McManus BM. WNT3A induces a contractile and secretory phenotype in cultured vascular smooth muscle cells that is associated with increased gap junction communication. Laboratory investigation. 2012;92:246-55.

[520] Song Z-T, Speakman PT. Isoelectric focusing of silk fibroin polypeptides. Portland Press Ltd.; 1985.

[521] Gupta P, Adhikary M, Kumar M, Bhardwaj N, Mandal BB. Biomimetic, osteoconductive non-mulberry silk fiber reinforced tricomposite scaffolds for bone tissue engineering. ACS applied materials & interfaces. 2016;8:30797-810.

[522] Chen W-H, Liu H-Y, Lo W-C, Wu S-C, Chi C-H, Chang H-Y, et al. Intervertebral disc regeneration in an ex vivo culture system using mesenchymal stem cells and platelet-rich plasma. Biomaterials. 2009;30:5523-33.

[523] Stannard JT, Edamura K, Stoker AM, O'Connell GD, Kuroki K, Hung CT, et al. Development of a whole organ culture model for intervertebral disc disease. Journal of orthopaedic translation. 2016;5:1-8.

[524] Beadon K, Johnston JD, Siggers K, Itshayek E, Cripton PA. A repeatable ex vivo model of spondylolysis and spondylolisthesis. Spine. 2008;33:2387-93.

[525] Showalter BL, Elliott DM, Chen W, Malhotra NR. Evaluation of an in situ gelable and injectable hydrogel treatment to preserve human disc mechanical function undergoing physiologic cyclic loading followed by hydrated recovery. Journal of biomechanical engineering. 2015;137.

[526] Malhotra NR, Han WM, Beckstein J, Cloyd J, Chen W, Elliott DM. An injectable nucleus pulposus implant restores compressive range of motion in the ovine disc. Spine. 2012;37:E1099.

[527] Chirila TV, Suzuki S, Papolla C. A comparative investigation of Bombyx mori silk fibroin hydrogels generated by chemical and enzymatic cross-linking. Biotechnology and applied biochemistry. 2017;64:771-81.

[528] Adachi E, Hopkinson I, Hayashi T. Basement-membrane stromal relationships: interactions between collagen fibrils and the lamina densa. International review of cytology. 1997;173:73-156.

[529] Giancotti FG, Ruoslahti E. Integrin signaling. Science. 1999;285:1028-33.

[530] Rahman S, Patel Y, Murray J, Patel KV, Sumathipala R, Sobel M, et al. Novel hepatocyte growth factor (HGF) binding domains on fibronectin and vitronectin coordinate a distinct and amplified Met-integrin induced signalling pathway in endothelial cells. BMC cell biology. 2005;6:1-17.

[531] Comoglio PM, Boccaccio C, Trusolino L. Interactions between growth factor receptors and adhesion molecules: breaking the rules. Current opinion in cell biology. 2003;15:565-71.

[532] Gilbert TW, Sellaro TL, Badylak SF. Decellularization of tissues and organs. Biomaterials. 2006;27:3675-83.

[533] Chen F, Yoo JJ, Atala A. Acellular collagen matrix as a possible “off the shelf” biomaterial for urethral repair. Urology. 1999;54:407-10.

[534] Franc S, Rousseau J-C, Garrone R, Van Der Rest M, Moradi-Ameli M. Microfibrillar composition of umbilical cord matrix: characterization of fibrillin, collagen VI and intact collagen V. Placenta. 1998;19:95-104.

[535] Ahmadi M, Seyedjafari E, Zargar SJ, Birhanu G, Zandi-Karimi A, Beiki B, et al. Osteogenic differentiation of mesenchymal stem cells cultured on PLLA scaffold coated with Wharton's Jelly. EXCLI journal. 2017;16:785.

[536] Li D, Chiu G, Lipe B, Hopkins RA, Lillis J, Ashton JM, et al. Decellularized Wharton jelly matrix: a biomimetic scaffold for ex vivo hematopoietic stem cell culture. Blood advances. 2019;3:1011-26.

[537] Xiao T, Guo W, Chen M, Hao C, Gao S, Huang J, et al. Fabrication and in vitro study of tissue-engineered cartilage scaffold derived from Wharton's jelly extracellular matrix. BioMed research international. 2017;2017.

[538] Lin L, Xu Y, Li Y, Gong X, Wei M, Zhang W, et al. Nanofibrous Wharton's jelly scaffold in combination with adipose-derived stem cells for cartilage engineering. Materials & Design. 2020;186:108216.

[539] Penolazzi L, Pozzobon M, Bergamin LS, D'Agostino S, Francescato R, Bonaccorsi G, et al. Extracellular Matrix From Decellularized Wharton's Jelly Improves the Behavior of Cells From Degenerated Intervertebral Disc. Frontiers in bioengineering and biotechnology. 2020;8:262.

[540] Jadalannagari S, Converse G, McFall C, Buse E, Filla M, Villar MT, et al. Decellularized Wharton's Jelly from human umbilical cord as a novel 3D scaffolding material for tissue engineering applications. PLoS One. 2017;12:e0172098.

[541] Bakhtyar N, Jeschke MG, Herer E, Sheikholeslam M, Amini-Nik S. Exosomes from acellular Wharton's jelly of the human umbilical cord promotes skin wound healing. Stem cell research & therapy. 2018;9:1-14.

[542] Mandal BB, Park S-H, Gil ES, Kaplan DL. Multilayered silk scaffolds for meniscus tissue engineering. Biomaterials. 2011;32:639-51.

[543] Segnani C, Ippolito C, Antonioli L, Pellegrini C, Blandizzi C, Dolfi A, et al. Histochemical detection of collagen fibers by sirius red/fast green is more sensitive than van gieson or sirius red alone in normal and inflamed rat colon. PLoS One. 2015;10:e0144630.

[544] Saldin LT, Cramer MC, Velankar SS, White LJ, Badylak SF. Extracellular matrix hydrogels from decellularized tissues: Structure and function. Acta biomaterialia. 2017;49:1-15.

[545] Crapo PM, Gilbert TW, Badylak SF. An overview of tissue and whole organ decellularization processes. Biomaterials. 2011;32:3233-43.

[546] Brown BN, Badylak SF. Extracellular matrix as an inductive scaffold for functional tissue reconstruction. Translational Research. 2014;163:268-85.

[547] Taylor DA, Sampaio LC, Ferdous Z, Gobin AS, Taite LJ. Decellularized matrices in regenerative medicine. Acta biomaterialia. 2018;74:74-89.

[548] Soto-Gutierrez A, Zhang L, Medberry C, Fukumitsu K, Faulk D, Jiang H, et al. A whole-organ regenerative medicine approach for liver replacement. Tissue Engineering Part C: Methods. 2011;17:677-86.

[549] Gilbert TW, Freund JM, Badylak SF. Quantification of DNA in biologic scaffold materials. Journal of Surgical Research. 2009;152:135-9.

[550] Yu C, Gao H, Li Q, Cao X. Injectable dual cross-linked adhesive hyaluronic acid multifunctional hydrogel scaffolds for potential applications in cartilage repair. Polymer Chemistry. 2020;11:3169-78.

[551] Koivusalo L, Kauppila M, Samanta S, Parihar VS, Ilmarinen T, Miettinen S, et al. Tissue adhesive hyaluronic acid hydrogels for sutureless stem cell delivery and regeneration of corneal epithelium and stroma. Biomaterials. 2019;225:119516.

[552] Chandrasekharan A, Seong KY, Yim SG, Kim S, Seo S, Yoon J, et al. In situ photocrosslinkable hyaluronic acid-based surgical glue with tunable mechanical properties and high adhesive strength. Journal of polymer Science part A: polymer Chemistry. 2019;57:522-30.

[553] Schneider-Barthold C, Baganz S, Wilhelmi M, Scheper T, Pepelanova I. Hydrogels based on collagen and fibrin–frontiers and applications. BioNanoMaterials. 2016;17:3-12.

[554] Chang R, Nam J, Sun W. Effects of dispensing pressure and nozzle diameter on cell survival from solid freeform fabrication–based direct cell writing. Tissue Engineering Part A. 2008;14:41-8.

[555] Garantziotis S, Savani RC. Hyaluronan biology: A complex balancing act of structure, function, location and context. Matrix Biology. 2019;78:1-10.

[556] Isa ILM, Srivastava A, Tiernan D, Owens P, Rooney P, Dockery P, et al. Hyaluronic acid based hydrogels attenuate inflammatory receptors and neurotrophins in interleukin-1β induced inflammation model of nucleus pulposus cells. Biomacromolecules. 2015;16:1714-25.

[557] Kennon JC, Awad ME, Chutkan N, DeVine J, Fulzele S. Current insights on use of growth factors as therapy for intervertebral disc degeneration. Biomolecular concepts. 2018;9:43-52.

[558] Ge J, Gan M, Wu C, Yan Q, Chen Y, Yang H, et al. Effects of PDGF-B Overexpression on the biological activity of nucleus pulposus cells. Journal of Hard Tissue Biology. 2019;28:147-52.

APPENDIX

APPENDIX

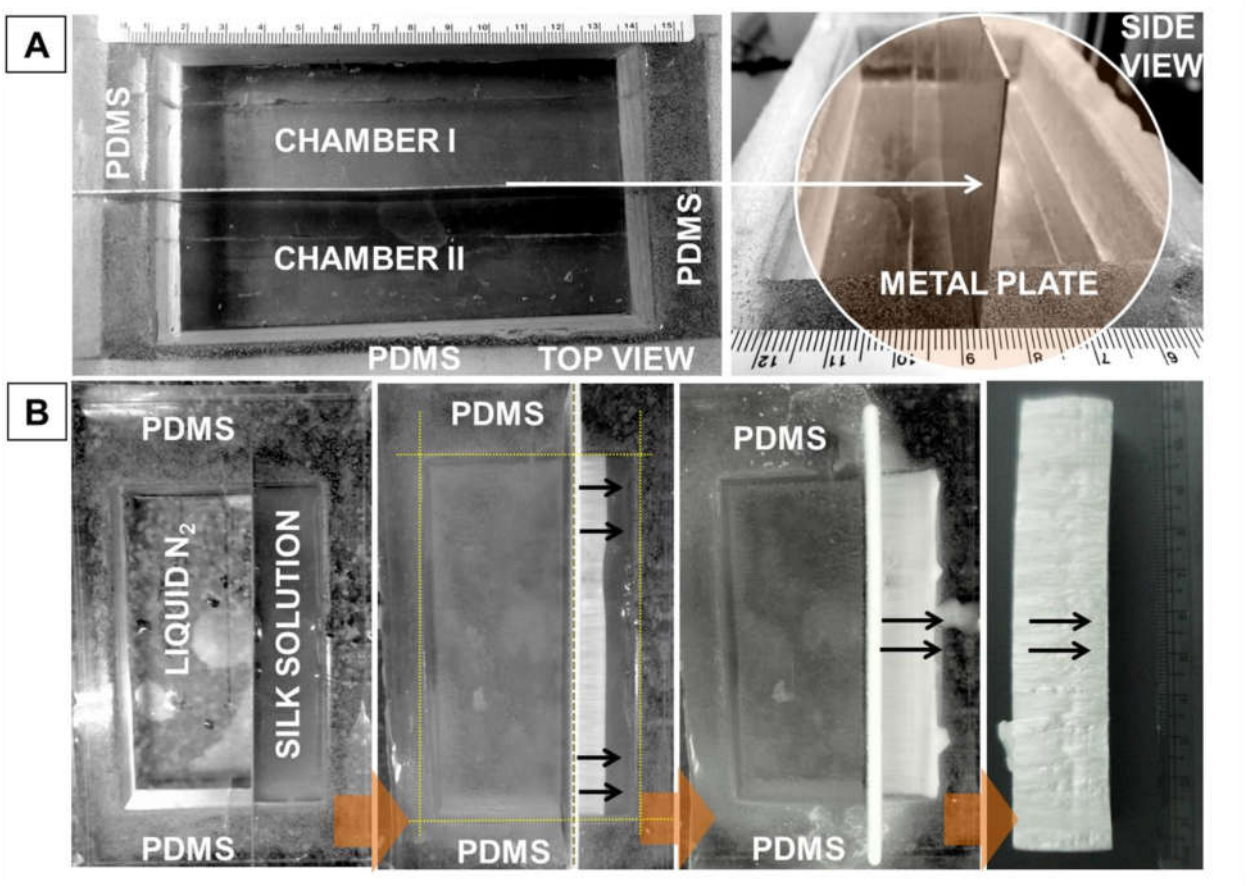

Figure A2.1. *Fabrication of lamellar scaffolds; (A) Polydimethylsiloxane (PDMS) mold for preparation of lamellar scaffolds, (B) directional freezing of silk solution by liquid nitrogen.*

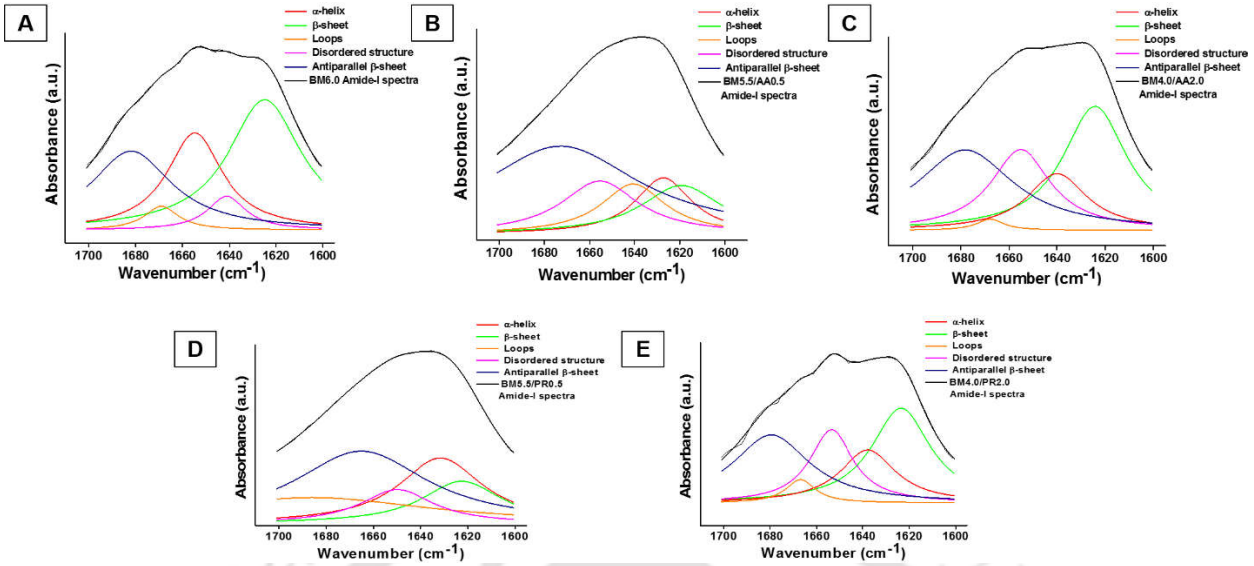

Figure A3.1. *Secondary structures analysis of different SF lamellar constructs by deconvolution of amide I region (1600-1700 cm^{-1}) using second order derivative method; (A) BM6.0, (B) BM5.5/AA0.5, (C) BM4.0/AA2.0, (D) BM5.5/PR0.5 and (E) BM4.0/PR2.0*

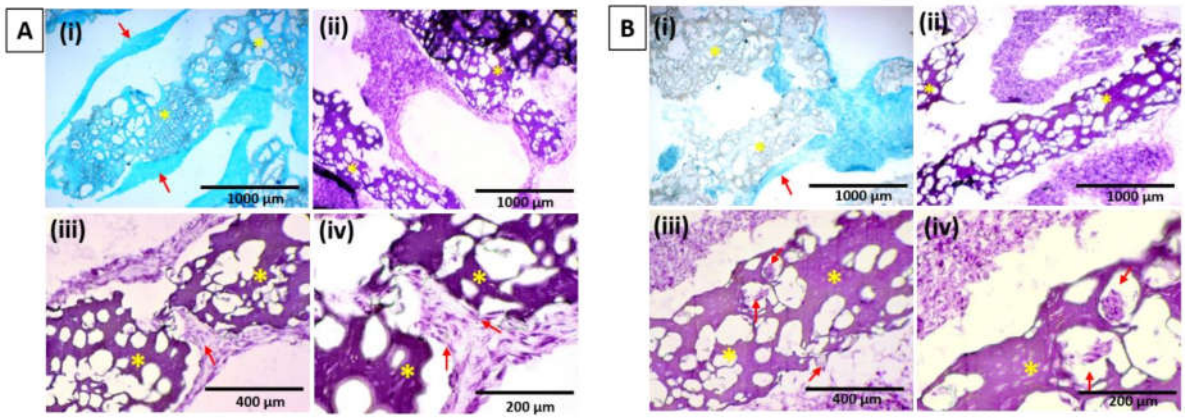

Figure A4.1: *Histological analysis of cell seeded 3D-printed angle-grid constructs maintained for 4 weeks: (A) AF cells and (B) ADSCs; (i) alcian blue staining for deposited GAGs, (ii) gross structure in low magnification, (iii) cellular alignment and infiltration and (iv) magnified image*

of (iii). Yellow asterisk symbol represents the scaffold part and cells are pointed out with red arrows.

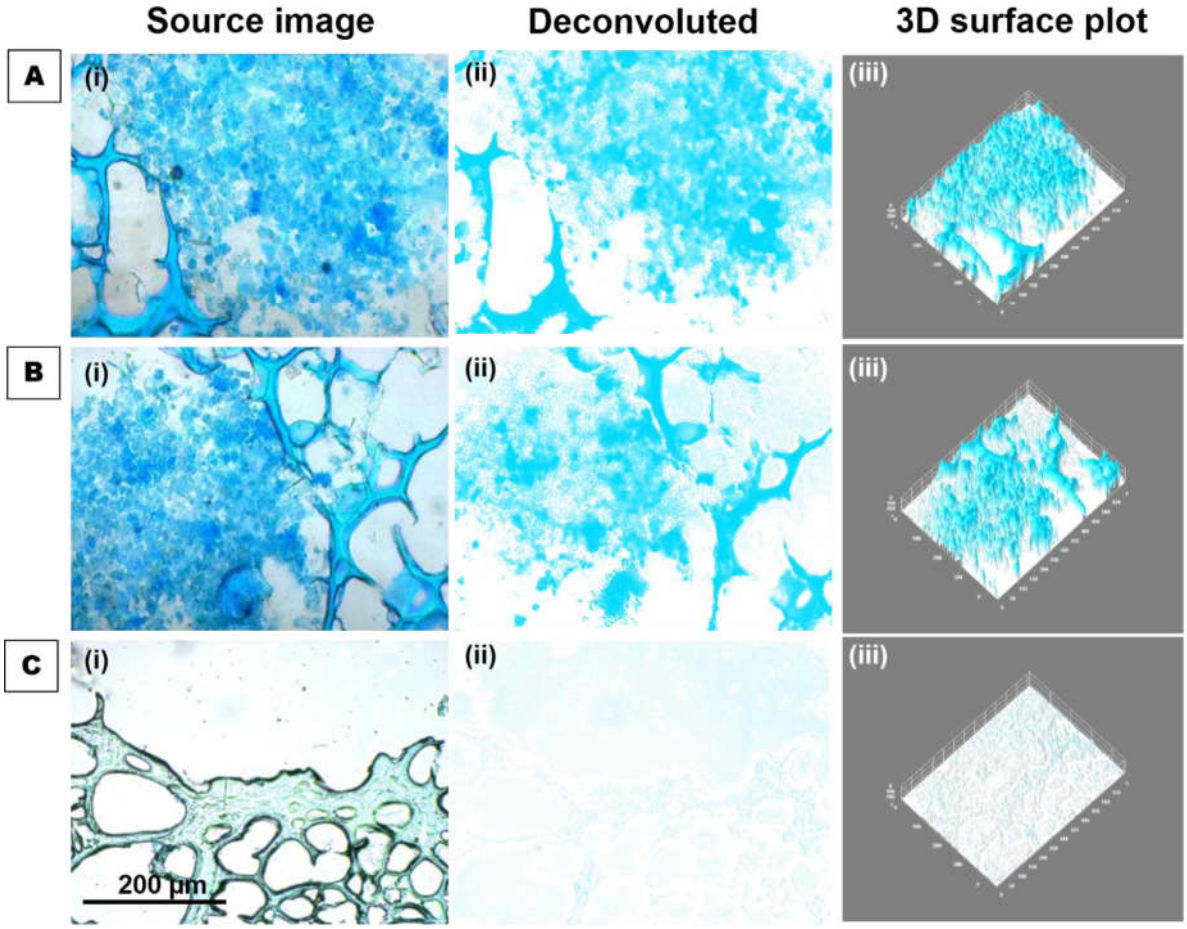

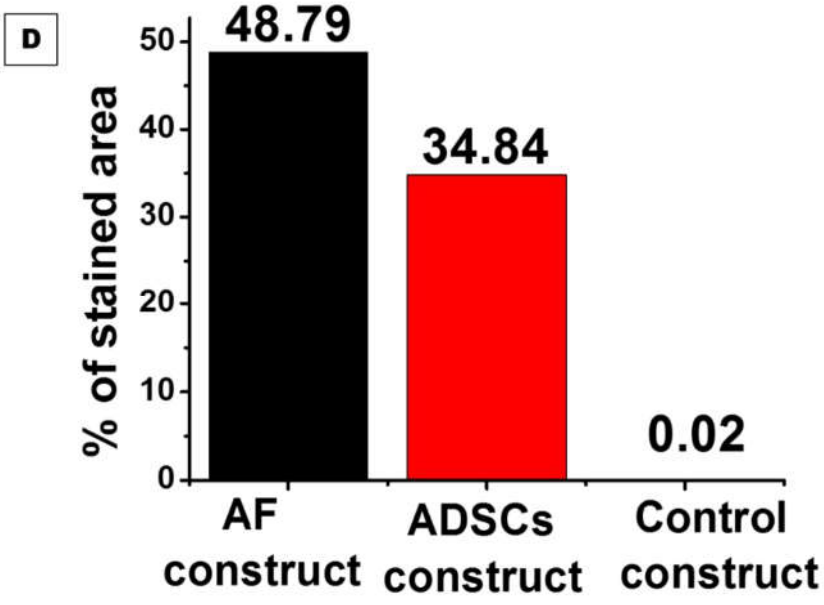

Figure A4.2: *sGAG Quantification using image analysis tool of alcian blue staining; 3D-printed angle-grid constructs seeded with (A, i-iii) AF cells, (B, i-iii) ADSCs, and (C, i-iii) blank as a control. The left, middle and the right column representing original images, deconvoluted images and the 3D surface plots, respectively, (D) the quantification of % of stained area after deconvolution.*

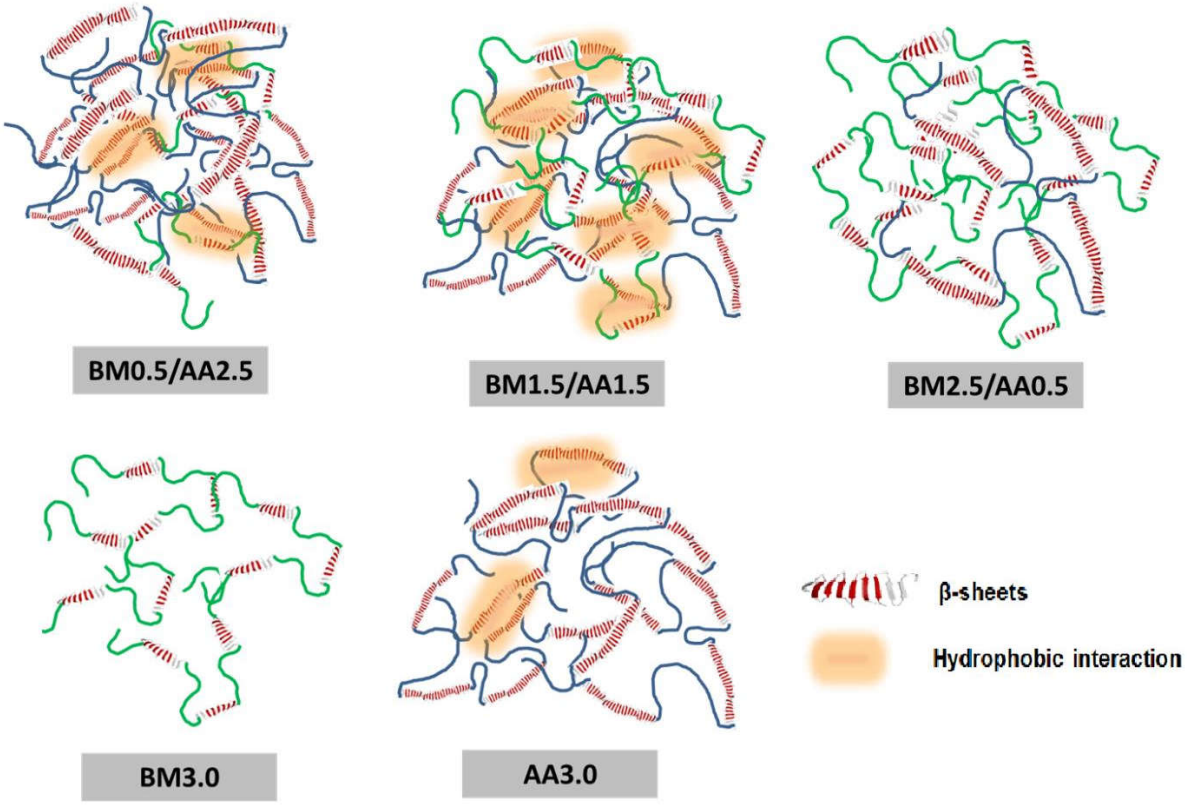

Figure A5.1. *Schematic representation of hydrophobic interaction among the protein chains of two blended protein in different ratios.*

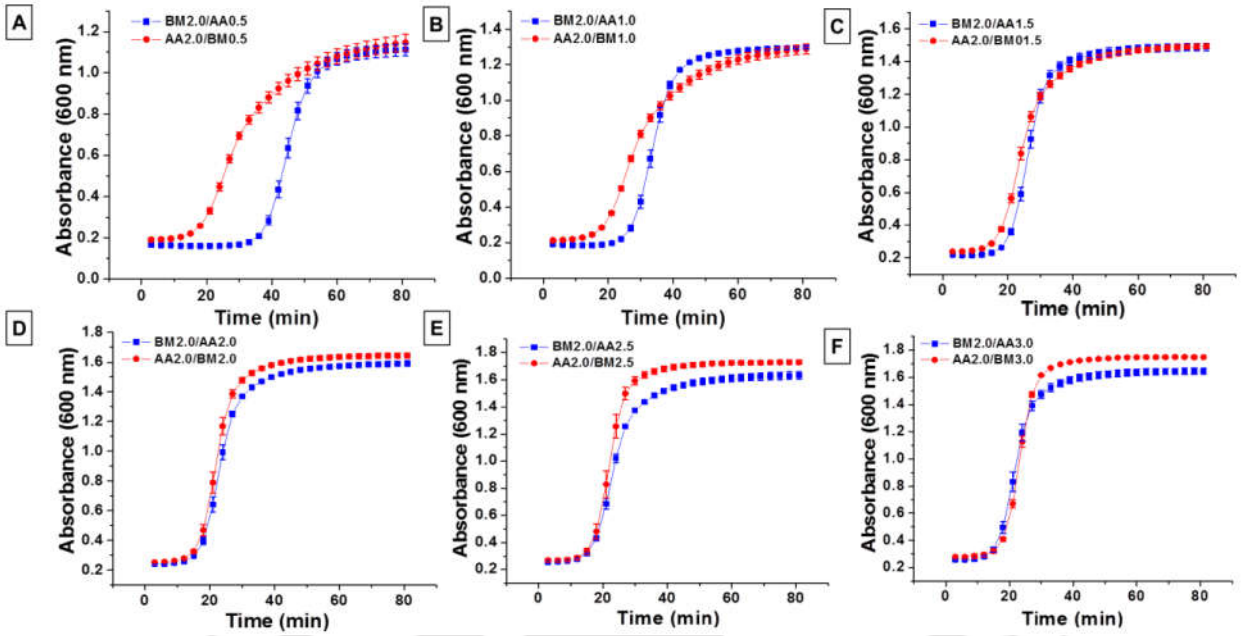

Figure A5.2. *Comparison between two groups of same combination but different concentrations; (A) BM2.0/AA0.5 and AA2.0/BM0.5, (B) BM2.0/AA1.0 and AA2.0/BM1.0, (C) BM2.0/AA1.5 and AA2.0/BM1.5, (D) BM2.0/AA2.5 and AA2.0/BM2.5 (D) BM2.0/AA2.0 and AA2.0/BM2.0, (E) BM2.0/AA2.5 and AA2.0/BM2.5 and, (F) BM2.0/AA3.0 and AA2.0/BM3.0. Data represents mean ± SD (n = 3).*

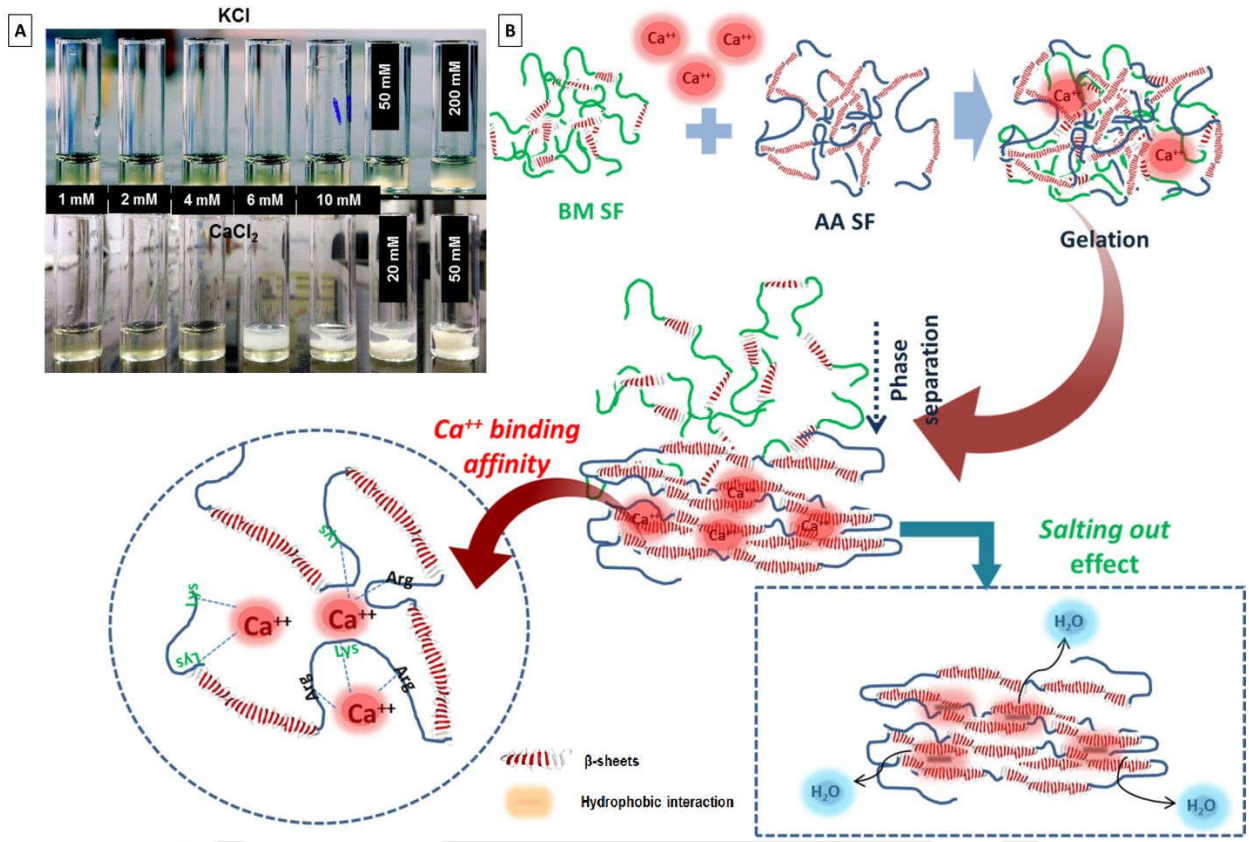

Figure A5.3. *Effect of ionic concentration on gelation; (A) BM SF precipitation in response of KCl and $CaCl_2$, (B) proposed mechanism of Ca^{2+} ion effect on gelation.*

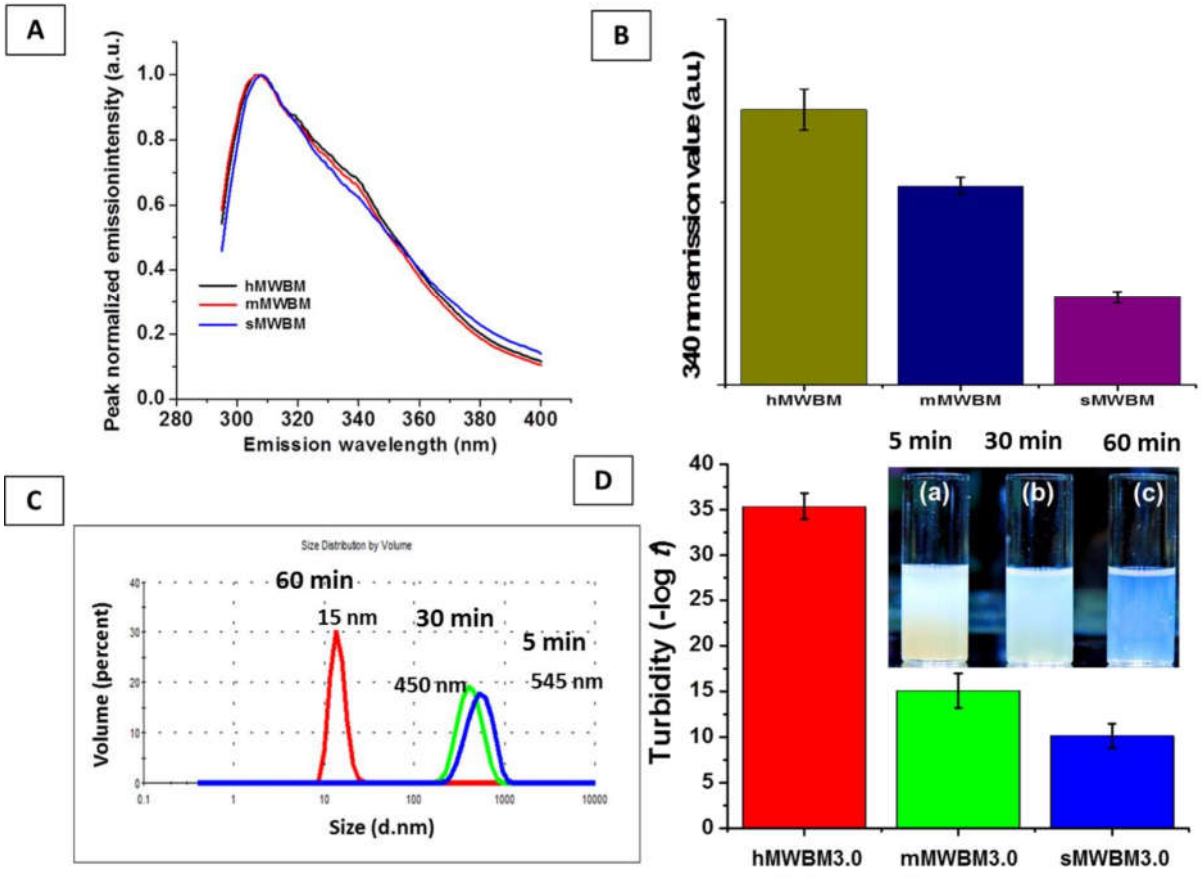

Figure A5.4. *Detection of molecular size of BM SF, degummed at three different time points; (A) fluorescent emission spectra (B) normalized value fluorescence intensity at 340 nm (C) particle size distribution by DLS, and (D) turbidity assessment of SF solution degummed at three different time points, insert is the representing images of the same; (a) hMWBM, (b) mMWBM and (c) sMWBM.*

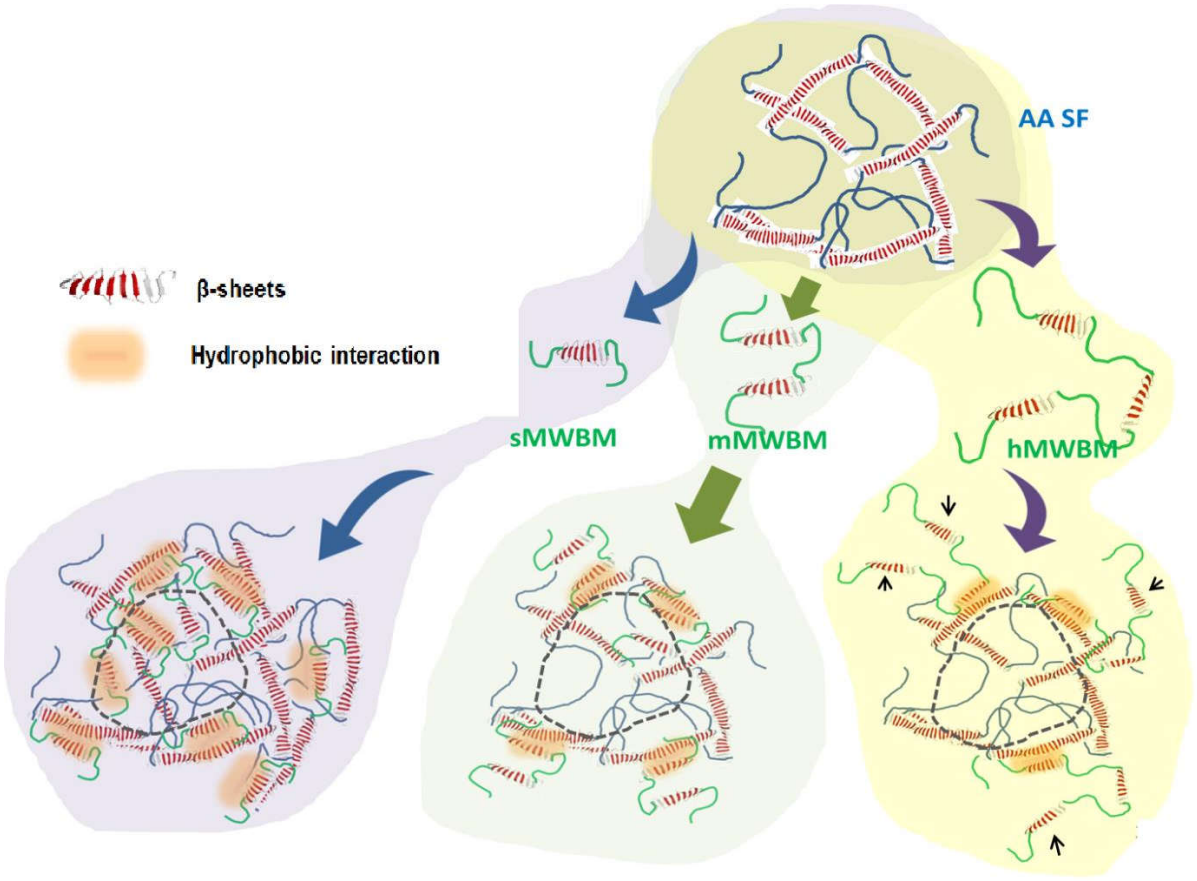

***Figure A5.5**. Proposed mechanism of molecular weight (BM SF) effect on gelation.*

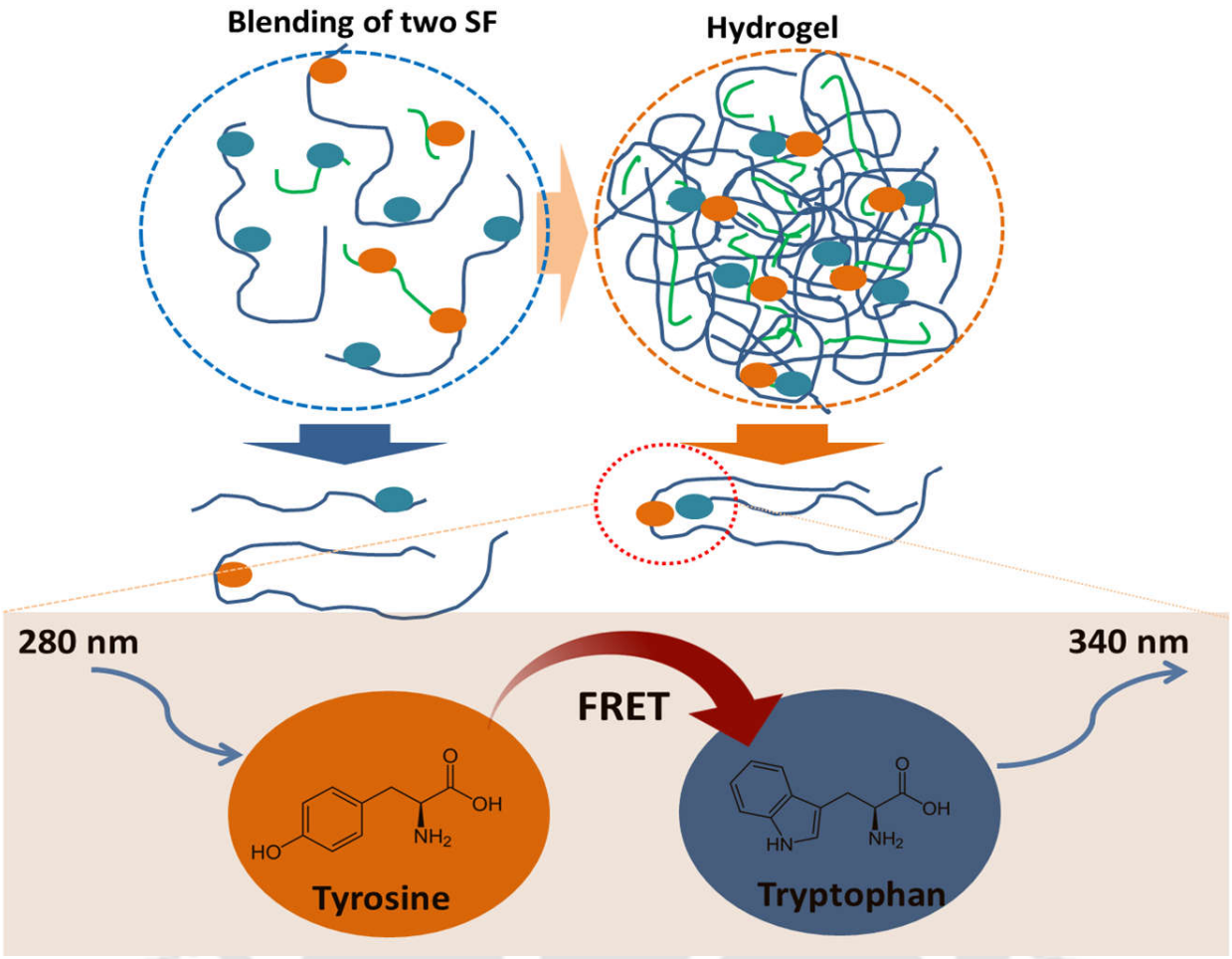

***Figure A5.6**. Schematic representation of FRET during gelation*

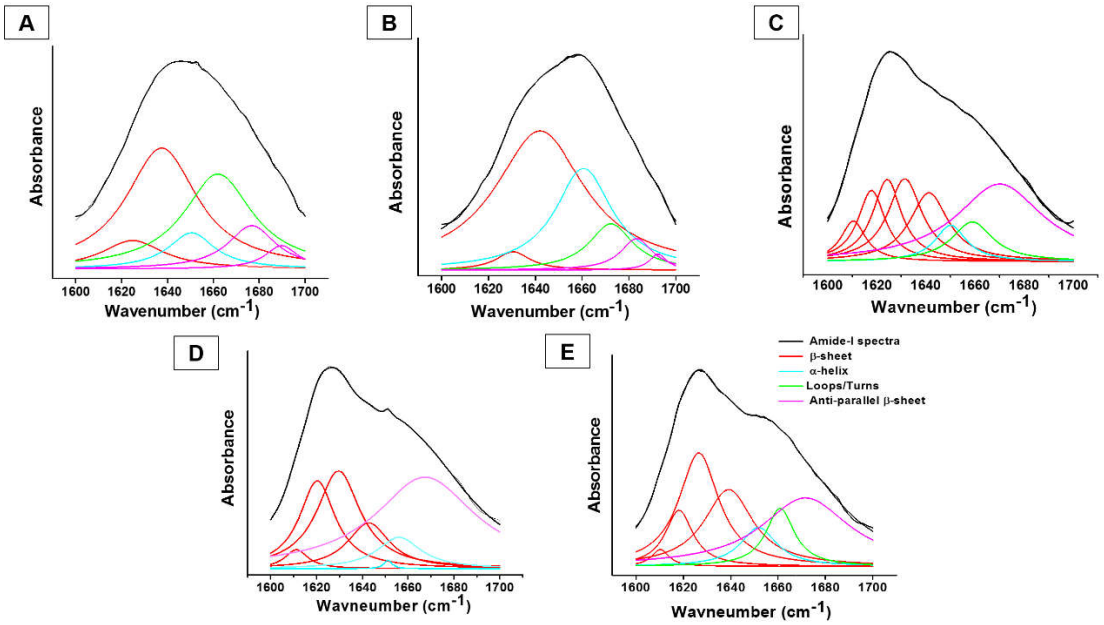

***Figure A5.7**: Determination of different secondary structures in hydrogels by deconvolution of amide I region (1600-1700 cm^{-1}) using second order derivative method; (A) BM3.0, (B) AA3.0, (C) BM0.5/AA2.5, (D) BM1.5/AA1.5 and (E) BM2.5/AA0.5*

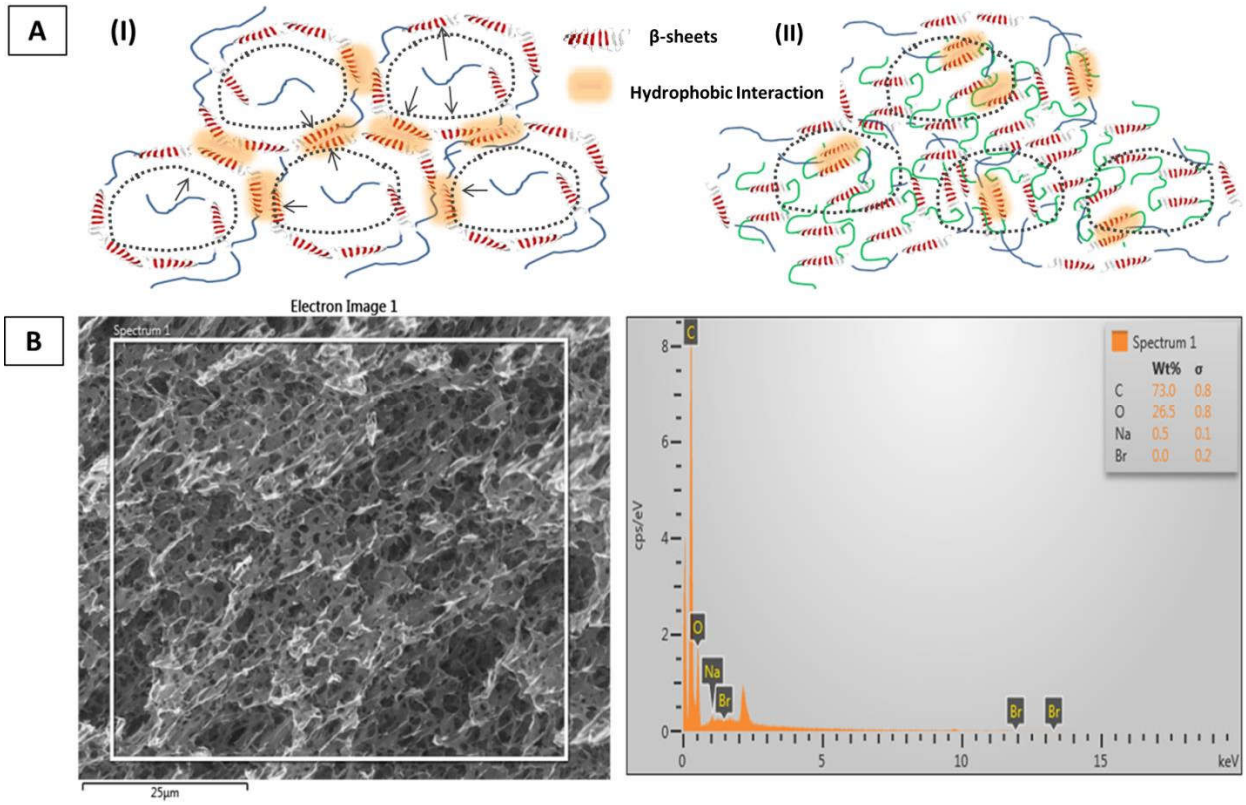

Figure A5.8. *(A) Schematic representation of mechanism behind SF types dependent pore formation in hydrogel; (I) High AA SF content hydrogel and (II) high BM SF content hydrogel and (B) elemental analysis of hydrogels through EDX analysis.*

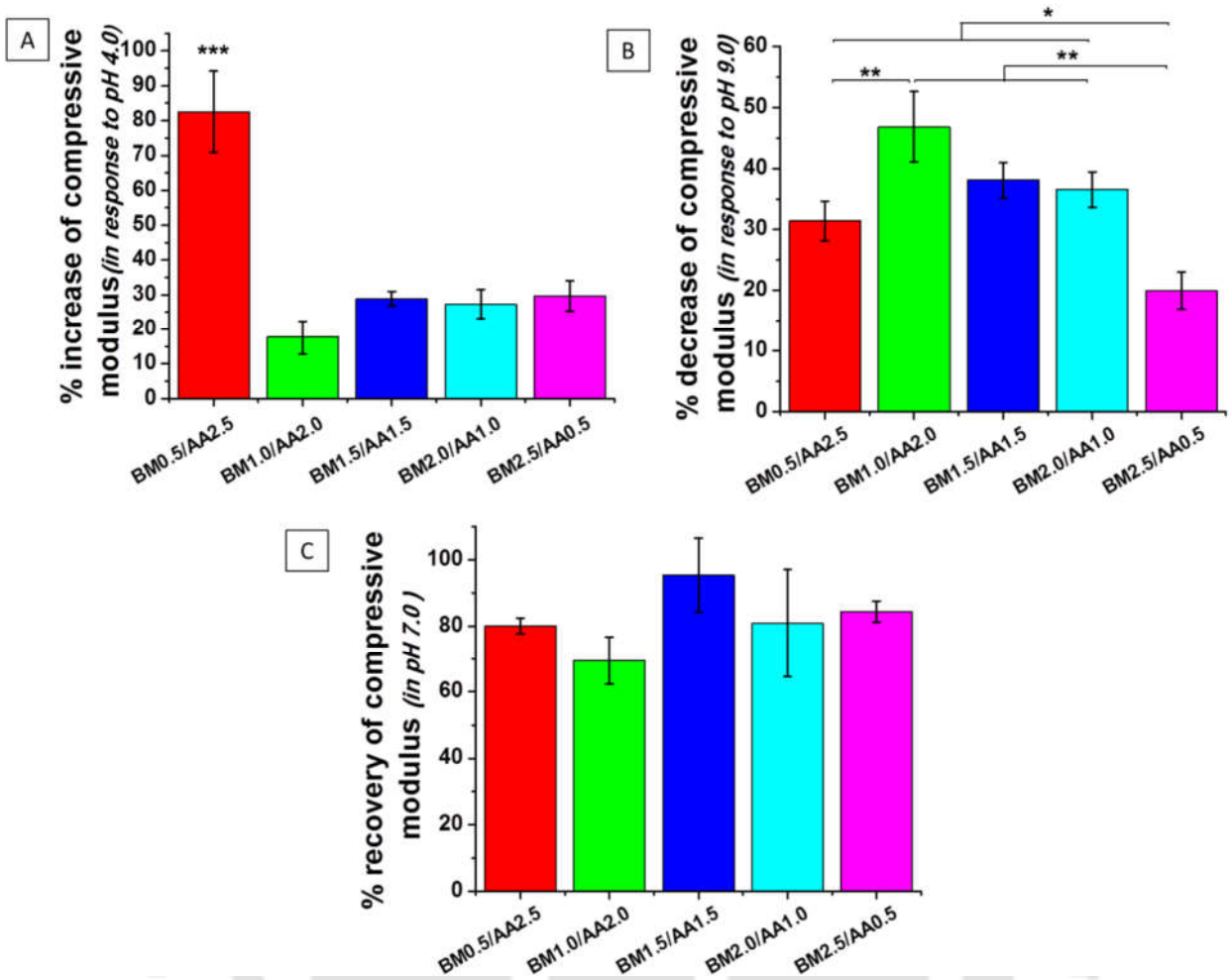

Figure A5.9. *Mechanical properties of hydrogels in response to pH changes; (A) Percentage increase of compressive modulus at pH 4.0, (B) percentage reduction of compressive modulus at pH 9.0, (C) percentage recovery of compressive modulus after transferring hydrogels from pH 9.0 to pH 7.4. Values are plotted as a mean ± standard deviation, n = 3, where *** p≤0.001, ** p≤0.01 and * p≤0.05.*

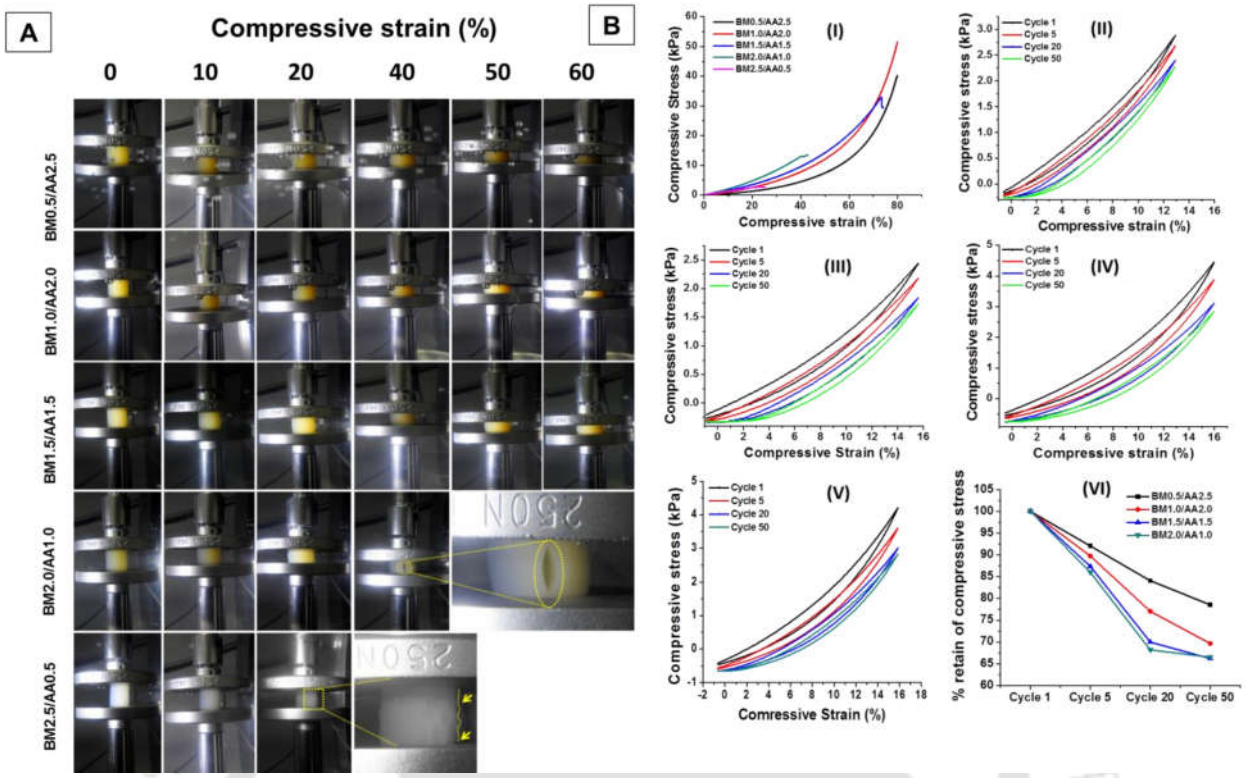

Figure A5.10. *Cyclic mechanical testing of hydrogels; (A) visual images of cyclic testing for all hydrogels, (B) Cyclic compressive testing: (I) typical stress-strain curve, (II) BM0.5/AA2.5 (III) BM1.0/AA2.0 (IV) BM1.5/AA1.5 (V) BM2.0/AA1.0 (VI) percentage retain of compressive stress by hydrogel.*

Table A3.1. Different secondary conformations of SF lamellar constructs obtained through deconvolution of amide-I spectra.

Secondary structure (%)	SF lamellar constructs				
	BM6.0	**BM5.5/AA0.5**	**BM4.0/AA2.0**	**BM5.5/PR0.5**	**BM4.0 /PR2.0**
β-sheet	15.67	23.63	22.17	23.61	22.08
Random coil	5.24	23.64	9.9	17.95	9.36
α-helix	32.11	22.12	38.17	23.44	34.89
Loops	30.18	21.55	19.90	24.90	19.73
β-turn	16.81	7.9	14.90	11.11	13.95

Table A5.1. TT, VT and GT for different hydrogels at different temperatures.

Sample code	25 °C			37 °C			42 °C		
	TT (min)	**VT (min)**	**GT (min)**	**TT (min)**	**VT (min)**	**GT (min)**	**TT (min)**	**VT (min)**	**GT (min)**
BM0.5/AA2.5	0-18	18-60	>60	0-12	12-50	>50	0-12	12-45	>45
BM1.0/AA2.0	0-12	12-55	>55	0-8	8-40	>40	0-8	8-35	>35
BM1.5/AA1.5	0-10	10-50	>50	0-8	8-35	>35	0-8	8-30	>30
BM2.0/AA1.0	0-40	40-70	>70	0-20	20-40	>40	0-18	18-30	>30
BM2.5/AA0.5	N.D.	N.D.	N.D.	N.D.	N.D.	N.D.	0-65	>65	N.D.
BM3.0	N.D.	N.D.	N.D.	N.D.	N.D.	N.D.	N.D.	N.D.	N.D.
AA3.0	N.D.	N.D.	N.D.	0-45	>45	N.D.	0-30	30-70	N.D.

TT = translucent time, VT = viscous time, GT = gelation time and N.D. = not detected

Table A5.2. TT, VT and GT for different hydrogels depending on SF types and concentration.

Sample code	37 °C		
	TT (min)	VT (min)	GT (min)
BM0.5/AA0.5	0-40	40-65	>65
BM1.0/AA1.0	0-30	30-50	>50
BM1.5/AA1.5	0-12	12-38	>38
BM2.0/AA2.0	0-8	9-30	>30
BM2.0/AA0.5	0-38	38-60	>60
AA2.0/BM0.5	0-18	18-45	>45
BM2.0/AA1.0	0-20	20-40	>40
AA2.0/BM1.0	0-12	12-45	>45
BM2.0/AA1.5	0-18	18-35	>35
AA2.0/BM1.5	0-16	16-35	>35
BM2.0/AA2.0	0-10	10-30	>30
AA2.0/BM2.5	0-10	10-30	>30
BM2.0/AA2.5	0-10	10-28	>28
AA2.0/BM2.5	0-10	10-40	>40
BM2.0/AA3.0	0-10	10-28	>28
AA2.0/BM3.0	0-10	10-40	>40

TT = translucent time, VT = viscous time, GT = gelation time

Table A5.3. TT, VT and GT for different hydrogels pH and ionic concentrations.

Conditions	BM1.5/AA1.5, 37 °C		
	TT (min)	**VT (min)**	**GT (min)**
Ca^{2+} concentration			
1 mM	0-15	15-38	>38
2 mM	0-30	30-50	>50
4 mM	0-80	>80	N.D.
K^{+} concentration			
1 mM	0-12	12-38	>38
2 mM	0-12	12-38	>38
4 mM	0-12	12-38	>38
Control	0-12	12-38	>38
pH			
7.4	0-15	15-35	>35
9.0	0-15	15-35	>35

TT = translucent time, VT = viscous time, GT = gelation time and N.D. = not detected

Table A5.4. TT, VT and GT for different hydrogels after addition of EDTA.

Conditions	BM1.5/AA1.5, 37 °C		
	TT (min)	**VT (min)**	**GT (min)**
W/O EDTA and Ca^{2+} (*+Ve* control)	0-15	15-38	>38
With only Ca^{2+} (*-Ve* control)	0-75	>75	N.D.
1 mM EDTA	0-65	65-75	>75
3 mM EDTA	0-65	65-75	>75
5 mM EDTA	0-55	55-62	>62
10 mM EDTA	0-48	48-60	>60
20 mM EDTA	0-20	20-38	>38

TT = translucent time, VT = viscous time, GT = gelation time and N.D. = not detected

Table A5.5. Effect of molecular weight on TT, VT and GT for different hydrogels.

Sample code	BM1.5/AA1.5, 37 °C		
	TT (min)	**VT (min)**	**GT (min)**
sMWBM1.5/AA1.5	0-12	15-35	>35
mMWBM1.5/AA1.5	0-15	15-40	>40
hMWBM1.5/AA1.5	0-20	20-55	>55
hMWBM3.0	N.D.	N.D.	N.D.
mMWBM3.0	N.D.	N.D.	N.D.
sMWBM 3.0	N.D.	N.D.	N.D.
AA3.0	0-50	>50	N.D.

TT = translucent time, VT = viscous time, GT = gelation time and N.D. = not detected

Table A5.6. Different secondary conformations of hydrogels constructs obtained through deconvolution of amide-I spectra

Secondary structure (%)	Hydrogels				
	BM3.0	**AA3.0**	**BM0.5/AA2.5**	**BM1.5/AA1.5**	**BM2.5/AA0.5**
Parallel β-sheet	48.36	59.10	46.58	43.14	19.17
Anti-parallel β-sheet	13.18	5.65	37.98	49.17	46.68
α-helix	7.84	26.14	6.43	0.35	29.16
Loops/turn	30.60	9.09	9.16	1.44	12.79

LIST OF PUBLICATIONS

List of publications

Publications from Ph.D. Thesis:

(A) Journal publications:

1) **Bhunia BK,** Dey S, Bandyopadhyay A, Mandal BB. 3D printing of annulus fibrosus anatomical equivalents recapitulating angle-ply architecture for intervertebral disc replacement. **Applied Materials Today**. 2021;23:101031.
2) **Bhunia BK**, Mandal BB. Exploring gelation and physico-chemical behavior of in-situ bioresponsive silk hydrogels for disc degeneration therapy. **ACS Biomaterials Science & Engineering**. 2019;5:870-886.
3) **Bhunia BK,** Mandal BB. Modulation of extracellular matrix by annulus fibrosus cells on tailored silk based angle-ply intervertebral disc construct. **Materials & Design**. 2018;158:74-87.
4) **Bhunia BK,** Kaplan DL, Mandal BB. Silk-based multilayered angle-ply annulus fibrosus construct to recapitulate form and function of the intervertebral disc. **Proceedings of the National Academy of Sciences of the United States of America**. 2018;115:477-82.
5) **Bhunia BK,** Bandyopadhyay A, Dey S, Mandal BB. Silk-hydrogel functionalized with human decellularized Wharton's jelly extracellular matrix (dWJECM) as a minimally invasive injectable hydrogel system for potential nucleus pulposus tissue replacement therapy. (Manuscript under revision in **Journal of Colloid and Interface Science**).

(B) Conference proceeding (s):

1) **Bhunia BK,** Kumar M, Mandal BB. Development of silk-based angle-ply construct for annulus fibrosus tissue engineering. **European Cells & Materials**. 2017;33:425.

(C) List of workshop/seminars/conferences (oral/poster) presentations:

1) **Bhunia BK,** Bandyopadhyay A, Dey S, Mandal BB. "Fabrication of a minimally invasive injectable nucleus pulposus equivalent bioactive silk-hydrogel functionalized with decellularized human Wharton's jelly extracellular matrix for disc regeneration therapy". International e-Symposium on "Smart Polymers: Applications in current scenario" (SP-ACS) 15-16th January 2021 on virtual platform (**Poster presentation**).
2) **Bhunia BK,** Bandyopadhyay A, Dey S, Mandal BB. "Development of nucleus pulposus equivalent silk-hydrogel functionalized with decellularized human Wharton's jelly extracellular matrix for disc regeneration therapy". Young Scientist Conference (YSC) in India International Science Festival (IISF 2020) 22-25th December 2020 on virtual platform (**Oral presentation**)
3) **Bhunia BK,** Dey S, Bandyopadhyay A, Mandal BB. "Silk hydrogel functionalized with human decellularized Wharton's jelly matrix as a minimally invasive injectable hydrogel for nucleus pulposus tissue engineering". International conference on biomedical materials innovation 2020 (ICBMI 2020). 30th SBAOI annual meeting and 12th STERMI annual meeting, 6-9th December, 2020, Virtual conference. (**Oral presentation**)
4) **Bhunia BK,** Dey S, Bandyopadhyay A, Mandal BB. "3D Printing of Annulus Fibrosus Anatomical Equivalents Recapitulating Angle-ply Architecture for Intervertebral Disc Replacement". Young Scientist Conference (YSC) in India International Science Festival (IISF Kolkata 2019) 5-8th November 2019 at Biswa Bangla Convention Center, Kolkata, West Bengal, India (**Poster presentation**)
5) **Bhunia BK**, Mandal BB. "Design, fabrication and behavioral study of in situ forming silk hydrogel for nucleus pulposus tissue engineering". Research conclave 2019, IIT Guwahati, 14-17th March, 2019 (**Oral presentation**)
6) **Bhunia BK,** Mandal BB. "Tailoring mechanical properties of silk based engineered disc to modulate matrix deposition of annulus fibrosus cells". Research Conclave 2018, IIT Guwahati, 9-11th March, 2018. (**Oral presentation**)
7) **Bhunia BK,** Mandal BB. "Development of Bio-artificial Disc for Low Back Pain Management". Workshop-Innovation Management & Product Commercialization, Indian Institute of Advanced study in Science and Technology, 3rd March, 2017. (**Oral presentation**)

8) **Bhunia BK,** Mandal BB. "A novel strategy to develop silk based multilayered disc-like angle-ply construct to recapitulate form and function of annulus fibrosus". International Conference of Young Researchers on Advanced Materials (IUMRS-ICYRAM 2016), Indian Institute of Science, Bangalore, 11-15th December, 2016. (**Poster presentation**)

(D) List of award(s):

1) **Bhunia BK,** Dey S, Bandyopadhyay A, Mandal BB. "Design and fabrication of 3D-printed biomimetic constructs to recapitulate form and function of annulus fibrosus tissue". 1st Departmental retreat (Biotech Express) organized by Department of Biosciences and Bioengineering (BSBE), IIT Guwahati on 21st December 2019 (**Best poster award**)
2) **Bhunia BK,** Mandal BB. "Exploring in situ gelling and physicochemical behavior of bioresponsive silk hydrogel for nucleus pulposus tissue engineering". Poster presented at International Conference on Functional Nanomaterial (ICFNM) 2019 organized by Department of Physics, Indian Institute of Technology (BHU) Varanasi, 22-25th February, 2019. (**Best poster award**)
3) **Bhunia BK,** Mandal BB. "Engineered disc-like angle-ply construct to recapitulate form and function of annulus fibrosus". Poster presentation at Indo-Japan Bilateral Symposium on Future Perspective of Bioresource Utilization in North-Eastern Region (IJBS 18), 1-4th February, 2018. (**ACS Omega best poster award**)
4) **Bhunia BK,** Mandal BB. "Affordable bio-artificial disc for low back pain management". Proposal presented in Assam Biotech Conclave, organized by Guwahati Biotech Park. 5-6th January, 2017. (**Best oral presentation awarded with Rs. 30000/**)

Publications from other collaborative research projects:

(A) Journal publications:

1) Arora D, **Bhunia BK**, Janani G, Mandal BB. Bioactive three-dimensional silk composite in vitro tumoroid model for high throughput screening of anticancer drugs. **Journal of Colloid and Interface Science**. 2021;589:438-52.
2) Parbat D, **Bhunia BK**, Mandal BB, Manna U. Bio-inspired underwater super-oil-wettability for controlling platelet adhesion. **Chemistry–An Asian Journal**. 2021;16:1081-85.

3) Shome A, Rather AM, Ghosal A, **Bhunia BK**, Mandal BB, Manna U. Rational chemical engineering in natural protein derived functional interface. **ACS Sustainable Chemistry & Engineering**. 2019;7:7502-09.
4) Rather AM, Shome A, **Bhunia BK**, Panuganti A, Mandal BB, Manna U. Simultaneous and controlled release of two different bioactive small molecules from nature inspired single material. **Journal of Materials Chemistry B**. 2018;6:7692-702.
5) Soni SR, Kumari N, **Bhunia BK**, Sarkar B, Mandal BB, Ghosh A. *In vitro* and *in vivo* evaluation of pirfenidone loaded acrylamide grafted pullulan-poly (vinyl alcohol) interpenetrating polymer networks. **Carbohydrate Polymers**. 2018;202:288-98.
6) Soni SR, Kumari N, **Bhunia BK,** Sarkar B, Mandal BB, Ghosh A. Synthesis and characterization of a non-cytotoxic and biocompatible acrylamide grafted pullulan–application in pH responsive controlled drug delivery. **International Journal of Biological Macromolecules**. 2018;120:753-62.
7) Soni SR, **Bhunia BK,** Kumari N, Dan S, Mukherjee S, Mandal BB, Ghosh A. Therapeutically effective controlled release formulation of pirfenidone from nontoxic biocompatible carboxymethyl pullulan-poly (vinyl alcohol) interpenetrating polymer networks. **ACS Omega**. 2018;3:11993-2009.
8) Rather AM, Shome A, Kumar S, **Bhunia BK,** Mandal BB, Srivastava HK, Manna U. Alkali metal-ion assisted Michael addition reaction in controlled tailoring of topography in a superhydrophobic polymeric monolith. **Journal of Materials Chemistry A**. 2018;6:17019-31.
9) Dalapati R, Nandi S, Reinsch H, **Bhunia BK**, Mandal BB, Stock N, Biswas S. Fluorogenic naked-eye sensing and live-cell imaging of cyanide by hydrazine-functionalized CAU-10 metal-organic framework. **CrystEngComm**. 2018;20:4194-201.
10) Singh Y, **Bhunia BK,** Nandi SK, Mandal BB. Hierarchically structured seamless silk scaffolds for osteochondral interface tissue engineering. **Journal of Materials Chemistry B**. 2018;6:5671-88.
11) Das A, Deka J, Rather AM, **Bhunia BK,** Saikia PP, Mandal BB, Raidongia K, Manna U. Strategic formulation of graphene oxide sheets for flexible monoliths and robust polymeric coatings embedded with durable bioinspired wettability. **ACS Applied Materials & Interfaces**. 2017;9:42354-65.

12) Singh YP, Adhikary M, Bhardwaj N, **Bhunia BK,** Mandal BB. Silk fiber reinforcement modulates *in vitro* chondrogenesis in 3D composite scaffolds. **Biomedical Materials**. 2017;12:045012.
13) Konwarh R, **Bhunia BK,** Mandal BB. Opportunities and challenges in exploring Indian nonmulberry silk for biomedical applications. **Proceedings of the Indian National Science Academy**. 2017;83:85-101.
14) Singh SK, **Bhunia BK,** Bhardwaj N, Gilotra S, Mandal BB. Reloadable silk-hydrogel hybrid scaffolds for sustained and targeted delivery of molecules. **Molecular Pharmaceutics**. 2016;13:4066-81.
15) Biswas S, **Bhunia BK**, Janani G, Mandal BB. Silk fibroin composite powder as hemostatic agent. (Manuscript under revision in **ACS Biomaterial Science and Engineering**)

(B) Conference proceeding (s):

1) Singh YP, Christakiran JM, **Bhunia BK**, Mandal BB. Bi-phasic silk scaffolds for osteochondral tissue engineering. (TERMIS-EU Meeting, 28th June – 1st July 2016) June 2016, **European Cells & Materials**. 06/2016; 31:326.
2) Singh Y, Adhikary M, Bhardwaj N, **Bhunia BK**, Mehrotra S, Mandal BB. Bioinspired three dimensional construct with silk fiber reinforcement for regeneration of load bearing soft tissues. **Tissue Engineering Part A**. 2017;23:S102.

(C) Patent (s):

1) Mandal BB, Biswas S, **Bhunia BK**. Hemostatic silk fibroin composite powder. Indian patent submitted on 28th November, 2020 with application no. **202031051948**.
2) Mandal BB, Singh YP, Bandyopadhyay A, Mehrotra S, Moses JC, **Bhunia BK**, Janani G, Chouhan D. Development of silk based bioinks for 3D printing and uses thereof. Indian patent submitted on 12th October, 2019 with application no. **201831038727**.
3) Mandal BB, **Bhunia BK "**Affordable antimicrobial spray based coating for personal protective equipment's". Indian patent submitted on 2nd April, 2021 with application no. **202031014932**.

(D) Book chapter (s):

1) Singh YP, Mehrotra S, Kumar JP, **Bhunia BK**, Bhardwaj N, Mandal BB. "Regeneration of sensory system: tissue engineering therapies for ocular regeneration". Biomaterials and Nanotechnology for Tissue Engineering, edited by Sethuraman S, Krishnan UM, and Subramanian A. CRC press, Taylor & Francis Group, 2016;173. (ISBN 9780367736729).

(E) List of seminars/conferences (oral/poster) presentations:

1) Dey S, Bandyopadhyay A, **Bhunia BK,** Mandal BB. "Demonstration of 3D printing" 6th National Workshop on NEMS/MEMS and Theranostics Devices (NWNTD 2020), Centre for excellence in research and development of nanoelectronics theranostic devices under the aegis of Centre for Nanotechnology at the Indian Institute of Technology Guwahati (IIT Guwahati). 1-3rd December 2020, virtual conference. (Video presentation).
2) Dey S, Kumar M, Chouhan D, Gangrade A, **Bhunia BK**, Mehrotra S, Gupta P, Singh YP, Christakiran J, Janani G, Bandyopadhyay, Mandal BB. "Northeast silk based healthcare technologies". The day-long workshop IITG Socity and Northeast India (ISANI-an Introspection) on 21st February at the Conference Center (**Poster presentation**)
3) Singh YP, Christakiran JM, **Bhunia BK**, Nandi SK, Mandal BB. "Seamless biphasic silk construct for the repair of osteochondral defect". Advanced Functional Polymers for Medicine (AFPM) 2018, Montpellier, France, 16-18th May, 2018. (sciencesconf.org:afpm2018:202183) (**Poster presentation**)
4) Singh YP, Adhikary M, Bhardwaj N, **Bhunia BK**, Mehrotra S, Mandal BB. "Bio-inspired three dimensional construct with silk fiber reinforcement for regeneration of load bearing soft tissue". Tissue Engineering and Regenerative Medicine International Society America 2017 (TERMIS-AM 2017), Charlotte, North Carolina, 3-6th December, 2017. (**Poster presentation**)
5) **Bhunia BK,** Singh YP, Chouhan D, Jasmine S, Mandal BB. "Silk based tissue engineering. Research Conclave-2015". Organized by Indian Institute of Technology Guwahati (IITG), Guwahati, Assam, India. 17-19th April, 2015 (**Poster presentation**)

6) Participated in national seminar on "Recent advances in cancer biology and therapeutics-2014" organized by Department of Biotechnology (currently known as Department of Biosciences and Bioengineering), Indian Institute of Technology Guwahati, 5th December, 2014.

(F) List of award (s):

1) Team (Silk based 3D bioprinted human tissue, members include Bandyopadhyay A, Mehrotra S, Dey S, **Bhunia BK**, Mandal BB), presented our work on "3D Bioprinting" and awarded with "**Best project from IIT Guwahati**" in TechExpo 2018 organized during Techniche 2018 at IIT Guwahati during 30th August to 2nd September 2018.
2) Singh YP, Chouhan D, Kumar M, **Bhunia BK**, Mnadal BB. "Silk based affordable healthcare solution". Model presentation at Techniche 2017, IIT Guwahati during 31st August to 3rd September 2017. (**Team won 2nd Prize, awared with Rs. 40000/)**
3) Singh SK, **Bhunia BK** (presenting author), Bhardwaj N, Gilotra S, Mandal BB. "Reloadable silk-hydrogel hybrid scaffolds for sustained and targeted delivery of molecules". Poster presented at Research Conclave 2017, Indian Institute of Technology Guwahati, 16-19th March, 2017. (**Best poster award**)
4) **Bhunia BK,** Chouhan D, Singh YP, Kumar M, Gupta P, Mandal BB. "Silk based affordable tissue grafts and health care products". IITG-TIC inovation competition, 29th October 2016. (**won 2nd Prize, awared with Rs. 15000/)**

(G) Product development and technology transfer:

1) The developed *silver-nanoparticle based antimicrobial agent* is now commercially available as brand name "**Breath Easy Safe 24**" manufactured by ***Berger Paints India Ltd***.